

Ministry of education and science of Ukraine  
Odessa I. I. Mechnikov National University

# ФОТО ЭЛЕКТРОНИКА

**PHOTOELECTRONICS**  
**INTER-UNIVERSITIES SCIENTIFIC ARTICLES**

Founded in 1986

Number 17

Odessa  
«Astroprint»  
2008

The results of theoretical and experimental studies in problems of optoelectronics, solar power and semiconductor material science for photoconductive materials are adduced in this collection. The prospective directions for photoelectronics are observed.

The collection is introduction into the List of special editions of Ukrainian Higher Certification Commission in physics-mathematics and technical sciences.

For lecturers, scientists, post-graduates and students.

У збірнику наведені результати теоретичних і експериментальних досліджень з питань оптоелектроніки, сонячної енергетики і напівпровідникового матеріалознавства фото-провідних матеріалів. Розглянуто перспективні напрямки розвитку фотоелектроніки.

Збірник включено до Списку спеціальних видань ВАК України з фізико-математичних та технічних наук.

Для викладачів, наукових працівників, аспірантів, студентів.

**E d i t o r i a l   b o a r d :**

**SMYNTYNA V.A.** (editor-in-chief)—academician, Higher School Academy of Ukraine; **KUTALOVA M.I.** (executive secretary); **МАК V.T.**—Dr.Sci. (Physics and Mathematics); **LITOVCHENKO V.G.**—Associate Member of Ukrainian Academy of Sciences; **VIKULIN I.M.**—Dr. Sci. (Physics and Mathematics), Professor; **CHEMERESYUK G.G.**—Professor; **SHEINKMAN M.K.**—Associate Member of Ukrainian Academy of Sciences.

**A d d r e s s   o f   e d i t o r i a l   b o a r d :**

Odessa I.I.Mechnikov National University 42, Pasteur str, Odessa, 65026, Ukraine  
e-mail: wadz@mail.ru, tel.: +38-0482-7266356.

Information is on the site: <http://www.photoelectronics.onu.edu.ua>.

**DOCTOR IN PHYSICS AND MATHEMATICS, PROFESSOR SMYNTYNA  
VALENTIN ANDRYOVICH (TO THE 60-TH ANNIVERSARY)**



On the September 8, 2008, well-known scientist, Doctor in Physics and Mathematics, Professor, The Rector of I. I. Mechnikov Odesa National University, Head of the Editorial Board of our magazine **Smyntyna Valentin Andriyovich** will celebrate the 60-th birth anniversary.

Smyntyna Valentin Andriyovich was born on September 8, 1948 in the settlement Vishneve, Tatarbunar district, Odesa region, Ukraine. He has graduated with Honor the Physical Faculty of I. I. Mechnikov Odesa State University and, afterwards, the postgraduateship at the Chair of Experimental Physics, Physical Faculty of the said University. He has prepared and successfully maintained the Ph. D. Thesis (Candidate level) in Physics of Semiconductors and Dielectrics in the year of 1977.

In the period of 1981–1984 years Valentin A. Smyntyna was the Deputy Dean in scientific purposes of the Physical Faculty of I. I. Mechnikov Odesa State University. Valentin A. Smyntyna has prepared and successfully maintained the Doctor of Sciences Dissertation in the Scientific Council of the Institute of Physics of Semiconductors, National Academy of Sciences, Ukraine, in 1988.

Beginning from the year of 1990, D. Sc. Valentin A. Smyntyna is the scientific leader of the sensor electronics and technology laboratory as well as the lecturing professor at the Chair of Experimental Physics. He becomes the Head of this Chair afterwards. Professor Valentin A. Smyntyna was appointed to the Post of Vice-Rector in International Cooperation and External Economic activities.

Professor Valentin A. Smyntyna was elected the Rector of I. I. Mechnikov Odesa National University in 1995. During the successful activities of the Rector Valentin A. Smyntyna, the University has occupied the leading position (3<sup>rd</sup>–4<sup>th</sup> places) according to the main parameters among classic Universities of Ukraine. The I. I. Mechnikov Odesa State University was awarded with the title National due to the Decree of the President of Ukraine on September 11, 2000.

Professor Valentin A. Smyntyna is widely and well known among the scientists and researchers in the field of semiconductors. His scientific interests are connected with the research of electronic-molecular processes on the surface and layer borders, what have initiated the new direction of the research in this field. Under his leadership, the active group of scien-

tists and researchers who initiated the creation of new research laboratory devoted to the sensor electronics and technologies. Among the results of the laboratory activities there are the group of sensors of the gaseous ambient state and the imaging sensors of new generation.

Professor Valentin A. Smyntyna has headed the group of researchers engaged in complex research of the electro-physical properties of non-ideal heterogeneous junctions what allows to develop the principally new image signals generator with the intrinsic amplification. Such a device has, as well, the ability of the signals' storage and memory even at room temperatures. Professor Valentin A. Smyntyna has participated personally in research resulted in development of the experimental devices for images' visualization and storage obtained with the sensors. It was established experimentally that the developed imaging sensors have significant sensitivity in X-ray range of wavelengths. This sensing ability could be put in the basement of their wide applications in various branches of science and technology which need the fast input of the obtained X-ray images' elements such as the sensing element of the computer X-ray tomography. Obtained optical and X-ray images certify the usefulness of the developed transformers. It should be mentioned, that the new applications of the developed sensors are based on such their properties which were considered previously as the anomalous ones, which affects negatively the regular way of the photo-sensor use.

The results of the research in the field of non-ideal heterogeneous junctions photo-electrical properties as well as their applications in the form of imaging sensors developed under personal leadership of Professor Valentin A. Smyntyna, were published many times in our magazine.

Along with the administrative, research and lecturing activities of Professor Valentin A. Smyntyna, mentioned in part above, we would like to emphasize his personal participation in the international scientific programs, accompanied by scientists from Italy, France, Germany, Great Britain, the Netherlands, Belgium and Finland. He is the acting member (Academician) of the Academy of Higher Education of Ukraine and of some branch Academies, the founding Member of the International Academy of Computer Sciences and Systems, the Deputy Head of the Board of Southern Center of the National Academy of Sciences of Ukraine, the Member of the European Committee of the "EUROSENSOR" Society, National Coordinator and Member of the European Council of the "NEXUS" Programmes, the Expert of the State Awards Committee of Ukraine, the Member of European and Ukrainian Physical Societies (the Vice-President of the last).

Academician Valentin A. Smyntyna is the Head of the scientific specialized Council for D. Sc. in Physics approval, The Chief Editor of the magazines "Odesa University Herald", "Photoelectronics" and "Sensor

Electronics & Microsystem Technology". Academician Valentin A. Smyntyna is the coordinating consultant of the International Humanitarian Association "Italy-Ukraine". Academician Valentin A. Smyntyna is the Member of the World-Wide Association of the Universities Presidents and of the Association of the Ukrainian Universities Rectors, the Member of the Scientific Council for the Sensoric Systems at the Presidium of the National Academy of Sciences of Ukraine and of the Scientific Council of the National Academy of Sciences of Ukraine. Academician Valentin A. Smyntyna is the Honor Member of the Senate of the Academic Szegeed University, Hungary and the Merited Statesman of Science and Technology of Ukraine (2000). He is the Honored Doctor of the Slavonic Humanitarian University, Moscow, Russia, The Honored Professor of the Kherson National Technical University, Kherson, Ukraine, of the By-Dniester State University, Tiraspol.

Academician Valentin A. Smyntyna was awarded with the State Prize of Ukraine (2008). The valuable input of Doctor of Sciences, Professor Valentin A. Smyntyna to the development of the national science was indicated with the following awards:

— The Honor Sign of the Ministry of the Education and Science of Ukraine "For Scientific Achievements" (2006, 2007);

— The Honor Signs of the National Academy of Sciences of Ukraine "For the Preparation of the Scientific Youth" (2007) and "For Scientific Merit" (2008);

— The Golden Medal of the 1<sup>st</sup> grade of the Ministry of the Education and Science of Ukraine "10 years of Independence".

Academician Valentin A. Smyntyna was awarded also with:

— The Order "For the Merit" of the 3<sup>rd</sup> grade (2004);

— The Order "200-th Anniversary of the Christmas" of the 2<sup>nd</sup> grade;

— The Order "Saint Volodymyr" of 4<sup>th</sup> grade;

— The Order "Saint Nestor Historian" of 2<sup>nd</sup> grade;

— The Order of the Italian President "Italian Solidarity" of 3<sup>rd</sup> grade;

— The Order "Golden Cross of Saints Peter and Paul" (Vatican);

— The Golden Medal of the Society of the Industrial Support (France).

Academician Valentin A. Smyntyna is the author and co-author of more than 400 papers, has 19 Author Certificates on the inventions, 5 monographs and manuals approved by the Ukrainian Ministry of Education and Science of Ukraine. Under his personal tutorship 3 Doctor and 6 Candidate dissertations were successfully maintained.

The Editorial Board of the magazine and the colleagues greet kindheartedly Valentin A. Smyntyna with the Jubilee and wish good health, inspiration and further creative successes.

## TABLE OF CONTENT

<i>V. A. SMYNTYNA, L. N. FILEVSKAYA, V. S. GRINEVICH</i> Surface and optical properties of tin dioxide nano-films influenced by the initial solution composition .....	4
<i>O. V. LYASHENKO, A. P. ONANKO, V. P. VELESCHUK, I. O. LYASHENKO, Y. A. ONANKO</i> Structural defects relaxation during complex thermal and dynamical mechanic processing of CdTe .....	8
<i>A. V. GLUSHKOV, O. Yu. KHETSELIUS, L. V. NIKOLA, Yu. V. DUBROVSKAYA</i> Quantum calculation of Auger spectra for atoms and semiconductors: New approach .....	12
<i>G. S. FELYNSKIY</i> Spectroscopic methods of active srs photonics devices modeling for telecommunication systems with terbyte velocity .....	16
<i>V. A. SMYNTYNA, V. A. BORSCHAK, M. I. KUTALOVA, N. P. ZATOVSKAYA, A. P. BALABAN</i> External bias influence on transmission processes in nonideal heterojunction .....	21
<i>E. P. GURNITSKAYA</i> The ground state lamb shift in hydrogenic germanium within the qed theory .....	26
<i>A. S. PHOMIN, V. P. MYGAL, A. V. BUT</i> The Research OF PHOTORESPONSE SPECTRAL instability of the CdZnTe crystals .....	30
<i>O. O. PTASHCHENKO, F. O. PTASHCHENKO, N. V. MASLEYEVA, O. V. BOGDAN, V. V. SHUGAROVA</i> Effect of sulphur atoms on surface current in GaAs P-N junctions .....	34
<i>D. GAMOV, G. KALISTIY, O. OBEREMOK, V. POPOV, I. HATSEVYCH</i> Influence of Al <sup>+</sup> and Ti <sup>+</sup> implantation on radiating properties of the nano-cluster structures .....	38
<i>A. A. SVINARENKO, N. G. SERBOV, Yu. G. CHERNYAKOVA</i> Wavelet and multifractal analysis of oscillations in a grid of coupled autogenerators: a case of strong non-linearity .....	42
<i>S. L. KHRYPKO</i> Investigation of the solar cells with porous silicon films .....	45
<i>A. V. GLUSHKOV, Ya. I. LEPIKH, S. V. AMBROSOV, O. Yu. KHETSELIUS, Yu. G. CHERNYAKOVA</i> Computer modelling optimal schemes of the laser photoionization method for preparing the films of pure composition at atomic level .....	51
<i>E. RUSU, V. URSKI, G. NOVITSCHI, A. BURLACU, P. PETRENKO, L. KULIUK</i> Luminescence of ZnGa <sub>2</sub> O <sub>4</sub> and ZnAl <sub>2</sub> O <sub>4</sub> spinels doped with Eu <sup>3+</sup> AND Tb <sup>3+</sup> ions .....	54
<i>V. A. SMYNTYNA, O. A. KULINICH, M. A. GLAUBERMAN, G. G. CHERMERESYUK, I. R. YATSUNSKIY</i> The structure investigation of near-surface layers in silicon – dioxide silicon systems .....	59
<i>E. V. BRITAVSKY, Y. M. KARAKIS, M. I. KUTALOVA, G. G. CHERMERESYUK</i> On the charge state of rapid and slow recombination centers in semiconductors .....	62
<i>I. B. OLENYCH, L. S. MONASTYRSKII</i> Influence of electric field on photoluminescence of porous silicon .....	68
<i>A. V. LOBODA</i> Quantum theory of collisions of the ultracold atoms with nanostructures .....	71
<i>G. S. FELINSKIY, P. A. KOROTKOV</i> Optical-fibre raman amplifiers with 6.3–12.2 thz working band .....	74
<i>Yu. F. VAKSMAN, Yu. A. NITSUK, Yu. N. PURTOV, A. S. NASIBOV, P. V. SHAPKIN</i> Preparation and optical properties of ZnSe:Co films .....	79
<i>S. V. AMBROSOV, O. Yu. KHETSELIUS, A. V. IGNATENKO</i> Wannier-mott excitons and H, Rb atoms in a dc electric field: stark effect .....	82
<i>I. M. VIKULIN, SH. D. KURMASHEV, S. N. NIKIFOROV, M. I. PANFILOV</i> Photodetector on the base of uni-junction transistor and photo-diode .....	86
<i>A. V. GLUSHKOV, Ya. I. LEPIKH, A. P. FEDCHUK, O. Yu. KHETSELIUS</i> Electrodynamical and quantum - chemical modelling the electrochemical and catalytic processes on metals and semiconductors: lanthanide perovskites .....	89
<i>V. V. KOVALCHUK, O. V. OSIPENKO</i> Silicon Surface with Clusters .....	94
<i>R. M. BALABAY, D. V. RYABCHIKOV</i> Electronic structure of the surface of the single-walled carbon nanotube: <i>ab initio</i> calculation .....	98
<i>T. N. SHCHUROVA, N. D. SAVCHENKO, A. B. KONDRAT, K. O. POPOVYCH, V. M. RUBISH, G. LEISING</i> Simulation of the surface bending of energy band for binary chalcogenide semiconductors .....	102
<i>A. F. BUTENKO, S. N. FEDOSOV, A. E. SERGEEVA</i> Components of depolarization currents in polyvinylidene fluoride caused by relaxation of homo- and heterocharge .....	106
<i>F. O. PTASHCHENKO</i> Effect of ammonia vapors on surface currents in InGaN P-N junctions .....	111
<i>R. BALABAY, E. CHERNONOG</i> Investigations of Si/Si-O <sub>y</sub> -Si <sub>4-y</sub> nanosystem by the computer simulation method .....	115
<i>A. A. SVINARENKO</i> Wavelet and multifractal analysis of nonlinear features in the acoustic detecting the granulated materials .....	118
<i>A. N. NAZAROV, I. N. OSIYUK, I. P. TYAGULSKYY, V. S. LYSENKO, S. I. TIAGULSKIY, V. N. TORBIN, V. V. OMELCHUK, T. M. NAZAROVA, T. GEBEL, L. REBOHLE, W. SKORUPA</i> Electroluminescence, charge trapping and degradation of the silicon dioxide implanted by carbon and silicon ions .....	121
<i>O. Yu. KHETSELIUS, E. P. GURNITSKAYA, A. V. LOBODA, L. A. VITAVETSKAYA</i> Consistent quantum approach to quarkony energy spectrum and semiconductor superatom and in external electric field .....	127
<i>G. YA. KOLBASOV, I. A. RUSETSKII</i> Photosensitivity of nanostructured gallium arsenide in contact with electrolyte .....	130
<i>A. G. BALOGH, S. M. DUVANOV, D. I. KURBATOV, A. S. OPANASYUK</i> Rutherford backscattering and x-ray diffraction analysis of Ag/ZnS/glass multilayer system .....	134
ТРЕБОВАНИЯ К ОФОРМЛЕНИЮ СТАТЕЙ В СБОРНИК «ФОТОЭЛЕКТРОНИКА» ИНФОРМАЦИЯ ДЛЯ АВТОРОВ .....	140

V. A. SMYNTYNA, L. N. FILEVSKAYA, V. S. GRINEVICH

Odessa I. I. Mechnikov National University,  
st. Dvoryanskaya, 2, Odessa 65082, Ukraine, phone/fax 38-048-7317403, e-mail [grinevich@onu.edu.ua](mailto:grinevich@onu.edu.ua)

## SURFACE AND OPTICAL PROPERTIES OF TINDIOXIDE NANO-FILMS INFLUENCED BY THE INITIAL SOLUTION COMPOSITION

The surface morphology and optical absorption results of nanostructured SnO<sub>2</sub> films, obtained using polymers are presented in the work. Optical densities dependencies and evaluation of electronic parameters of films are fulfilled for solutions with different contain of tin component. The forbidden zone width correlation is noticed for different compositions of solutions. The dimensional quantization energy, calculated by two different methods has similar results.

### INTRODUCTION

Tin dioxide is one of few materials, which may be obtained and preserved in a nano scale. It has good chemical resistance in aggressive medias and is highly sensitive to the environmental changes. These properties define the preferable use of this material in a gas analysis as adsorptive-sensitive elements [1]. Quantum-dimensional effects, typical for nanosized grains' materials, allows to extend their application to electronic technique. Such materials' properties essentially depend upon the technique of their production and many technological parameters. The reagent composition, temperature and time peculiarities of the technology essentially influence the chemical methods of production.

Structure's difference and film materials' properties are practically well developed in the optical investigations.

An optical radiation interaction investigation results in transmission spectra of semiconductor films, allow to define forbidden zone width, optical transitions at the absorption edge, and to evaluate phonons' and electrons' dimensional quantization energy.

### SAMPLES PRODUCTION TECHNIQUE AND THE INVESTIGATIONS METHODS

Transparent thin films of nanostructured tin dioxide were obtained using the polymer materials. The technique described in [2] comprised several stages, which include the polymer material solution preparation in the solvent and the thin containing organic compound insertion into it. The solution formed was deposited on the glass substrate, dried and annealed in a muffle. The temperature and time of annealing corresponded to the temperature and time of polymer's decomposition. After the polymer's decomposition products were fully taken away, and the oxidation was over, the thin tin dioxide layers were formed with developed nanoscale structure.

Aiming to determine the initial gels' composition influence (as a technological factor) upon their surface morphology the samples were prepared with different quantity of the tin containing filler in the initial solu-

tion. The four-valent tin acetyl acetonate (Sn(acac)<sub>4</sub>) of 1%, 5% and 10% concentrations were used. The polymer concentration was one and the same in all types of films and was 0,1% of polyvinylacetate.

The tin dioxide layers' surface morphology was investigated by the industrial atom-force microscope (AFM) NanoScope IIIa (Digital Instruments, USA) – Courtesy of Lashkarev Institute of Semiconductors Physics of Ukrainian National Academy of Sciences. Measures were fulfilled by silicon probe with nominal radius ~10 nm (firm-producer NT-MDT, Russia), in a regime of a periodical contact (Tapping Mode™). The investigated area surface was 500×500 nm<sup>2</sup>.

The optical absorption for transitions in the waves' interval 300–750 nm was measured for SnO<sub>2</sub> layers aiming the evaluation the initial solutions' (acetyl acetonate of Sn (1, 5 and 10%) influence upon the layers electronic properties. The standard methods were used for spectrophotometer CF-46 measurements.

### EXPERIMENTAL RESULTS

The 3-D AFM images for films' surfaces are given at Fig. 1. The least uniform structure is seen for the layers, obtained of the solvent with the initial content of Sn(acac)<sub>4</sub> (1%). The layers become more uniform with Sn(acac)<sub>4</sub> concentration growth in the initial solvents.

The optical density absorption spectra  $D(h\nu)$  are given at fig. 2, while analyzing the edge of absorption band form it is important to know, only the spectral changes of the absorption coefficient, but not it's value.

In the optical density spectrum there are two peaks: in the red region (1,85 eV for 1%, 1,88 for 5% and 1,84 eV for 10% Sn(acac)<sub>4</sub> and specific for tin dioxide peak in the nearest UV region (for 1% — 3,6 eV; for 5% — 3,5 eV; for 10% — 3,6 eV). The sharp break in the UV spectrum may be caused by different reasons. It is known [3] that tin dioxide is transparent for the nearest UV, and besides that, the glass substrate absorption gives principal changes to investigated films' spectrum.

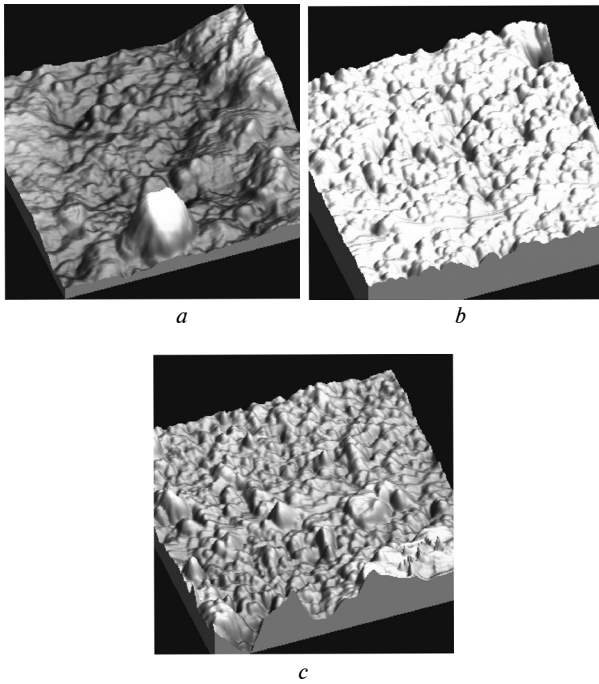


Fig. 1. 3-D AFM images of films' surfaces: *a* – 1%, *b* – 5%, *c* – 10% Sn(acac)<sub>4</sub> in the initial solvent (image size 500×500 nm<sup>2</sup>)

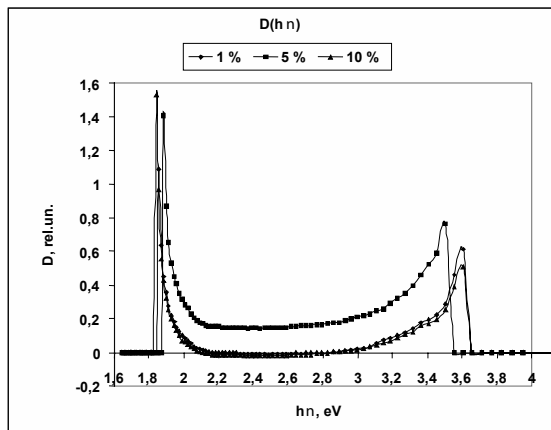


Fig. 2. The optical density spectra of nanostructured SnO<sub>2</sub> films, obtained from 0,1% PVA solutions and different Sn(acac)<sub>4</sub> content (1, 5 and 10 %)

## DISCUSSION OF RESULTS

The AFM images analysis allows concluding about grain nanoscale structure in the films. Average grains' size, determined from the images, consists 10–15 nm. The least uniform films were obtained of low concentration Sn(acac)<sub>4</sub> solution.

The forbidden zone width and optical transitions character were defined using optical absorption edge investigation. The optical density in the absorption edge region is presented at fig. 3.

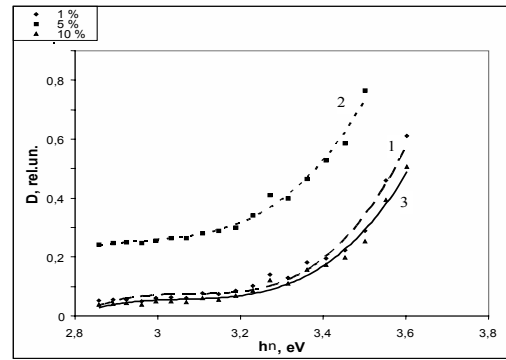


Fig. 3. Optical density spectra at the absorption edge region: 1 – 1%, 2 – 5%, 3 – 10% Sn(acac)<sub>4</sub> in the initial solution.

The results were replotted in  $D_0^{1/s} = f(\hbar\omega)$  ( $s = 1/2, 3/2, 2, 3$ ) coordinates for the optical transitions types definition, and presented at fig. 4.

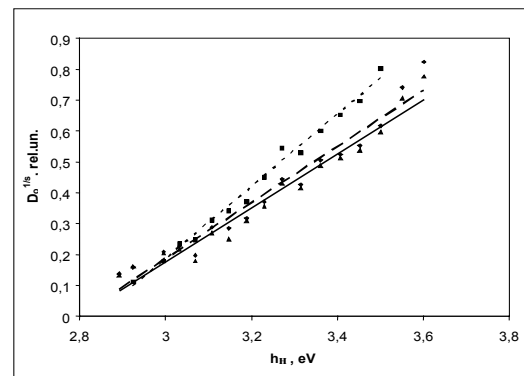


Fig. 4. The replotted optical density of the investigated layers in the absorption edge region at  $s=3$ . Dot and dash line corresponds to the same one at fig. 3

The best rectification of a curve takes place at  $1/s = 1/3$  corresponding to optical density dependence

$D_0^{1/s} = f(\hbar\omega)$ ; This corresponds to indirect forbidden transitions with phonons participation.

The nearest UV zone absorption, which corresponds to the absorption edge at calculation gives the forbidden zone width: for 1% – 2,96 eV, for 5% – 2,95 eV, for 10% Sn(Acac)<sub>4</sub> – 2,935 eV. Phonons' energy is – 0,14 eV for 1%, 0,07 eV for 5%, 0,135 eV for 10% Sn(Acac)<sub>4</sub>.

The calculations results are given at a table

Table

Sn(acac) <sub>4</sub> content in the solution for films production	1%	5%	10%
$E_g$	2,96 eV	2,95 eV	2,935 eV
$\hbar\Omega$	0,14 eV	0,07 eV	0,135 eV

The forbidden zone width values obtained for SnO<sub>2</sub> layers exceed the known values of amorphous layers of this material, which are 2,75–2,8 eV [3]. At the same time these values are lower  $E_g$  values of crystal tin dioxide. Thus, it may be supposed the considerable amount of nanosize crystal clusters in tin dioxide amorphous film.

As it may be seen from the table, the forbidden zone width decreases with the tin containing component concentration growth. This coincides with the conclusion in [4] that the zone width grows with pores' and grains' sizes decrease in nanoscale which is a specific one. Hence, it may be concluded about nanocrystals' sizes decrease in the investigated films, with Sn(Acac)<sub>4</sub> concentration decrease.

For the cases 1% and 10% Sn(Acac)<sub>4</sub> in the initial solution phonons' energies are nearly similar 0,14 and 0,135 eV. For the second case it is divisible by 0,07 eV, which allows to suppose several phonons participation in the optical absorption. The possibility of phonon 34 meV in SnO<sub>2</sub> is reported in [5]. Taking this into account it is possible to say about multi phonons (2 and 4) transitions in the material at the light absorption.

The optical absorption character witnesses about density states tails in the forbidden zone, which defines the energy  $E_g$  difference, obtained in our research from the reported crystal SnO<sub>2</sub> value. The absorption peak for IR zone, which corresponds energies: (1,85 eV for 1%, 1,88 for 5% и 1,84 eV for 10% Sn(Acac)<sub>4</sub>) is situated in the forbidden zone of the material. This may witness about some density states in the forbidden zone and is specific for amorphous or degenerated semiconductor [6].

The results obtained gave the possibility to calculate the dimensional quantization energy for the films. The effective mass values for SnO<sub>2</sub> carriers are different in different sources. The Bohr's exciton radius

$$a_B = \frac{\epsilon \hbar^2}{\mu e^2}$$
 for tin dioxide crystal calculation using data of [7] gives the value ~2,67 nm, and using data of [3] — ~1,28 nm. The holes localization on the quantum dimensional object was supposed, therefore  $a_B$  value practically approaches the Bohr's radius for electron in SnO<sub>2</sub> (~2,75 nm).

Using AFM data and  $m_e$  values from literature, the dimensional quantization energy may be estimated according formula in [8]:

$$E_{01}^e = \frac{0.71 \hbar^2 \Phi_{01}^2}{2m_e (\bar{r})^2}.$$

Nanocrystallites' radius mean value in our case according to atom force microscopy data was 5–7 nm. By substituting these values to the dimensional quantization energy formula given in [9], we shall obtain

dimensional quantization energy value  $E_{01}^e$  (for levels with  $l = 0$   $n = 1$ ) using effective masses data from [7] ~0,63 eV, and from [3] - ~0,31 eV. If the same energy is calculated from the measured optical density spectra results, as a difference of the first absorption maximum energy value, corresponding to energy  $E_g + E_{01}^e$ , and forbidden zone energy values (2,96 eV – 1%, 2,95 eV – 5% and 2,935 eV – 10% Sn(acac)<sub>4</sub>), then we shall obtain the following mean values [0,64±0,09] eV for 1%; [0,55±0,08] eV for 5%; [0,66±0,1] eV for 10%. The 15% error is considered.

In our case, the Bohr's mean radius for nanocrystallite is twice exceeds Bohr's radius value. At the same time, as it is shown in [8], holes dimensional quantization energy, practically did not influence the

absorption spectra types. The calculations methods using optical absorption spectra give good matching of results.

## CONCLUSIONS

After the surface morphology and optical absorption investigations of tin dioxide films obtained from solutions of various compositions, the following results were obtained:

— The forbidden band value dependence on the tin containing substance quantity in the initial solution. The band gap was 2,96 eV for 1%, 2,95 eV for 5%, 2,935 eV for 10% Sn(Acac)<sub>4</sub>. Thus, the tin containing fuller concentration growth in the initial solution gives the forbidden zone value decrease in the obtained films. This may witness about nanocrystallites' sizes growth in the films.

— The phonons' component plays the principal role in the light absorption. The phonons' energies, which took part in the optical transitions were 0,14 eV for 1%, 0,07 eV for 5% and 0,135 eV for 10% of Sn(Acac)<sub>4</sub> and correspond to multiphonons transitions.

— The optical absorption character, witnesses about density states "tails" in the forbidden zone. This defines energy  $E_g$  difference between obtained in our work and for crystal SnO<sub>2</sub>.

— evaluation of a dimensional quantization is fulfilled by two methods: analytically using AFM data, and by means of optical density spectra; results obtained by these two methods are in a good agreement.

## References

1. *Microstructure* and physical properties SnO<sub>2</sub> thin films / S. I. Rembeza, T. V. Svistova, E. S. Rembeza, O. I. Borsyakova // *Semiconductors (Russian Academy of Sciences Journal)*, 2001, Vol. 35, ed.7, P. 796–799.
2. *Production* and properties of thin nanostructured films of tin dioxide / V. S. Grinevich, L. N. Filevskaya, V. A. Smytyna, Yu. N. Anisimov, S. N. Savin, T. V. Borovskaya. — Collection of scientific works. The Chernivtsy University Scientific Herald. Chernivtsy: Ruta, 2005. — P. 72–76.
3. *Optical* and electrical properties of tin dioxide doped films / G. P. Skornyakov, T. P. Surkova, V. I. Sokolov, S. I. Martynova, T. P. Chukina. — In the book: *Optical investigations of semiconductors*. Sverdlovsk. 1980. — P. 90–93.
4. *Bisi O., Ossicini S., Pavesi L.* Porous silicon: a quantum sponge structure for silicon based optoelectronics // *Surface Science Reports*, 38, 2000, P. 1–126.
5. *Peercy S., Morosin B.* Pressure and temperature dependence of the Raman-active phonons in SnO<sub>2</sub>, *Phys. Rev.* **B7**, 2779 (1973).
6. *Emin D.* in L. Kazmersky (ed.) *Polycrystalline and amorphous thin films and device*, translation in to Russian, ("MIR" publishing house ed., Moscow, 1983). — P. 24–66.
7. *Button K. J., Fonstad C. G., Debrodt W.* Determination of the electron masses in stannic oxide by submillimeter cyclotron resonance, *Phys. Rev.* **B4**, 4539 (1971).
8. *Kulish N. R., Kunets V. P., Lisitsa M. P.* The semiconductor microcrystals absorption spectra at the condition of dimensional quantization. *Ukrainian Physical Journal*, **35**, 1817–1821 (1990).
9. *The absorption* spectra evolution at the transition from bulk to quantum-dimensional crystals CdS<sub>x</sub>Se<sub>1-x</sub> / N. R. Kulish, V. P. Kunets, M. P. Lisitsa, N. I. Malyshe. — *Ukrainian Physical Journal*, **37**, 1141–1146 (1992).

UDC 621.315.592

V. A. Smyntyna, L. N. Filevskaya, V. S. Grinevich

#### **SURFACE AND OPTICAL PROPERTIES OF TINDIOXIDE NANO-FILMS INFLUENCED BY THE INITIAL SOLUTION COMPOSITION**

The surface morphology and optical absorption results of nanostructured SnO<sub>2</sub> films, obtained using polymers are presented in the work. Optical densities dependencies and evaluation of electronic parameters of films are fulfilled for solution with different tin component. The forbidden zone width correlation is noticed for different compositions of solutions. The dimensional quantization energy, calculated by two different methods has similar results.

УДК 621.315.592

В. А. Сминтина, Л. Н. Филевська, В. С. Гриневич

#### **ВПЛИВ СКЛАДУ ВИХІДНИХ РОЗЧИНІВ НА ПОВЕРХНЕВІ Й ОПТИЧНІ ВЛАСТИВОСТІ НАНОПЛІВОК ДВО-ОКИСУ ОЛОВА**

У роботі представлені результати досліджень поверхневої морфології й оптичного поглинання наноструктурованих плівок SnO<sub>2</sub>, отриманих з використанням полімерів. Розглянуто залежності оптичної густини і розраховані електронні параметри плівок з розчинів з різним вмістом олововміщуючої речовини. Помічено кореляцію ширини забороненої зони плівок і складу гелів для одержання плівок. Енергія розмірного квантування, розрахована по двох різних методиках, дає близькі значення.

УДК 621.315.592

В. А. Смынтына, Л. Н. Филевская, В. С. Гриневич

#### **ВЛИЯНИЕ СОСТАВА ИСХОДНЫХ РАСТВОРОВ НА ПОВЕРХНОСТНЫЕ И ОПТИЧЕСКИЕ СВОЙСТВА НАНОПЛЕНОК ДВУОКИСИ ОЛОВА**

В работе представлены результаты исследований поверхностной морфологии и оптического поглощения наноструктурированных пленок SnO<sub>2</sub>, полученных с использованием полимеров. Рассмотрены зависимости оптической плотности и рассчитаны электронные параметры пленок из растворов с различным содержанием оловосодержащего вещества. Замечена корреляция ширины запрещенной зоны пленок и состава растворов для получения пленок. Энергия размерного квантования, рассчитанная по двум различным методикам, дает близкие значения.

## STRUCTURAL DEFECTS RELAXATION DURING COMPLEX THERMAL AND DYNAMICAL MECHANIC PROCESSING OF CdTe

Influence of ultrasonic deformation on temperature dependencies of internal friction and elastic module of CdTe were studied. The relaxation process is proposed to be determined by the changes of vacancies number in complexes.

### 1. INTRODUCTION

The problem of perfect semiconducting crystals manufacturing of binary compounds of CdTe type occupies one of the important places in modern solid-state technologies concerning infrared (IR) photoelectric instruments design and production [1-3]. The other scope of interest to CdTe and  $Cd_{1-x}Zn_xTe$  compounds is their use in detectors for X-rays range [4, 5].

The procedure of CdTe crystals preparation demand constant perfection that is caused, in turn, by objective difficulties of cultivation, in particular heats and pressures, and their gradient.

The electro-physical properties of CdTe crystals and the functional devices design on their basis, in particular with high specific resistance, are determined substantially by the type and concentration of point and linear defects. These defects are in non-equilibrium state and the enrichment of crystals surface with defects is predetermined, in particular, by its components — Te and Cd atoms and the formation of over-stoichiometric layers with chemically non-tied Te on a surface as a result of interaction of surface modification through polishing and changing surface layer during melting as a result of pulse laser influence [6–9] with adsorption of atmospheric  $O_2$ .

Accordingly, structural defects such as inhomogeneities and diversion from stoichiometric composition are capable to change essentially the crystals properties as a whole and that of devices prepared on their basis both at the stages of their manufacturing, operation and storage. Importance of specific features of the defect structure of the sample knowledge is obvious (for a crystal or device) as transition in an equilibrium state is possible only through individual metastable states clusters monitoring, the order of transition between which depends on character of current exterior influence.

Accordingly, for a crystals quality monitoring and that of corresponding devices, the different procedures are necessary, which could give the information not only on their real crystal structure, but also on a current state of system of structural defects in comparison. In particular, the measurement of internal friction (IF) at different temperatures, amplitudes of ultrasonic strain  $\epsilon$  and on different frequencies  $f$  allows to receive the additional significant information not only on properties and symmetries of structural

defects, but also on dynamics of their interaction at alternating exterior influence [10,11].

The annealing of structural defects, with the velocity depending on temperature, could assist to detect the form of and temperature spectrum of IF [11]. The continuous recession of the resonant frequency with temperature growth was observed in the range and IF maximum location temperature dependence was registered as well as the relaxation of the resonant frequency. The character of IF curve has not changed at repeated heating as well as the heights of IF maxima. The lack of point defects drain such as dislocations could be considered as the necessary condition of IF maximum observation caused by created point defects.

### 2. MATERIALS AND METHODS

As the physical parameters of the device created in semiconductors radiation processing technique, are connected with the certain array of space lattice defects, the given influence of radiation, thermal and ultrasonic on temperature dependences of IF and elastic modulus  $E$  in CdTe crystals of  $\langle 111 \rangle$  and  $\langle 110 \rangle$  orientations with dislocation density  $N_d \sim 5 \cdot 10^4 \text{ cm}^{-2}$  in Se component, after their mechanical cutting and grinding were investigated.

For measurement of IF and elastic modulus  $E$  temperature dependences of IF and elastic modulus  $E$ , the four-composite piezoelectric vibrator on frequency  $f \approx 117 \text{ kHz}$  used and resonant bending vibrations on frequency  $f \approx 1 \text{ kHz}$  at alternating strain  $\epsilon \approx 10^{-6}$  in vacuum  $P \approx 10^{-3} \text{ Pa}$  was used. The measurement error IF does not exceed 10%, and that of the relative change of an elastic modulus  $\Delta E - 0.1\%$ .

After transient during  $t \approx 2 \cdot 10^3 \text{ sec}$  at  $T_{an} \approx 580 \text{ K}$ , it is revealed (Fig. 1, curve 2), that IF background has considerably decreased, that testifies the improvement of crystal structure in CdTe samples. Small maximum IF was observed at  $T_{M1} \approx 370 \text{ K}$  with activation energy  $H_1 = 0.4 \pm 0.1 \text{ eV}$ . This maximum is caused, most probably, by relaxation process of V-V vacancies reorientation at the appendix of ultrasonic alternating strain during IF measuring.

With the influence of variable ultrasonic strain  $\epsilon$  we have found out (Fig. 1, curves 1 and 3) that the dominating maximum IF in CdTe is located at the temperature  $T_{M2} \approx 500 \text{ K}$ . According to the Wert-Marx

formula, the mean energy of activation equals to  $H_2 = 0.6 \pm 0.1$  eV was determined [11]. The relaxation time constant of this maximum IF equals to  $\tau_{02} \approx 7.7 \cdot 10^{-11}$  sec, and the corresponding frequency factor of relaxation is  $f_{02} \approx 1.3 \cdot 10^{10}$  Hz.

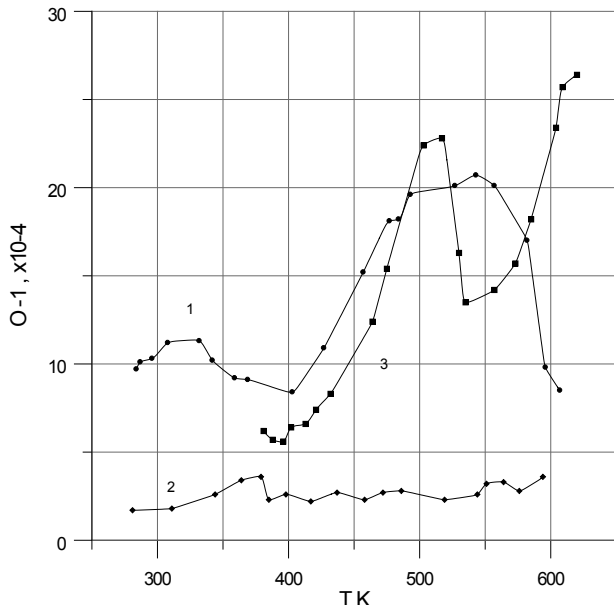


Fig. 1. Temperature dependence of internal friction  $Q^{-1}$  in  $CdTe$ : 1 – after mechanical cutting, 2 – after annealing at  $T_m \approx 580$  K during  $t \approx 2 \cdot 10^3$  sec, 3 –  $t \approx 2,6 \cdot 10^6$  sec at 300 K

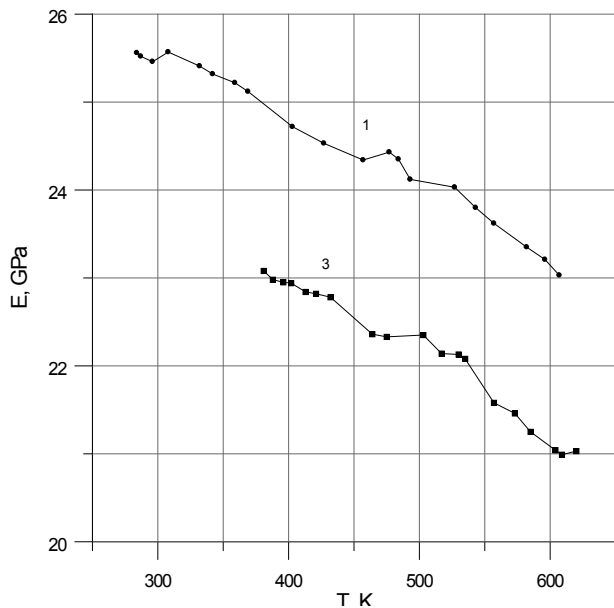


Fig. 2. Temperature dependence of elastic moduli  $E$  of  $CdTe$ : 1 – after mechanical cutting, 2 –  $t \approx 2,6 \cdot 10^6$  sec at 300 K

The relaxation of relative elastic modulus  $\Delta E/E$ , that is registered in the same temperature interval (Fig. 2, curves 1 and 3), confirms, that the relaxation process is connected, reliably, with the change of vacancies number in vacancy complexes.

After the natural aging at  $T \approx 300$  K during time  $t \approx 0.4 \cdot 10^6$  sec, IF maximum of the given sample already missed after heating and has showed itself again only after the return to a course (after the sample cooling) at the temperature field of  $T_{M2} \approx 500$  K.

One could assume, that the aging at  $T \approx 300$  K has created the vacancy complexes and following heat-

ing up to  $T \approx 580$  K has accelerated diffusion process, and, as a whole, it has led to occurrence of relaxation maximum IF at cooling the sample [11].

It is known, that machining of the  $CdTe$  crystals surface by abrasive materials usually leads to formation of the surface micro-cracks. There is no provided enrichment of interior surfaces of micro-cracks by electronegative Te atoms and, as well, no formation of oxide during chemical polishing of  $CdTe$ . These processes could cause the occurrence of inelastic relaxation.

The registered fact of a strong dependence of IF maximum amplitude on the value of ultrasonic strain  $\epsilon$ , namely the maximum height growth with magnification of amplitude of variable ultrasonic strain, has indicated the presence of the inelastic relaxation mechanism.

Near to the vertexes of micro-cracks formed during surface machining always exists certain initial excessive value of a local dislocation density. The instantaneous distribution of these dislocations in case of low concentrated defects and at the influence of exterior alternating ultrasonic a mechanical voltage could differ essentially. Correspondingly, the force that acts on a top of a micro-crack, breaks a condition of thermodynamic stability of an initial state of this top that leads to its jump-like motion to a new metastable equilibrium state. This process, as it is known from [12], is accompanied by magnification of radius of a micro-crack top and formation of the closed dislocation loops complex around of a top, which, in addition, hinders the micro-crack development.

The effect of  $CdTe$  monocrystals surface enrichment with the electronegative atoms of the free chemically non-bound Te results in formation of a nano-dimensional layer Te means also an opportunity of state change of interior surfaces near the surface of micro-cracks. It leads to the change of a centers' charge state not only at the surface (aside the negative values of the surface potential), which is accompanied by the corresponding destruction of the electron-hole equilibrium in near-surface layer of the Debye depth of screening.

As a result of chemical machining, in polishing and etching processes, not only the  $CdTe$  crystal surfaces' properties are changed, in particular – surface conductance, work function, lifetime of non-equilibrium charge carriers and a level of a photo-sensitivity of monocrystals [13, 14], but also they demonstrate the separate local (near-surface) volume of the crystals which size, as a result of diffusion, could change and increase in due course process.

It is obvious, that the intensive processes of local structural re-organization with the participation of volume and linear defects are accompanied by a state change and that the density of point defects changes simultaneously with processes of exterior uptake and elucidation (due to different mechanisms) initiated by the local-superfluous energy.

In particular, except for an energy liberation in a form of acoustic emission [15], the given process causes the occurrence of IF maximum which temperature state is determined as well by the dynamics of a defect tip drift.

The comparison of the basic performance of IF peaks in CdTe, after machining, with IF peaks of CdTe crystals implanted as a pine forest, specifies that activation energies  $H$ , the frequency factor  $f$ , annealing temperature  $T_{an}$  and their dependence on orientation, as well as the crystal structure of a specimen, in both cases have similar details. Exception is made for the height of IF maxima ( $Q^1_m$ ), which in the case of ion-implantation processing by pine forest  $Q^1_m$  is much less.

It could be stated reliably, that relaxation processes in both cases of influence on a crystal surface, have the identical nature, and the role of centers of inelastic relaxation (micro-cracks), in case of the ionic implantation, makes them to be the local sources of structural defects and play the role of sources (clusters), which arise on a surface of a crystal through the strong disordering at the significant doses of the implanted ions. The relaxation of such type was observed as well during the implantation by other sources and at an oxidizing process as well.

We have carried out the temperature studies of energy losses of the mechanical oscillations  $Q^1$  but the elastic moduli  $E$  of CdTe crystals specify that due of the annealing, the background level of IF ( $Q^1_o$ ) could decrease by up to 5 times what demonstrate the formal improvement of the defect structure. Thus, after annealing at the temperature  $T_{an2} \approx 710$  K during  $t \approx 2 \cdot 10^3$  sec, the relative changes of the defect CdTe structure at a room temperature are not observed during time range of  $t \approx 2.6 \cdot 10^6$  sec (1 month).

## CONCLUSIONS

The experimental results received in this work allow to state that the measurement of IF peak dependence in CdTe is sensitive enough as a tool for quality monitoring of the local micro-plastic strain concerning fragile semiconducting crystals. However, as data on IF generally concern the cumulative influence of both local and screw dislocations, the subsequent quantitative evaluation is necessary to determine the relative input of each dislocations type resulting in IF peak dependence.

UDC 548: 539.3

O. V. Lyashenko, A. P. Onanko, V. P. Velechuk, Y. A. Onanko, I. O. Lyashenko

## RELAXATION OF STRUCTURAL DEFECTS AT COMPLEX THERMAL AND DYNAMICAL MECHANIC PROCESSING ON CdTe

Influence of ultrasonic deformation on temperature dependencies of internal friction and elastic module of CdTe were studied. The relaxation process is connected with the changes of number of vacancies in complex.

## Literature

1. *Kurbatov L. N.* Optoelectronics of visible and infra-red ranges of spectrum M.: MFTI Publ., 1999. — 320 p.
2. *Sizov F. F.* Infrared photoelectronics: state and progress trends // LED and Lasers. — 2002. — N 1–2. — P. 5–23.
3. *Vlasenko O. I., Vlasenko Z. I.* Extended defects and their influence on the electronic properties of narrow-gap CdHgTe (review) // Optoelectronics and Semiconducting Techniques. — 2004. — N 39. — P. 27–50.
4. *Growth of high resistivity CdTe and (Cd,Zn)Te crystals / M. Fiederle, V. Babentsov, J. Franc, A. Fauler, J.-P. Konrath // Cryst. Res. Technol. — 2003. — Vol. 38, N 7–8. — P. 588–597.*
5. *Szeles Cs.* CdZnTe and CdTe materials for X-ray and gamma ray radiation detector application // Phys. Stat. Sol. (b) — 2004. — Vol. 241, N3. — P. 783–790.
6. *Artamonov V. V., Baydullayeva A., Vlasenko A. I.* et al. Atomic force microscopy and Raman scattering by laser-induced structural disordering on the p-CdTe surface (in Russian) // Fizika tverdogo tela — 2004. — Vol. 46, N.8 — P. 1489–1493.
7. *Babentsov V. N., Baydullayeva A., Gorban S. I.* et al. Transformation of point defects in CdTe under the influence of laser irradiation (in Russian) // Quantum electronics — 1992. — N. 43 — P. 61–66.
8. *Golovan L. A., Kashkarov P. K., Lakeenkov V. M.* et al. Studies of laser-induced defects creation in CdTe crystals by Rutherford back scattering (in Russian) // Fizika tverdogo tela. — 1998. — Vol. 40, N 2 — P. 209–211.
9. *Determination of CdTe melting threshold using acoustic response under pulse laser irradiation (in Ukrainian) / A. Baydullaeva, V. P. Velechuk, O. I. Vlasenko, O. V. Lyashenko, P. O. Mozol // Herald of Taras Shevchenko Kyiv National University, ser. Physics/Mathematics. — 2006. — N 2. — P. 355–360.*
10. *Lyashenko O. V., Onanko A. P.* Influence of electrical current on elastic and unelastic properties of GeSi // Photoelectronics, 2006, N15. — P. 95–97.
11. *Nikanorov S. P., Kardashev B. K.* Elasticity and Dislocation-Induced Non-Elasticity in Crystals (in Russian). — Moscow: Nauka Publishers, 1985. — 253 p.
12. *Dharmadasa I. M.* Recent Development and Progress in Electrical Contacts to CdTe, CdS and ZnS with special reference to barrier contacts in CdTe // Progress in Crystal Growth and Characterization. — 1998. — N 36. — P. 249–290.
13. *Bilevich E. O., Sukach A. V., Teterkin V. V.* Influence of Surface Chemical Processing on the Potential Barrier Height in Au / p-CdTe Schottky Diodes (in Russian) // Optoelectronics and Semiconducting Techniques. — 2004. issue 39. — P. 144–151.
14. *Kravtsov M. V., Lyashenko O. V., Onanko A. P.* Relaxation of Defect Structures in Ultrasonic Wave Field and Acoustic Emission in LiF Single Crystals // Functional Materials. — 2004. — 11, N 2. — P. 353–355.

УДК 548: 539.3

О. В. Ляшенко, А. П. Онанко, В. П. Велещук, Ю. А. Онанко, И. О. Ляшенко

**РЕЛАКСАЦИЯ СТРУКТУРНЫХ ДЕФЕКТОВ ПРИ КОМПЛЕКСНОМ ТЕРМИЧЕСКОМ И ДИНАМИЧЕСКОМ ВЛИЯНИЯХ НА CdTe**

Изучалось влияние ультразвуковой деформации на температурные зависимости внутреннего трения и модуля упругости CdTe. Релаксационный процесс обусловлен, по-видимому, с изменением числа вакансий в вакансионных комплексах.

УДК 548: 539.3

О. В. Ляшенко, А. П. Онанко, В. П. Велещук, Ю. А. Онанко, И. О. Ляшенко

**РЕЛАКСАЦІЯ СТРУКТУРНИХ ДЕФЕКТІВ ПРИ КОМПЛЕКСНОМУ ТА ДИНАМІЧНОМУ ВПЛИВАХ НА CdTe**

Вивчався вплив ультразвукової деформації на температурні залежності внутрішнього тертя і модуля пружності CdTe. Релаксаційний процес зв'язаний, вірогідно, зі зміною числа вакансій у вакансійних комплексах.

## QUANTUM CALCULATION OF AUGER SPECTRA FOR ATOMS AND SEMICONDUCTORS: NEW APPROACH

It is proposed new approach to calculation of characteristics of the Auger decay in the atomic systems and semiconductors on the basis of the gauge-invariant QED perturbation theory. The cross-sections of ionization of the internal shells for a number of atoms (Na,Si) and energies of Auger electron transitions in solids (Si,Ge) are calculated.

### INTRODUCTION

In this paper a new calculation method of the Auger decay characteristics for complex atomic systems basing on the gauge-invariant QED perturbation theory [7–13] is applied to calculation of those characteristics for atoms and semiconductors. The Auger electron spectroscopy is an effective method to study the chemical composition of solid surfaces and near-surface layers [1-8]. When considering the method principles, the main attention is given as a rule to the models for drawing chemical information from the Auger spectra and to the surface composition determination methods by the Auger spectrum decoding. It is just the two-step model that is used most widely when calculating the Auger decay characteristics. Since the vacancy lifetime in an inner atomic shell is rather long (about  $10^{-17}$  to  $10^{-14}$ s), the atom ionization and the Auger emission are considered to be two independent processes. In the more correct dynamic theory of the Auger effect [1-3] the processes are not believed to be independent from one another. The fact is taken into account that the relaxation processes due to Coulomb interaction between electrons and resulting in the electron distribution in the vacancy field have no time to be over prior to the transition. In fact, a consistent Auger decay theory has to take into account correctly a number of correlation effects, including the energy dependence of the vacancy mass operator, the continuum pressure, spreading of the initial state over a set of configurations etc. [1-7]. Note that the effects are not described adequately to date, in particular within the Auger decay theory [2]. The novel element of our method is in an using the optimized basis of the electron state functions. The basis is derived from the *condition that the calibration-non-invariant contribution of the second order polarization diagrams to the imaginary part of the multi-electron system energy is minimized already at the first non-disappearing approximation of the QED perturbation theory (PT) [4–11].* The method has been applied to calculate the ionization cross-sections of inner shells in various atoms and the Auger electron energy in semiconductors (Si,Ge).

### METHOD FOR CALCULATING THE LINE INTENSITIES AND WIDTHS IN THE AUGER SPECTRA

Within the frame of QED PT approach [5–10] to the Auger effect description, the Auger transition probability and, accordingly, the Auger line intensity are defined by the square of an electron interaction matrix element having the form [12–16]:

$$V_{1234}^{\omega} = [(j_1)(j_2)(j_3)(j_4)]^{-1/2} \sum_{\lambda, \mu} (-1)^{\mu} \begin{pmatrix} j_1 j_3 & \lambda \\ m_1 - m_3 & \mu \end{pmatrix} \times \text{Re} Q_{\lambda}(1234);$$

$$Q_{\lambda} = Q_{\lambda}^{\text{Coul}} + Q_{\lambda}^{\text{Bre}}. \quad (1)$$

The terms  $Q_{\lambda}^{\text{Coul}}$  and  $Q_{\lambda}^{\text{Bre}}$  correspond to subdivision of the potential into Coulomb part  $\cos|\omega|r_{12}/r_{12}$  and Breat one,  $\cos|\omega|r_{12}\alpha_1\alpha_2/r_{12}$ . The real part of the electron interaction matrix element is determined using expansion in terms of Bessel functions:

$$\frac{\cos|\omega|r_{12}}{r_{12}} = \frac{\pi}{2\sqrt{r_1 r_2}} \times \sum_{\lambda=0} (\lambda) J_{\lambda+1/2}(|\omega|r_{<}) J_{-\lambda-1/2}(|\omega|r_{>}) P_{\lambda}(\cos \mathbf{r}_1 \hat{\mathbf{r}}_2) \quad (2)$$

where  $J$  is the 1<sup>st</sup> order Bessel function,  $(\lambda)=2\lambda+1$ .

The Coulomb part  $Q_{\lambda}^{\text{Coul}}$  is expressed in terms of radial integrals  $R_{\lambda}$ , angular coefficients  $S_{\lambda}$  [5]:

$$\text{Re} Q_{\lambda}^{\text{Coul}} = \frac{1}{Z} \text{Re} \{ R_{\lambda}(1243) S_{\lambda}(1243) + R_{\lambda}(\tilde{1}24\tilde{3}) S_{\lambda}(\tilde{1}24\tilde{3}) + R_{\lambda}(\tilde{1}\tilde{2}43) S_{\lambda}(\tilde{1}\tilde{2}43) + R_{\lambda}(\tilde{1}\tilde{2}\tilde{4}\tilde{3}) S_{\lambda}(\tilde{1}\tilde{2}\tilde{4}\tilde{3}) \} \quad (3)$$

As a result, the Auger decay probability is expressed in terms of  $\text{Re} Q_{\lambda}(1243)$  matrix elements:

$$\text{Re} R_{\lambda}(1243) = \iint dr_1 r_1^2 r_2^2 f_1(r_1) f_3(r_1) f_2(r_2) f_4(r_2) Z_{\lambda}^{(1)}(r_{<}) Z_{\lambda}^{(1)}(r_{>}) \quad (4)$$

where  $f$  is the large component of radial part of single electron state Dirac function and function  $Z$  is:

$$Z_{\lambda}^{(1)} = \left[ \frac{2}{|\omega_{13}| \alpha Z} \right]^{\lambda+1/2} \frac{J_{\lambda+1/2}(\alpha|\omega_{13}|r)}{r^{\lambda} \Gamma(\lambda+3/2)}.$$

The angular coefficient is defined by standard way [7]. The other items in (3) include small components of the Dirac functions; the sign « $\sim$ » means that in (3) the large radial component  $f_i$  is to be changed by the small  $g_i$  one and the moment  $l_i$  is to be changed by  $\tilde{l}_i = l_i - 1$  for Dirac number  $\alpha_1 > 0$  and  $l_i + 1$  for  $\alpha_i < 0$ . The Breat interaction is known to change considerably the Auger decay dynamics in some cases (c.f. [5]). The Breat part of  $Q$  is defined as the sum:

$$Q_{\lambda}^{\text{Br}} = Q_{\lambda, \lambda-1}^{\text{Br}} + Q_{\lambda, \lambda}^{\text{Br}} + Q_{\lambda, \lambda+1}^{\text{Br}}, \quad (5)$$

where the contribution of our interest is determined as:

$$\begin{aligned} Q_{\lambda}^{\text{Br}} = & \frac{1}{Z} \text{Re} \left\{ R_{\lambda} (12\tilde{4}3) S'_{\lambda} (12\tilde{4}3) + \right. \\ & + R_{\lambda} (\tilde{1}243) S'_{\lambda} (1243) + R_{\lambda} (\tilde{1}2\tilde{4}3) S'_{\lambda} (\tilde{1}2\tilde{4}3) + \\ & \left. + R_{\lambda} (\tilde{1}2\tilde{4}\tilde{3}) S'_{\lambda} (\tilde{1}2\tilde{4}\tilde{3}) \right\} \end{aligned} \quad (6)$$

The Auger width is obtained from the adiabatic Gell-Mann and Low formula for the energy shift [9].

The contribution of the  $A_d$  diagram to the Auger level width with a vacancy  $n_{\alpha} l_{\alpha} j_{\alpha} m_{\alpha}$  is:

$$\sum_{\lambda} \frac{2}{(\lambda)(j_{\alpha})} \sum_{\beta\gamma \leq f} \sum_{k>f} Q_{\lambda}(\alpha k \gamma \beta) Q_{\lambda}(\beta \gamma k \alpha), \quad (7)$$

while contribution of the  $A_{\text{ex}}$  one is:

$$\frac{2}{(j_{\alpha})} \sum_{\lambda_1 \lambda_2} \sum_{\beta\gamma \leq f} \sum_{k>f} Q_{\lambda_1}(\alpha k \gamma \beta) Q_{\lambda_2}(\beta \gamma k \alpha) \begin{Bmatrix} j_{\alpha} & j_{\gamma} & \lambda_2 \\ j_k & j_{\beta} & \lambda_1 \end{Bmatrix}. \quad (8)$$

The formulas (7),(8) define the full Auger level width. The partial items of the  $\sum_{\beta\gamma} \sum_k$  sum answer to contributions of  $\alpha^{-1} \rightarrow (\beta\gamma)^{-1} K$  channels resulting in formation of two new vacancies  $\beta\gamma$  and one free electron  $k$ :  $\omega_k = \omega_{\alpha} + \omega_{\beta} - \omega_{\alpha}$ . The final expression for the width in the representation of jj-coupling scheme of single-electron moments has the form:

$$\begin{aligned} & \Gamma(2j_1^{\alpha} l_1^{\alpha}, 2j_2^{\alpha} l_2^{\alpha}; J) = \\ & = 2 \sum_{j_k l_k} |\Gamma(2j_1^{\alpha} l_1^{\alpha}, 2j_2^{\alpha} l_2^{\alpha}; l_o, k j l)|^2. \end{aligned} \quad (9)$$

Here the summation is made over all possible decay channels. The basis of electron state functions was defined by the solution of Dirac equation (integrated numerically using the Runge-Cutt method). The calculation of radial integrals  $\text{Re} R_{\lambda}(1243)$  is reduced to the solution of a system of differential equations [5]:

$$\left. \begin{aligned} y_1' &= f_1 f_3 Z_{\lambda}^{(1)}(\alpha|\omega|r) r^{2+\lambda}, \\ y_2' &= f_2 f_4 Z_{\lambda}^{(1)}(\alpha|\omega|r) r^{2+\lambda}, \\ y_3' &= [y_1 f_2 f_4 + y_2 f_1 f_3] Z_{\lambda}^{(2)}(\alpha|\omega|r) r^{1-\lambda} \end{aligned} \right\}. \quad (10)$$

In addition,  $y_3(\infty) = \text{Re} R_{\lambda}(1243)$ ,  $y_1(\infty) = X_{\lambda}(13)$ . The system of differential equations includes also equations for functions  $f/r^{|\alpha|-1}$ ,  $g/r^{|\alpha|-1}$ ,  $Z_{\lambda}^{(1)}$ ,  $Z_{\lambda}^{(2)}$ . The formulas for the Auger decay probability include the radial integrals  $R_{\alpha}(\alpha k \gamma \beta)$ , where one of the functions describes electron in the continuum state. When calculating this integral, the correct normalization of the function  $\Psi_k$  is a problem. The correctly normalized function should have the following asymptotic at  $r \rightarrow 0$

$$\left. \begin{aligned} f \\ g \end{aligned} \right\} \rightarrow (\lambda \omega)^{-1/2} \begin{cases} \left[ \omega + (\alpha Z)^{-2} \right]^{-1/2} \sin(kr + \delta), \\ \left[ \omega - (\alpha Z)^{-2} \right]^{-1/2} \cos(kr + \delta). \end{cases} \quad (11)$$

When integrating the master system, the function is calculated simultaneously:

$$N(r) = \left\{ \tau \omega_k \left[ f_k^2 \left[ \omega_k + (\alpha Z)^{-2} \right] + g_k^2 \left[ \omega_k + (\alpha Z)^{-2} \right] \right] \right\}^{1/2}.$$

It can be shown that at  $r \rightarrow \infty$ ,  $N(r) \rightarrow N_k$ , where  $N_k$  is the normalization of functions  $f_k$ ,  $g_k$  of continuous spectrum satisfying the condition (11).

The energy of an electron formed due to a transition  $jkl$  is defined by the difference between energies of an atom with a hole at the  $j$  level and double-ionized atom at  $kl$  levels in the final state:

$$E_A(jkl, {}^{2S+1}L_J) = E_A^+(j) - E_A^{2+}(kl, {}^{2S+1}L_J). \quad (12)$$

To single out the above-mentioned correlation effects, the equation (12) can be presented as:

$$\begin{aligned} E_A(jkl, {}^{2S+1}L_J) &= E(j) - E(k) - \\ &- E(l) - \Delta(k, l; {}^{2S+1}L_J), \end{aligned} \quad (13)$$

where the item  $\Delta$  takes into account the dynamic correlation effects (relaxation due to hole screening with electrons etc.) To take these effects into account, the set of procedures elaborated in the atomic theory [2–5] is used. For solid phase, the more precise form of equation (13) is [1]:

$$E_A^s(jkl, {}^{2S+1}L_J) = E_A(jkl, {}^{2S+1}L_J) + \Delta E^s + R_{\text{rel}} + e\Phi, \quad (14)$$

where  $\Delta E^s$  is a correction for the binding energy change in the solid;  $R_{\text{rel}}$ , the same for out-of-atom relaxation;  $e\Phi$  takes into account the work of exit.

## CALCULATION RESULTS AND CONCLUSIONS

An exit probability of Auger electrons from an atom via different channels associated with ionization from a core level is defined by the matrix element (1). In addition, the proportionality coefficient in the equation coincides with the electron impact ionization cross-section  $\sigma_j$  of the level  $j$ . Of course, two aspects are to be considered when determining the exit probability of Auger electrons from an atom, namely, the radiative transition under neutralization of a hole at the level  $j$  and the possibility of a considerable change in the initial hole distribution at the core levels at the Auger decay via the radiative channel  $jkl$  associated as a rule with a considerable distinctions in the non-ra-

diative transition probabilities. For definiteness sake, let the ionization of L levels in a multi-electron atom be considered. The probability of the Auger electron emission from the atom via the channel  $L_3KI$  (taken as an example) is defined by the ionization cross-section of the level  $L_3$  as well as by a certain effective cross-section depending on the ionization cross-sections of the levels  $L_1, L_2$ . The Auger line intensity is defined by three atomic constants:  $A_{jkl} = \sigma_j f_{jkl}$ , where  $a_{jkl}$  is the non-radiative transition probability;  $f_i$  is the Korster-Kronig coefficient;  $\sigma_j$ , the ionization cross-section defined by the matrix element (1) calculated for wave functions of bound state and continuum one. In the table 1 presented are the ionization cross-sections ( $\text{cm}^2$ ) calculated for inner shells of some atoms basing on the method proposed in this paper as well as the experiment data available [1]. Note that, unlike the widely used calculation method of the cross-sections within the frame of Born approximation (c.f.[2,3]) our approach is more correct theoretically, thus resulting in a good agreement between theory and experiment. The important moment is connected with an accurate account for inter-electron correlations. More accurate account of the complicated many-body correlations improves earlier obtained data [16].

Table 1  
Inner shell ionization cross-sections for some atoms

Element	Level	Ionization Energy, $E_i, \text{eV}$	Incident electrons energy, $U = E/E_i$	Ionization cross-section: Experiment	Ionization cross-section: Theory
Na	K	1075	4	$0,7 \cdot 10^{-20}$	$0,74 \cdot 10^{-20}$
Si	$L_3$	103	4	$6,15 \cdot 10^{-19}$	$6,26 \cdot 10^{-19}$

Table 2 gives the data on the Auger electron energy for some solids calculated using our method and the semi-empirical method with Larkins' equivalent core approximation [2] as well as experimental data. The calculation accuracy using method [2] is within about 2 eV as an average. Our approach provides more accurate results that is due to a considerable extent to more correct accounting for complex electron interaction. To conclude, note that the use of the Auger electron spectroscopy in analysis of the surface chemical composition requires consideration of Auger spectra and the corresponding characteristics of the Auger transitions, interpretation of effects like the shape transformations of the valence Auger spectra due to appearance of new lines, position and intensity changes of individual lines caused by the redistribution in the electron state density of the valence band.

Table 2  
Experimental data for Auger electron energy for solids and calculated values  
(A, semi-empirical method [2]; B, [16]; C, this work)

Element	Auger line	Experiment	Theory: A	Theory: B	Theory: C
Si	$KL_{2,3}L_{2,3}^1D_2$	1616,4	1614,0	1615,9	1614,8
Ge	$L_3M_{4,5}M_{4,5}^1G_4$	1146,2	1147,2	1146,6	1146,9

## References

1. Kulekshov V. F., Kukhareenko Yu. A., Fridrikhov S. A. et al. Spectroscopy and Electron Diffraction in Solid Surfaces Studies. Nauka: Moscow, 1985.
2. Aberg T., Hewat G. Theory of Auger effect. Springer-Verlag: Berlin, 1979.
3. Amusia M. Ya. Atomic photoeffect. Acad. Press: N.-Y., 2003.
4. Ivanova E. P., Ivanov L. N. Modern Trends in Spectroscopy of Multicharged Ions // Physics Rep. — 1991. — Vol. 166, N 6. — P. 315–390.
5. Glushkov A. V. Relativistic and correlation effects in spectra of atomic systems. Odessa: Ecoprint, 2006. — 400 p.
6. Glushkov A. V. Atom in an electromagnetic field. — Kiev: KNT, 2005. — 400 p.
7. QED Calculation of Electron Satellites Spectra in Intense Laser Field in Multicharged Ion / A. V. Glushkov, S. V. Malinovskaya, A. A. Svinarenko, Yu. G. Chernyakova // Int. J. Quant. Chem. — 2004. — Vol. 99, N 5. — P. 673–678.
8. High order corrections in the Relativistic Perturbation Theory with the model Zeroth Approximation, Mg-like and Ne-like ions / E. P. Ivanova, L. N. Ivanov, A. V. Glushkov, A. E. Kramida // Phys. Scripta. — 1985. — Vol. 32, N 4. — P. 512–524.
9. Glushkov A. V., Ivanov L. N. Radiation Decay of Atomic States: atomic residue and gauge non-invariant contributions // Phys. Lett. A. — 1992. — Vol. 170(1). — P. 33–38.
10. Glushkov A. V. Negative Ions of inert Gases // JETP Lett. — 1992. — Vol. 55(2). — P. 97–100.
11. QED calculation of the superheavy elements ions: energy levels, radiative corrections and hfs for different nuclear models / A. V. Glushkov, S. V. Ambrosov, A. V. Loboda, Yu. G. Chernyakova, A. A. Svinarenko, O. Yu. Khetselius // Nucl. Phys. A.: Nucl. and Hadr. Phys. — 2004. — Vol. 734. — P. 21–28.
12. QED calculation of heavy multicharged ions with account for correlation, radiative and nuclear effects / A. V. Glushkov, S. V. Ambrosov, A. V. Loboda, E. P. Gurnitskaya, O. Yu. Khetselius // Recent Advances in Theor. Phys. & Chem. Systems. — 2006. — Vol. 15. — P. 285–300.
13. Glushkov A. V., Ambrosov S. V., Nikola L. V. Sensing the Auger spectra for solids: New quantum approach // Sensor Electr. and Microsyst. Techn. — 2006. — N 3. — P. 46–50.
14. Nikola L. V. Quantum calculation of Auger spectra for Na, Si atoms and solids // Photoelectronics. — 2007. — N 16. — P. 102–105.
15. Sensing the finite size nuclear effect in calculation of the Auger spectra for atoms and solids / O. Yu. Khetselius, L. V. Nikola, A. V. Turin, D. E. Sukharev // Sensor Electr. and Microsyst. Techn. — 2007. — N 1. — P. 18–21.
16. Cooperative Laser-Electron-Nuclear Processes: QED Calculation of Electron Satellites Spectra for Multi-Charged Ion in Laser Field / A. V. Glushkov, S. V. Malinovskaya, Yu. G. Chernyakova, A. A. Svinarenko // Int. Journ. Quant. Chem. — 2004. — Vol. 99, N 5. — P. 889–893.

UDC 539.142 : 539.184

A. V. Glushkov, O. Yu. Khetselius, L. V. Nikola, Yu. V. Dubrovskaya

### **QUANTUM CALCULATION OF AUGER SPECTRA FOR ATOMS AND SEMICONDUCTORS: NEW APPROACH**

It is proposed new approach to calculation of characteristics of the Auger decay in the atomic systems and semiconductors on the basis of the gauge-invariant QED perturbation theory. The cross-sections of ionization of the internal shells for a number of atoms (Na,Si) and energies of Auger electron transitions in solids (Si,Ge) are calculated.

УДК 539.142 : 539.184

А.В. Глушков, О. Ю. Хецелиус, Л. В. Никола, Ю. В. Дубровская

### **КВАНТОВЫЙ РАСЧЕТ ОЖЕ СПЕКТРОВ АТОМОВ И ПОЛУПРОВОДНИКОВ: НОВЫЙ ПОХОД**

Развит новый подход к расчету характеристик Оже распада в атомных системах и полупроводниках на основе калибровочно-инвариантной КЭД теории возмущений. Рассчитаны сечения ионизации внутренних оболочек ряда атомов (Na,Si) и энергий Оже переходов в полупроводниках (Si,Ge)

УДК 539.142 : 539.184

О. В. Глушков, О. Ю. Хецелиус, Л. В. Никола, Ю. В. Дубровська

### **КВАНТОВИЙ РОЗРАХУНОК ОЖЕ СПЕКТРІВ АТОМІВ ТА НАПІВПРОВІДНИКІВ: НОВИЙ ПІДХІД**

Розвинуто новий підхід до розрахунку характеристик Оже розпаду в атомних системах та напівпровідниках на підставі калібровочно-інваріантної КЕД теорії збурень. Розраховані перерізи іонізації внутрішніх оболонок ряду атомів (Na,Si) та енергій Оже переходів у твердих тілах (Si,Ge).

## SPECTROSCOPIC METHODS OF ACTIVE SRS PHOTONICS DEVICES MODELING FOR TELECOMMUNICATION SYSTEMS WITH TERBYTE VELOCITY

Present paper is devoted to the SRS amplification profile modeling in single-mode fibers which are used widely in modern SRS lasers and amplifiers. The spectroscopic model of RS spectrum decomposition in a random single-mode fiber with numerous oscillating modes which could be considered as the further generalization of the actual band model developed before. The modeling results are presented using the sample of the SRS amplification spectra restoration in some extended fibers made of melted quartz. The use of the RS amplification profile non-linear approximation procedure according to the method of Levenberg-Markwardt allows to obtain the practically precise approximation of the registered RS amplification spectrum in quartz fibers. The integral intensity of the model spectrum coincides with the experimental one as precisely as  $< 0.3\%$ . The optimal set of the amplification parameters is introduced into analytical expressions which be differentiated and integrated in analytical form and which could be calculated easily in digital way. The results of the basic set of fiber RS amplifiers modeling are presented by: amplification non-regularity, amplified frequencies range, group delay as well as the noise parameters. The model could be applied to the analysis of RS amplifiers functioning in the fibers with known SRS spectrum of random complexity.

### INTRODUCTION

Physical details of the stimulated Raman scattering (SRS) convert the optical fiber into active medium for lasers and optical amplifiers. Creation of SRS lasers could be attributed to the brightest achievements of modern laser physics and the use of the fiber RS amplifiers (FRSA) in the contemporary far and super-far systems of information transfer has become almost necessary [1–3].

The fiber RS amplifiers with multi-wavelengths pumping (MWP-FRSA) allow to cover all the frequency band of C+L ranges [3, 4] and to widen the amplification band up to the theoretical border what equals approximately to 12 THz. Despite the simplicity of the RS amplifier structure, the direct calculations of the amplification profile made with the use of the standard chain equations cause a lot of difficulties [4–5, 12], which induced by the SRS spectra complexity registered in fibers. That's why, the creation of the more or less precise theoretical model for the SRS in fibers description is the object of the intensive research. The spectroscopic classification, SRS spectra decomposition to some oscillating modes as well their interpretation was presented in paper [6]. After the RS spectrum was restored from the experimental SRS spectrum [7, 8], the RS amplification profile decomposition to some oscillating modes with the use of the intermediate widening model [9].

The results of the RS amplification coefficient theoretical analysis under the pumping with one wavelength and its dependence on the pumping wavelength, modes' overlapping and on the material composition of the fiber are presented in the paper [10]. We have proposed already [15] the spectroscopic model of actual band for the MWP-FRSA design what allows to realize the optimal choice of the pumping wavelengths for the given amplification band as well as for the amplification regularity.

The spectroscopic model of RS spectrum analysis is presented and is extended herewith for the case of numerous oscillating modes as well as its application to MWP-FRSA design.

### THEORY OF RS AMPLIFICATION AND ACTUAL MODE MODEL

In the framework of semi-classical SRS discussion [10], the connection between the molecular differential polarization ( $\partial\alpha_{ij}/\partial q_n$ ) and the non-linear permeability  $\chi^{(3)}$ :

$$\chi_{ijkl}^{(3)}(\omega) = \frac{N}{12m\varepsilon_0V} \frac{1}{\omega_v^2 - \omega^2 + i\omega\Gamma} \cdot \sum_n \frac{\partial\alpha_{ij}}{\partial q_n} \left( \frac{\partial\alpha_{kl}}{\partial q_n} \right)^*, \quad (1)$$

where  $\omega_v$  – the resonant frequency of the phonon,  $\omega$  – angular phonon frequency,  $\Gamma$  – phonon decay constant,  $q_k$  – normal coordinate, describing the local shifts,  $m$  – mass connected with the oscillation,  $N$  – number of oscillators in the volume of the interaction  $V$ ,  $\varepsilon_0$  – dielectric constant.

As the tensor of the fourth range  $\chi^{(3)}$  is the isotropic one, the RS amplification coefficient at the Stokes frequency  $\omega_s = \omega_p - \omega_v$  could be presented in the form [10]:

$$g_R(\omega) = -\frac{3\omega_s}{\varepsilon_0 c^2 n_p n_s} \frac{\text{Im}[\chi_{iii}^{(3)}(\omega) + \chi_{iji}^{(3)}(\omega)]}{2A_{eff}}, \quad (2)$$

where  $A_{eff}$  – the effective area of the pumping beam. The amplification coefficient  $g_R$  depends linearly on the Stokes wave frequency and the intrinsic frequency dependence is determined by the imaginary part of the non-linear polarization  $\chi^{(3)}$ , which has the resonant denominator as for the phonon harmonic oscillator (see, please, the relationship (1)).

The SRS normalized amplification line-form  $S(\nu)$  on a single harmonic phonon oscillator should be presented, taking into account the relationships (1) та (2), in the form:

$$S_R(\nu) = \frac{\nu_0 \nu \gamma^2}{(\nu_0^2 - \nu^2)^2 + \nu^2 \gamma^2}, \quad (3)$$

where  $\nu$  – хвильові числа ( $\nu_0 = \omega_\nu/2\pi c$ ,  $\nu = \omega/2\pi c$  and  $\gamma = \Gamma/2\pi c$ ), and  $\gamma$  approximately equals to the line's full width at the half of its height (FWHM) for function  $S(\nu)$ . The relationship (3) is the basis of the actual band model [15]. But, the complicated enough spectra modeling needs the use of the model with multiple oscillating modes through the inclusion of the corresponding set of the approximation functions.

### SPECTROSCOPIC MODEL OF RS AMPLIFICATION SPECTRUM MULTI-MODE DECOMPOSITION

RS amplification spectrum includes the significant number of oscillating modes [8], and in the preceding paper [6] the analytic methodology of the spontaneous RS quartz fiber amplification spectrum decomposition into the set of Gauss components. The result of the decomposition could be presented as a set of relative amplitudes along with the widths of the used components. It was shown that using only 10 components located between 0 and 900  $\text{cm}^{-1}$ , one could approximate the experimental results with the precision better than 1%.

Some of the seven maxima of RS spectrum in the standard fiber are so asymmetric that they could correspond to the resulting line for 10–15 oscillating modes. Such a spectrum couldn't be described with one simple function while the problem of spectrum modeling requests the use of decomposition into several oscillating modes.

Each oscillating mode in melted quartz fiber is extremely wide and could have Gauss profile in the case of non-monotonous widening or to remain in the line which is typical for the oscillator (Lorentz-type) in the case of monotonous widening. Model analysis of RS spectrum with the use of Gauss line profiles is being based on the following expression:

$$g_R(\omega) = \sum_{i=1}^{N_m} A_i \exp[-(\omega - \omega_{\nu,i})^2 / \Gamma_i^2], \quad (4)$$

where  $N_m$  – the number of decomposition modes,  $\omega_{\nu,i}$  – central frequency of  $i$ -th Gaussian profile, parameter  $\Gamma_i = FWHM_i / (2\sqrt{\ln 2}) \approx 0.6 \cdot FWHM_i$ , where  $FWHM_i$  – full line-width at the maximum half. The values  $A_i$  along with  $\omega_{\nu,i}$  and  $\Gamma_i$  are the parameters for non-linear approximation.

In the case of monotonous widening of the oscillating frequencies chosen for the spectrum decomposition, we propose to use the set of normalized functions of phonon oscillator according to (3):

$$g_R(\omega) = \sum_{i=1}^{N_m} \frac{A_i}{\omega_{\nu,i}} \cdot \frac{\omega_{\nu,i} \gamma_i^2 \omega}{(\omega^2 - \omega_{\nu,i}^2)^2 + (\omega \gamma_i)^2}. \quad (5)$$

It should be noted that the use of decomposition procedure has, at least, two aspects.

Firstly, it is the spectroscopic aspect when decomposition is the method of the states density function division into the parts provided before.

Secondly, the applied aspect of decomposition exists when the maximal preciseness of RS amplification profile  $g_R(\omega)$  by simplest functions (4) and (5) is the principal scope. Being concentrated at the second aspect in the present paper, we have used the programming procedure of non-linear approximation according to Levenberg-Marquardt method.

### MODELING RESULTS AND APPLICATIONS

At Fig. 1 the results of SRS amplification non-linear approximation are presented for the fibers based on fused quartz fibers: (a) – pure quartz; (b) – fiber of True Wave RS<sup>TM</sup> type; (c) – fiber with compensated dispersion (DCF); (d) – RS fiber containing ~20% GeO<sub>2</sub>. The experimental data were taken from the paper [7]. The integral intensities of the model and experimental spectra coincide with the precision better than 0.3%.

Taking into account the preciseness of the modeling results presented at Fig. 1, it should be mentioned that extreme complexity of the model of intermediate widening [9], as to our opinion, shouldn't be considered as the proper. Vice versa, the high precision along with the relatively simple analytical expressions (4) or (5) for the RS amplification profile could be proven in the case of non-linear approximation. The parameters, which are the result of the non-linear approximation, are presented at Table 1 for the case of Gauss decomposition of the experimental RS profiles for all fibers presented at Fig. 1.

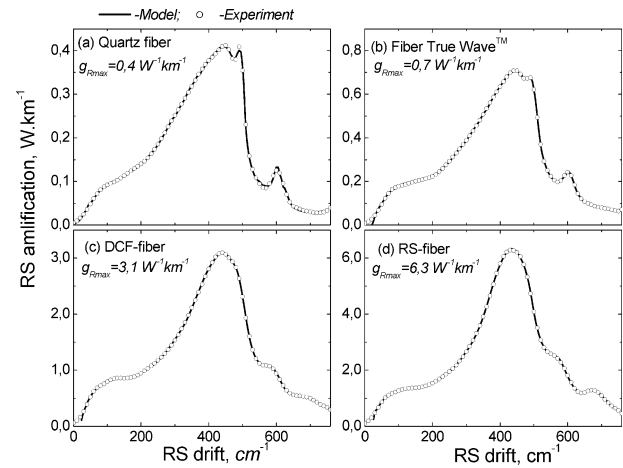


Fig. 1. The results of SRS amplification profile non-linear approximation for the fused silica fibers: (a) – pure quartz fiber; (b) – fiber of True Wave RS<sup>TM</sup> type; (c) – fiber with the compensated dispersion (DCF); (d) – RS fiber with ~20% GeO<sub>2</sub>. Experimental data are taken from the paper [7]

The spectroscopic model of RS amplification allows to calculate the spectrum of amplified spontaneous radiation (ASR). The results of the ASR spectrum for the amplifier with 6 pumping sources are presented at Fig. 2 for two modeling methods – the model with some oscillating modes (full line) and the model of one actual mode (dotted line). The color dots represent the data for effective noise coefficient taken from the paper [11]. 6 experimental wavelengths were used

as follows: 1428, 1445, 1466, 1480, 1494 and 1508 nm, while the pumping powers were equaled to 338, 215, 83, 30, 19 and 39 mW.

During the amplification coefficient equalizing, the significant (almost 7 dB) amplification decrease emerges in the noise coefficient distribution. This decrease is determined by the pumping power non-regular distribution over the wavelengths' range. Both models, as it is seen from Fig.2, give almost the same values of SRS coefficient with almost equal decrease value in the wavelengths range of interest.

It should be mentioned that the experimental data exposed at Fig. 2, are obtained in RS amplifier using the fiber of True-Wave RS type [11]. For such a fiber, the RS amplification profile approximation' precision, obtained with the use of only one oscillating mode, couldn't be considered as satisfactory. But, the similarity of the results for both numerical calculations of the SRS amplification coefficient's tendency as well as the registered correlation of its inclination and the results of the noise coefficient's direct measurement for the real amplifier do support the fact that the framework of the actual model is somewhat wider than those expected before, and it could be applied, in certain borders, to the SRS noise parameters' evaluation and to the engineering design realization.

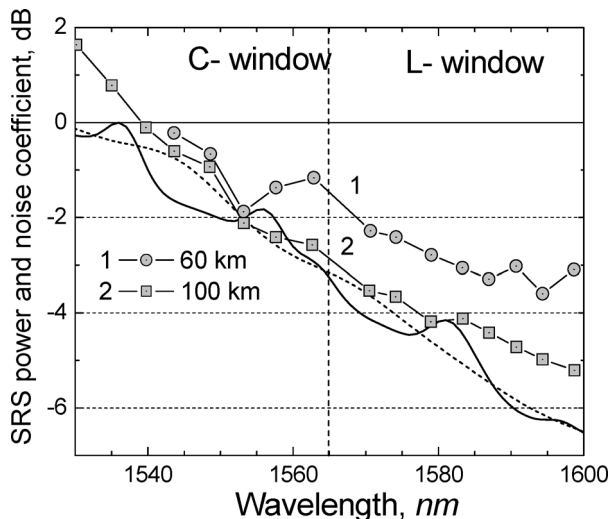


Fig. 2. Calculated SRS spectrum for FRSA with the scheme of some pumpings from the model of some oscillating modes (full line) and from the model of actual band (dotted line). The points correspond to the direct measurement of noise coefficient for RS amplifier with 6-wavelengths pumping [11]

In other cases, for example for the SFRSA dispersion parameters' modeling, the actual mode model is not applicable. The right approach to the specific non-regularities of RS amplification at the place of maximum description for real fibers could be realized with the use of some oscillating modes model only.

The RS amplification dispersive parameters for amplifier with one pumping source are presented at Fig. 3, where the amplifier's group delay dependence on the RS frequency drift in THz is presented in the amplification range of 3 dB.

The advantage of the method proposed is due to the fact that all the derivatives of the spectral function could be obtained both in the analytical and in digital form. The last peculiarity could be very useful for the

FRSA with multi-wavelengths pumping group delay optimization as well as for the correction devices' design.

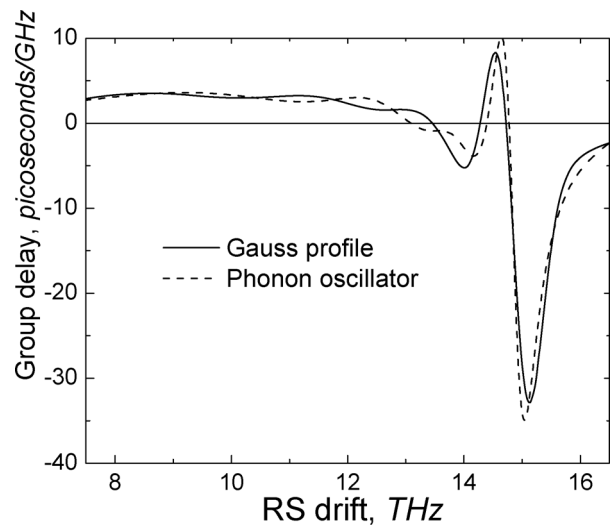


Fig. 3. Dispersion parameters for RS amplification in fused silica, calculated according to the functions for the profile with some oscillating modes

Both approximations, as obtained in Gauss' way as well as with the use of phonon oscillator's functions, give very close dependencies of group delay time on the frequency. This is the result of good approximation of the output RS amplification profile, which, along with simple analytical view of the approximation functions (4) or (5), is a significant

At Fig. 4 the optical noise spectral densities (both for Stokes and anti-Stokes SRS) generated by the signal at 1.56-micron at 300 K. In our calculations of Stokes and anti-Stokes SRS spectra the maximal value was chosen as  $g_R = 0.5 \text{ (W}\cdot\text{km)}^{-1}$ . It should be mentioned that the Stokes and anti-Stokes SRS components is being caused by different dependencies on phonons' temperature density  $n_p(\omega)$ . The results of our modeling presented at Fig. 4, are in full concordance to those measured directly for the spectral density of the amplified SRS radiation [5].

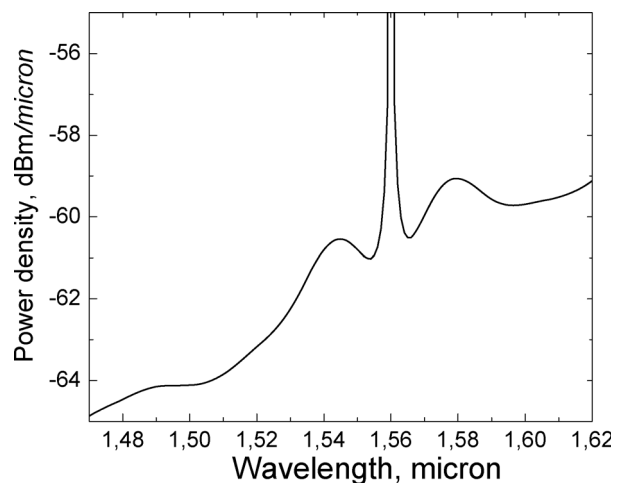


Fig. 4. Spectral density of the optical noise (Stokes and anti-Stokes SRS) generated by the signal 1.56 micron at 300 K. Peak RS amplification is  $g_R = 0.5 \text{ (W}\cdot\text{km)}^{-1}$

Output parameters of Gauss approximation according to Levenberg-Marquardt method

Mode	Quartz fiber $g_{Rmax} = 0.4 (W \cdot km)^{-1}$			True Wave RS TM $g_{Rmax} = 0.74 (W \cdot km)^{-1}$			DCF $g_{Rmax} = 3.1 (W \cdot km)^{-1}$			Raman fiber $g_{Rmax} = 6.3 (W \cdot km)^{-1}$		
	$A_i$	$\omega_i$ [cm <sup>-1</sup> ]	$\Gamma_i$ [cm <sup>-1</sup> ]	$A_i$	$\omega_i$ [cm <sup>-1</sup> ]	$\Gamma_i$ [cm <sup>-1</sup> ]	$A_i$	$\omega_i$ [cm <sup>-1</sup> ]	$\Gamma_i$ [cm <sup>-1</sup> ]	$A_i$	$\omega_i$ [cm <sup>-1</sup> ]	$\Gamma_i$ [cm <sup>-1</sup> ]
1	0.11	77.3	48.8	0.11	72.5	41.2	0.06	56.7	28.9	0.06	55.6	33.8
2	0.23	162.8	81.4	0.19	133.4	70.4	0.16	103.4	61.5	0.15	104.7	65.6
3	0.44	295.1	89.9	0.45	298.5	123.2	0.30	235.6	124.6	0.20	217.2	93.4
4	0.75	418.4	90.3	0.56	418.5	85.7	0.65	401.3	106.3	0.42	355.1	94.3
5	0.25	465.0	36.2	0.28	465.3	47.5	0.42	464.2	70.6	0.57	427.8	62.5
6	0.35	494.7	13.9	0.24	496.9	19.1	0.09	489.5	22.0	0.22	477.0	36.0
7	0.17	603.8	24.7	0.13	603.3	21.3	0.16	584.9	39.4	-0.21	628.6	47.0
8	0.14	542.0	190.5	0.25	544.2	146.3	0.18	708.8	206.4	0.44	601.7	172.1
9	0.13	809.6	50.6	-0.63	804.8	57.5	1.22	805.1	45.2	1.11	808.6	68.3
10	-0.01	858.5	30.3	0.05	858.8	29.9	0.11	858.8	29.9	0.06	858.8	29.9

## CONCLUSIONS

1. As the result of the model discussion and application, we have demonstrated the possibilities of the SRS signal spectroscopic analysis and their influence on the SRS lasers with single mode fibers design and technology as well as the review of the SRS amplification oscillating decomposition original methods in fibers of different type.
2. The model of actual band along with the method of multi-mode SRS amplification spectrum decomposition with the spectrum's approximation precision of 0.3%. The results are presented for some widely used fibers.
3. It was shown that the spectroscopic model allows to obtain in a simple and direct way the whole set of RS amplifiers, including: the amplification band and its non-regularity, group delay time and amplifier's noise parameters.

### Literature

1. *Distributed Fiber Raman Amplifiers With Localized Loss* / S. K. Kim, S. H. Chang, J. S. Han, M. J. Chu and J. H. Lee // *Journal of Lightwave Technology*, 21(5). — P. 1286–1293 (2003).
2. *Islam M. N. Raman Amplifiers for Telecommunications* // *IEEE Journal of Selected Topics in Quantum Electronics*, 8(3). — P. 548–559 (2002).
3. *Perlin V. E., Winful H. G. On Distributed Raman Amplification for Ultrabroad-Band Long-Haul WDM Systems* // *Journal of Lightwave Technology*, 20(3). — P. 409–416 (2002).
4. *Pump interactions in 100 nm bandwidth Raman amplifier* / H. Kidorf, K. Rottwitt, M. Nissov, M. Ma, E. Rabarjaona

// *IEEE Photonics Technology Letters*, 11(5). — P. 530–532 (1999).

5. *Mandelbaum I., Bolshtyansky M. Raman Amplifier Model in Single-Mode Optical Fiber* // *IEEE Photonics Technology Letters*, 15(12). — P. 1704–1706 (2003).
6. *Walrafen G. E., Krishnan P. N. Model analysis of the Raman spectrum from fused silica optical fibers* // *Applied Optics*, 21(3). — P. 359–360 (1982).
7. *Raman response function of silica-core fibers* / R. H. Stolen, J. P. Gordon, W. J. Tomlinson, H. A. Haus // *Journal of Optical Society of America*, B6(6). — P. 1159–1166 (1989).
8. *Stolen R. H., Lee C., Jain R. K. Development of the stimulated Raman spectrum in single-mode silica fibers* // *Journal of Optical Society of America*, B1(4), P. 652–657 (1984).
9. *Hollenbeck D., Cantrell C. D. Multiple-vibrational-mode model for fiber-optic Raman gain spectrum and response function* // *Journal of Optical Society of America*, B 19(12). — P. 2886–2892 (2002).
10. *Scaling of the Raman Gain Coefficient: Applications to Germanosilicate Fibers* / K. Rottwitt, J. Bromage, A. J. Stentz, L. Leng, M. E. Lines, H. Smith // *Journal of Lightwave Technology*, 21(7). — P. 1652–1662 (2003).
11. *Six-wavelength Raman fibre laser for C- and L-band Raman amplification and dynamic gain flattening* / M. D. Mermelstein, C. Horn, S. Radic, C. Headley // *Electronics Letters*, 38(13). — P. 636–638 (2002).
12. *Agrawal G. P. Nonlinear Fiber Optics*. Second ed. // San Diego, CA: Academic. — 1995.
13. *Loudon R. The Quantum Theory of Light*. Second ed. // Clarendon Press, Oxford. — 1983.
14. *Dakss L. M., Melman P. Amplified Spontaneous Raman Scattering and Gain in Fiber Raman Amplifiers* // *Journal of Lightwave Technology*, LT-3(4). — P. 806–813 (1985).
15. *Felinskyi G. S., Korotkov P. A. Actual band model for design of optical fiber Raman amplifier with multiwave pumping* // *Proceeding SPIE/Ukraine*, 6(1-6). — P. 409–417 (2006).

UDC 532

G. S. FELINSKYI

## SPECTROSCOPIC METHODS OF ACTIVE SRS PHOTONICS DEVICES MODELING FOR TELECOMMUNICATION SYSTEMS WITH TERBYTE VELOCITY

The simulation method of the Raman gain profile in single mode fibers which is put in the base of modern Raman lasers and fiber Raman amplifiers (FRA) is considered in this work. The spectroscopic model for the Raman gain spectrum decomposition in arbitrary optical fiber using multiple oscillating modes is presented. Modeling results is given for examples of development of stimulated Raman gain spectra in several wide-spread fibers on fused silica base. Nonlinear fitting procedure with Levenberg-Marquardt method of Raman gain profile was applied and it gives practically exact approximation of the observed Raman gain spectrum in silica fiber. The integrated intensities of model spectra are coincided with experimental spectrum within < 0.3 %. The optimal set of Raman gain parameters is compiled to simple analytical expressions that can be integrated and differentiated in symbolic form and are easy to evaluate numerically. Modeling results on the set of basic Raman amplifier characteristics such us: gain ripple, bandwidth, group delay, and noise performance is presented. Model is applicable to FRA design in fiber materials with known SRS spectra of any complexity.

УДК 532

Г. С. Фелінський

### **СПЕКТРОСКОПІЧНІ МЕТОДИ МОДЕЛЮВАННЯ АКТИВНИХ ВКР ПРИСТРОЇВ ФОТОНІКИ ДЛЯ ТЕЛЕКОМУНІКАЦІЙНИХ СИСТЕМ З ТЕРАБІТНОЮ ШВИДКІСТЮ**

В запропонованій роботі вивчається методика моделювання профіля ВКР підсилення в одномодових волокнах, які складають основу сучасних ВКР лазерів і підсилювачів. Розглянута спектроскопічна модель декомпозиції спектру КР підсилення у одномодовому волокні з багатьма коливними модами, яка являється узагальненням раніше розробленої моделі полоси. Результат моделювання викладається на прикладі відбудови спектра примусового КР підсилення в декількох розповсюджених волокнах з розплавленого кварцу. Застосування нелінійної апроксимації профіля КР підсилення за методом Левенберга-Марквардта дозволяє одержувати практично точну апроксимацію спостереженого спектра КР підсилення у кварцевих волокнах. Інтегральна інтенсивність модельного спектра співпадає з експериментальним спектром з точністю  $< 0,3\%$ . Оптимальний набір параметрів спектра підсилення входить у прості аналітичні формули, які можуть бути продиференцьовані і інтегровані аналітично і легко обчислюються. Запропоновано результати моделювання базового набору параметрів волоконних КР підсилювачів: нерівномірність підсилення, полоса підсилюваних частот, групова затримка а також шумові параметри. Модель можна застосувати до аналізу функціонування КР підсилювачів у волокнах з відомим спектром ВКР різної складності.

УДК 532

Г. С. ФЕЛИНСКИЙ

### **СПЕКТРОСКОПИЧЕСКИЕ МЕТОДЫ МОДЕЛИРОВАНИЯ АКТИВНЫХ ВКР УСТРОЙСТВ ФОТНИКИ ДЛЯ ТЕЛЕКОММУНИКАЦИОННЫХ СИСТЕМ С ТЕРАБИТНОЙ СКОРОСТЬЮ**

В настоящей работе рассматривается методика моделирования профиля ВКР усиления в одномодовых волокнах, составляющих основу современных ВКР лазеров и усилителей. Представлена спектроскопическая модель декомпозиции спектра КР усиления в произвольном одномодовом волокне со многими колебательными модами, которая является обобщением ранее разработанной модели актуальной полосы. Результаты моделирования излагаются на примере восстановления спектра вынужденного КР усиления в нескольких распространенных волокнах из плавленного кварца. Применение процедуры нелинейной аппроксимации профиля КР усиления по методу Левенберга-Марквардта позволяет получить практически точную аппроксимацию наблюдаемого спектра КР усиления в кварцевых волокнах. Интегральная интенсивность модельного спектра совпадает с экспериментальным спектром с точностью  $< 0,3\%$ . Оптимальный набор параметров спектра усиления входит в простые аналитические выражения, которые могут быть продиференцированы и интегрированы аналитически и легко вычисляются в численном виде. Представлены результаты моделирования базового набора параметров волоконных КР усилителей: неравномерность усиления, полоса усиливаемых частот, групповая задержка, а также шумовые параметры. Модель применима к анализу функционирования КР усилителей в волокнах с известным спектром ВКР произвольной сложности.

## EXTERNAL BIAS INFLUENCE ON TRANSMISSION PROCESSES IN NONIDEAL HETEROJUNCTION

Optimum conditions for nonequilibrium positive charge accumulation and storages are determined. The maximal charge accumulation speed for a sample, which basic cadmium sulfide layer is obtained by liquid electrohydrodynamical spraying (LEHDS) method in the air, is achieved at small negative biases (-0.3 V), and for a sample obtained by vacuum deposition method - at any negative or zero bias. The speed reduction of nonequilibrium charge ejection (optimum storage conditions) located on capture centers in RSC for a case when sensor obtained by LEHDS method in the air realizes at any negative bias, and for a sample obtained by vacuum deposition — at  $V = -0,4V$ .

For a long time the attention of the researchers was given to studying CdS-Cu<sub>2</sub>S nonideal heterojunction which can be applied for original effective converters of the optical and X-ray image into an electric signal creation, as it was convincingly shown [1]. At the same time, processes of emission and accumulation of nonequilibrium charge which determine the basic characteristics of converter in such structure are investigated insufficiently.

A lot of the phenomena in CdS-Cu<sub>2</sub>S heterojunction are anyhow determined by the form of potential barrier on heteroboundary. In this connection it is expedient to investigate processes in accumulation and emission of nonequilibrium charge under the influence of external bias applied to heterojunction.

Let's consider the influence of external bias on the character of the photoconverter signal ( $j_{sc}$ ) increase. The signal increase processes were investigated at continuous sensor excitation by light source with  $\lambda = 520$  nm. At the investigation in character of the signal recession, the sample was initially illuminated by powerful flash of white light (without external bias). The signal registration was made on the pulse values at the oscillograph screen under illumination of converter by light-emitting diode IR-pulses. Pulses registration was made without external bias.

Simultaneously with investigation of the samples obtained by liquid electrohydrodynamical spraying (LEHDS) method in the air (samples of group No 1), the samples obtained by vacuum evaporation method (samples of group No 2) were investigated too.

The measurements experimental results are submitted in fig. 1 and 2.

Figures show the curves for signal increase under samples excitation by light with  $\lambda = 520$  nm at different applied bias for typical samples of groups No 1 and No 2, accordingly. It is seen, that various stationary values of short circuit current, and, hence, the different accumulated stationary hole charge on traps in RSC (fig. 1–2) correspond to different applied biases.

On the basis of fig. 1 and 2 we constructed the dependence of charge accumulation speed on value of external bias (fig. 3). The analysis of the curves obtained show, that charge accumulation speed decreases sharply in the region of positive biases and on the

abscissa cuts off the voltage about 1 V, that approximately corresponds to barrier height  $\phi_0$  in CdS-Cu<sub>2</sub>S heterojunction. For the samples obtained by LEHDS method the cutoff voltage is some less that can be caused by the greater degree of structure imperfection in comparison with the samples obtained by vacuum evaporation method.

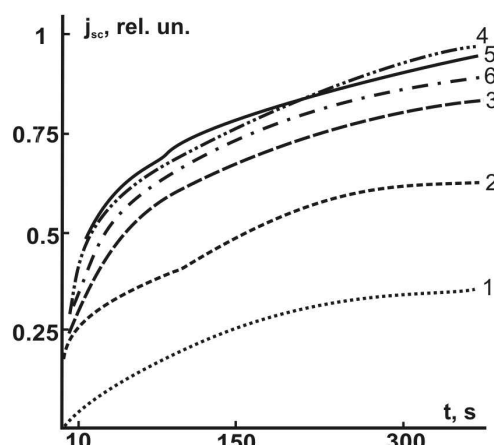


Fig. 1. The curves of ( $j_{sc}$ ) signal dependence on time of samples excitation by light with  $\lambda = 520$  nm at different values of applied external bias. The sample was obtained by LEHDS method in the air (group No 1): 1 (+1 V), 2 (+0,6 V), 3 (+0,3 V), 4 (-0,3 V), 5 (-0,5 V), 6 (-0,9 V)

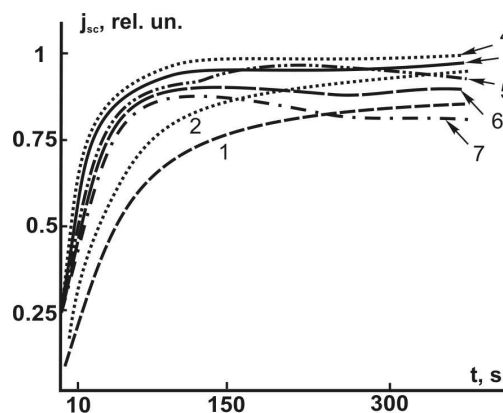


Fig. 2. The curves of ( $j_{sc}$ ) signal dependence on time of samples excitation by light with  $\lambda = 520$  nm at different values of applied external bias. The sample was obtained by vacuum evaporation method (group No 2): 1 (+0,9 V), 2 (+0,6 V), 3 (+0,3 V), 4 (+0,1 V), 5 (-0,1 V), 6 (-0,4 V), 7 (-0,9 V)

Let's pay attention to the fact that with reduction of positive bias the value of signal increase speed raises, reaches the maximal values at small negative biases, and decreases again at high values of negative bias (fig. 3).

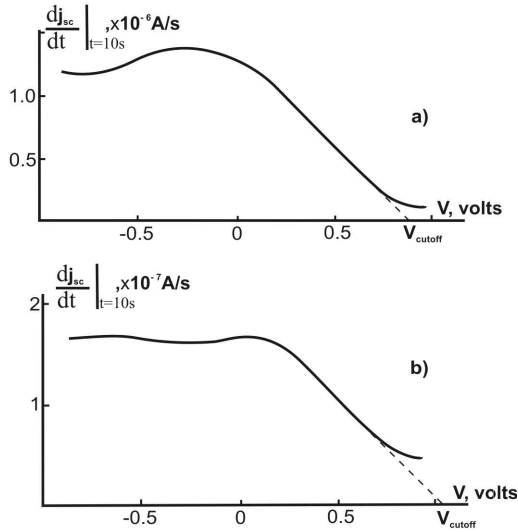


Fig. 3. Dependence of the charge accumulation speed (a derivative  $j_{sc}$  on time) on voltage of external bias for samples of groups No 1 - (a) and No 2 - (b)

Let's observe the influence of external bias value on accumulation, and, hence, on current transfer of charge in RSC of CdS-Cu<sub>2</sub>S heterojunction.

Conditions of current transfer and recombination on CdS-Cu<sub>2</sub>S heterojunction heteroboundary are determined by a kind of  $\varphi(x)$  function which describes the behavior of potential barrier in heterojunction RSC. As it was already noted, this is connected with, the fact that the short circuit current ( $j_{sc}$ ) generated by IR-light in Cu<sub>2</sub>S is determined not only by the intensity of illumination, the quantum yield and the collecting factor in Cu<sub>2</sub>S but also by the ratio between speed of surface recombination for free electron being generated by light in Cu<sub>2</sub>S, and their drift speed in heteroboundary (formula 1).

$$j_{sc} = j_{sc}^0 \frac{\mu_n \frac{1}{q} \frac{d\varphi}{dx} \Big|_{x=0}}{\mu_n \frac{1}{q} \frac{d\varphi}{dx} \Big|_{x=0} + S_s} \quad (1)$$

For unlighted heterojunction, the potential  $\varphi(x)$  depends only on bias  $V$  and is expressed by the formula

$$\varphi(x) = (\varphi_0 - qV) \left(1 - \frac{x}{W}\right)^2 + qV + \Delta F_0, \quad (2)$$

where  $\varphi_0$  – heterojunction barrier height,  $W$  – RSC width,

$\Delta F_0$  – depth of occurrence for Fermi level in cadmium sulfide quasi-neutral region.

When heterojunction is illuminated, minor carriers (holes) generated in wideband cadmium sulfide are captured in RSC on the traps there which concentration is equal  $N_t$ . Because of zones curvature in RSC, distribution of the localized charge along axis  $x$  is determined by expression (3).

$$\Delta p(x) = \Delta p_0 \exp \left[ \frac{\varphi_0}{kT} \left( \frac{W-x}{W} \right) \right]. \quad (3)$$

The solving of Poisson equation (4)

$$\frac{d^2 \varphi}{dx^2} = \frac{\rho(x)}{\varepsilon \varepsilon_0}, \quad (4)$$

where

$$\rho(x) = q \left[ N_d + \Delta p(x) - n(x) \right] \quad (5)$$

at external bias in view of expression (3) and (5) allows to receive dependence of potential barrier for illuminated heterojunction on coordinate:

$$\varphi(x) = \frac{\varphi_0 - qV}{1 + \frac{\Delta p_0}{\alpha N_d}} \left[ 1 + \frac{x^2}{W^2} + \left( \frac{2\Delta p_0}{\alpha N_d} - 2 \right) \frac{x}{W} \right] + \frac{2\Delta p_0}{\alpha^2 N_d} \left( e^\alpha e^{-\alpha \frac{x}{W}} - 1 - \alpha \right) + \Delta F_0, \quad (6)$$

$$\alpha = \frac{\varphi_0 - qV}{kT}.$$

where

Expressions (2) and (6) show that external bias  $qV$  influences essentially on the form of potential barrier and, hence on the value  $\left. \frac{d\varphi}{dx} \right|_{x=0}$  which determines short circuit current.

It is obvious, that current transfer in investigated structure is determined by concentration of nonequilibrium charge located in RSC. We shall consider the current dynamics at different external biases. As at heterojunction illumination simultaneously with charge accumulation emission takes place, for the simplicity let's observe the case of decay relaxation (when stimulating light is cut off).

Experimental curves for current value dependence on time, passed after end of sensor excitation by flash of white light and the speed of current decrease (a derivative  $\left. \frac{dj_{sc}}{dt} \right|_{t=10s}$ ) are given in fig. 4 and 5, accordingly,

at different values of external bias.

Thermal ejection (fig. 6, transition 1) does not depend on bias  $V$ . Direct tunneling (transition 2) weakly depends on  $V$ , but two-level tunneling process with the subsequent recombination (transition 3) and tunnel-jumping recombination process (transition 4) depend on the applied external bias. At  $V \rightarrow \varphi_0/q$  the recombination in the way 3 becomes considerable, that results in high  $j_{sc}$  drop speed for a typical sample of group No 1 (fig. 4, and fig. 5, a). In this sample cadmium sulfide was obtained by LEHDS method with the subsequent pyrolysis in the air that results in strongly developed surface and the crystallite sizes being smaller than 0,5 microns.

Cadmium sulfide for samples of group No 2 was obtained by vacuum dispersion method. Its crystallite size is the order more, but the density defects is much lower. This causes low speed of signal drop (fig. 4, b),

and can be connected with the fact that process (4) does not contribute essentially the recombination.

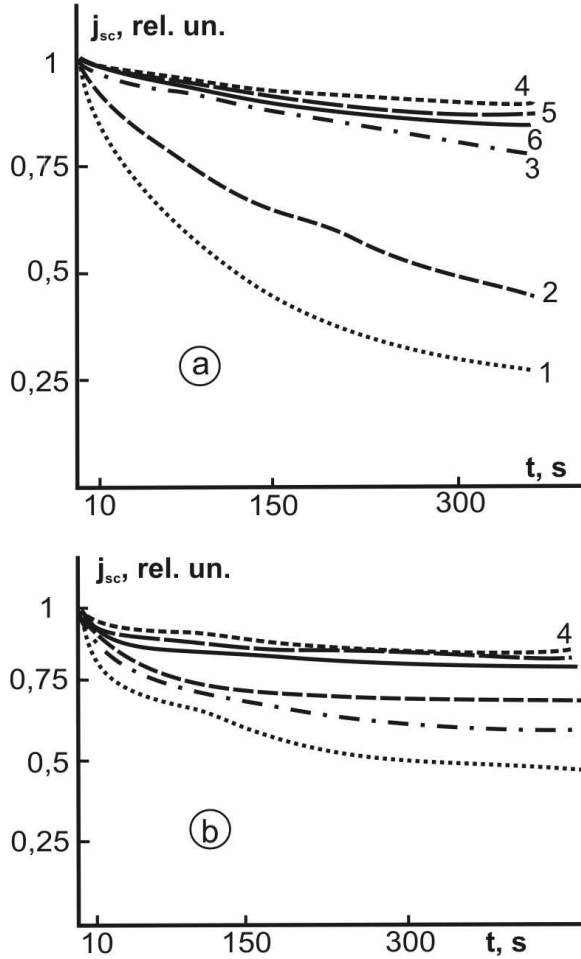


Fig. 4. Dependence of signal  $j_{sc}$  value on time after sample excitation by white light pulse at different bias values. For typical sample of group No 1 — a and for sample of group No 2 — b: 1 (+0,9 V), 2 (+0,5 V), 3 (+0,2 V), 4 (-0,2 V), 5 (-0,5 V), 6 (-0,9 V)

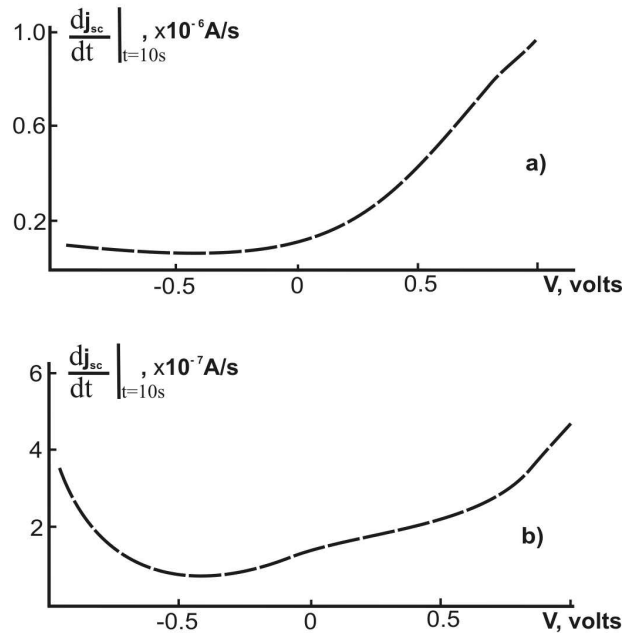


Fig. 5. Dependence for relaxation speed of charge decrease (current  $j_{sc}$  derivative in time) for various bias values on bias value for samples of group No 1 — a and No 2 — b

Let's observe the influence of external bias on hole emission mechanisms (fig. 6).

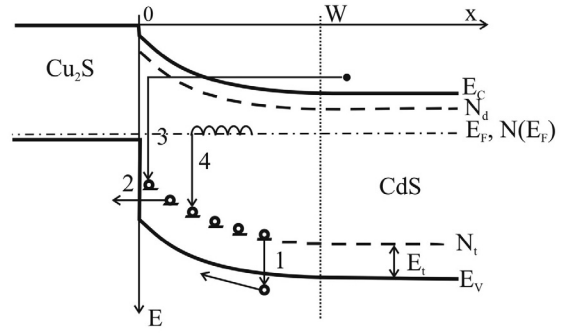


Fig. 6. Mechanisms to remove holes captured on traps out of CdS-Cu<sub>2</sub>S heterojunction RSC. 1 — thermal emission into the valence band; 2 — direct hole tunneling from trap centers into Cu<sub>2</sub>S valence band; 3 — free electron two-level tunneling from CdS quasi-neutral region into RSC and the subsequent recombination with nonequilibrium hole; 4 — tunnel-jumping recombination

In homogeneous materials tunnel-jumping mechanism on the located states is usually observed at rather low temperatures [2]. At the same time, for barrier structures, concentration of free carriers which determines thermal activation current, at small biases ( $V \ll \phi_0/q$ ) is too small, that makes jumping conductivity mechanism the basic one even at rather high temperatures. Cadmium sulfide obtaining by LEHDS method and formation of CdS-Cu<sub>2</sub>S heterojunction by vacuum deposition method, results in formation of significant amount of defects in transient region. At defects concentration  $10^{18}$ - $10^{21}$  sm<sup>-3</sup> quasi-continuous density of states  $N(E)$  appears in RSC by which current transfer can be carried out.

With the increase of positive bias, the energy position of Fermi level  $E_F(x)$  in all points  $x$  is increased, hence, the states density, near the Fermi level  $N(E_F)$  increases, and tunnel-jumping recombination speed in a way 4 raises. However, as it was earlier mentioned, for a sample obtained by vacuum deposition method, the absolute values  $N(E_F)$  are lower, that's why this process cleared weakly. At high negative biases, because of barrier form changing for the sample of group No 2 hole tunneling into Cu<sub>2</sub>S V-zone increase, but for sample of group No 1 this effect is less noticeable, this can be connected with high barrier width, or the presence of deep centers (fig. 5, a, b).

Let's turn back now to the process of current signal increase in heterojunction at photoexcitation. The rate of nonequilibrium charge increase in heterojunction RSC will be determined by expression (7):

$$\frac{dp_t}{dt} = f - p_t \bar{v} S_{pt} P_v \exp\left[-\frac{E_t}{kT}\right] - p_t \bar{v} S_{pt} P_v D_1(x) - p_t \bar{v} S_{nt} n_0 D_2(x) - p_t \bar{v} S_{nr} N(E_F), \quad (7)$$

where  $f$  — the generation function that has constant value;  $\bar{v}$  — average thermal speed of carriers;  $S_{pt}$  and  $S_{nt}$  — holes and electrons capture cross section;  $P_v$  — effective state density in CdS valence band;  $n_0$  — free electrons concentration in quasineutral CdS region;  $S_{nr}$  — capture cross section of electron by recombination center on interface boundary;  $N(E_F)$  state density

in vicinity of Fermi level;  $D_1(x)$ ,  $D_2(x)$  — transparency factors of barriers corresponded to direct hole tunneling from traps centers into  $\text{Cu}_2\text{S}$  valence band and two-level free electron tunneling from CdS quasi-neutral region into RSC with subsequent recombination with nonequilibrium hole;  $\bar{v}$  — effective thermal speed of carriers at jumping conductivity ( $\bar{v} = R'w$ , where  $w$  — probability of a jump for the most probable length  $R'$ ).

Generation function  $f$  and thermal ejection do not depend on voltage bias. At the high positive biases, as in the case of excitation absence, charge accumulation speed decreases essentially because of two-level recombination intensity growth (transition 3) and tunnel-jumping recombination (transition 4). Therefore, according to the formula (3.1),  $dp_i/dt$  thus decreases,

that results in experimentally observed  $\left. \frac{dj_{sc}}{dt} \right|_{V=0.5}$  reduction (fig. 3). At  $V \rightarrow \varphi_0/e$  recombination barrier for process (2) disappears and recombination in this way becomes so high, that charge accumulation on centers  $N_t$  practically does not occur, i. e.  $\Delta p = 0$  and the profile  $\varphi(x)$  does not change, and hence  $j_s$  current value does not change too. However, at  $V \rightarrow \varphi_0/e$  the part of voltage decays on series resistance of cadmium sulfide layer.

From above-stated follows, that for the optimization of accumulation information process (the maximal charge accumulation speed) for sample of group No 1 (cadmium sulfide obtained in the air) it is possible to apply low negative bias, and for sample of group No 2 (cadmium sulfide obtained in vacuum) — any negative or zero biases (fig. 3). The optimum conditions for information storage (located nonequilibrium charge ejection minimal speed) realize at any negative

biases for sample of group No 1, and for sample of group No 2 at  $V = -0,4V$  (fig. 5). Process of the accelerated informative charge ejection from RSC (for both variants to produce heterojunction), can be carried out by applying positive bias at value of about 1 V.

## CONCLUSION

Optimum conditions for nonequilibrium positive charge accumulation and storages are determined. The maximal charge accumulation speed for a sample, which basic cadmium sulfide layer is obtained by liquid electrohydrodynamical spraying (LEHDS) method in the air, is achieved at small negative biases ( $-0.3$  V), and for a sample obtained by vacuum deposition method — at any negative or zero bias. The speed reduction of nonequilibrium charge ejection (optimum storage conditions) located on capture centers in RSC for a case when sensor obtained by LEHDS method in the air realizes at any negative bias, and for a sample obtained by vacuum deposition — at  $V = -0,4V$ .

## References

1. *Sensor on the basis of nonideal heterojunction for registration of the x-ray images* / V. A. Smyntyna, V. A. Borschak, M. I. Kutalova, N. P. Zatovskaya, A. P. Balaban // Proc. of Eurosensors XVIII Conf. — Rome. — 12–15 sep. — 2004. — P. 67.
2. *Application of thin film nonideal heterojunctions to produce sensor for optical and X-ray images* / V. A. Smyntyna, V. A. Borschak, N. P. Zatovskaya, M. I. Kutalova, A. P. Balaban // Photoelectronics, N 11, 2002. — P. 3–5.
3. *Mott N., Davis A. Electron processes in non-crystal matters.* — Moscow: Mir Publishers, 1982. — Vol. 1. — P. 368.

UDC 621.315.592

V. A. Smyntyna, V. A. Borschak, M. I. Kutalova, N. P. Zatovskaya, A. P. Balaban

## EXTERNAL BIAS INFLUENCE ON TRANSMISSION PROCESSES IN NONIDEAL HETEROJUNCTION

Optimum conditions for nonequilibrium positive charge accumulation and storages are determined. The maximal charge accumulation speed for a sample, which basic cadmium sulfide layer is obtained by liquid electrohydrodynamical spraying (LEHDS) method in the air, is achieved at small negative biases ( $-0.3$  V), and for a sample obtained by vacuum deposition method — at any negative or zero bias. The speed reduction of nonequilibrium charge ejection (optimum storage conditions) located on capture centers in RSC for a case when sensor obtained by LEHDS method in the air realizes at any negative bias, and for a sample obtained by vacuum deposition — at  $V = -0,4V$ .

УДК 621.315.592

В. А. Сминтина, В. А. Боршак, М. І. Куталова, Н. П. Затовська, А. П. Балабан

## ВПЛИВ ЗОВНІШНЬОГО ЗМІЩЕННЯ НА ПЕРЕХІДНІ ПРОЦЕСИ В НЕІДЕАЛЬНОМУ ГЕТЕРОПЕРЕХОДІ

Визначено оптимальні умови для нагромадження і збереження нерівноважного позитивного заряду. Максимальна швидкість нагромадження заряду для зразка, базовий шар сульфід кадмію якого отриманий методом електрогідродинамічного розпилення рідини (ЕГДРР) у повітрі, досягається при невеликих негативних зсувах ( $-0.3$  В), а для зразка, отриманого вакуумним осадженням — при будь-яких негативних зсувах або нульовому зсуві. Зменшення швидкості викиду локалізованого на центрах захоплення в ОПЗ нерівноважного заряду (оптимальні умови збереження) для випадку одержання сенсора методом ЕГДРР у повітрі здійснюється при будь-яких негативних зсувах, а для зразка, отриманого вакуумним осадженням — при  $V = -0,4V$ .

УДК 621.315.592

В. А. Смытына, В. А. Боршак, М. И. Куталова, Н. П. Затовская, А. П. Балабан

**ВЛИЯНИЕ ВНЕШНЕГО СМЕЩЕНИЯ НА ПЕРЕХОДНЫЕ ПРОЦЕССЫ В НЕИДЕАЛЬНОМ ГЕТЕРОПЕРЕХОДЕ.**

Определены оптимальные условия для накопления и хранения неравновесного положительного заряда. Максимальная скорость накопления заряда для образца, базовый слой сульфида кадмия которого получен методом электрогидродинамического распыления жид кости (ЭГДРЖ) на воздухе, достигается при небольших отрицательных смещениях ( $-0,3$  В), а для образца, полученного вакуумным осаждением – при любых отрицательных или нулевом смещении. Уменьшение скорости выброса локализованного на центрах захвата в ОПЗ неравновесного заряда (оптимальные условия хранения) для случая получения сенсора методом ЭГДРЖ на воздухе осуществляется при любых отрицательных смещениях, а для образца, полученного вакуумным осаждением – при  $V = -0,4V$ .

## THE GROUND STATE LAMB SHIFT IN HYDROGENIC GERMANIUM WITHIN THE QED THEORY

Calculating the 1s-2p Lyman  $\alpha$  transitions in the hydrogenic germanium has been carried out on the basis of gauge-invariant quantum electrodynamics (QED) theory with an account of relativistic, nuclear and radiative (Lamb shift) effects

### 1. INTRODUCTION

At present time a studying the spectra of heavy and super heavy atoms and ions is of a great interest (c.f. [1-26]). It is provided by necessity of further developing the modern atomic spectra theory. Besides, such studying is stimulated by the great progress in experimental technique, connected with using new powerful lasers and accelerators [1-5]. One of the advanced experimental technique for making measurements of the atomic spectra is developed in the GSI (Germany) centre [1-3]. In particular, the hydrogenic germanium, bismuth, Uranium and lithium-like same elements have been the objects of the especial interest. From the other side, similar experiments represent a great challenge to a modern atomic spectra theory. More over, the precise experiment stimulates also a developing more consistent and precise theories for taking into account of the radiative, QED effects, in particular, the Lamb shift. In calculations of the heavy ions, the well-known Dirac or multi-configuration Dirac-Fock (for multielectron systems) approach is widely used. It provides the most reliable version of calculation for atomic systems. Nevertheless, as a rule, detailed description of the method for studying role of the nucleus finite size effect is lacking. Besides, hitherto absolutely advanced, comprehensive theory of the Lamb shift is absent. As result there many attempts to achieve the corresponding theory. One could mention here the perturbation theory (PT) formalism on parameters  $1/Z$ ,  $\alpha Z$  ( $\alpha$  is a fine structure constant). It permits evaluations of the relative contributions of different expansion energy terms: non-relativistic, relativistic ones, as the functions of  $Z$ . But, the serious problems are connected with correct definition of the QED corrections: the Lamb shift, the Lamb shift self-energy part, vacuum polarization, the nuclear finite size correction etc. Very effective consistent QED perturbation theory method has been developed in the series of papers [10-18]. The further improvement of the method was connected with using the gauge invariant procedures of generating relativistic orbitals basis's and developing principally new QED approach of treating the nuclear and QED effects. In refs. [19-26] it has been developed a new ab initio approach to calculating spectra of heavy systems with account of relativistic, correlation, nuclear, QED effects, based on the gauge-invariant QED PT [13] and new effective procedures for accounting the nuclear and radiative corrections. It has been earlier used for calculat-

ing energy spectra, QED corrections, the hyperfine structure parameters for heavy and super heavy atoms and ions and also for positronium. In this paper calculating the 1s-2p Lyman  $\alpha$  transitions in the hydrogenic germanium has been carried out on the basis of gauge-invariant (QED) theory and compared with the precise GSI experiment as an important test.

### 2. METHOD OF CALCULATION

As the detailed description of basis's for new QED perturbation theory approach has been given in the earlier papers [10-14] and new procedures for correct accounting of the correlation, nuclear and radiative effects are described in papers [15-26], further let us present describe in brief the important moments of our calculation method.

The wave functions zeroth basis is found from the Dirac equation solution with potential, which includes ab initio electric, vacuum-polarization potentials of nucleus (the gaussian form for charge distribution in the nucleus is used). We set the charge distribution in the nucleus by the Gaussian function:

$$\rho(r|R) = (4\gamma^{3/2}/\sqrt{\pi}) \exp(-\gamma r^2) \quad (1)$$

Here  $\gamma = 4/\pi R^2$ ;  $R$  is an effective nucleus radius, defined as:  $R = 1.60 \times 10^{-13} Z^{1/3}$  (cm). The Coulomb potential for spherically symmetric density  $\rho(r/R)$  is:

$$V_{nuc}(r|R) = -((1/r) \int_0^r dr' r'^2 \rho(r'|R) + \int_r^\infty dr' r' \rho(r'|R)) \quad (2)$$

Further one can write the one-electron bi-spinor Dirac-like equation for hydrogenic germanium. Formally it falls into one-electron Dirac equations for the orbitals  $1s, nlj$  with potential  $V(r)$ . This potential includes the electrical and vacuum-polarization potentials of the nucleus. The corresponding basis of relativistic orbitals is further checked and corrected according to the gauge invariant QED procedure [12]. The VP part is usually accounted in the first PT order by using the Uehling potential (c.f. [12, 18-23]):

$$U(r) = -\frac{2\alpha}{3\pi r} \int_1^\infty dt \exp(-2rt/\alpha Z) (1 + 1/2t^2) \frac{\sqrt{t^2 - 1}}{t^2} \equiv \\ \equiv -\frac{2\alpha}{3\pi r} C(g), \quad g = \frac{r}{\alpha Z}. \quad (3)$$

In our scheme this potential is approximated by quite precise analytical function [9, 14, 21]

$$\begin{aligned}\tilde{C}(g) &= \tilde{C}_1(g)\tilde{C}_2(g)/(\tilde{C}_1(g)+\tilde{C}_2(g)) \\ \tilde{C}_2(g) &= \tilde{C}_2(g)f(g), \\ \tilde{C}_2(g) &= -1.8800\exp(-g)/g^{3/2}, \\ \tilde{C}_1(g) &= \ln(g/2)+1.410548-1.037845g, \\ f(g) &= ((1.1022/g-1.3362)/g+0.8028)\end{aligned}\quad (4)$$

The using this formula permits one to decrease the calculation errors for this term down to  $\sim 0.1\%$ . Error of usual calculation scheme is  $\sim 10\%$ . The procedure of calculating the SE correction is based on the idea that radiative shift and relativistic part of atomic energy are, in principle, defined by the same physical field [9]. This version with different approximations has been realized in ref. [9,10,13]. We call it as QED-PT-1. In ref.[19-26] it was developed principally new approach to calculating the SE part of the Lamb shift, which is based on the gauge-invariant Green's function method. The calculation of the self-energy correction is carried out on the basis of the Mohr covariant regularization of the Feynman S-matrice. As usually, we start from the operator perturbation theory approach for Dirac equation. The self-energy correction is expressed through Feynman S-matrix elements and has the Mohr form [19, 24, 25]:

$$E = E_L + E_H(\Lambda) - \frac{1}{\alpha\pi Z} \left( \frac{3}{2} \ln \Lambda \alpha^2 + \frac{3}{8} \right) \langle \beta \rangle, \Lambda \rightarrow \infty. \quad (5)$$

The high-energy part is as follows:

$$E_H(\Lambda) = \text{Re} \frac{1}{\pi Z} \int_0^\infty d\xi [E(\xi, 0) - E(\xi, \Lambda)], \quad (6)$$

$$\begin{aligned}E(\xi, \Lambda) &= \iint dr_1 dr_2 \frac{1}{r_{12}} \exp \left[ (E_0 - i\xi)^2 - \Lambda^2 \right]^{1/2} \\ &\quad \psi^+(r_2) \alpha^\mu G(r_1 r_2) \alpha^\mu \psi(r_1)\end{aligned}\quad (7)$$

all notations are standard [5, 21, 25]. We call it as QED-PT-2. It should be noted that these approaches are more justified than using the expansions by the parameter  $\alpha Z$  [5–9]. Below we use the QED-PT-2 algorithm [1, 9, 21, 25].

### 3. RESULTS AND DISCUSSION

The precise experiment with hydrogenic germanium has been fulfilled in the GSI [1]. A beam of bare germanium nuclei at an energy of 1,108 GeV (15MeV/amu,  $\beta=0,1772$ , where  $\beta$  is the ion velocity divided by the speed of light) from Gesellschaft für Schwerionenforschung (GSI) UNILAC was passed through a thin carbon foil. Some of the nuclei capture an electron in the foil and one can find that

under these excitation conditions lines in the Balmer series are clearly seen for upper level principal quantum numbers  $n$  to about  $n=7$ . In particular, there is a good probability for the production of the  $n=4$  to  $n=2$  hydrogenic transitions. The spectrometer used was a dual-arm Johann curved crystal spectrometer developed by the Lawrence Livermore National Laboratory (c.f.[1-4]). The dispersing crystal used in the experiment was Si 111, with a 2d spacing of 6,271 Å. The detailed spectra were recorded for hydrogenic germanium [1] and the corresponding data are presented in the table.

We carried out the calculation of the Lyman  $\alpha$   $1s^2S_{1/2}-2p^2P_{3/2}$ ,  $1s^2S_{1/2}-2p^2P_{1/2}$  transitions wavelengths in the hydrogenic germanium on the basis of our QED perturbation theory method and compared the obtained results with data of the precise experiment [1]. One of the main purposes of calculation was to check an accuracy of the new QED approach in the theory of atomic spectra. In table 1 we present our calculation results for the Lyman  $\alpha$   $1s^2S_{1/2}-2p^2P_{3/2}$ ,  $1s^2S_{1/2}-2p^2P_{1/2}$  transitions wavelengths in the hydrogenic germanium. In whole, one could note that an agreement between the obtained theoretical data and experimental results is excellent. The same conclusion is naturally right for the Lamb shift value.

Table 1  
Lyman  $\alpha$  transition wavelengths (in Å): precise experiment [1] and QED perturbation theory calculation (present work)

Contribution	Experiment [1]	Present theory
1s2S1/2-2p2P3/2	1,166882±0,000016 1,166858±0,000016 1,166854±0,000017	1,166868
1s2S1/2-2p2P1/2	1,172326±0,000015 1,172296±0,000020 1,172327±0,000016	1,172321

There are several reasons, which explain an excellent agreement between our theory and the precise experiment. First of all, we use in the QED perturbation theory zeroth approximation the gauge-invariant bases of the relativistic orbitals, checked according to the consistent QED procedure. Secondly, we are carrying out the precise modeling the nuclear finite size effects. Thirdly, we have used the principally new approach to estimating the radiative QED effects, in particular, the Lamb shift correction, which is not out the usual schemes of the  $1/\alpha Z$  etc expansions. As the QED theory used is absolutely ab initio approach, it easily understand that it could be usefully applied to calculation of the corresponding properties for atoms and multicharged ions when any experimental or theoretical data are absent. Especially, it can be regarding the heavy and superheavy relativistic atomic systems.

#### References

1. *A differential measurement of the ground state Lamb shift in hydrogenic germanium* / J. Laming, C. T. Chantler, J. D. Silver, D. D. Dietrich, E. C. Finch, P. H. Mokler, S. D. Rosner // Nucl.Instr. and Methods in Phys. Res. —1998. — Vol. B31. — P. 21–23.
2. *Measurement of the Lamb shift in lithiumlike uranium ( $U^{89+}$ )* / J. Schweppe, A. Belkacem, L. Blumenfeld, N. Clayton, B. Feinberg, H. Gould, V. E. Kostroum, L. Levy, S. Misawa, J.

- R. Mowst, M. H. Priour // Phys. Rev. Lett. — 1991. — Vol. 66. — P. 1434–1437.
3. *Gould H.* Lamb shift measurement in lithium-like uranium ( $U^{89+}$ ) // Phys. Scripta T. — 1993. — Vol. 46. — P. 61–64.
  4. *Precision* laser spectroscopy of ground state hyperfine splitting of H-like  $^{209}Bi^{82+}$  / I. Klaft, S. Borneis, T. Engel, B. Fricke, R. Grieser, G. Huber, T. Kuhl, D. Marx, R. Neumann, S. Schroder, P. Seelig, L. Volker // Phys. Rev. Lett. — 1994. — Vol. 73. — P. 2425–2427
  5. *Mohr P. J.* Quantum Electrodynamics Calculations in few-Electron Systems// Phys. Scripta. — 1993. — Vol. 46, N 1. — P. 44–52.
  6. *Blundell S. A.* Ab initio Calculations of QED Effects in Li-like, Na-like and Cu-like Ions// Phys. Scripta. — 1993. — Vol. 46, N 1. — P. 144–150.
  7. *Persson H., Lindgren L., Salomonson S.* A new approach to the electron self-energy calculation // Phys. Scripta. T. — 1993. — Vol. 46. — P. 125–131.
  8. *Quiney H. M., Grant I. P.* Partial-wave mass renormalization in atomic QED calculation// Phys. Scripta T. — 1993. — Vol. 46. — P. 132–138.
  9. *Ivanov L. N., Ivanova E. P., Kalinkin A. N.* Nuclear and radiative effects in spectra of heavy and superheavy hydrogen-like ions // Nucl. Phys. — 1985. — Vol. 42. — P. 355–362.
  10. *Ivanova E. P., Ivanov L. N., Aglitsky E. V.* Modern Trends in Spectroscopy of Multicharged Ions // Physics Rep. — 1991. — Vol. 166, N 6. — P. 315–390.
  11. *Glushkov A. V.* Negative Ions of inert Gases// JETP Lett. — 1992. — Vol. 55, N 2. — P. 97–100.
  12. *Glushkov A. V., Ivanov L. N.* Radiation Decay of Atomic States: atomic residue and gauge non-invariant contributions // Phys. Lett. A. — 1992. — Vol. 170, N 1. — P. 33–37.
  13. *High order corrections in the Relativistic Perturbation Theory with the model Zeroth Approximation, Mg-like and Ne-like ions / E. P. Ivanova, L. N. Ivanov, A. V. Glushkov, A. E. Kramida // Phys. Scripta. — 1985. — Vol. 32, N 4. — P. 512–524.*
  14. *Glushkov A. V., Ivanova E. P.* Theoretical Study of Multicharged Ions Spectra of F- and Ne- Isoelectronic Sequence// J. Quant. Spectr. Rad. Transfer. — 1986. — Vol. 36, N 2. — P. 127–145.
  15. *Resonance* states of compound super-heavy nucleus and EPPP in heavy nucleus collisions / A. V. Glushkov, V. D. Rusov, S. V. Ambrosov, A. V. Loboda // New Projects and New Lines of research in Nuclear physics. Eds. Fazio G., Hanappe F. — Singapore: World Sci., 2003. — P. 142–154.
  16. *QED* Calculation of Electron Satellites Spectra in Intense Laser Field in Multicharged Ion / A. V. Glushkov, S. V. Malinovskaya, A. A. Svinarenko, Yu. G. Chernyakova // Int. J. Quant. Chem. — 2004. — Vol. 99, N 5. — P. 889–896.
  17. *Glushkov A. V., Malinovskaya S. V.* Co-operative laser nuclear processes: border lines effects// In: New projects and new lines of research in nuclear physics. Eds. G. Fazio and F. Hanappe, Singapore: World Scientific. — 2003. — P. 242–250.
  18. *Glushkov A. V., Ambrosov S. V., Loboda A. V., et al.* QED calculation of the superheavy elements ions: energy levels, radiative corrections and hfs for different nuclear models // Nucl. Phys. A.: Nucl. and Hadr. Phys. — 2004. — Vol. 734. — P. 21–24.
  19. *Glushkov A. V., Gurnitskaya E. P., Loboda A. V.* Advanced quantum mechanical calculation of superheavy ions: energy levels, Radiation and Finite Nuclear size effects // Low Energy Antiproton Phys., AIP Serie. — 2005. — Vol. 796. — P. 217–220.
  20. *Glushkov A. V., Gurnitskaya E. P.* New QED perturbation theory formalism for relativistic atomic systems: Green's function method // Preprint of Institute for physics of I. I. Mechnikov Odessa National University. — 2004. — S3. — 35 p.
  21. *QED* calculation of heavy multicharged ions with account for the correlation, radiative and nuclear effects / A. V. Glushkov, S. V. Ambrosov, A. V. Loboda, E. P. Gurnitskaya, O. Yu. Khetselius // Recent Advances in Theor. Phys. and Chem. Systems. — 2006. — Vol. 15. — P. 285–300.
  22. Consistent QED approach to calculation of electron-collision excitation cross-sections and strengths: Ne-like ions / A. V. Glushkov, S. V. Ambrosov, A. V. Loboda, E. P. Gurnitskaya, G. P. Prepelitsa // Int. Journ. Quant. Chem. — 2005. — Vol. 104, N 4. — P. 562–569.
  23. *Khetselius O. Yu.* Hyper fine structure of radium // Photoelectronics. — 2005. — N 14. — P. 83–85.
  24. *Gurnitskaya E. P.* Calculation of energy levels for heavy li-like ions with account for the radiative effects within the qed perturbation theory: new scheme for lamb shift // Photoelectronics. — 2007. — N 16. — P. 126–128.
  25. *Khetselius O. Y., Gurnitskaya E. P.* Sensing the electric and magnetic moments of a nucleus in the N-like ion of Bi // Sensor Electr. and Microsyst. Techn. — 2006. — N 3. — P. 35–39.
  26. *Gurnitskaya E. P.* Sensing the de fontenau-aux-roses tokamak plasma parameters by means x-ray theoretical spectroscopy method: new advanced scheme//Sensor Electronics and Microsystems Technologies. — 2005. — N 4. — P. 43–46.

UDC 539.142:539.184

E. P. Gurnitskaya

#### THE GROUND STATE LAMB SHIFT IN HYDROGENIC GERMANIUM WITHIN THE QED THEORY

Calculating the 1s-2p Lyman  $\alpha$  transitions in the hydrogenic germanium has been carried out on the basis of gauge-invariant quantum electrodynamics (QED) theory with an account of relativistic, nuclear and radiative (Lamb shift) effects.

УДК 539.142:539.184

Е. П. Гурницкая

#### ЛЭМБОВСКИЙ СДВИГ ОСНОВНОГО СОСТОЯНИЯ ВОДОРОДОПОДОБНОГО ГЕРМАНИЯ В РАМКАХ КЭД ТЕОРИИ

Выполнен расчет характеристик 1s-2p Ляман  $\alpha$  переходов в водородоподобном германии на основе калибровочно-инвариантной квантово-электродинамической теории с учетом релятивистских, ядерных и радиационных (лэмбовский сдвиг) эффектов.

УДК 539.142 : 539.184

О. П. Гурницька

**ЛЕМБІВСЬКИЙ ЗСУВ ОСНОВНОГО СТАНУ ВОДНЕПОДІБНОГО ГЕРМАНІЯ В МЕЖАХ КЕД ТЕОРІЇ**

Виконано розрахунок характеристик  $1s-2p$  Lyman  $\alpha$  переходів в воднеподібному германії на підставі калібровочно-інваріантної квантово-електродинамічної теорії з урахуванням релятивістських, ядерних та радіаційних (лембівський зсув) ефектів.

A. S. PHOMIN, V. P. MYGAL, A. V. BUT

National Space University named after N.E. Zhukovsky «KhAi», Ukraine, Kharkov, 61070, Chkalov Street, 17, phone (057) 707-41-78, [khai\\_physical\\_lab@xai.edu.ua](mailto:khai_physical_lab@xai.edu.ua)

## THE RESEARCH OF PHOTO RESPONSE SPECTRAL INSTABILITY OF THE CdZnTe CRYSTALS

For the research and analysis of thin features of the CdZnTe crystals spectral instability the diagrams  $dI/d\nu = f(I)$ , built on the basis of photocurrent spectral dependences, and wavelet-spectrograms of spectra  $I(h\nu)$ , are offered. It is shown, that these methods mutually complement each other and expose the evolution character of the interconnections between structural inhomogeneities of sensor materials different by scale.

The nonequilibrium conditions of the CdZnTe crystals growing not only are origin of structural defects variety (dislocations, twins, defects of packing, blocks, sliding strips and others) but also result in to self-organization of them in structural inhomogeneities (SI) at different scale level. They form the character of distributing of the interconnected internal elastic and electric fields individual for every crystal. In extreme conditions (strong fields, high energies of ionizing or laser radiation and etc.) of exploitation here is interconsistency alteration of the internal elastic and electric fields, the character of which specifies on transformation the structures of interconnections between SI. Disparity of the dynamics of internal and external factors changes, different pliability of the electric fields SI to external influences result in instability of detectors and spectrometers photoresponse, which stipulates the ambiguity of information, spectral artifacts and is the one of reasons of the monitoring systems failures [1]. Therefore the search of new methods of revealing and analysis of spectral instability of sensor characteristics of the CdZnTe crystals is an actual task, that and was the purpose of this article.

### RESULTS AND DISCUSSION

We studied the steady-state photocurrent  $I$  as a function of the radiation frequency  $\nu$  of Cd<sub>1-x</sub>Zn<sub>x</sub>Te ( $x = 0.05-0.2$ ) crystals with resistivity  $\rho \sim 10^{10} \div 10^{11}$   $\Omega \cdot \text{cm}$ , grown from the melt by vertical solidification under various conditions. The shape of the crystallization front was monitored by examining the shape of the Zn isoconcentration curve. The growth defects were studied by optical, dielectric, and acoustic methods [2]. The In-Ga and Au contacts were deposited onto the opposite faces of the parallelepiped-shaped samples with the sizes  $5 \times 5 \times 2$  mm and  $11 \times 11 \times 2$  mm. The steady-state photocurrent was measured in the field with the strength 100–500 V/cm with automated scanning of the spectrum. The signal was converted to a digital form and computer-processed in Matlab package. All the samples studied that were cut from ingots of a diameter 50 mm, can be conventionally divided into two groups. The first group involves crystals that are most optically uniform and have an insignificant concentration of small voids and inclusions. The

samples of the second-group, which were cut from the ingots grown with a higher curvature of the crystallization front contain various boundaries formed by two-dimensional structural defects, namely, twins, blocks, slip bands, etc.

A typical photocurrent spectra  $I(h\nu)$  for the first group are virtually identical and independent of the direction of scanning the spectrum over the scale of wavelengths (photon energies  $h\nu$ ) and scanning time. However, the photocurrent spectra for the second-group samples cover a wider spectral region. They are not only different from each other but depend on the scanning direction over the wavelength scale (Fig. 1, *a*, curves 2, 3).

It turned out that these spectra also depend on the rate of variation in the frequency (photon energy  $h\nu$ ) or scanning time of the spectrum. This circumstance is associated with the fact that the photocurrent kinetics depend on the photoexcitation frequencies and the spectrum, while kinetics depend on photoactive or electrical history, i.e., on the optical or electric-field exposure time of the samples. It is natural to attribute the features of spectrum and kinetics of photocurrent to the multimode dynamics of processes of the crystal's internal fields alteration. This circumstance is confirmed by the features of the variation in the kinetics as the intensity of photoexcitation increases and by the dependence of the photocurrent spectrum on its scanning time, i.e., on the rate of varying the wavelength. Almost imperceptible kinks in the photocurrent spectrum emerge in this case. These kinks are transformed into the extrema of the differential spectrum  $dI/d\nu = f(\nu)$  (Fig. 1, *b*) via computer processing of the results of measurements by averaging the slope in two neighboring points.

In this case, the response ambiguity increases, i.e., more than two frequencies can correspond to a definite value of  $dI/d\nu$ . It is noteworthy that the number of extrema is as a rule larger in the short-wavelength spectral region than in the long-wavelength region for all the samples studied. To examine and analyze the resistance of the photoresponse of a specific detector to external effects, we suggested the diagrams  $dI/d\nu = f(I)$  (Fig. 2).

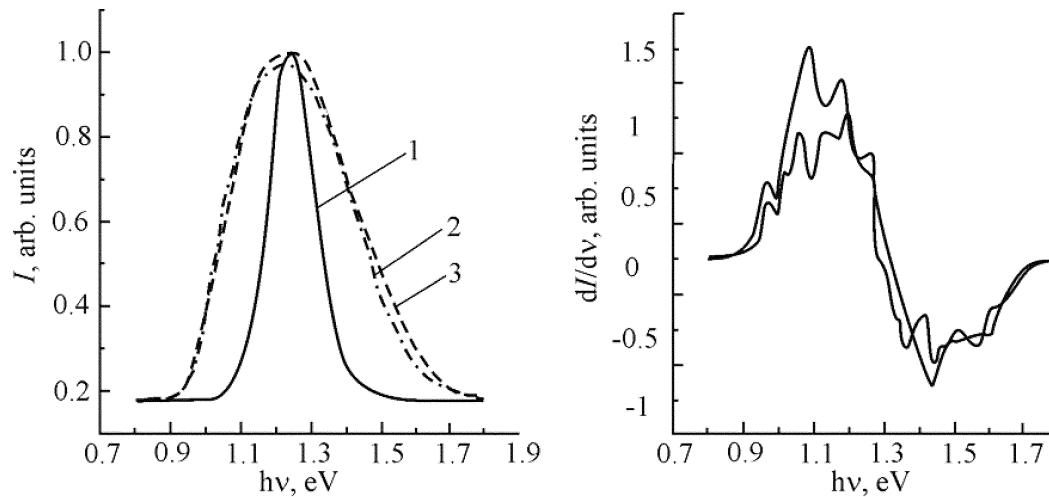


Fig. 1. A photocurrent spectrum of  $Cd_{1-x}Zn_xTe$  crystals and a differential spectra of the two second group samples different by structural perfection. 1 – the first group sample; 2, 3 – the second group sample. A dashed line – spectrum scanning at frequency increasing, dash-dot – spectrum scanning at frequency reduction

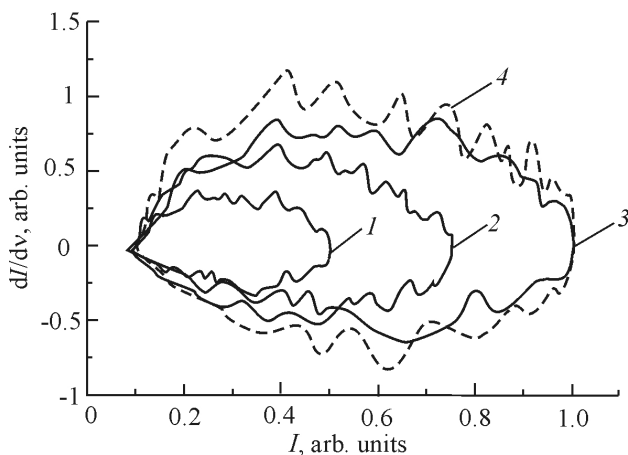


Fig. 2. Diagrams for second group  $Cd_{1-x}Zn_xTe$  samples: 1, 2 – at levels of intensity of photoexcitation  $F_1$  and  $F_2 = 1F_1$ , accordingly; 3, 4 – level of intensity of photoexcitation  $F_3 = 3F_1$  at reduction and increase in radiation frequency, accordingly

They represent the photocurrent spectra in a parametric form [1]. For all investigated samples of the second group such diagrams are individual and allow revealing spectral ranges of the unstable photoresponse by measuring sequentially the spectrum of the same sample under identical conditions in which local degradation of diagrams is observed.

The photocurrent spectrum is influenced also by photoactive history (preliminary photoexcitation, etc.) or variation of scanning time of a spectrum. It is reasonable to analyze the revealed features of the diagrams  $dI/dv = f(I)$  (Fig. 2), namely, the dependence on prehistory and the direction and scanning time of the spectrum, as well as their significant reconstruction with an increase in photoexcitation intensity, within the limits of generalized relaxation models [2].

In particular, the  $dI/dv = f(I)$  diagram can be considered as set of the induced dynamic conditions which displays influence SI on dynamics of electronic, elastic and electric subsystems interaction of a crystal. Obviously, its geometrical configuration is defined by the organization of structure of interrelations between

crystals SI. The specific features connected with change of the spectrum scanning direction is confirm this assumption (Fig. 2, curves 3, 4).

Therefore natural local changes in sequence of such diagrams received at repeated scanning of the photocurrent spectrums, is a source of the information of the interrelations stability between SI. Really, for samples of the second group with photoelectric history, i.e. exposed to preliminary simultaneous influence of radiation and strong electric field on the  $dI/dv = f(I)$  diagrams at repeated scanning the directed change of scale and curvature of separate bow-shaped parts towards their increase or reduction has been revealed.

And for some samples scale reduction of instabilities of the separate ranges of a spectrum occurred to rather high speed up to occurrence of peak in spectrum  $I(hv)$  which, however, not always were reproduced. It has complicated the analysis of alteration of the photocurrent spectrums by means of the  $dI/dv = f(I)$  diagrams and has caused necessity of search of other ways of the  $CdZnTe$  crystals spectral photoresponse features revealing. Results of research of the photoresponse dynamics also testify to difficult character of transition from stability to instability at periodic photoexcitation of detectors by  $\Pi$ -shaped monochromatic pulses [3]. So, it has been established, that only samples of the first group possess the stable photoresponse which on a phase level  $dI/dv = f(I)$  is revealed as attractor. Phase portraits of the photocurrent kinetics of samples of the second group in one spectral ranges are stable, and in others – are not present. Considering a phase portrait of the photoresponse as the subset of the photoinduced states can be offered an indicator of spectral stability  $K_v$  which is defined through operation of the subsets relation  $K_v = \Delta SRS_n$  where  $\Delta S = |S_1| \cap |S_2| \cap \dots \cap |S_n|$  – capacity of subsets product of the photoinduced conditions of a crystal which is graphically displayed by crossing of the diagrams areas  $dI/dv = f(I)$  received at repeated scanning of  $I(hv)$  spectrums, and  $S_n = |S_1| \cup |S_2| \cup \dots \cup |S_n|$  – ca-

capacity of the subsets sum of the crystal photoinduced conditions (Table 1).

Table 1  
The comparative analysis of spectral characteristics stability for two groups of CdZnTe crystals

Characteristics	Crystals groups	
	1-st group	2-nd group
Coefficient of spectral stability $K_s$ , arb. units	0,9 ... 0,99	0,4 ... 0,9
Number spectral unstable ranges	No more than 1	To 8
Presence loop-like sites on the diagrams	No	Are present on $I(\nu)$ spectrums of the certain samples

Obviously,  $K_s$  displays integrally the degree of structure stability of interrelations between structural inhomogeneties at various scale levels. However such approach to revealing and the analysis of spectral stability and other characteristics is work contently and is not always unequivocal.

In [4] it is shown, that an effective method capable of recognizing very slight individual features in the photocurrent spectra  $I(h\nu)$  is offered by wavelet transform analysis, which as a matter of fact is the spectral analysis of local agitation.

The wavelet transform provides a projection of the one-dimensional photoresponse  $I(h\nu)$  onto the scale  $N$  (wavelet coefficient number) versus photon energy plane ( $N-h\nu$  diagram), which is called the wavelet spectrogram. The bottom part of such a spectrogram represents the set of wavelet coefficients with small numbers (corresponding to higher frequencies), which characterize fast variations of the photoresponse as a function of  $\nu$ . The top part of the spectrogram represents the set of wavelet coefficients with large numbers, which provide a rough pattern of the signal and correspond to lower frequencies (i. e., slow photocurrent variations with the wavelength).

For transformation of PhC spectrum we are used Dobeshy, Haar and Morlet wavelets. The biggest values of wavelet coefficient have been received for Haar wavelet that specifies in high conformity photoresponse signal envelope and wavelet in the local spectral ranges. The typical wavelet spectrogram constructed for one of the CdZnTe crystals studied is presented in the inset to Fig. 3. As can be seen, the photocurrent spectrum can be divided into two parts, which correspond to the low- and high-frequency regions. By virtue of the Haar wavelet properties [5], the envelopes of the subsets of wavelet coefficients in fact represent the derivatives of the photocurrent spectrum with respect to the wavelength which is confirmed by their similarity to the  $dI/d\nu = f(\nu)$  diagrams constructed using direct numerical differentiation of the spectra  $I(h\nu)$  [1].

That is the wavelet-spectrogram represents set of the  $dI/d\nu = f(\nu)$  diagrams received at various steps of averaging the slope in two neighboring points, which allows to reveal simultaneously evolution of internal fields at various scale levels.

Really, the wavelet spectrogram in Fig. 3 reveals two peaks in the photon energy interval 1.55–1.7 eV, which are not resolved in the photocurrent spectrum (region 2). It is characteristic, that the corresponding area on the wavelet-spectrogram has the highest brightness and crosses all bending around subsets. It specifies in multiscale of the spectral instability development character and testifies to complementarities of the spectrum analysis ways by means of  $dI/d\nu = f(\nu)$  diagrams and wavelet-spectrograms. On the other hand, set of the  $dI/d\nu = f(\nu)$  diagrams received at repeated scanning of a spectrum allows to trace evolution of the structure interrelations organization and to reveal the latent instability. As a matter of fact, sets of  $dI/d\nu = f(\nu)$  diagrams and the wavelet-spectrograms of the corresponding spectrums are complementary ways of revealing of dynamic features of the crystal photoresponse.

An increase in the velocity of scanning leads to the disappearance of separate peaks and arc-shaped segments in the envelopes of subsets of wavelet coefficients on the spectrograms. This behavior is probably indicative of the transformation of internal fields, which corresponds to a certain frequency interval in the wavelet spectrogram. At the same time, this is also evidenced by features observed in the photoresponse spectrum, which fall within a frequency interval of 8.5–10.5 kHz.

For this reason, it was of interest to study the spectra of photocurrent in the presence of an additional modulation field with a frequency in this and a broader range. As expected, only the modulation field with frequencies 8.5–10.5 kHz induced a change in the shape of the spectrum. The pattern was also dependent on the voltage polarity: positive  $\Pi$ -shaped pulses led to the appearance of two peaks at 1.58 eV and 1.65 eV instead of the region of spectral instability at 1.55–1.7 eV (Fig. 3, region 2), whereas negative modulation pulses favored an increase in the reproducibility of a peak at  $h\nu = 1.19$  eV and a decrease in the photosensitivity in the energy interval 1.18–1.20 eV (Fig. 3, region 1).

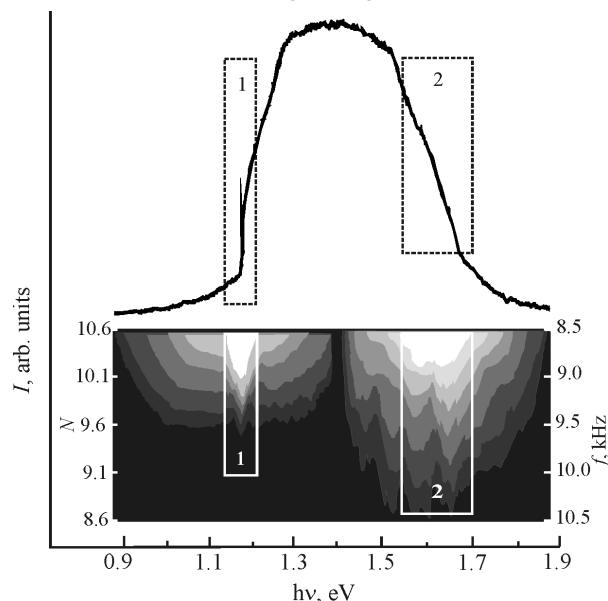


Fig. 3.  $I = f(h\nu)$  dependence of the  $\text{Cd}_{0.9}\text{Zn}_{0.1}\text{Te}$  sample and its wavelet-spectrogram (insert).  $E_b = 300 \text{ V/cm}$

## THE CONCLUSION

Thus, spectral instability of the photoresponse has thin dynamic features which can be revealed and analyzed as by means of photocurrent spectra in a parametrical form, and by means of wavelet-spectrogram of the  $I(h\nu)$  spectrums. These methods mutually supplement each other and can be used for the control of irreversible changes of spectral characteristics of the crystals caused by technological processing or extreme conditions of operation.

UDC 548.522:539.219.1

A. S. Phomin, V. P. Mygal, A. V. But

### THE RESEARCH OF PHOTORESPONSE SPECTRAL INSTABILITY OF THE CdZnTe CRYSTALS

For the research and analysis of thin features of the CdZnTe crystals spectral instability the diagrams  $dI/d\nu = f(I)$ , built on the basis of photocurrent spectral dependences, and wavelet-spectrograms of spectra  $I(h\nu)$ , are offered. It is shown, that these methods mutually complement each other and expose the evolution character of the interconnections between structural inhomogeneities of sensor materials different by scale.

УДК 548.522:539.219.1

А. С. Фомин, В. П. Мигаль, А. В. Бут

### ИССЛЕДОВАНИЕ СПЕКТРАЛЬНОЙ НЕУСТОЙЧИВОСТИ ФОТООТКЛИКА КРИСТАЛЛОВ CdZnTe

Для исследования и анализа тонких особенностей спектральной неустойчивости кристаллов CdZnTe предложены диаграммы  $dI/d\nu = f(I)$ , построенные на основе спектральных зависимостей фототока, и вейвлет-спектрограммы спектров  $I(h\nu)$ . Показано, что эти методы взаимно дополняют друг друга и раскрывают характер эволюции взаимосвязей между разномасштабными структурными неоднородностями сенсорных материалов.

УДК 548.522:539.219.

А. С. Фомін, В. П. Мігаль, А. В. Бут

### ДОСЛІДЖЕННЯ СПЕКТРАЛЬНОЇ НЕСТАБІЛЬНОСТІ ФОТОВІДКЛИКУ КРИСТАЛІВ CdZnTe

Для дослідження і аналізу тонких особливостей спектральної нестабільності кристалів CdZnTe запропоновані діаграми  $dI/d\nu = f(I)$ , побудовані на основі спектральних залежностей фотоструму, та вейвлет-спектрограми спектрів  $I(h\nu)$ . Показано, що ці методи взаємно доповнюють один одного і розкривають характер еволюції взаємозв'язків між різномасштабними структурними неоднорідностями сенсорних матеріалів.

## References

1. *Stability of the Photoresponse of Cd<sub>1-x</sub>Zn<sub>x</sub>Te* / V. K. Komar, V. P. Mygal, S. V. Sulima, A. S. Phomin // *Semiconductors*. – 2006. – Vol. 40, N 2. – P. 129–130.
2. *Migal V. P., Klimenko I. A. Generalized Dielectric Response of CdTe Crystals* // *Fiz. Tekh. Poluprovodn.* 2002. – Vol. 36. N 4. – P. 397–401.
3. *Mygal V. P., Phomin A. S. The Temporal and Spatial Instability of the Photoelectric Response of the CdZnTe crystals* // *Semiconductors*. – 2006. – Vol. 40, N 4. – P. 403–405.
4. *Mygal V. P., Phomin A. S. The Multiscale Spectral and Spatial Character of Photoresponse in CdZnTe crystals* // *Technical Physics Letters*. – 2006. – Vol. 32, N 11. – P. 44–51.
5. *Dremin I. N., Ivanov O. V., Nechitajlo V. A. Wavelets and their use* // *Usp. Fiz. Nauk* – 2001. – Vol. 171, N 5. – P. 465–501.

## EFFECT OF SULPHUR ATOMS ON SURFACE CURRENT IN GAAS P-N JUNCTIONS

Sulphur atoms passivation of GaAs surface and its influence on  $I$ - $V$  characteristics of forward and reverse currents, photocurrent spectrum, and sensitivity of GaAs p-n structures as gas sensors were studied. The passivation reduces the excess forward current and reverse current in p-n junctions, enhances the photosensitivity in the spectral region of strong absorption, substantially increases the sensitivity to ammonia vapors. All these effects are explained, taking into account lowering of the surface states density as a result of sulphur atoms deposition.

### 1. INTRODUCTION

Gas sensors on p-n junctions [1, 2] have some advantages in comparison with these, based on oxide polycrystalline films [3] and Schottky diodes [4, 5]. P-n junctions on wide-band semiconductors have high potential barriers for current carriers, which results in low background currents. Sensors on p-n junctions [1, 2] have crystal structure, high sensitivity at room temperature, selectivity to the gas components, and can be manufactured in microelectronic technology. The ammonia sensitivity of these sensors is due to forming of a surface conducting channel in the electric field induced by the ammonia ions adsorbed on the surface of the natural oxide layer [1, 2]. The surface current induced by adsorption of  $\text{NH}_3$  molecules in p-n structures on GaAs linearly depends on the applied voltage (at low biases) and on the ammonia partial pressure (in some range depending on device parameters).

The threshold  $\text{NH}_3$  partial pressure of a sensor on p-n junction depends on the surface states density in the semiconductor [6]. The results of calculations [6] predict rise of the sensitivity to low concentrations of a donor gas when the surface states density in the p-n junction is diminished. The surface states density in GaAs can be lowered by sulphur atoms deposition from some solutions [7].

The purpose of this work is a study of the influence of sulphur atoms on surface currents in GaAs p-n junctions, as well as on their parameters as ammonia vapors sensors. Effect of sulphur-atoms passivation on  $I$ - $V$  characteristics of forward and reverse currents, photocurrent spectrum, and gas sensitivity of GaAs p-n structures was studied.

### 2. EXPERIMENT

$I$ - $V$  measurements were carried out on GaAs p-n junctions with the structure described in previous works [1, 2]. The effect of saturated ammonia vapors over water solutions of several  $\text{NH}_3$  concentrations was studied on stationary  $I$ - $V$  characteristics, as well as on kinetics of surface current in p-n junctions.

The sulphur atoms deposition (passivation) was carried out by a treatment of different durations in 30% water solutions of  $\text{Na}_2\text{S}$   $\text{H}_2\text{O}$ .

$I$ - $V$  characteristic of the forward current in a typical p-n structure is presented as curve 1 in Fig. 1. Over the current range between  $1\mu\text{A}$  and  $1\text{mA}$  the  $I$ - $V$  curve can be described with the expression

$$I(V) = I_0 \exp(qV/nkT), \quad (1)$$

where  $I_0$  is a constant;  $q$  is the electron charge;  $V$  denotes bias voltage;  $k$  is the Boltzmann constant;  $T$  is temperature;  $n \approx 2$  is the ideality constant. Such  $I$ - $V$  curves can be ascribed to recombination on deep levels in p-n junction and (or) at the surface [8]. And the corresponding current is known as a recombination current.

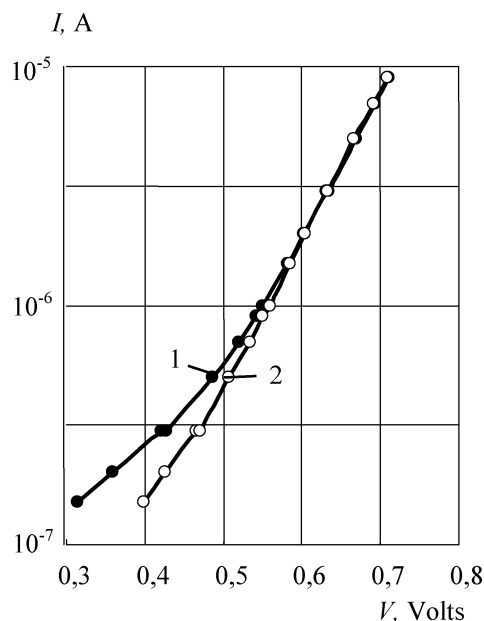


Fig. 1. Forward branches of  $I$ - $V$  characteristics of a p-n structure: 1 – initial; 2 – after passivation during 20s

At lower biases curve 1 has a section of an excess current, which has an ideality constant  $n > 2$  and corresponds to the phonon-assisted tunnel recombination at deep centers [8]. This recombination is located at the p-n junction non-homogeneities, which cause local increase of the electric field [8].

Curve 2 in Fig. 1 was measured after p-n junction passivation during 20s. It is evident that passivation does not affect the recombination current (at  $I > 1\mu\text{A}$ ) and remarkably lowers the excess current. This means that

passivation during 20s reduces the surface states density only in surface non-homogeneities, which are responsible for the excess current.

Fig. 2 depicts the reverse branches of the  $I-V$  characteristic of the same sample, obtained before (curve 1) and after passivation (curve 2). It is seen that sulphur atoms deposition substantially reduces the reverse current in a GaAs p-n junction. This indicates that the reverse current is due to the same surface non-homogeneities in the studied p-n junctions as the excess forward current.

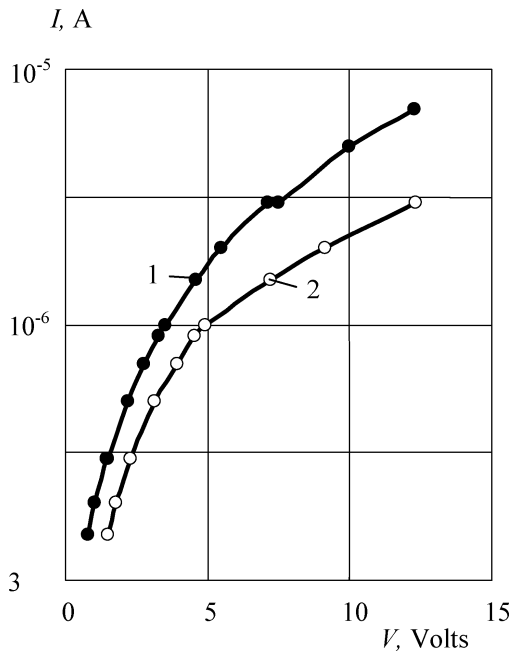


Fig. 2. Reverse branches of  $I-V$  characteristics of a p-n structure: 1 – initial; 2 – after passivation during 20s

Curve 1 in Fig. 3 depicts the photocurrent spectrum in one of the studied samples. The photocurrent strongly falls off at the photons energies  $h\nu > E_g$ , where the electron-hole pairs are generated in a thin layer at the surface. It indicates that the lifetime (and the effective diffusion coefficient) of current carriers at the surface is much lower at the surface, than in the bulk. Curve 2 in Fig. 3, measured after 20s passivation, practically coincides with curve 1, which means that this treatment does not change the surface recombination velocity and consequently, does not lower the deep states density on much of the GaAs surface. It is in an agreement with the fact that the 20s-passivation does not lower the recombination current component.

Curve 3 in Fig. 3, measured after passivation for 60s, has a high-energy shoulder, which argues that this treatment is sufficient for a substantial reducing of the surface recombination states density.

Fig. 4 illustrates the effect of the sulphur passivation on the sensitivity of GaAs p-n junctions as gas sensors. Curves 1 and 2 are measured in air and in ammonia vapors at a  $\text{NH}_3$  partial pressure of 4000 Pa, respectively. The curves practically coincide, which means that the surface current in this p-n junction is not sensitive to ammonia vapors. Curve 3 is obtained on the same sample in ammonia vapors at a  $\text{NH}_3$  partial pressure of 200 Pa (20 times lower, than curve 2) after passivation for 20s. It is seen that placing the passivated p-n junction in ammonia vapors strongly increases the forward excess current. Similarly behaves the reverse current. It indicates that sulphur-at-

oms passivation essentially enhances the sensitivity of GaAs p-n junctions as ammonia sensors.

$S$ , arb. units

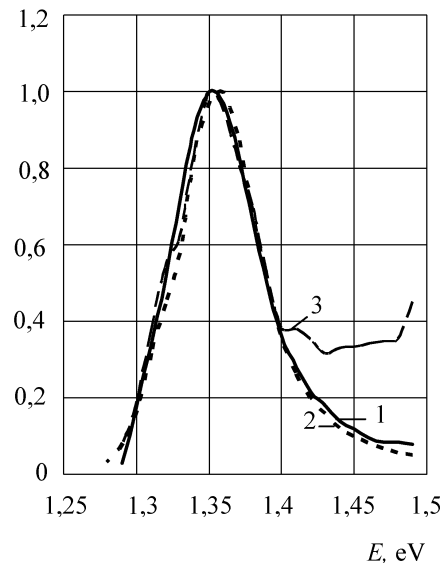


Fig. 3. Photocurrent spectra of a p-n structure: 1 – initial; 2 – after passivation during 40s; 3 – after 60s

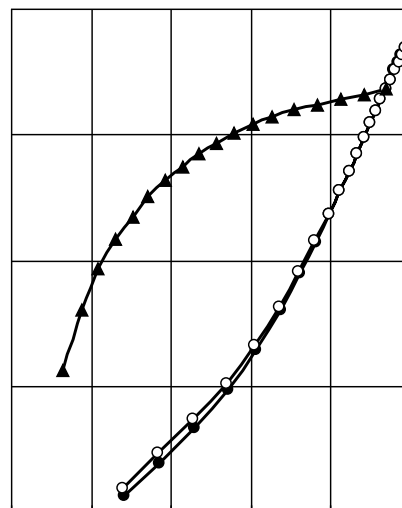


Fig. 4. Forward branches of  $I-V$  characteristics of a p-n structure: 1 – in air; 2 – at ammonia partial pressure 4000 Pa; 3 – after passivation, at ammonia pressure 200 Pa

### 3. DISCUSSION

One of mostly interesting questions, which appear in the light of presented experimental results, is why the low-duration (20s) sulphur passivation substantially reduces the excess current (at  $I < 1\mu\text{A}$ ) and does not affect the recombination current (at  $I > 1\mu\text{A}$ ). For an explanation of this phenomenon one must take into account some features of these two currents. The recombination current passes at much of the surface and is proportional to the surface recombination velocity, which linearly depends on the surface states density. Therefore low decrease in the surface states density only slightly lowers the recombination current. At the other hand, the excess current is located at the non-homogeneities, where the surface depletion layer

is thinner than in the average and the electric field is stronger. Ideality coefficient of  $I-V$  characteristic of the excess current  $n > 2$ , which is due to the dependence of the surface recombination center cross section on the field.

The cross section of surface states for current carriers capture, due to phonon-assisted tunneling [8], can be expressed as

$$C_i = C_{i0} \exp \left[ \frac{(q\hbar E_m)^2}{24m_i(kT)^3} \right], \quad (2)$$

where  $C_{i0}$  is a constant;  $E_m$  is the maximum electric field on the surface;  $m_i$  is the effective mass of the tunneling carrier. In turn,  $E_m$  linearly depends on the local surface states density. Therefore the surface centers capture cross section (and the excess current) is predicted by this model to exponentially grow with the local surface states density. This effect must be observed in electric fields of the order of  $10^5$  V/cm.

Thus, the excess current in GaAs p-n junctions is much more sensitive to the change in the surface states, caused by sulphur atoms deposition, than the recombination current, which agrees with a prediction of model calculations [8].

A substantial decrease in the reverse current in p-n junctions, due to sulphur-atoms passivation as illustrated in Fig. 2, can be explained, taking into account that reverse current is located at the same non-homogeneities as the forward excess current.

The results of photocurrent measurements presented in Fig. 3 can be explained taking into account that the light was directed along the p-n junction, and the photons were directed on the lateral surface. In the case

$$\alpha d < 1, \quad (3)$$

where  $\alpha$  is the absorption coefficient;  $d$  is the p-n structure width, for the photocurrent can be written

$$I_{ph} \sim (1-r)\alpha d L_b \Phi, \quad (4)$$

where  $r$  is the reflectivity;  $L_b$  is the bulk minority-carriers diffusion length;  $\Phi$  is the photon flux. If the inequalities are valid

$$1/d < \alpha < 1/L_b, \quad (5)$$

the photocurrent is proportional to  $L_b$  as

$$I_{ph} \sim (1-r)L_b \Phi, \quad (6)$$

And in the case of

$$\alpha < 1/L_b \quad (7)$$

the photocurrent is proportional to the effective surface diffusion length  $L_s$  as

$$I_{ph} \sim (1-r)L_s \Phi, \quad (8)$$

where

$$L_s = \sqrt{D_s w_s / S}, \quad (9)$$

$D_s$  is the surface diffusion coefficient for minority carriers;  $w_s$  is the effective thickness of the surface layer where the carriers are located;  $S$  is surface recombination velocity.

From the photocurrent spectrum, by using (6) and (8), we obtain

$$I_{ph}^m / I_{ph}^M \approx L_s / L_b, \quad (10)$$

where  $I_{ph}^M$  and  $I_{ph}^m$  are the photocurrent values in the spectral maximum and at  $h\nu > E_g$ , respectively.

An analysis of curves 1 and 2 in Fig. 3 by using (10) yields  $L_s/L_b \approx 0.06$  before passivation and  $L_s/L_b \approx 0.3$  after the treatment.

The effect of passivation on the ammonia-sensitivity of p-n structures can be interpreted by using the model [6], schematically depicted in fig 5.

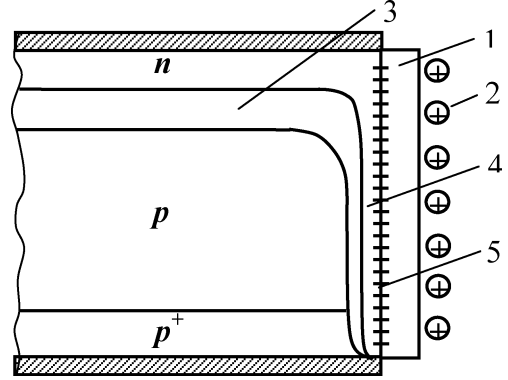


Fig. 5. Schematic of the p-n structure in  $\text{NH}_3$  vapors: 1 – oxide layer; 2 – ions; 3 – depletion layer; 4 – conducting channel; 5 – surface states

Ionized molecules of  $\text{NH}_3$  are placed on the external side of the natural oxide layer. The electric field of ions bends down c- and v- bands in the crystal. If a conducting surface channel is formed, as is depicted in Fig. 5, the n-layer surrounds the p-region at the perimeter and shorts the p-n junction.

The electric field at the semiconductor surface is given by

$$E = e/(\varepsilon\varepsilon_0)(Q_s + \Delta Q_s), \quad (11)$$

where  $\varepsilon_0$  and  $\varepsilon$  is the permittivity of vacuum and of the semiconductor, respectively;  $\Delta Q_s$  is the surface density of the adsorbed ions charge. The density of the charge on surface states was calculated as

$$Q_s = eN_s(p-n)/(p+n+2n_i), \quad (12)$$

where  $N_s$  is the surface density of these states;  $p$ ,  $n$  are the electrons and holes concentrations at the surface;  $n_i$  is the intrinsic carriers concentration. In  $\text{NH}_3$  vapors, the charge on surface states is negative, and the conducting channel is formed only in the case of the inequality

$$N_i > N_s, \quad (13)$$

The absence of the ammonia-sensitivity of the initial samples, as seen comparing curves 1 and 3 in Fig. 4, can be explained, taking into account that the surface states density is very high, and the inequality (13) cannot be satisfied at  $\text{NH}_3$  concentrations used. A high sensitivity, that arises after passivation, as seen comparing curves 1 and 3 in Fig. 4, is the result of the reduction of the surface states density due to the treatment.

#### 4. CONCLUSIONS

Sulphur atoms deposition (sulphur passivation) substantially reduces forward and reverse currents in GaAs p-n junctions, increases the photocurrent in the spectral region of  $h\nu > E$ . The passivation also enhances the sensitivity of GaAs p-n structures as ammonia sensors.

These effects are due to lowering the surface states density as a result of such treatment. Mostly sensitive to the passivation is the excess current, which passes thru non-homogeneities, where the depletion layer is thinned and phonon-assisted tunnel recombination occurs.

#### References

1. Ptashchenko O. O., Artemenko O. S., Ptashchenko F. A. Vliyanie gazovoi sredi na poverhnostnyi tok v p-n heterostrukturakh na osnove GaAs-AlGaAs // Fizika i khimiya tverdogo tela. – 2001. – Vol. 2, N 3. – P. 481–485.
2. Ptashchenko O. O., Artemenko O. S., Dmytruk M. L. et al. Effect of ammonia vapors on the surface morphology and surface current in p-n junctions on GaP. // Photoelectronics. – 2005. – N. 14. – P. 97–100.

3. Bugayova M. E., Koval V. M., Lazarenko B. I. et al. Gazovi senzory na osnovi oksydu tsynku (oglyad) // Sensorna elektronika i mikrosistemni tehnologii. – 2005. – N 3. – P. 34–42.
4. Bomk O. I., Il'chenko L. G., Il'chenko V. V. et al. Pro pryrodu chutlyvosti do amiaku gazovykh sensoriv na osnovi struktur nadtonka tytanova plivka – kremniy // Ukr. fiz. journ. – 1999. – Vol. 44, N 9. – P. 759–763.
5. Baluba V. I., Gritsyk V. Y., Davydova T. A. et al. Sensory amiaka na osnove diodov Pd-n-Si // Fizika i tekhnika poluprovodnikov. – 2005. – Vol. 39, N 2. P. 285–288.
6. Ptashchenko O. O., Ptashchenko F. A. P-n – perekhody na osnove GaAs i drugikh poluprovodnikov A<sup>III</sup>B<sup>V</sup> kak gazovye senzory // Devyataya konferenciya “Arsenid galliya i poluprovodnikovye soyedineniya grupy III-IV”: Materialy konferencii/ – Tomsk: Tomskiy gosuniversitet, 2006. – P. 496–499.
7. Dmytruk N. L., Borkovskaya O. Yu., Mamonova I. B. Sulfidnaya passivatsiya teksturovannoy granitsy rozdela poverkhnostnobaryernogo fotopreobrazovatelya na osnove arsenida galliya // Journal tekhnicheskoy fiziki. – 1999. – Vol. 69, N 6. – P. 132–134.
8. Ptashchenko A. A., Ptashchenko F. A. Tunnel surface recombination in optoelectronic device modelling // Proc. SPIE. – 1997. – Vol. 3182. – P. 145–149.

UDC 621.315.592

O. O. PTASHCHENKO, F. O. PTASHCHENKO, N. V. MASLEYEVA, O. V. BOGDAN, V. V. SHUGAROVA

#### EFFECT OF SULPHUR ATOMS ON SURFACE CURRENT IN GAAS P-N JUNCTIONS

Sulphur atoms passivation of GaAs surface and its influence on  $I$ - $V$  characteristics of forward and reverse currents, photocurrent spectrum, and sensitivity of GaAs p-n structures as gas sensors were studied. The passivation reduces the excess forward current and reverse current in p-n junctions, enhances the photosensitivity in the spectral region of strong absorption, substantially increases the sensitivity to ammonia vapors. All these effects are explained, taking into account lowering of the surface states density as a result of sulphur atoms deposition

УДК 621.315.592

О. О. ПТАЩЕНКО, Ф. О. ПТАЩЕНКО, Н. В. МАСЛЕЕВА, О. В. БОГДАН, В. В. ШУГАРОВА

#### ВПЛИВ АТОМІВ СІРКИ НА ПОВЕРХНЕВИЙ СТРУМ У P-N ПЕРЕХОДАХ НА ОСНОВІ GAAS

Досліджено пасивацію поверхні GaAs атомами сірки та її вплив на ВАХ прямого і зворотного струмів, спектр фотоструму і чутливість p-n переходів на основі GaAs як газових сенсорів. Пасивація зменшує надлишковий прямий струм та зворотний струм у p-n переходах, підвищує fotocутливість у спектральній області сильного поглинання, суттєво збільшує чутливість до парів аміаку. Всі ці явища пояснюються зменшенням щільності поверхневих станів у результаті нанесення на поверхню атомів сірки.

УДК 621.315.592

А. А. ПТАЩЕНКО, Ф. А. ПТАЩЕНКО, Н. В. МАСЛЕЕВА, О. В. БОГДАН, В. В. ШУГАРОВА

#### ВЛИЯНИЕ АТОМОВ СЕРЫ НА ПОВЕРХНОСТНЫЙ ТОК В P-N ПЕРЕХОДАХ НА ОСНОВЕ GAAS

Исследованы пассивация поверхности GaAs атомами серы и ее влияние на ВАХ прямого и обратного токов, спектр фототока и чувствительность p-n переходов на основе GaAs как газовых сенсоров. Пассивация уменьшает избыточный прямой ток и обратный ток в p-n переходах, повышает fotocувствительность в спектральной области сильного поглощения, существенно повышает чувствительность к парам аммиака. Все эти явления объясняются уменьшением плотности поверхностных состояний в результате нанесения на поверхность атомов серы.

## INFLUENCE OF Al<sup>+</sup> AND Ti<sup>+</sup> IMPLANTATION ON RADIATING PROPERTIES OF THE NANO-CLUSTER STRUCTURES

Photoluminescence (PL) spectra have been investigated for the SiO<sub>x</sub> films implanted by Al and Ti (dose interval from 2.5·10<sup>15</sup> to 2·10<sup>16</sup> cm<sup>-2</sup>). It has been shown that after thermal annealing four PL bands with maxima at 550 and 850 nanometers were observed. Implantation of Al leads to increase in PL intensity due to the origin of nc-Si structures stimulation. Implantation of Ti ions leads to reduction of PL intensity in all investigated spectral range. The mechanism of the implanted ions of Al and Ti influence on the luminescent properties of SiO<sub>x</sub> films is being to be based on the results obtained and the data of literature.

### INTRODUCTION

One of the methods of nano-clusterized silicon (nc-Si) synthesis is the thermal decomposition of the SiO<sub>x</sub> phase (x < 2). SiO<sub>x</sub> phase starts to dominate on nc-Si and SiO<sub>2</sub> phases at high-temperature annealing (T > 1000°C). The size of nano-crystals is defined by quantity of excess silicon in initial SiO<sub>x</sub> film. Reduction of concentration of excess Si results not only in desirable shift of a photoluminescence (PL) spectrum to the short wavelengths region, but also in reduction of radiation intensity [1–3]. The methods stimulating nucleation of nc-Si due to introduction of the certain impurities are perspective. One of such methods is the introduction of impurity that interacts actively with oxygen and could stimulate nc-Si formation due to binding both oxygen and impurity atoms during annealing.

Being based on this fact, we have investigated the influence of implantation of chemically active metals Al and Ti into SiO<sub>x</sub> film on radiating properties of such structures. Aluminum and titanium are widely used in micro-electronics as the dopants. At the same time, they do have essentially different properties in relation to chemical interaction with silicon and oxygen, what causes our interest to the present research.

### EXPERIMENTAL

SiO<sub>x</sub> films synthesized by PECVD were fabricated at the temperature of Si substrate of 100°C. Monosilane SiH<sub>4</sub> was used as the starting ingredient. A thickness of (d = 326 nm) and a refraction index (n = 1,67) of the initial SiO<sub>x</sub> films were defined by a method of ellipsometry. SiO<sub>x</sub> films enriched by silicon and reference SiO<sub>2</sub> films were implanted by:

- 1) Al<sup>+</sup> ions with energy of 75 keV and doses of 0.10 to 1.15·10<sup>16</sup> cm<sup>-2</sup>;
- 2) Ti<sup>+</sup> ions with energy of 125 keV and a dose of 8.5·10<sup>15</sup> cm<sup>-2</sup>.

All samples were annealed at temperature of 1150°C in argon atmosphere. Time of annealing was changed from 1 minute (RTA) to 3 hours.

Elemental composition and impurity depth distribution of the samples were measured by SNMS technique using the INA-3 system.

PL spectra were excited by N<sub>2</sub> laser (λ = 337 nm) and PL spectra were registered — with the use of photomultiplier tube.

### RESULTS AND DISCUSSION

Results of the SNMS measurements for samples, implanted by Al and Ti ions are shown at Fig. 1. Implanted Al and Ti ions are distributed mainly in the SiO<sub>x</sub> film, with a maximum of distribution near 150 nm from a film surface, what corresponds to the data of theoretical calculations, made by the TRIM 98 software.

Measurements of PL spectra of annealed SiO<sub>x</sub> films have shown the existence of PL bands with a maximum near 550 nm and 850 nm (Fig. 2).

PL intensity of the samples implanted by Al<sup>+</sup> ions was higher in comparison with non-implanted SiO<sub>x</sub> films. Implantation of Ti<sup>+</sup> ions with the subsequent sample annealing has led to decrease in PL intensity in the whole of the spectral range.

The type of the implanted impurity has not change the spectral position of the PL band maxima in comparison with PL spectrum of non-annealed SiO<sub>x</sub> films.

The shorter wavelength band is the most interesting for practical applications, therefore further research is concentrated basically on it. The increase of annealing duration has led to appreciable growth of intensity of 550 nm of PL band for the samples implanted by Al ions (Fig. 3). The increase of annealing time from 1 to 20 min has led, also, to appreciable broadening of this PL band in the long wavelength area, but without changing the spectral position of PL maximum.

Dependence of the 550 nm PL band intensity on annealing time is shown at Fig. 4. For the samples, implanted by Ti, the intensity of the given PL band shows some increase at the change of annealing duration from 1 to 20 min. The further increase of annealing time does not change the intensity of PL radiation in contrast to SiO<sub>x</sub> films implanted with Al ions. For Al-implanted samples the intensity of 550 nm PL band increases at increase of annealing duration to 90 min., then approaches the saturation. Dependence

of integrated PL intensity in the investigated range of wavelengths on annealing time practically repeats dependence of intensity of 550 nm PL band (Fig. 5). Only the increase of integrated PL intensity for all the samples is more detectable, and it proceeds after 90 min of annealing, what could be connected with the appearance of a shoulder in the long-wavelength area of a spectrum (Fig. 3). Dependence of integrated PL intensity (a 550 nm band) on Al implantation dose is shown in Fig. 6.

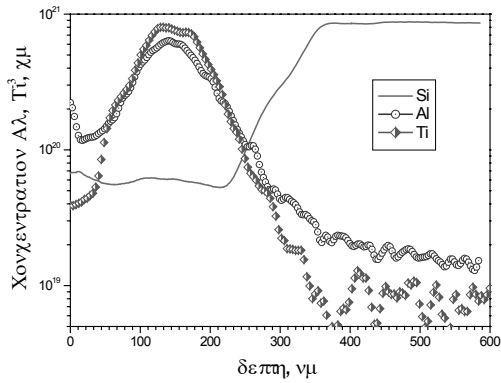


Fig. 1. SNMS – profiles of Al and Ti implanted samples

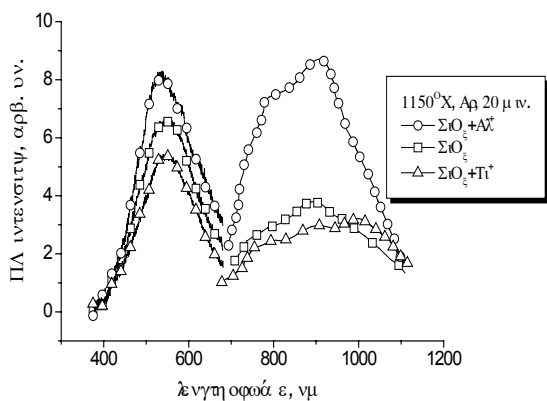


Fig. 2. PL spectra of the samples annealed at temperature of 1150°C (20 min) in Ar atmosphere. Doses of Al and Ti –  $8,5 \times 10^{15} \text{ cm}^{-2}$

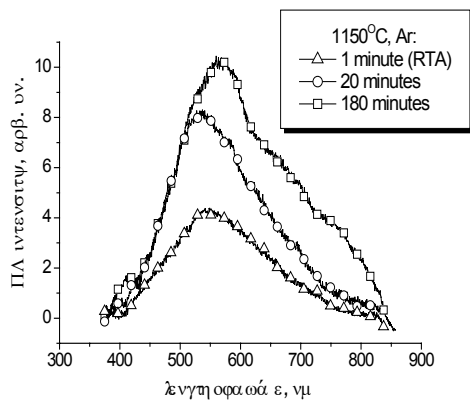


Fig. 3. PL spectra of the sample implanted by Al at different duration of annealing. Dose of Al –  $8,5 \times 10^{15} \text{ cm}^{-2}$

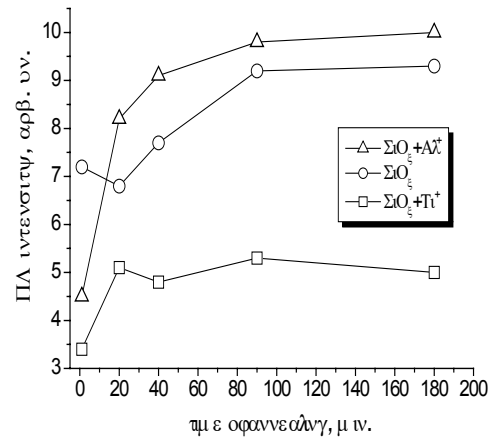


Fig. 4. Dependence of intensity of 550 nm PL band maximum on annealing time. Doses of Al and Ti  $8.5 \times 10^{15} \text{ cm}^{-2}$

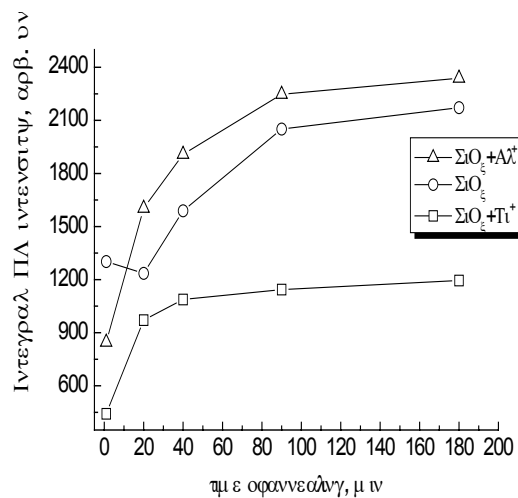


Fig. 5. Dependence of PL intensity, integrated over spectrum, on annealing time. Doses of Al and Ti –  $8,5 \times 10^{15} \text{ cm}^{-2}$

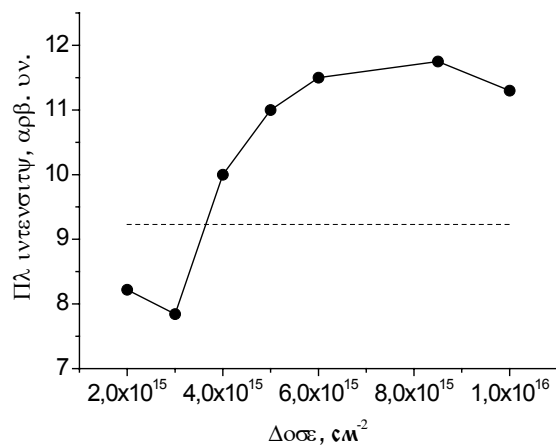


Fig. 6. Dependence of PL intensity (a 550 nm band) on implanted Al dose (annealing at 1150°C, 20 min, in Ar); -----without implantation

The influence of Al on Si nano-cluster formation during the annealing of  $\text{SiO}_x\text{-Si}$  systems could be related to several factors. Firstly, at high-temperature annealing, atoms of aluminum mainly react with oxygen atoms, creating Al-O bonds, and the occurrence

of Al-Si bonds is not observed [4]. The given process should stimulate decomposition of a  $\text{SiO}_x$  phase to  $\text{SiO}_2$  and excess silicon, and creation of  $\text{Al}_2\text{O}_3$  phase, and, at a high temperature, – to diffusion of Si atoms, creation of Si-Si bonds and formation of additional Si nano-clusters, or growth of existing ones.

Really, as the enthalpy of a  $\text{Al}_2\text{O}_3$  phase creation has the value of  $\Delta H \sim 1675$  kJ/mol, what is much greater than the value of enthalpy for a  $\text{SiO}_2$  phase ( $\Delta H \sim 900$  kJ/mol), the presence of Al in a  $\text{SiO}_x$  film leads mainly to formation of  $\text{Al}_2\text{O}_3$  phase, and excess silicon causes the nc-Si formation. This process is complicated enough, as the important role is played by mechanisms of impurity diffusion at the multiphase system formation. The critical parameters are Al concentration and the  $x$  value.

Furthermore, it is necessary to consider, that nc-Si - dielectric film interface contains the same defects as the valence dangling bonds [5], which could be the centers of non-radiative recombination. Implantation of Al could promote the reduction of their concentration. Also, according to some models, which explain a photoluminescence in nc-Si structures, the excitation of charge carriers occurs in nc-Si, and their radiating recombination occurs in the  $\text{SiO}_x$ -Si interface layer, as well as the formation of a  $\text{Al}_2\text{O}_3$  phase as an intermediate layer between wide-bandgap  $\text{SiO}_2$  phase (bandgap is about of 9 eV) and silicon (bandgap  $\sim 1,1$  eV) is optimum for formation of the centers of radiating recombination in the visible area of a spectrum (1.8–3.0 eV) as  $\text{Al}_2\text{O}$  bandgap makes  $\sim 3$  eV. In [6] the possible mechanism of increase intensity of radiating recombination of  $\text{SiO}_x$  films also is offered at injection of Al impurity due to formation of defects or impurity, which serves as the luminescence centers.

According to our opinion, the first of the considered mechanisms works, when the drop of PL intensity is not observed during the increase of annealing temperature and its duration, while the defects annealing prevails.

Apparently from Fig. 3, the PL intensity increases at the increase of annealing time, what is caused by the process of aluminum oxidation and formation of additional nc-Si. Concerning the dynamics of PL intensity increase, it is possible to assume, that the significant part of aluminum is oxidized at the initial stages of annealing (20 minutes). At following stages the basic role is played by the process nc-Si diffusion growth due to diffusion of Si atoms. At increase in annealing duration up to 3 hours, the longer-wave shoulder emerges in PL spectrum (fig. 2). As it is known, the shift of PL spectrum of nc-Si structures to longer-wave area is concerned with increase of crystallites sizes.

As it could be seen from the dose dependences of intensity of the short-wavelength PL peak (Fig. 6), at small doses some reduction of PL intensity in comparison to the not-implanted samples occurs. In our opinion it is connected with ion-beam disorder of nano-inclusions, which exist in the initial (not-implanted) sample; quantity of the implanted aluminum is not enough for effective stimulation of silicon nano-cluster growth. With the increase of Al dose, the effect of this influence prevails, what leads to the increase of PL intensity according to the proposed mechanism.

The PL band with a maximum near to 550 nm was observed in samples of sol-gel  $\text{SiO}_2$ , that contained implanted Ti ions ( $\sim 0.1$  mol %) [7]. However, the authors [7] do not connect the origin of this PL band with nc-Si, specifying their existence, and also that such band is characteristic also for a material, which did not contain Ti impurity. Reduction of PL intensity in our  $\text{SiO}_x$  samples implanted by Ti testifies that mechanisms of Al and Ti interaction with a  $\text{SiO}_x$  matrix are different and dependent on the type of the implanted ions. Really, it is shown in [8] that titanium actively interacts at annealing temperatures with silicon instead of oxygen. Besides, titanium creates the deep recombination-active centers in the Si forbidden zone which increases non-radiative recombination of non-equilibrium charge carriers. Aluminum, as it is known, forms the shallow centers with small recombination probability.

Absence of a luminescence signal in studies of implanted control  $\text{SiO}_2$  films could be explained by the implanted aluminum dose insufficiency. Having admitted that all atoms of the implanted aluminum create Al-O bonds as a result of annealing of  $\text{SiO}_2$  films, while the quantity of excess silicon in a layer ( $\text{SiO}_x - \text{Al}_y\text{O}_z - \text{Si}$ ) will be less than 1% at. As authors of [9] have shown, the substantial increase of speed of Si-Si bond formation occurs at doses of excess silicon of  $> 1\%$  at.

## CONCLUSIONS

Studies of the influence of ion implantation of chemically active metals Al and Ti to  $\text{SiO}_x$  film on radiating properties of  $\text{SiO}_x/\text{Si}$  structures were carried out. Application of such approach shows that implantation of impurity, which interact actively with oxygen (in our case – aluminum), stimulates nc-Si formation and allows to raise the intensity of a photoluminescence essentially without change of a spectral position of radiation peaks.

This work was supported by the Ministry of Education and Science of Ukraine (grant M/175-2007).

## References

1. Wu R. et al. Kinetic Oscillations of red photoluminescence from nanocrystalline Si/SiO<sub>2</sub> films // Appl. Phys. Lett. — Vol. 77, N 5. — 2000.
2. Vandyshchev E. N. et al. // Physics and Technology of Semiconductors (in Russian). — 2005. — Vol. 39, N 11.
3. Jacona F. et al. Correlation between luminescence and structural properties of Si nano-crystals // J. Appl. Phys. — Vol. 87, N 3. — 2000.
4. Mjurarka S. Silicides for SBIS: — M.: MIR Publishers, 1986. — 176 p.
5. Ran G. Z., Wang S. T., Fu J. S. et al. Enhancement of electroluminescence from Au/nano-scale Si-rich SiO<sub>2</sub> film/p-Si by doping Al into the SiO<sub>2</sub> film and  $\gamma$ -ray irradiation // Journal of Luminescence. — Vol. 93. — 2001. — P. 75–80.
6. Kachurin G. A. etc. About formation of silicon nano-crystals during annealing of SiO<sub>2</sub> layers implanted by ions Si // Physics and Technology of Semiconductors. — Vol. 36, N 6. — 2002. — 685–689 p.
7. Morita M., Kajiyama S., Rau D. et al. Luminescence of closed shell molecular complex centers in nanoporous sol-gel SiO<sub>2</sub> glasses // Journal of Luminescence. — Vol. 102–103. — 2003. — P. 608–613.

8. Assasi L. V. C., Machado W. V. M., Justo J. F. Titanium impurities in silicon, diamond, and silicon carbide // Brazilian J. Phys. — Vol. 34, N 2B. — 2004. — P. 602–604.

9. Lejer A. F., Safronov L. N., Kachurin G. A. // Physics and Technology of Semiconductors. — Vol. 33, N 4. — 1999.

UDC 78.67

D. Gamov, O. Oberemok, V. Popov, I. Hatshevykh

#### **“INFLUENCE OF Al<sup>+</sup> AND Ti<sup>+</sup> IMPLANTATION ON RADIATING PROPERTIES OF THE NANOCLUSTER STRUCTURES”**

Photoluminescence (PL) spectra have been investigated for the SiO<sub>x</sub> films implanted by aluminum and titan (dose interval of 2,5·10<sup>15</sup> to 2·10<sup>16</sup> cm<sup>-2</sup>). It has been shown that after thermal annealing there were observed two PL bands with maxima at 550 and 850 nanometers. Implantation of aluminum leads to increase in PL intensity due to stimulation of origin of nc-Si structures. Implantation of ions of the titan leads to reduction of PL intensity in all investigated spectral range. The mechanism of influence of the implanted ions of Al and Ti on the luminescent properties of SiO<sub>x</sub> films is proposed basing on the results obtained and data of the literature.

УДК 78.67

Г. Гамов, Г. Калістій, О. Оберемок, І. Попов, І. Хацевич

#### **ВПЛИВ ІМПЛАНТАЦІЇ Al<sup>+</sup> ТА Ti<sup>+</sup> НА ЛЮМІНЕСЦЕНТНІ ВЛАСТИВОСТІ НАНОКЛАСТЕРНИХ СТРУКТУР**

Досліджено спектри фотолюмінесценції (ФЛ) плівок SiO<sub>x</sub> імплантованих алюмінієм та титаном (в інтервалі доз від 2,5·10<sup>15</sup> до 2·10<sup>16</sup> см<sup>-2</sup>). Показано, що після термічного відпалу спостерігається дві смуги ФЛ з максимумами біля 550 нм та 850 нм. Імплантація алюмінію приводить до збільшення інтенсивності ФЛ за рахунок стимулювання зародження кремнієвих нанокластерів. Імплантація іонів титану приводить до зменшення інтенсивності ФЛ в усьому досліджуваному спектральному діапазоні. На основі отриманих експериментальних результатів та даних з літератури запропоновано механізм впливу імплантації іонів Al та Ti на люмінесцентні властивості плівок SiO<sub>x</sub>.

УДК 78.67

Г. Гамов, Г. Калистий, О. Оберемок, И. Попов, И. Хацевич

#### **ВЛИЯНИЕ ИМПЛАНТАЦИИ Al<sup>+</sup> И Ti<sup>+</sup> НА ЛЮМИНЕСЦЕНТНЫЕ СВОЙСТВА НАНОКЛАСТЕРНЫХ СТРУКТУР**

Исследовано спектры фотолюминесценции (ФЛ) пленок SiO<sub>x</sub> имплантированных алюминием и титаном (в интервале доз от 2,5·10<sup>15</sup> до 2·10<sup>16</sup> см<sup>-2</sup>). Показано, что после термического отжига наблюдаются две полосы ФЛ с максимумами возле 550 нм и 850 нм. Имплантация алюминия повышает интенсивность ФЛ за счет стимулирования зарождения кремниевых нанокластеров. Имплантация ионов титана уменьшает интенсивность ФЛ во всем исследованном спектральном диапазоне. На базе полученных экспериментальных результатов и литературных данных предложен механизм влияния имплантации ионов Al и Ti на люминесцентные свойства пленок SiO<sub>x</sub>.

## WAVELET AND MULTIFRACTAL ANALYSIS OF OSCILLATIONS IN A GRID OF COUPLED AUTOGENERATORS: A CASE OF STRONG NON-LINEARITY

It has been carried out an analysis of oscillations in system of the large (indefinite) number of the coupled semiconductor quantum generators (autogenerators) in a case of the strong non-linearity on the basis of wavelet analysis and multifractal formalism. The corresponding fractals dimensions are lying in the interval [1,6–2,1].

In last years it is of a great importance the experimental and theoretical studying of the non-linear dynamical systems with aim to discover the fractal features and elements of dynamical chaos (c.f. [1–17]). One of the important examples is system, consisted of autogenerators, which interact with retarding. Many physical and biological systems – multielement semiconductors and gas lasers, different radiotechnical devices, etc can be considered in the first approximation as set of autogenerators, coupled by different way. Schemes of two autogenerators (semiconductor) quantum generators (1), coupled by means optical waveguide (2) (fig. 1), have been in details considered in ref. [16, 17] and consideration is fulfilled for a case of weak non-linearity in a system. In ref. [4, 8] it has been numerically studied a regular and chaotic dynamics of the system of the Van-der-Poll autogenerators with account of finiteness of the signals propagation time between them and also with special kind of inter-oscillators interaction forces. In the cited papers it has been considered a cases of little non-linearity in the system. Here we have carried out an analysis of oscillations in system of the large (indefinite) number of the coupled semiconductor quantum generators (autogenerators) in a case of the strong non-linearity on the basis of wavelet analysis and multifractal formalism. The corresponding fractals dimensions are lying in the interval [1,6–2,1]. An important feature of these systems is connected with possibility of realizing the stochastic regime of oscillations and manifesting the chaotic features.

For system of vibrating dipoles, situated in the points with coordinates  $r_i (i=1...N)$ ; and dipole moment vectors directed along axe  $z$ ;  $d_i=(0,0,d)$ ,  $d=e_i x_i$  ( $e_i$  – effective charge of the  $i$ -th dipole) the motion equations are as follows:

$$\ddot{x}_i + \varepsilon_i (\dot{x}_i^2 - \gamma_i) \dot{x}_i + \omega_i^2 x_i = - \sum_{l \neq i} f_{il} \ddot{x}_l (t - \tau_{il}), \quad (1)$$

where  $\omega_i$  are the eigen autovibration frequencies. The force in the right part describes an action on  $l$ -th oscillator from the radiation field of other ones. One can define the corresponding force as follows [8]:

$$f_{il} = (e_i e_l / m c^2) \exp[-\delta |r_i - r_l|] (1 / |r_i - r_l|). \quad (2)$$

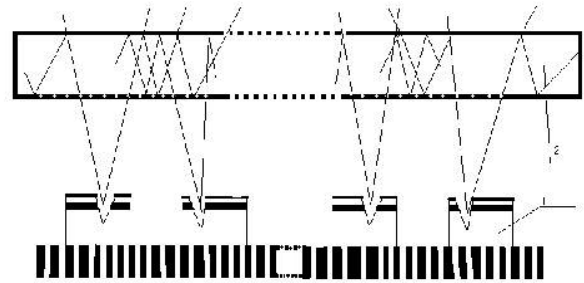


Fig. 1. The grid of autogenerators (semiconductor) quantum generators (SQG), coupled by means of the general resonator: 1-SQG, 2-resonator (dielectric plate)

In a case of the force definition (2) one can get the equation for eigen frequencies of the system as follows:

$$y \left( 1 + \frac{1}{2} f \ln [1 - 2e^{-\gamma} \cos x + e^{-2\gamma}] \right) = y_0. \quad (3)$$

In a case of the infinite square grid of the same vibrating dipoles the eigen frequencies equation is as follows ( $y = \omega \tau$ ,  $y_0 = \omega_0 \tau$ ):

$$y \left( 1 + 2f \sum_{p,q \geq 0} \ln \left| \frac{1}{2} \sin \left( y \sqrt{p^2 + q^2} / 2 \right) \right| \right) = y_0. \quad (4)$$

In refs. [4, 5, 8] the authors carried out the numerical studying the oscillation spectra for system considered and found the corresponding regimes of the oscillations (see fig. 1). Further we used these results for analysis of oscillations in system of the coupled autogenerators in a case of the strong non-linearity on the basis of wavelet analysis and multifractal formalism [10–15] and to find the corresponding fractals dimensions range.

Following refs. [10–17], let us remember the key moments of the used wavelet analysis and multifractal formalism. Wavelets are fundamental building block functions, analogous to the sine and cosine functions. Fourier transform extracts details from the signal frequency, but all information about the location of a particular frequency within the signal is lost.

At the expense of their locality the wavelets have advantages over Fourier transform when non-stationary signals are analyzed. Here, we use non-decimated wavelet transform that has temporal resolution at coarser scales.

The dilation and translation of the mother wavelet  $\psi(t)$  generates the wavelet as follows:  $\psi_{j,k}(t) = 2^{j/2}\psi(2^j t - k)$ . The dilation parameter  $j$  controls how large the wavelet is, and the translation parameter  $k$  controls how the wavelet is shifted along the  $t$ -axis. For a suitably chosen mother wavelet  $\psi(t)$ , the set  $\{\psi_{j,k}\}_{j,k}$  provides an orthogonal basis, and the function  $f$  which is defined on the whole real line can be expanded as

$$f(t) = \sum_{k=-\infty}^{\infty} c_{0k} \varphi_{0,k}(t) + \sum_{j=1}^J \sum_{k=-\infty}^{\infty} d_{jk} \psi_{j,k}(t) \quad (5)$$

where the maximum scale  $J$  is determined by the number of data, the coefficients  $c_{0k}$  represent the lowest frequency smooth components, and the coefficients  $d_{jk}$  deliver information about the behaviour of the function  $f$  concentrating on effects of scale around  $2^{-j}$  near time  $k \times 2^{-j}$ . This wavelet expansion of a function is closely related to the discrete wavelet transform (DWT) of a signal observed at discrete points in time. In practice, the length of the signal, say  $n$ , is finite and, for our study, the data are available monthly, i.e. the function  $f(t)$  in Eq. (1) is now a vector  $f = (f(t_1), \dots, f(t_n))$  with  $t_i = i/n$  and  $i = 1, \dots, n$ . With these notations, the DWT of a vector  $f$  is simply a matrix product  $d = Wf$ , where  $d$  is an  $n \times 1$  vector of discrete wavelet coefficients indexed by 2 integers,  $d_{jk}$ , and  $W$  is an orthogonal  $n \times n$  matrix associated with the wavelet basis. For computational reasons, it is simpler to perform the wavelet transform on time series of dyadic (power of 2) length. One particular problem with DWT is that, unlike the discrete Fourier transform, it is not translation invariant. This can lead to Gibbs-type phenomena and other artefacts in the reconstruction of a function. The non-decimated wavelet transform (NWT) of the data  $(f(t_1), \dots, f(t_n))$  at equally spaced points  $t_i = i/n$  is defined as the set of all DWT's formed from the  $n$  possible shifts of the data by amounts  $i/n$ ;  $i = 1, \dots, n$ . Thus, unlike the DWT, there are  $2^j$  coefficients on the  $j$ th resolution level, there are  $n$  equally spaced wavelet coefficients in the NWT:  $d_{jk} = n^{-1} \sum_{i=1}^n 2^{j/2} \psi[2^j(i/n - k/n)] y_i$ ,  $k = 0, \dots, n-1$ , on each resolution level  $j$ . This results in  $\log_2(n)$  coefficients at each location. As an immediate consequence, the NWT becomes translation invariant. Due to its structure, the NWT implies a finer sampling rate at all levels and thus provides a better exploratory tool for analyzing changes in the scale (frequency) behaviour of the underlying signal in time. An evolutionary wavelet spectrum (EWS) quantifies the contribution to process variance at the scale  $j$  and time  $k$ . From the above paragraphs, it is easy to plot any time series into the wavelet domain. Another way of viewing the result of a NWT is to represent the temporal evolution of the data at a given scale. This type of representation is very useful to compare the temporal variation between different time series at given scale. To obtain the results, smooth signal  $S_0$  and the detail signals  $D_j$  ( $j = 1, \dots, J$ ) are

$$S_0(t) = \sum_{k=-\infty}^{\infty} c_{0k} \varphi_{0,k}(t) \quad \text{and} \quad D_j(t) = \sum_{k=-\infty}^{\infty} d_{jk} \psi_{j,k}(t). \quad (6)$$

The fine scale features (high frequency oscillations) are captured mainly by the fine scale detail components  $D_j$  and  $D_{j-1}$ . The coarse scale components  $S_0$ ,  $D_1$ , and  $D_2$  correspond to lower frequency oscillations of the signal. Note that each band is equivalent to a band-pass filter. Further we use the Daubechies wavelet (db15) as mother wavelet. Using a link between wavelets and fractals, one could make calculating the multi-fractal spectrum. Homogeneous fractals are described by single fractal dimension  $D(0)$ . Non-homogeneous or multifractal objects are described by spectrum  $D(q)$  of fractal dimensions or multifractal spectrum  $A$  problem of its calculation reduces to definition of singular spectrum  $f(\alpha)$  of measure  $\mu$ . It associates Hausdorff dimension and singular indicator  $\alpha$ , that allows calculating a degree of singularity:  $N_\alpha(\epsilon) = \epsilon^{-f(\alpha)}$ . Below we use a formalism, which allows defining spectra of singularity and fractal dimension without using standard Legendre transformations. This idea at first used in ref.[8]. Wavelet transformation of real function  $F$  can be also defined as:

$$W_\psi[F](b, a) = (1/a) \int_{-\infty}^{+\infty} F(x) \Psi\left(\frac{x-b}{a}\right) dx, \quad (7)$$

where parameter  $b$  denotes shift in space; parameter  $a$  defines a space scale. The analyzing splash  $\Psi$  has to be localized as in space as on frequency characteristics. The most correct way of estimate of the function  $D(h)$ ,  $f(\alpha)$  is in analysis of changing a dependence of distribution function  $Z(q, a)$  on modules of maximums of the splash-transfers under scale changes:

$$Z = \sum_{i=1}^{N(a)} (\omega_i(a))^q, \quad (8)$$

where  $I=1, \dots, N(a)$ ;  $N(a)$  is a number of localized maximums of transformation  $W_\psi[F](b, a) =$  (for each scale  $a$ , where function  $x$  is considering; function  $\omega(a)$  can be defined in terms of coefficients of the splash-transformations as:

$$\omega_i(a) = \max_{\substack{(x, a') \in L \\ a' < a}} |W_\psi[F](x, a')|, \quad (9)$$

where  $l_i \in L(a)$ ;  $L(a)$  is a set of such lines, which make coupling the splash-transformation coefficient maximums (they reach or make cross-sectioning a level, which is corresponding to scale  $a$ ) In limit  $a \rightarrow 0^+$  the distribution function  $Z(q, a)$  manifestes behaviour, corresponding to degree law:  $Z(q, a) \sim a^{\tau(q)}$ . To calculate the singularity spectrum, a canonical approach can be used and based on such functions:

$$h(a, q) = \frac{1}{Z(a, q)} \frac{\partial Z(a, q)}{\partial q}, \quad (10)$$

where

$$\frac{\partial Z}{\partial q} = \sum_{i=1}^{N(a)} \omega_i(a)^q \ln \omega_i(a), \quad (11)$$

$$D(a, q) = qh(a, q) - \ln Z(a, q). \quad (12)$$

Spectra  $D(q)$  and  $h(q)$  are defined by standard way:

$$D(q) = \lim_{a \rightarrow 0} \frac{D(a, q)}{\ln a}, \quad h(q) = \lim_{a \rightarrow 0} \frac{h(a, q)}{\ln a}.$$

We have applied the wavelet and multifractal formalism to analysis of system of the many ( $n=12$ ) coupled oscillators and autogenerators using the PC numerical complex "Geomath" (c.f. [12]). The numerical estimates show that fractals dimensions for oscillations in system of coupled autogenerators in a case of strong non-linearity are lying in the range [1,6–2,1].

#### References

1. *Likhtenberg A., Liberman M.* Regular and stochastic dynamics, Mir, Moscow, 1994.
2. *Schertzer D., Lovejoy S.* Fractals: Physical Origin and Properties. Ed. L. Peitronero, Plenum Press, N-Y., 1990. — P. 71–92.
3. *Zaslavsky G. M.* Stochasticity of dynamical systems, Nauka, Moscow, 1998.
4. *Vedenov A. A., Ezhov A. A., Levchenko E. B.* Non-linear systems with memory and functions of neuron ensembles, In: Non-linear waves. Structure and bi-furcations Eds Gaponov-Grekhov A. V., Rabinovich M. I. Nauka, Moscow, 1987. — P. 53–69.
5. *Ezhov A. A., Knizhnikova L. A., Levchenko E. B.* Chaotic oscillations in system of autogenerators // *Izv. Vuzov. Ser. Phys.* — 1001. — Vol. 36. — P. 1167–1169.
6. *Glushkov A. V.* Thomas-Fermi model of multibody oscillator // *Soviet Physics. Izv. Vuzov. Ser. Phys.* — 1992. — Vol. 37. — P. 41–47.

7. *Minabudinova S. A., Yugay K. I.* Dynamical chaos in high-excited states of ungarmonic oscillator in external electric field // *Izv. Vuzov. Ser. Phys.* 43. — P. 11–18 (1998).
8. *Svinarenko A. A.* Regular and chaotic dynamics of multi-oscillator dynamical systems // *Photoelectronics.* — 2002. — Vol. 11. — P. 81–84.
9. *Stochastic* instability of multioscillator systems and highly excited atoms in electromagnetic field and chaotic dynamics of diatomic molecules in resonance high-intensity IR field / A. V. Glushkov, S. V. Ambrosov, V. M. Ignatenko, G. P. Prepelitsa // *Proc. V Int. Conf. On Atomic and Molecular Physics.* — Berlin (Germany). — 2001. — P. A313.
10. *Daubechies I.* Ten Lectures on Wavelets. Philadelphia: SIAM. — 1992.
11. *Wave* propagation and sampling theory J. Morlet, G. Arens, E. Fourgeau, D. Giard // *Geophysics.* — 1982. — Vol. 47. — P. 203–236.
12. *Nason G., von Sachs R., Kroisand G.* Wavelet processes and adaptive estimation of the evolutionary wavelet spectrum // *J. Royal Stat. Soc.* — 2000. — Vol. B-62. — P. 271–292.
13. Wavelet analysis and sensing the total ozone content in the earth atmosphere: Mycros technology "Geomath" / A. V. Glushkov, V. N. Khokhlov, A. A. Svinarenko, Yu. Ya. Bunyakova, G. P. Prepelitsa // *Sensor Electr. and Microsys. Techn.* — 2005. — Vol. 2(3). — P. 51–60.
14. *Glushkov A. V., Khokhlov V. N., Tsenenko I. A.* Atmospheric teleconnection patterns: wavelet analysis // *Nonlin. Proc. in Geophys.* — 2004. — Vol. 11, N 3. — P. 285–293.
15. *Loboda N. S.* Stochastic statistical modelling of the irrigation and man-made effects on hydrological systems and water resources // *Environm. Inf. Arch.* — 2003. — Vol. 1. — P. 267–273.
16. *Serbov N. G., Svinarenko A. A.* Wavelet and multifractal analysis of oscillations in system of couled autogenerators in chaotic regime // *Photoelectronics.* — 2006. — N 15. — P. 27–30.
17. *Serbov N. G., Svinarenko A. A.* Wavelet and multifractal analysis of oscillations in a grid of couled autogenerators // *Photoelectronics.* — 2007. — N 16. — P. 53–56.

UDC 539.124:541.47

A. A. Svinarenko, N. G. Serbov, Yu. G. Chernyakova

#### WAVELET AND MULTIFRACTAL ANALYSIS OF OSCILLATIONS IN A GRID OF COULED AUTOGENERATORS: A CASE OF STRONG NON-LINEARITY

It has been carried out an analysis of oscillations in system of the large (indefinite) number of the coupled semiconductor quantum generators (autogenerators) in a case of the strong non-linearity on the basis of wavelet analysis and multifractal formalism. The corresponding fractals dimensions are lying in the interval [1,6–2,1].

УДК 539.124 : 541.47

А. А. Сви́наренко, Н. Г. Сербов, Ю. Г. Чернякова

#### ВЕЙВЛЕТ И МУЛЬТИФРАКТАЛЬНЫЙ АНАЛИЗ КОЛЕБАНИЙ В РЕШЕТКЕ СВЯЗАННЫХ АВТОГЕНЕРАТОРОВ: СЛУЧАЙ СИЛЬНОЙ НЕЛИНЕЙНОСТИ

Выполнен анализ колебаний в системе достаточно большого числа связанных полупроводниковых квантовых генераторов (автогенераторов) в случае сильной нелинейности на основе вейвлет и мультифрактального формализма. Соответствующий спектр фрактальных размерностей лежит в интервале [1,6–2,1].

УДК 539.124 : 541.47

А. А. Сви́наренко, М. Г. Сербов, Ю. Г. Чернякова

#### ВЕЙВЛЕТ І МУЛЬТИФРАКТАЛЬНИЙ АНАЛІЗ ОСЦИЛЯЦІЙ У СИСТЕМІ ЗВ'ЯЗАНИХ АВТОГЕНЕРАТОРІВ: ВИПАДОК СИЛЬНОЇ НЕЛІНІЙНОСТІ

Виконано аналіз осциляцій в системі досить значного числа зв'язаних напівпровідникових квантових генераторів (автогенераторів) у випадку сильної нелінійності на підставі вейвлет та мультифрактального формалізму. Відповідний спектр фрактальних розмірностей лежить у інтервалі [1,6–2,1].

## INVESTIGATION OF THE SOLAR CELLS WITH POROUS SILICON FILMS

The experimental results of the solar cells parameters covered with films  $\text{In}_x\text{Sn}_y\text{O}_z$ , and solar cells covered with films, obtained by dispersion of alcoholic solutions of three-chloride indium acetyl acetonate of aluminium are presented. The spectral dependencies of reflection factor and open circuit voltage of the film-covered solar cells are discussed. The conditions of preparation and properties of porous silicon as well as parameters of the solar cells with films of porous silicon and covers, forming a potential barrier, are investigated. It is shown that for optimum parameters of films preparation, the solar cells with efficiency 15.8% become real.

### INTRODUCTION

The silicon is one of the basic semiconductors of modern solar power technology. One of perspective directions of studies connected with a raise of effectiveness of solar radiation transformation into electric energy, is the development of the photo-electric converters based on the semiconductor-dielectric-semiconductor structures [1-2]. Such solar cells demonstrate high effectiveness of photo-electric transformation, the construction simplicity and process engineering with small power consumption. However, here is a set of the physical and engineering problems, which successful solution, in many respects, influences the scale of use of the solar cells in semiconductor technology.

With the purpose of the technological requirements meeting, the raise of efficiency and maximum diminution of the reflection losses in the field of spectral sensitivity of the solar element, the use of covers of  $\text{SnO}_2$ ,  $\text{In}_2\text{O}_3$ ,  $\text{In}_x\text{Sn}_y\text{O}_z$ ,  $\text{ZnO}$  etc. [3, 4] has been proposed. The width of these materials' forbidden zone is about 3.0–3.65 eV. Therefore, these materials are transparent for a greater part of a solar radiation energy range. Their refraction factor is in the limits of 1.6–2.1 and they could be used together with many semiconductors. Besides, optimally selected  $\lambda/4$  – anti reflecting cover can reduce reflection factor, for given wavelengths, almost up to zero. For deriving a zero reflection in a certain interval of wavelengths, one could use the multilayer anti-reflecting cover.

Except the listed above materials, the film of porous silicon, having refraction index of the order of  $1.95 \pm 0.05$ , could be used as anti-reflecting cover as well. The porous silicon cover reduces optical losses in silicon from 37% up to 8%, that actually coincides with the effectiveness of cover of  $\text{SiO}_2$ , obtained by the evaporation in vacuum. Due to a high porosity of cover, it is necessary to expect the magnification of a short-circuit current, open circuit voltage and the efficiency of the photo-electric converters.

The purpose of the present work is the research of a structural and electro-physical properties of film covers for different conditions of their manufacture as well as the influence of these properties on basic parameters of the photo-electric converters.

### EXPERIMENTAL

The research was fulfilled on the silicon wafers, which have been brought up in a Czochralski method, having p-type conductivity and boron doped resulting with a resistivity of  $0,5 \text{ Ohm} \cdot \text{cm}$  and of n+-type conductivity, antimony doped with a resistivity of  $0,01 \text{ Ohm} \cdot \text{cm}$ . The porous silicon films were created by anodic oxidation of the wafer front face in HF-electrolyte. The density of an anode current has been varied in the range from 1.0 to  $30 \text{ mA/cm}^2$ . The time of anodic oxidation has not exceeded 10 minutes. Intensity of illumination for anodic oxidation of n-type conductivity specimens was chosen to be  $20 \text{ mW/cm}^2$  [5–7]. For the security of uniformity of the anodization, the reverse side of silicon specimens were covered with the evaporated films of aluminum (98% Al + 2% Si), which were annealed at the temperature of  $575^\circ\text{C}$  afterwards. The micro-contour of a porous silicon film surface was investigated with the use of optical and electronic microscopy. The thickness of porous silicon films was determined by the oblique grind method. The density of porous silicon was calculated with the use of the formula:

$$\rho_{\text{porous}} = \rho_{\text{Si}} - \Delta P / S \cdot h_{\text{porous}}, \quad (1)$$

where  $\rho_{\text{Si}} = 2,33 \text{ gramm/cm}^3$  – density of monocrystalline silicon;  $\Delta P$  – alteration of a sample weight after anodic handling (gramm);  $S$  – surface area of a silicon wafer, subjected to anodic oxidation ( $\text{cm}^2$ );  $h_{\text{porous}}$  – thickness of a porous silicon film (cm).

The  $\text{In}_x\text{Sn}_y\text{O}_z$  films were formed on the front face of silicon specimens by pulverization of  $\text{InCl}_3$ :  $\text{SnCl}_4(5\text{H}_2\text{O})$ :  $\text{H}_2\text{O}$ :  $\text{CH}_3\text{CH}_2\text{OH}$  alcoholic solution taken in a weight relation 34:1:150:150. The temperature of specimens was  $430^\circ\text{C}$ . The thickness of covering films depends on the time of covering procedure and was in the range of 500–1500 Å.

The solar cells were produced through sequential covering of a porous silicon film and film  $\text{In}_x\text{Sn}_y\text{O}_z$  on a surface of silicon specimens. The contacts were created by vacuum evaporation of In-Cu-Cr film. The radiation power at the surface was  $100 \text{ mW/cm}^2$ , and the active area of the solar element was about  $8,82 \text{ cm}^2$ .

The surface resistance of  $\text{In}_x\text{Sn}_y\text{O}_z$  films, their photo-response spectral dependencies and the influ-

ence of film parameters on current-voltage plot view of the solar cells were investigated.

## RESULTS AND DISCUSSION

### Properties of porous silicon films

The dependencies of a thickness of porous silicon films on the time of anodic oxidation in 15 % HF solution for slices n<sup>+</sup>-type are presented on Fig.1. This figure shows that the thickness of a porous silicon film increases linearly with the magnification of the anodic oxidation process' duration.

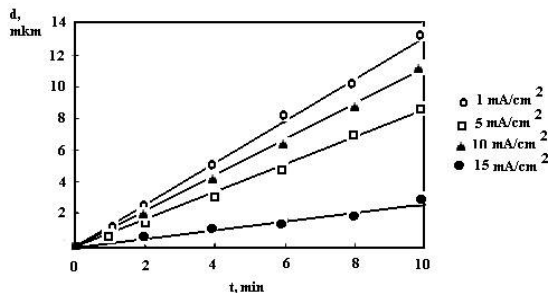


Fig. 1. Dependence of a porous silicon film thickness on time of anodic processing in 15% a fluoridic acid solution and on density of an anodic current (mA/cm<sup>2</sup>). Specific resistance samples of a n<sup>+</sup>-type – 0,01 Ohm • cm

The plot slope increases with density growth of the anode current. Also, the growth rate of porous silicon films increases linearly in indicated interval and makes the following figures for: plot 1 – 4.3 nm/s, plot 2 – 4.2 nm/s, plot 3 – 19.0 nm/s, plot 4 – 21.6 nm/s.

Fig. 2 shows the dependencies of the porous silicon films thickness obtained on samples of p-type silicon with a resistivity 0,5 Ohm • cm on the time of anodic oxidation in the concentrated HF (49 %). For these conditions of handling, the growth rate of a porous silicon film makes for: plot 1 – 2.2 nm/s, plot 2 – 10.8 nm/s, plot 3 – 15.0 nm/s, plot 4 – 18.3 nm/s, plot 5 – 21.4 nm/s.

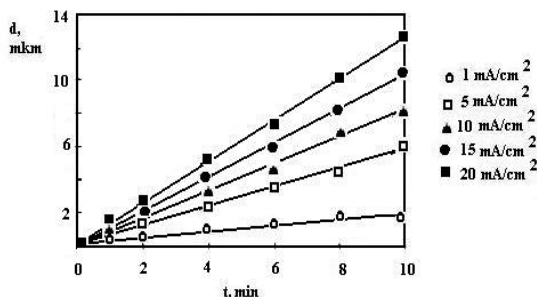


Fig. 2. Dependence of a porous silicon film thickness on time of anodic processing in 49 % fluoridic acid solution and on the density of an anodic current (in mA/cm<sup>2</sup>). Specific resistance of a p-type samples – 0.5 Ohm • cm.

The linearity of a porous silicon film thickness dependence on the anodization time testifies the constant growth rate of a film with constant density of anode current.

The observed magnification of the growth rate could be connected with the increase of anodic current density with the magnification of the dissolved silicon amount in accordance with the magnification of the soluted ions amount which participates in a current process.

The process of formation of porous silicon is determined mainly by two factors: by delivery of F ions in reaction zone with formation of silicon bi-fluor and presence of a positive sign charge carriers, at the surface layer of the silicon anode.

Therefore, a process of anode handling of n- and p- type silicon differs due to difference in concentration of mobile positive charge carriers.

As in the case of acceptor-type semiconductor, the holes in doped silicon are the basic charge carriers and their concentration in a considered case is supposed to be sufficient for the reaction running:



so, the basic influence on the anodization renders to the mechanism of F ions delivery.

In donor-type doped silicon, the holes concentration is small; therefore, the exterior stimulating factor is necessary for anodization running.

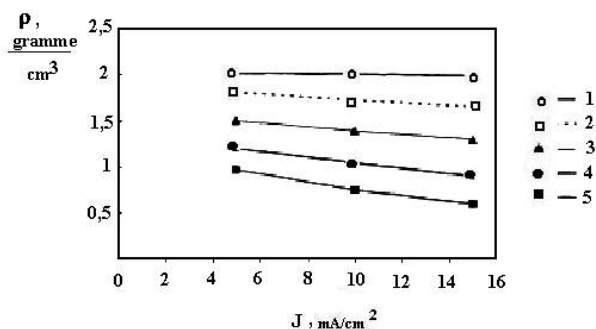


Fig. 3. Dependence of porous n<sup>+</sup>-type silicon volumetric density on the anodic current density for different films thicknesses (micron): 1 – 1.0; 2 – 2.0; 3 – 4.0; 4 – 6.0; 5 – 8.0

Fig.3. shows the experimental dependencies of a volumetric density of porous silicon obtained by n<sup>+</sup>-specimens handling in 15% HF solution on the density of anodic current.

The figure shows that the increasing of a porous silicon film thickness causes the change of the material density, which characterizes the structure of the material: Thus, there is the possibility to operate the structure of porous silicon with the changing conditions of anode handling.

The study of porous silicon structure shows, that the magnification of a current density causes the increase of the amorphous phase part in material. The REM imaging analysis of a surface with various volumetric densities has shown that there are reflexes, which correspond to crystallographic planes for samples presented with curves 1, 2 and 3 at Fig. 3.

However, on the REM data there are no Kikuchi lines that generally appear for mono-crystalline silicon. The dependence of a p-type porous silicon volumetric density on thickness of layer and the densities of anodic current is presented at Fig. 4.

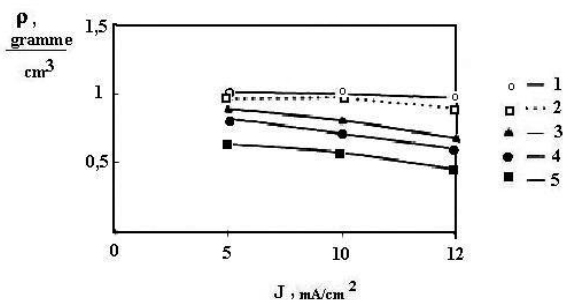


Fig. 4. The dependence of p-type silicon volumetric densities on the layer thickness and densities of anodic current.

The figure shows, that in a studied range of current densities and thicknesses, the volumetric density vanishes slightly, what testifies the homogeneity of the process of silicon dissolution. The pores diameter for investigated samples was 40–210 Å and pores number  $4 \cdot 10^8 - 8 \cdot 10^9 \text{ cm}^{-2}$ . The size of pores increases with the magnification of a current density, time of anode handling and thickness of a porous silicon film. The number of pores is maximal for pores with 40–80 Å in diameter. The further magnification of a pores' diameter happens in not only the size due to dissolution of silicon at the pores walls, but also at the expense of secondary effect of small and closely located pores joining.

#### Properties of $\text{In}_x\text{Sn}_y\text{O}_z$ films

Fig. 5 shows the dependence of the  $\text{In}_x\text{Sn}_y\text{O}_z$  surface resistance turn on the percentage  $\text{SnCl}_4(5x\text{H}_2\text{O})$  in a solution. The least magnitude of a surface resistance have the samples with an  $\text{In}_2\text{O}_3$  film. Increasing of a  $\text{SnCl}_4(5x\text{H}_2\text{O})$  content causes the rise of surface resistance from 20 up to 600 Ohm/□. It could be explained, apparently, by substitution of In atoms by small amounts of tin, that represents itself as the donor. However, with  $\text{SnCl}_4(5x\text{H}_2\text{O})$  content increasing the content of  $\text{SnO}_2$  phase in  $\text{In}_x\text{Sn}_y\text{O}_z$  film structure grows, that reduces the charge carriers concentration and the material conductivity.

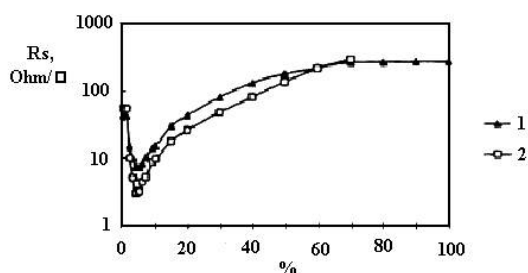


Fig. 5. Dependence of  $\text{In}_x\text{Sn}_y\text{O}_z$  films surface resistance on  $\text{SnCl}_4(5x\text{H}_2\text{O})$  content in solution (1) and  $\text{In}_x\text{Al}_y\text{O}_z$  films surface resistance on  $\text{Al}(\text{AA})_3$  contents in gas phase (2)

To reduce magnitude of oxide metal cover surface resistance, one could use the  $\beta$ -diketonates, for example acetyl acetonate of aluminium  $\text{Al}(\text{AA})_3$ .  $\text{Al}(\text{AA})_3$  was obtained from a solution of  $\text{AlCl}_3 \cdot 6\text{H}_2\text{O}$ , rectified by zone method and had the following crystalline and chemical characteristics: coordination of a metal ion – octahedron; space group –  $\text{P}2_1/c$ ; syngony – monoclinic; lattice parameters –  $a = 14.16 \text{ \AA}$ ,  $b = 7.48 \text{ \AA}$ ,

$c = 16.43 \text{ \AA}$ ,  $\beta = 98^\circ$ . The  $\text{In}_x\text{Al}_y\text{O}_z$  films were obtained by thermal decomposition on the heated surface (up to  $470^\circ\text{C}$ ) of silicon substrate in inert gas stream with oxidizer adding. The surface resistance of a film decreases and makes 7–10 Ohm/□. (Fig. 5, curve 2)

The spectral dependencies of  $\text{In}_x\text{Sn}_y\text{O}_z$  films reflection factor of a various thickness were investigated as well.

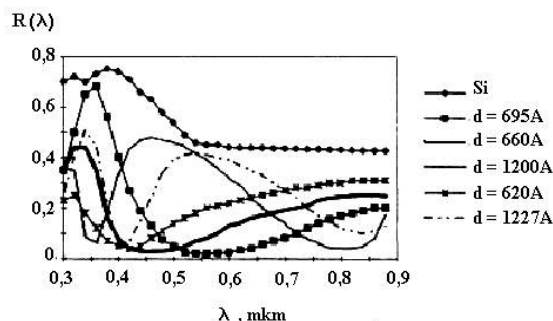


Fig. 6. Spectral dependences of a  $\text{In}_x\text{Sn}_y\text{O}_z$  films reflection factor with various thickness

The results are presented on Fig.6. The least reflection of radiation have the  $\text{In}_x\text{Sn}_y\text{O}_z$  films with thickness of 650–750 Å. The enlightenment is most hardly appears in a spectral range of 0.5–0.8 microns. The  $\text{In}_x\text{Sn}_y\text{O}_z$  film makes the surface of silicon more transparent than the film of  $\text{SiO}_2$ . In the field of a maximum transparency for specimens with  $\text{In}_x\text{Sn}_y\text{O}_z$  films the reflection factor is reduced up to practically zero.

At the surface of silicon substrate, for the normal conditions of the environment the film of native  $\text{SiO}_x$  grows. Strictly speaking, in this case, the structure  $\text{In}_x\text{Sn}_y\text{O}_z/\text{SiO}_x/\text{Si}$  is created on the surface of silicon.

Pre-oxidizing handling included growth of oxide by a thickness 5000 Å ( $T = 900^\circ\text{C}$  in a damp atmosphere). Then, this oxide was etched and the silicon wafers were washed in a boiling solution ( $\text{H}_2\text{O}_2:\text{NH}_4\text{OH}:\text{H}_2\text{O}=1:1:4$ ) and doubly de-ionized water wash was applied with consequent drying. After day-long stay in air, the thickness of natural oxide was about 14 Å, and after stay within 4 days – 43 Å. The structures  $\text{In}_x\text{Sn}_y\text{O}_z/\text{SiO}_x$  after day-long stay in air had a surface resistance of 65 Ohm/□, and after endurance during 4 days – 140 Ohm/□. Annealing of structures in air at the temperature of  $200^\circ\text{C}$  within 10 minutes increased the surface resistance from 65 Ohm/□ till 75–80 Ohm/□ and from 140 Ohm/□ up to 170 Ohm/□.

The annealing time about 20 minutes promoted further growth of a surface resistance. Cyclic annealing of  $\text{In}_x\text{Sn}_y\text{O}_z/\text{Si}$  structure in hydrogen and argon at the temperature of  $550^\circ\text{C}$  promoted a drop of  $\text{In}_x\text{Sn}_y\text{O}_z$  film surface resistance from 20 Ohm/□ up to 7–8 Ohm/□, and film  $\text{In}_x\text{Al}_y\text{O}_z$  - from 10 Ohm/□ up to 3–4 Ohm/□. During the annealing, the restoring of oxide and release of metal atoms occurs, presumably, therefore the surface resistance decreases.

#### Performances of the photo-electric converters

The condition for high effectiveness of the photo-electric converters must be matched with semiconductor-dielectric-semiconductor structures parameters: the width of a forbidden zone ( $E_g$ ) of cover, that

forms a potential barrier, should be  $\geq 3.0$  eV and the semiconductor should be degenerate. In case of a base semiconductor of p-type, work function (A) of semiconductor cover, forming a barrier, and value of electron affinity of a base semiconductor ( $\chi_s$ ) should satisfy the relation  $A < (\chi_s)$ . In case of a base semiconductor of n-type the validity of a relation  $A > \chi_s + E_g$  is necessary. The mismatch of lattice constants should be minimal.

The important parameters of semiconductor covers are thickness and temperature of covering layer.

In a Table 1 some data on a relation between A,  $\chi_s$  and  $E_g$  for some semiconductor covers forming on silicon a potential barrier are presented.

Table 1  
Parameters of semiconductors forming potential barrier with silicon

Semiconductor	$E_g$ (eV)	A(eV)	$\chi_s$ (eV)	$A - \chi_s$ (eV)	$\chi_s + E_g - A$ (eV)
Si	1.12	-	4.05	-	-
$In_2O_3$	3.00	4.30-4.45	-	0.25-0.40	0.85-0.70
$SnO_2$	3.50	4.60-4.90	-	0.55-0.85	0.55-0.25
$In_xSn_yO_z$	3.65	4.10-4.60	-	0.05-0.55	1.05-0.55
ZnO	3.20	4.20-4.57	-	0.15-0.52	0.95-0.58
CdO	2.70	4.47	-	0.42	0.68

These data show, that optimal pairs for silicon of p-type are  $In_2O_3$ ,  $In_xSn_yO_z$ , ZnO, CdO.

For silicon of n-type optimal cover forming a barrier is  $SnO_2$ .

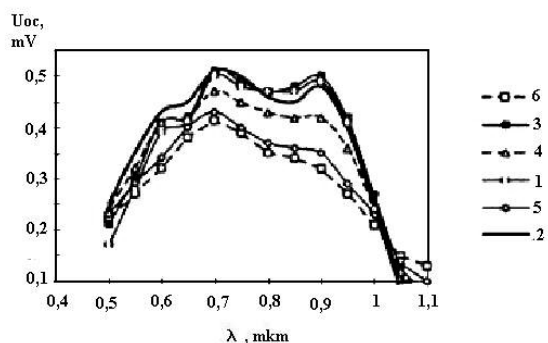


Fig. 7. Spectral characteristics of  $In_xSn_yO_z/SiO_x/pSi$  photo-electric converters: 1 – 350°C; 2 – 400°C; 3 – 425°C; 4 – 445°C; 5 – 500°C; 6 – 550°C

Fig. 7 shows the spectral performance of the photo-electric converters  $In_xSn_yO_z/SiO_x/pSi$  with the  $In_xSn_yO_z$  layer thickness of 800 Å, and covering temperature from 350°C to 550°C. The optimal temperatures of  $In_xSn_yO_z$  covering are 400–425°C. The maximal magnitude of open circuit voltage is being achieved for wavelength of 0.7 micron.

Fig. 8 shows the similar spectral performance for the  $In_xSn_yO_z/SiO_x/nSi$  photo-electric converters. For all the specimens time between drying and covering by

semiconductor layer, that forming a potential barrier, did not exceed 10 minutes. The figure shows, that in the range of temperatures 400–425°C a range of wavelengths, where the high values of open circuit voltage are observed, was shifted down from 0.65 micron to 0.85 micron and open circuit voltage have decreased. It confirms a high compatibility of  $In_xSn_yO_z/SiO_x/pSi$  structures.

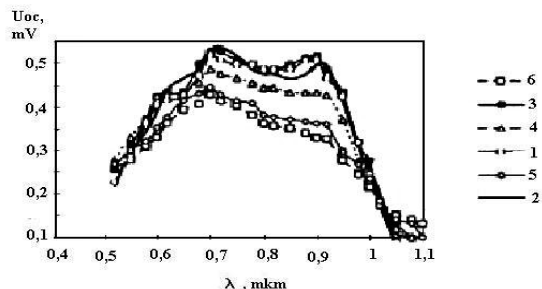


Fig. 8. Spectral characteristics of  $In_xSn_yO_z/SiO_x/nSi$  photo-electric converters: 1 – 350°C; 2 – 400°C; 3 – 425°C; 4 – 445°C; 5 – 500°C; 6 – 550°C

The spectral characteristics of photo-electric converters with structures  $In_xSn_yO_z/SiO_x/nSi$ ,  $In_xSn_yO_z/SiO_x/porousSi/nSi$ ,  $In_xAl_yO/SiO_x/porousSi/nSi$  are seen at Fig. 9.

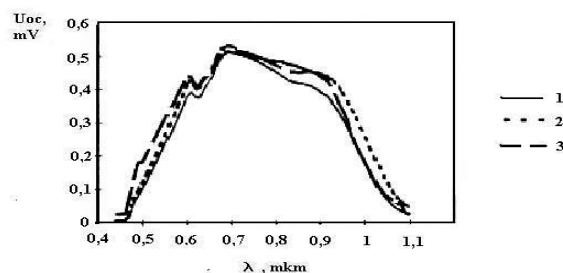


Fig. 9. Spectral characteristics of photo-electric converters based on: 1 –  $In_xSn_yO_z/SiO_x/nSi$ ; 2 –  $In_xSn_yO_z/SiO_x/porousSi/nSi$ ; 3 –  $In_xAl_yO/SiO_x/porousSi/nSi$

The thickness of silicon film is – 0.7 – 4.5 micron.

The best spectral performances have the  $In_xSn_yO_z/SiO_x/porousSi/nSi$  and  $In_xAl_yO/SiO_x/porousSi/nSi$  structures. In addition, the curve (2) is shifted more in long wavelength area of a spectrum, and curve (3) – in short wavelength one.

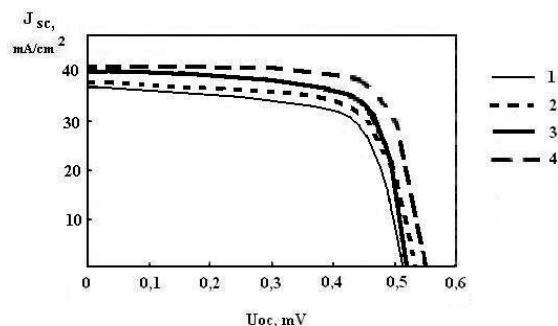


Fig. 10. Current-voltage characteristics of photo-electric converters with structures: 1 –  $In_xSn_yO_z/SiO_x/nSi$ ; 2 –  $In_xSn_yO_z/SiO_x/porousSi/nSi$ ; 3 –  $In_xAl_yO/SiO_x/porousSi/nSi$ ; 4 –  $In_xSn_yO_z/SiO_x/porousSi/pSi$

Table 2

## Characteristics of photo-electric converters

N	Structure	Jsc, mA/cm <sup>2</sup>	Uoc, mV	FF	η, %
1	In <sub>x</sub> Sn <sub>y</sub> O <sub>z</sub> /SiO <sub>x</sub> /nSi	37	510	0,57	12.5
2	In <sub>x</sub> Sn <sub>y</sub> O <sub>z</sub> /SiO <sub>x</sub> /porousSi/nSi	38	530	0,61	14.3
3	In <sub>x</sub> Al <sub>y</sub> O <sub>z</sub> /SiO <sub>x</sub> /porousSi/nSi	40,0	515	0,63	14.6
4	In <sub>x</sub> Sn <sub>y</sub> O <sub>z</sub> /SiO <sub>x</sub> /porousSi/pSi	41	550	0,74	15.8

The experimental light current-voltage characteristics of the silicon photoelectric converters with various covers are presented on Fig.10, and the basic parameters are shown in Table 2. These data testify, that for investigated structures the acceptable efficiency are obtained and they could be considered as perspective structures for a photo-electric converters.

## CONCLUSIONS

1. We have demonstrated that the covers, forming a potential barrier, could be successfully used for the effective solar cells creation.

2. The covers formed with the use of β-diketonates are the most effective.

3. Creation of a developed porous surface on silicon slices considerably increases the absorption of

light and improve parameters of the photo-electric converters.

## References

1. *An analysis of charges and surface states at the interfaces of semiconductor-insulator-semiconductor structures* / L. S. Berman, E. I. Beliakova, L. S. Kostina, E. D. Kim, S. C. Kim // *Physics and Technology of Semiconductors*. — 2000. — Vol. 34, N 7. — P. 814–817.
2. *Shewchun J., Druk D., Siughetal R.* The semiconductor-insulator-semiconductor (indium tin oxide on silicon) solar cell: characteristics and loss mechanisms // *J. Appl. Phys.* — 1979. — Vol. 50. — P. 6524–6533.
3. *Realization and characterization of ZnO/n-Si solar cells by spray pyrolysis* / H. H. Afify, S. H. El-Hefnawi, A. Y. Eliwa, M. M. Abdel-Naby, N. M. Ahmed // *Egypt. J. Solids*. — 2005. — Vol. 28, N 2. — P. 243–254.
4. *P-type silicon heterojunction solar cells with different interfaces and surface structures* / R. Bilyalov, A. Ulyashin, M. Scherff, K. Meusinger, J. Poortmans, W. Fahrner // *Proceedings of 3rd World Conference Photovoltaic Energy Conversion* 12-16 May. — 2003. — Vol. 2. — P. 1139–1142.
5. *Optical properties of porous silicon* / K. Kordas, S. Beke, A. E. Pap, A. Uusimaki, S. Leppavuori // *Optical Materials*. Part II: Fabrication and investigation of multilayer structures — 2003. — Vol. 25. — P. 257–260.
6. *Suntao W., Yanhua W., Qihua S.* Measurement and analysis of the characteristic parameters for the porous silicon / silicon using photovoltage spectra // *Applied Surface Science*. — 1999. — Vol. 158. — P. 268–274.
7. *Pincik E., Bartos P., Jergel M.* etc. The metastability of porous silicon — crystalline silicon structure // *Thin Solid Films*. — 1999. — Vol. 343–344. — P. 2.

UDC 673.40

S. L. Khrypko

## INVESTIGATION OF THE SOLAR CELLS WITH POROUS SILICON FILMS

The experimental results of a research of the solar cells parameters covered with films In<sub>x</sub>Sn<sub>y</sub>O<sub>z</sub>, and solar cells covered with films, obtained by dispersion of alcoholic solutions of three-chloride indium acetyl acetate of aluminium are represented. The spectral dependencies of reflection factor and open circuit voltage of the film-covered solar cells are obtained. The conditions of preparation and properties of porous silicon and parameters of the solar cells with films of porous silicon and covers, forming a potential barrier, are investigated. It is shown, that for optimum parameters of films, the preparation of the solar cells with efficiency 15.8% is quite real.

УДК 673.40

С. Л. Хрипко

## ДОСЛІДЖЕННЯ СОНЯЧНИХ ЕЛЕМЕНТІВ З ШАРАМИ ПОРУВАТОГО КРЕМНІЮ

Представлені експериментальні результати дослідження параметрів сонячних елементів, вкритих плівками In<sub>x</sub>Sn<sub>y</sub>O<sub>z</sub>, так само, як і плівками, отриманими шляхом розприскування спиртових розчинів трихлористого індій-ацетилацетонату алюмінію. Спектральні залежності коефіцієнту відбивання та напруги розкненого ланцюгу сонячних елементів, вкритих плівками отримані і досліджені. Умови приготування та властивості поруватого кремнію досліджені так само, як і параметри сонячних елементів та покриттів, які формують потенціальні бар'єри на поверхні кремнію. Показано, що за умов отримання оптимальних параметрів плівок, отримання сонячних елементів з ефективністю 15.8% є цілком можливим.

УДК 673.40

С. Л. Хрипко

### **ИССЛЕДОВАНИЕ СОЛНЕЧНЫХ ЭЛЕМЕНТОВ СО СЛОЯМИ ПОРИСТОГО КРЕМНИЯ**

Представлены экспериментальные результаты исследований параметров солнечных элементов, покрытых плёнками  $\text{In}_x\text{Sn}_y\text{O}_z$ , также, как и плёнками, полученными методом распыления спиртовых растворов трёххлористого индия – ацетилацетоната алюминия. Спектральные зависимости коэффициента отражения и напряжения разомкнутой цепи солнечных элементов, покрытых плёнками, получены и исследованы. Условия изготовления и свойства пористого кремния исследованы так же, как и параметры солнечных элементов и покрытий, которые формируют потенциальные барьеры на поверхности кремния. Показано, что при условии получения оптимальных параметров плёнок, получение солнечных элементов с эффективностью 15,8% вполне возможно.

A. V. GLUSHKOV<sup>2</sup>, Ya. I. LEPIKH<sup>1</sup>, S. V. AMBROSOV<sup>2</sup>, O. Yu. KHETSELIUS<sup>1</sup>, Yu. G. CHERNYAKOVA

<sup>1</sup>I. I. Mechnikov Odessa National University, Odessa

<sup>2</sup>Odessa State Environmental University, Odessa

<sup>3</sup>Odessa National Polytechnic University, Odessa

## COMPUTER MODELLING OPTIMAL SCHEMES OF THE LASER PHOTOIONIZATION METHOD FOR PREPARING THE FILMS OF PURE COMPOSITION AT ATOMIC LEVEL

The optimal laser photoionization scheme for preparing the films of pure composition on example of creation of the hetero structures (layers of GaAlAs) is proposed. New model of optimal realization of the first step excitation and further ionization of the As<sup>+</sup> ions in Rydberg states by DC electric field is developed.

Carrying out the effective methods for obtaining especially pure substances or their control and cleaning from admixtures (c.f. [1,2]) is considered as one of the actual problem of modern technology of the semiconductor and other materials. In particular, speech is about methods for control of the Al, B admixtures in Ge and other third group acceptor elements admixtures at the level of 10<sup>-8</sup>–10<sup>-10</sup>%. In some cases the similar sensitivity may be provided by traditional analytic methods [1] or their modifications. However, its sensitivity is limited by level of 10<sup>-7</sup>%. Selective photo physics methods (c.f. [2–17]) allow to develop a new approach to technologies of obtaining the pure substances at atomic level and solving many other problems. The basis for its successful realization is, first of all, in carrying out the optimal multi stepped photoionization schemes for different elements and, at second, availability of enough effective UV and visible range lasers with high average power. Our paper is devoted to the search and computer modeling the optimal schemes of laser photoionization method for control and cleaning the semiconducting substances. We will carry out modeling the laser photoionization scheme for preparing the films of pure composition on example of creation of the hetero structural super lattices (layers of Ga<sub>1-x</sub>Al<sub>x</sub>As with width 10E and GaAs of 60E). New models of optimal realization of the first step excitation and further ionization of the As<sup>+</sup> ions in Rydberg states by electric field are proposed and optimal parameters of the photo ionization process are found. Similar studying for Al and Ga ions had been carried out earlier [8–10].

The possible scheme for preparing the films of pure composition by means of the two-stepped selective ionization of atoms has been proposed by V. Letokhov [2]. Such scheme was not experimentally checked, however it is obvious that the two-stepped laser ionization scheme is not optimal one (see explanation below). The main innovation of our scheme is connected with using the electric field ionization pulse on the last ionization step. In ref. [8–10] we carried out modelling the optimal scheme for laser photoionization scheme of control and cleaning the substance and preparing pure films on atomic level for a number of elements, including Ga, Al etc. In a classic scheme, the laser excitation of admixture atoms is realized at

several steps: atoms are resonantly excited by laser radiation and then it is realized photo ionization of excited atoms (c.f. [2–8]). In this case photo ionization process is characterized by relatively low cross section  $\sigma_{\text{ion}}=10^{-17}-10^{-18}\text{cm}^2$  and one could use the powerful laser radiation on the ionization step. Alternative mechanism is a transition of atoms into Rydberg states and further ionization by electric field. As result, the requirements to energetics of ionized pulse are decreased at several orders.

As usually, the elements separation process is described by corresponding master system of equations for density matrix [2,8]. We supposed that a laser radiation acts on the admixtures atom and concentration of admixtures is quite little. The resonant exchange probability is less than ionization velocity, i.e.  $W_2 > \sigma_w vN$  ( $N$  - concentration of atoms) and the ions yield time from neutral atom cloud is less than re-charging time, i.e.:  $N\sigma_{\text{ci}}d < 1$ . At first step, the photo-ionization scheme includes an excitation of atoms by laser field and their transition into Rydberg states and then ionization by electric field. A creation of the films of pure composition (creation of the 3-D layers of Ga<sub>1-x</sub>Al<sub>x</sub>As with width 10E and GaAs of 60E) is directly connected with using the photo ion pensils of Ga<sup>+</sup>, Al<sup>+</sup>, As<sup>+</sup>. Similar pensils can be created by means of the selective photoionization method with ionization by electric field. Then electromagnetic focusing and deflecting systems will provide creation of the 3-D supper lattices (c.f.[2]).

We consider the ionization scheme of obtaining the As<sup>+</sup> ions. The transition scheme is as follows;  $4p^3 \ ^4S_{3/2} \rightarrow (50693,9\text{cm}^{-1}) \rightarrow 5s^4P_{1/2} \rightarrow (\lambda_2[n]) \rightarrow np^3D_{3/2}$  ( $n=10-25$ ). We carried out modeling the optimal parameters for last process, i.e. ionization of the Rydberg states by electric field. In figure 1 we present results of modeling the As atoms separation process by solving system (1). All necessary constants are preliminarily calculated and taken from refs [2, 3, 8–10, 15–17]. The following definitions are used:  $\delta$ -dashed line is corresponding to optimal form of laser pulse, curves 1 and 2 are corresponding to populations of the ground and excited states of As. The  $\delta$ -pulse provides maximum possible level of excitation (the excitation degree is about ~0,2; in experiment [2] with rectangular pulse this degree was ~ 0,1. In further the parasite processes

such as spontaneous relaxation, resonant re-exchange can't change the achieved excitation level during a little time. The last step of the process is an ionization of excited atoms by the electric field pulse.

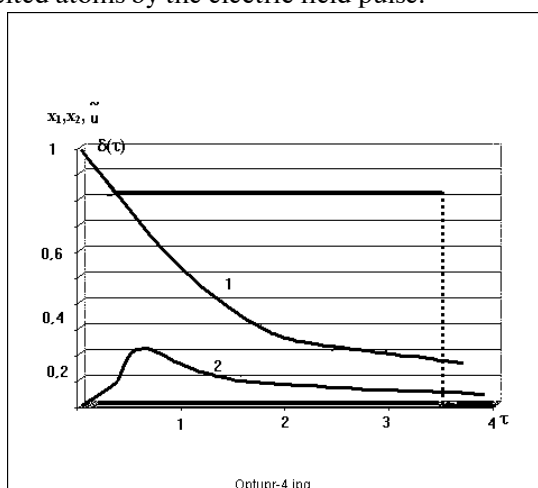


Fig. 1 Results of modeling As separation process by photoionization method ( $\delta$ +dashed – laser pulse optimal form; curves 1, 2 are corresponding to populations of the ground and excited states)

It is natural that in order to get a high level of the optimality an electric field has to be switched on during the time, which is less than the excited state radiative decay time. In figure 2 we present the results of our calculating dependence of the ionization velocity for high excited atoms of As upon the electric field strength for states with quantum numbers  $n=10-16$ . The dashed line is corresponding to velocity of the radiative decay.

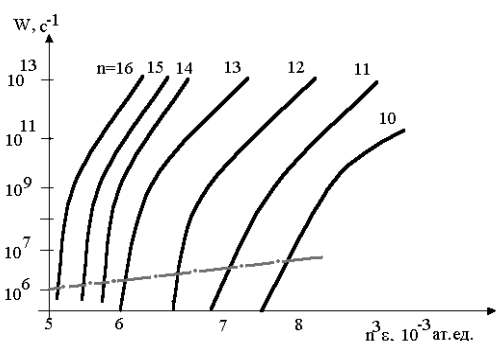


Fig. 2. Dependence of the velocity of ionization for high excited atoms of As on an electric field strength for states with quantum numbers  $n=10-16$

The decay of As atoms and ions in the high-excited state demonstrates qualitatively the properties of the H-like systems. However, there is quite significant quantitative difference. Indeed, the same situation takes a place for Al, Ga elements etc (c.f. [8]). Our estimate for the As atom ionization cross section is  $1,2 \cdot 10^{-13} \text{cm}^2$  that is higher than the corresponding cross section of ionization process by laser pulse in the two- stepped scheme ( $\sim 10^{-17} \text{cm}^2$  [2]). Using  $\delta$ -pulse provides a quick ionization, but the ionization yield will be less than 100% because of the sticking on intermediate levels. Experimentally obtained dependence of the critical ionization field strength E upon the effective quantum number  $n^*$  is usually approximated

by simple theoretical dependence  $E_{cr}=(2n^*)^{-4}$ . However, our calculation results show that this is not very exact approximation and only sophisticated quantum calculation [8–10] provide excellent agreement with experimental data. In any case, the laser photoionization scheme with ionization by electric field could provide significantly more high yield and effectiveness of the whole process than the other known schemes [2]. Naturally, the optimal set of energetic and radiative parameters (pulse form, duration, energetic for laser and electric field pulses etc) should be used. The scheme can be applied in the laser photoionization technologies for preparing the pure composition films, pure hetero structural super lattices, selective creating photo ions of B, As, P and other elements in equipment for ion legating the semiconductors. It is obvious that the optimal governing approaches may be also useful in a search of optimal realization of the photo-excitation and ionization processes in a number of tasks in molecular, semiconductors, surface physics etc.

## References

1. *Wainfordner J.* Spectroscopic Methods of determination for Elements Traces, Amsteradm: North Holland, 1979. — 520 p.
2. *Letokhov V. S.* Nonlinear Selective Photoprocesses in atoms and molecules, Moscow: Nauka, 1983. — 408 p.
3. *Glushkov A. V., Ambrosov S. V., Shpinareva I. M.* Quantum modelling and optimal governing by selective atomic photoprocesses. — Odessa: TEC, 2004. — 195 p.
4. *Ryabov E. A.* Laser separation of isotopes on the basis of IR multi-photon dissociation of molecules // *Usp. Phys. Nauk.* — 2004. — Vol. 174. — P. 684–688.
5. *Stoll W.* Present Status of industrial Isotope separation by laser technology // *Atomic and Molecular Pulsed Lasers.* — Tomsk: SO RAN, 2001. — P. 71.
6. *Laser separation of Silicon Isotopes by the AVLIS Technology / V. V. Buchanov, M. Kazaryan, M. Kalugin, A. M. Prokhorov // Atomic and Molecular Pulsed Lasers.* — Tomsk: SO RAN, 2001. — P. 82.
7. *Glushkov A. V., Ambrosov S. V.* Non-linear Selective Photoprocesses in Atoms and Molecules and their Optimal Governing. Optimized Isotope Separation Schemes // *Atomic and Molecular Pulsed Lasers.* — Tomsk: SO RAN, 2001. — P. 90.
8. *Ambrosov S. V.* New optimal schemes of the laser photoionization method and their use for cleaning the semiconductor materials and preparing the films of pure composition at atomic level // *Functional Materials.* — 2003. — Vol. 10, N 2. — P. 211–216.
9. *Ambrosov S. V.* Laser photoionization sensor of the separating isotopes and nuclear reactions products: theoretical foundations of new scheme // *Sensor Electr. MicroSyst. Techn.* — 2004. — N 2. — P. 37–45.
10. *Ambrosov S. V.* Selective Photoionization of atoms: resonant re-charging in vapours of alkali elements and uranium // *Photoelectronics.* — 2002. — Vol. 11. — P. 40–45.
11. *Ivanov L. N., Letokhov V. S.* Spectroscopy of autoionization resonances in heavy elements atoms // *Com. Mod. Phys. D.: At. Mol. Phys.* — 1985. — Vol. 4. — P. 169–184.
12. *Glushkov A. V., Ivanov L. N.* DC Strong-Field Stark-Effect: consistent quantum-mechanical approach // *J. Phys. B: At. Mol. Opt. Phys.* — 1993. — Vol. 26, N 16. — P. L379–L386.
13. *Glushkov A. V., Malinovskaya S. V., Ambrosov S. V. et al.* Resonances in Quantum Systems in Strong External Fields: Consistent Quantum Approach // *J. Techn. Phys.* — 1997. — Vol. 38, N 2. — P. 215–219.
14. *DC Stark Effect in Non-H atoms: Operator Perturbation theory / A. V. Glushkov, S. V. Ambrosov, D. Korchevsky, A. Ignatenko // Intern. Journ. Quant. Chem.* — 2004. — Vol. 99, N 5. — P. 936–942.
15. *Stark effect and resonances in the ionization continuum for hydrogen atom and Wannier-Mott excitons in DC electric field / A. V. Glushkov, S. V. Ambrosov, P. O. Fedchuk,*

O. P. Fedchuk // Journ. Phys.Stud. — 2003. — Vol. 7, N 3. — P. 31–35.

16. *Auger* effect in atoms and solids: Calculation of characteristics of Auger decay in atoms, quasi-molecules and solids with application to surface composition analysis / A. V. Glushkov, S. V. Ambrosov, V. P. Kozlovskaya, G. P. Prepelitsa // Functional Materials. — 2003. — Vol. 10, N 2. — P. 206–210.

17. *Radzig A. A., Smirnov B. M.* Parameters of atoms and atomic ions, Moscow: Energo-atomizd, 1986. — 320 p.

UDC 539.42:539.184

A. V. Glushkov, Ya. I. Lepikh, S. V. Ambrosov, O. Yu. Khetselius, Yu. G. Chernyakova

#### **COMPUTER MODELLING OPTIMAL SCHEMES OF THE LASER PHOTOIONIZATION METHOD FOR PREPARING THE FILMS OF PURE COMPOSITION AT ATOMIC LEVEL**

The optimal laser photoionization scheme for preparing the films of pure composition on example of creation of the hetero structures (layers of GaAlAs) is proposed.. New model of optimal realization of the first step excitation and further ionization of the As<sup>+</sup> ions in Rydberg states by DC electric field is developed.

УДК 539.42 : 539.184

О. В. Глушков, Я. И. Лепих, С. В. Амбросов, О. Ю. Хецелиус, Ю. Г. Чернякова

#### **КОМП'ЮТЕРНЕ МОДЕЛЮВАННЯ ОПТИМАЛЬНИХ СХЕМ ЛАЗЕРНОГО ФОТОІОНІЗАЦІЙНОГО МЕТОДУ ДЛЯ ПРИГОТУВАННЯ ПЛІВОК ЧИСТОГО СКЛАДУ НА АТОМНОМУ РІВНІ**

Запропоновано оптимальну лазерно-фотоіонізаційну схему приготування плівок особливо чистого складу на прикладі контролю побудови гетероструктур (типу GaAlAs). Розвинуто нову модель оптимальної реалізації збудження на 1-й стадії й подальшої іонізації іонів As<sup>+</sup> у рідбергових станах електричним полем

УДК 539.42 : 539.184

А. В. Глушков, Я. И. Лепих, С. В. Амбросов, О. Ю. Хецелиус, Ю. Г. Чернякова

#### **КОМПЬЮТЕРНОЕ МОДЕЛИРОВАНИЕ ОПТИМАЛЬНЫХ СХЕМ ЛАЗЕРНО-ФОТОИОНИЗАЦИОННОГО МЕТОДА ПРИГОТОВЛЕНИЯ ПЛЕНОК ОСОБО ЧИСТОГО СОСТАВА НА АТОМНОМ УРОВНЕ**

Предложена новая оптимальная лазерно-фотоионизационная схема приготовления пленок особо чистого состава на атомном уровне на примере контроля приготовления гетероструктур (типа GaAlAs). Развита новая модель оптимальной реализации возбуждения на первой стадии и дальнейшей ионизации ионов As<sup>+</sup> в ридберговых состояниях внешним электрическим полем.

*E. RUSU<sup>1</sup>, V. URSAKI<sup>1</sup>, G. NOVITSCHI<sup>2</sup>, A. BURLACU<sup>1</sup>, P. PETRENKO<sup>1</sup>, L. KULIUK<sup>1</sup>*

<sup>1</sup>Institute of Applied Physics, Academy of Sciences of Moldova, 5, Academiei str., Chisinau, MD-2029, Republic of Moldova, e-mail: rusue@lises.asm.md, tel. +373-22-739048, fax. +373-22-738149.

<sup>2</sup>Moldovan State University, 60, Mateevich str., Chisinau, MD-2029, Republic of Moldova

## LUMINESCENCE OF ZnGa<sub>2</sub>O<sub>4</sub> AND ZnAl<sub>2</sub>O<sub>4</sub> SPINELS DOPED WITH Eu<sup>3+</sup> AND Tb<sup>3+</sup> IONS

Spinel type mono-phase the ZnGa<sub>2</sub>O<sub>4</sub> and ZnAl<sub>2</sub>O<sub>4</sub> compounds doped with Eu<sup>3+</sup> and Tb<sup>3+</sup> ions were obtained using two methods: solid phase reactions and deposition from chemical solutions. The luminescent analysis of the materials shows that the rare earth ions are localised at the defect sites (regions) of the crystallite (grain) boundaries. The emission spectra of the samples with europium are characterized by an intense emission in red region due to the <sup>5</sup>D<sub>0</sub> → <sup>7</sup>F<sub>1,2</sub> transitions of Eu<sup>3+</sup> ions, whereas, in the case of terbium, the highest intensity corresponds to the green emission due to the <sup>5</sup>D<sub>4</sub> → <sup>7</sup>F<sub>3</sub> transitions of Tb<sup>3+</sup> ions. The intensities of the intra-shell emission of the Eu<sup>3+</sup> and Tb<sup>3+</sup> ions in comparison with luminescence intensity of the chromium impurity traces (residual small amount of the Cr<sup>3+</sup> ions) show that the materials doped with transition metals are more promising for development of phosphors based on oxide spinels than the materials doped with rare-earth elements.

### INTRODUCTION

Semiconductors, doped with rare earth elements, are considered to be perspective materials for optoelectronics and photonics due to the presence of narrow emission spectral lines. Wide band gap semiconductors and dielectrics are more preferable for doping, because the effects of thermal quenching of the radiation are inversely proportional to the band gap value [1]. Another advantage of the wide band gap materials is their chemical stability and stability of the physical characteristics in a large temperature interval. Actually, the most widely used phosphors for planar displays are sulfides. However, the chemical reactions stimulated by the electronic beam leading to the formation of a non-luminescent layer with the deficiency of sulfur at the surface of the phosphor are the important shortcomings of the sulfide phosphors. These reactions considerably reduce the efficiency of phosphors [2].

Besides, the reaction products, stimulated by electron beam, pollute electronic emitters. Many problems related to the degradation are avoided by using of the oxide phosphors. Among them, the ZnGa<sub>2</sub>O<sub>4</sub> compound is one of the best studied low voltage cathodoluminescent phosphors [3]. ZnAl<sub>2</sub>O<sub>4</sub> is another compound, which recently has attracted considerable interest for electroluminescent thin film displays and opto-mechanical sensors [4-6]. It was reported about the synthesis of bulk and nano-structured ZnAl<sub>2</sub>O<sub>4</sub> using solid phase reactions of zinc and aluminium oxides at temperatures higher than 800°C [7], or by means of chemical reactions in solutions [8-10]. Several papers have been dedicated to the investigations of luminescence properties of ZnAl<sub>2</sub>O<sub>4</sub> [4, 11-14] and ZnGa<sub>2</sub>O<sub>4</sub> doped with rare earth elements [3, 16]. However, the quantitative analysis of the emitted intensity, or a comparative analysis with the luminescence intensity of other radiative centers are not presented in these works.

In this paper the luminescence caused by intra-shell radiative transitions of Eu<sup>3+</sup> и Tb<sup>3+</sup> ions intro-

duced in ZnGa<sub>2</sub>O<sub>4</sub> and ZnAl<sub>2</sub>O<sub>4</sub> hosts is investigated. The comparison of this luminescence intensity with the emission intensity of the Cr<sup>3+</sup> ions existing in the host lattices as traces of residual impurity is carried out. The difficulties concerning the incorporation of the big radius rare earth ions in the octahedral sites of the oxide spinel hosts, that are not inherent in the case of small radius transition metal impurities, are revealed.

### PREPARATION OF SAMPLES AND EXPERIMENTAL TECHNIQUES

Undoped ZnGa<sub>2</sub>O<sub>4</sub> and ZnAl<sub>2</sub>O<sub>4</sub> compounds as well as the ones, doped with Eu and Tb, were prepared by means of two technological methods.

In the first process, the material has been obtained using solid phase reactions method by mixing ZnO (99.99%) and Ga<sub>2</sub>O<sub>3</sub> (99.99%), or ZnO (99.99%) and Al<sub>2</sub>O<sub>3</sub> (99.99%) powders in 1:1 ratio, followed by forming pellets under a press and sintering at 1200°C during 16-18 hours. Doping with rare earth elements was carried out by adding Eu<sub>2</sub>O<sub>3</sub> and Tb<sub>2</sub>O<sub>3</sub> powders with concentration of (0.1–2) %.

In the second process, the powders were obtained using the chemical deposition method, that allows the formation of ZnGa<sub>2</sub>O<sub>4</sub> and ZnAl<sub>2</sub>O<sub>4</sub> precipitates with spinel structure at temperature less than 300°C. For comparison, several samples simultaneously doped with phosphor and rare earth elements were prepared. The phase composition of the compounds was analyzed by EDX and XRD methods.

The luminescent properties of the obtained materials were studied at room temperature using different spectral lines of a Spectra Physics 2017 Ar<sup>+</sup> laser for optical excitation, SDL-1 double spectrometer (resolution better than 1meV), PEU-106 photomultiplier and a photon counting system.

## RESULTS AND DISCUSSION

The  $\text{ZnGa}_2\text{O}_4$  and  $\text{ZnAl}_2\text{O}_4$  materials with spinel structure, belong to the space group  $O_h^7$  with eight formula units in the unit cell. Thirty two oxygen atoms occupy sites with  $C_{3v}$  symmetry forming a closely packed cubic lattice with 64 tetrahedral ( $T_d$ ) and 32 octahedral ( $D_{3d}$ ) cation sites, only 8 tetrahedral (8A) and 16 octahedral (16B) of them being occupied by cations. Both compounds under study, belong to normal spinels, where all Zn atoms occupy the tetrahedral A sites, and atoms of Ga or Al occupy the octahedral sites. At the same time, insignificant inversion of the spinel structure, where a part of Ga or Al atoms may occupy the tetrahedral A sites, is possible.

Thus, rare-earth ions, potentially, may occupy both the tetrahedral and octahedral lattice sites. However, it is known that in the III–V and II–VI materials, due to a large ion radius, the rare-earth elements hardly occupy lattice sites with the tetrahedral coordination [15], preferring the sites with a coordination number greater than 6. Efficiency of the rare-earth ion occupation of sites with the octahedral coordination in  $A^{II}B^{III}O_4$  compounds with the spinel structure is studied insufficiently.

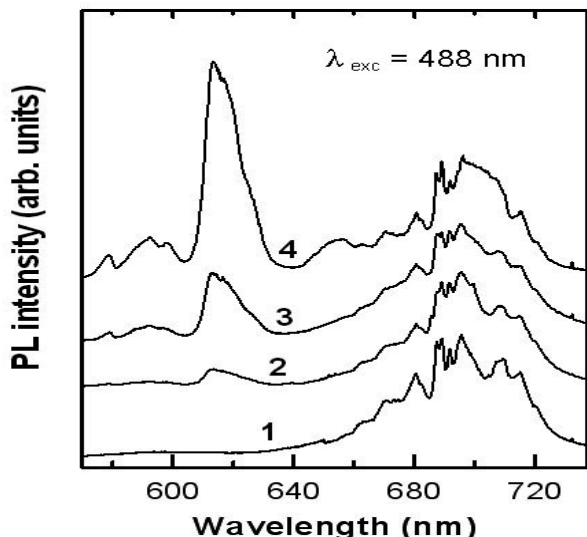


Fig. 1. PL spectra of  $\text{ZnGa}_2\text{O}_4$  powders doped with Eu concentrations: 1 – 0%; 2 – 1%; 3 – 0.5%; 4 – 2%

Figure 1 shows the luminescence spectra of  $\text{ZnGa}_2\text{O}_4$  with various concentrations of Eu doping impurity prepared from initial materials of high purity. Let us note that the form of the samples spectra, obtained by the method of solid phase reactions and by the chemical method is practically identical.

The luminescence spectrum consists of emission lines related to the  ${}^5D_0 \rightarrow {}^7F_1$  intra-shell transitions (in the range of 570–600 nm) and  ${}^5D_0 \rightarrow {}^7F_2$  (in the range of 600–630 nm) of  $\text{Eu}^{3+}$  ions as well as of the structured band in the range of 650–730 nm, corresponding to emission, induced by residual chromium impurity. The highest intensity of the luminescence, due to Eu ions presence, is obtained at excitation by the 465.8 nm laser line (see Fig. 2, curve 1), which quantum energy coincides with the energy of the  ${}^7F_0 \rightarrow {}^5D_2$  intra-shell transitions of  $\text{Eu}^{3+}$  ions, allowing their resonance excitation. Appearance of the band, induced by

the residual chromium impurity in the luminescence spectra, makes it possible to compare the efficiency of the incorporation of  $\text{Eu}^{3+}$  ions into the spinel structure with the respective efficiency of  $\text{Cr}^{3+}$  ions. Chromium concentration in  $\text{ZnGa}_2\text{O}_4$  powders, prepared from high purity materials is  $\sim 10$  ppm.

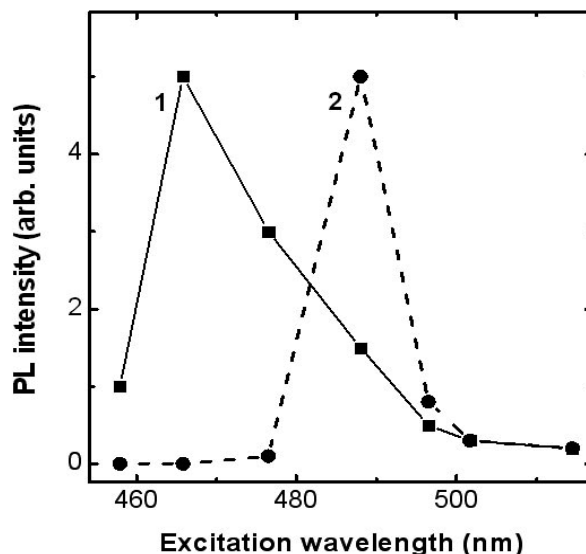


Fig. 2. PL intensity dependence in the spectral region of 600–630 nm for  $\text{ZnGa}_2\text{O}_4$  powders doped with Eu (curve 1, squares) and in the spectral region of 540–560 nm for  $\text{ZnGa}_2\text{O}_4$  powders doped with Tb (curve 2, circles) upon the excitation laser wavelength

As one could see from Fig. 1, the intensity of the luminescence due to the Eu doping impurity becomes comparable with the intensity of the luminescence of chromium impurity only at europium concentration of 1 %, i.e., by three orders of magnitude higher than the chromium concentration. This observation is a direct evidence of inefficiency of  $\text{Eu}^{3+}$  ion incorporation into the spinel lattice sites with a coordination number equal to 6.

Let us note that the  $\text{Eu}^{3+}$  ion radius is equal to 0.95 E and it is obviously greater than the radius of  $\text{Ga}^{3+}$  ions (0.62 E) practically coinciding with the radius of trivalent  $\text{Cr}^{3+}$  ions (0.615 E). The assumption of low efficiency of the rare-earth element ion incorporation is also confirmed by the form of the luminescence spectra in the region of the  $\text{Eu}^{3+}$  intra-shell transitions. Broad overlapping lines are observed instead of narrow lines due to the Stark splitting. This form of spectra is characteristic of amorphous materials and glasses.

On the other hand, the form of the X-ray diffraction patterns, shown at Fig. 3 indicates the presence of perfect crystallites with the spinel structure. The average size of the crystallites in powders was determined by the Scherer formula [16]

$$d = \frac{K\lambda}{(\beta^2 - \beta_0^2)^{1/2}} \cos\theta,$$

where  $\beta$  is the half-width of the diffraction peak in radians,  $\beta_0$  corresponds to the instrumental broadening,  $K = 180/\pi$ ,  $\lambda$  is the X-ray wavelength,  $\theta$  is the Bragg diffraction angle. The average crystallite size determined by the given formula is 20 nm. Discrepancy between the broad lines of the luminescence spectra and

the X-ray analysis data is explained by the presence on the crystallite boundaries of regions with defect structure close to the amorphous one. The Eu impurity penetrates in these defect boundary regions (being practically not incorporated into the volume of crystallites with perfect spinel structure); this determines the form of the luminescence spectra.

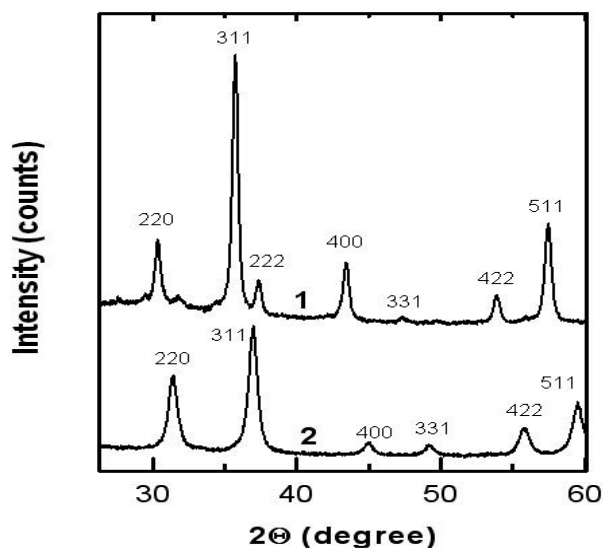


Fig. 3. XRD patterns for  $\text{ZnGa}_2\text{O}_4$  (1) and  $\text{ZnAl}_2\text{O}_4$  (2) compounds

As it was mentioned above, big rare-earth ions are incorporated more easily into places with high coordination number. Such a compound is  $\text{EuPO}_4$ , as it easily crystallizes in a monazite structure at the synthesis temperatures above  $600^\circ\text{C}$ . In the monoclinic monazite structure  $\text{P2}_1/\text{n}$  the coordination number for Eu ions is equal to 9. Taking this into account, we have prepared  $\text{ZnGa}_2\text{O}_4$  samples with Eu concentration of 1% being simultaneously doped with various phosphor concentrations and we have measured the luminescence spectra depending on phosphor concentration.

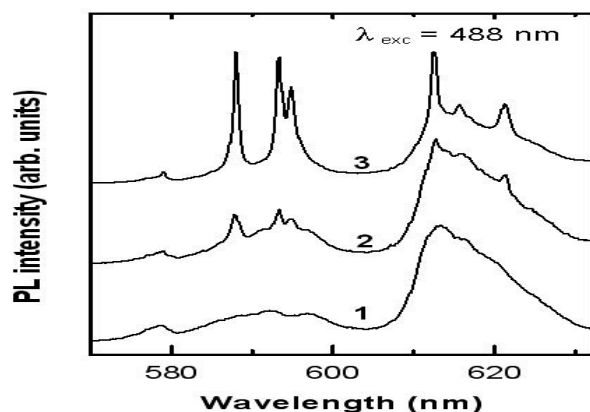


Fig. 4. PL spectra of  $\text{ZnGa}_2\text{O}_4$  powders doped with 1% wt concentration of Eu (1) and with addition of 0.3% wt (2) and 2% wt (3) phosphor impurity

As one could see from Fig. 4, additional narrow peaks appear in the luminescence spectrum instead of broad bands when concentrations of phosphorus and europium are comparable. The luminescence spectrum completely coincides with the known spectrum of  $\text{EuPO}_4$  compound when the phosphor concentration is equal to or is higher than the europium

concentration [17]. This experiment is an additional confirmation of the fact that for big  $\text{Eu}^{3+}$  ions it is easier to be incorporated into the lattice sites with a high coordination number forming a new  $\text{EuPO}_4$  compound, than to penetrate into amorphous regions on the boundaries of  $\text{ZnGa}_2\text{O}_4$  crystallite grains. The probability of their implantation directly into the spinel structure of the crystalline grains is even lower.

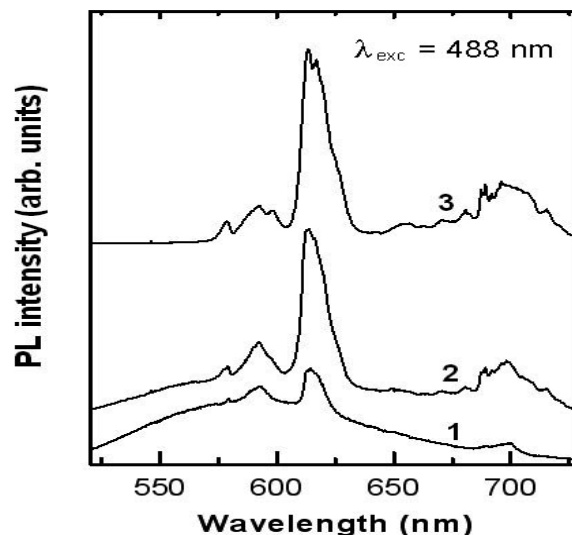


Fig. 5. PL spectra of  $\text{ZnGa}_2\text{O}_4$  powders doped with 1% wt Eu concentration prepared from high purity components before (1) and after annealing at  $500^\circ\text{C}$  (2) and  $700^\circ\text{C}$  (3)

Figure 5 shows the annealing influence on spectra of  $\text{ZnGa}_2\text{O}_4$  samples doped with  $\text{Eu}^{3+}$  ions prepared of high purity materials. The luminescence spectrum of the non-annealed sample consists of a broad band determined, apparently, by the crystal structure defects, whereupon narrow bands corresponding to the intra-shell transitions of  $\text{Eu}^{3+}$  ions impose.

Let us note, that in the given case, in the wavelength range of 650–730 nm, only a weak band due to the transitions  ${}^3\text{D}_0 \rightarrow {}^7\text{F}_4$  of  $\text{Eu}^{3+}$  ions is observed and the band due to presence of  $\text{Cr}^{3+}$  ions is not found because of extremely low concentration of residual chromium (1 ppm). As the annealing temperature increases above  $500^\circ\text{C}$  the broad band luminescence is quenched. This may be explained by annealing of the defects.

At the same time, the activation of Eu impurity takes place and spectral lines inherent to  $\text{Cr}^{3+}$  ions appear due to diffusion of the chromium impurity during annealing.

Similar behavior of the rare-earth ions is observed in the case of  $\text{ZnGa}_2\text{O}_4$  doped with terbium.

As one could see from Fig 6, where the luminescence spectra of  $\text{ZnGa}_2\text{O}_4$  doped with Eu and Tb are compared, in the sample with terbium, the overlapping of Stark lines takes place, and the luminescence from  $\text{Tb}^{3+}$  ions is comparable to the intensity of the luminescence due to the residual Cr impurity, while its concentration being less by three orders of magnitude.

The highest intensity of the luminescence due to Tb is obtained at excitation by 488 nm line (see Fig. 2, curve 2), its quantum energy coinciding with the energy of the intra-shell transitions  ${}^7\text{F}_6 \rightarrow {}^5\text{D}_4$  of  $\text{Tb}^{3+}$

ions allowing resonance excitation of these ions. The emission is due to the transitions  ${}^3D_4 \rightarrow {}^7F_{2,3,4,5}$ .

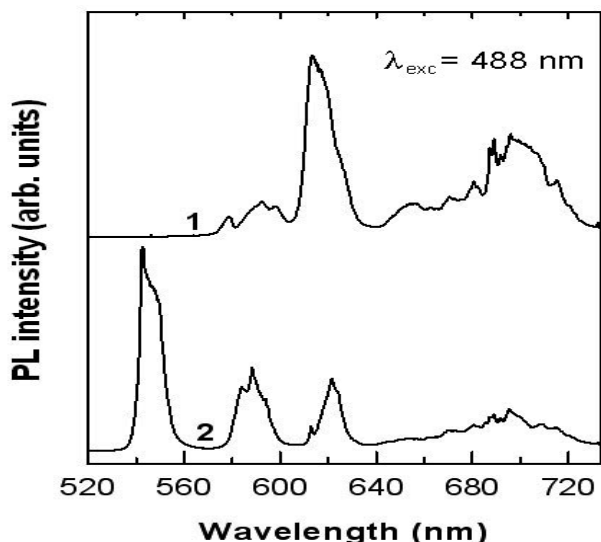


Fig. 6. PL spectra of  $ZnGa_2O_4$  powders doped with 2% wt Eu (1) and Tb (2)

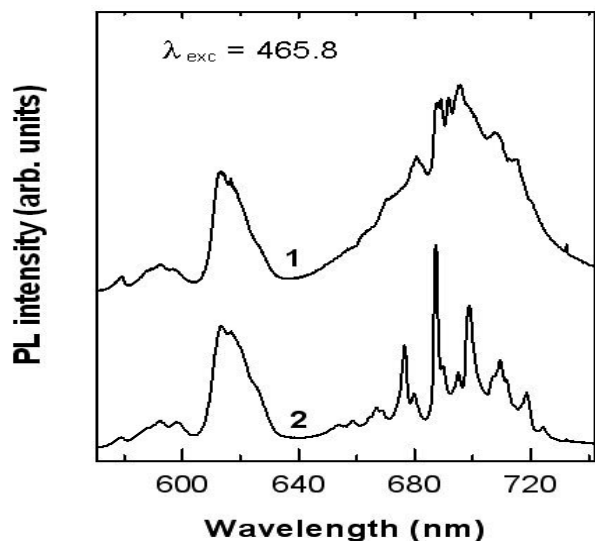


Fig. 7. PL spectra of  $ZnGa_2O_4$  (1) and  $ZnAl_2O_4$  (2) powders doped with 0.5% wt Eu

Let us note that the behavior of the rare-earth ions in  $ZnAl_2O_4$  is analogous to their behavior in  $ZnGa_2O_4$ . As it follows from Fig. 7, the bands of the intra-shell luminescence of rare-earth ions are identical for  $ZnAl_2O_4:Eu$  and  $ZnGa_2O_4:Eu$  compounds. This confirms that ions of Eu and Tb penetrate into amorphous regions on the grain boundaries.

Otherwise, the spectra must differ, since crystal fields are different for different materials. The latter statement is well illustrated by analysis of the luminescence due to Cr impurity. As one could see from Fig. 7, in the range of 650–730 nm, the forms of the luminescence spectra of  $ZnAl_2O_4$  and  $ZnGa_2O_4$  compounds are completely different.

Thus, in contrast to Eu ions, Cr ions are easily incorporated into the spinel crystal structure of the grains due to nearly the same value of ion radii of Ga and Cr, determining the luminescence intensity being incomparably higher than in the case of the intra-shell luminescence of Eu ions.

## CONCLUSIONS

1. The results of this work reveal the difficulties of the incorporation of the rare earth ions in the octahedral sites of the oxide spinel crystalline lattices. These difficulties are caused by the large radius of the RE ions, that prefer to be located in the sites with coordination number bigger than six.

2. The luminescent spectra analysis registered for  $ZnAl_2O_4$  and  $ZnGa_2O_4$ , doped with europium and terbium from the one side and containing a residual Cr impurity on the other side has shown that in comparison with rare earth elements the transition metal ions are much more efficient for using as activating impurity of phosphors based on spinel type materials.

## ACKNOWLEDGMENTS

This work was carried out within the framework of the State Program (Project 07.408.04.04PA)

## References

1. *Luminescence of erbium implanted in various semiconductors: IV, III–V and II–IV materials* / P. N. Favennec, H. L'Haridon, M. Salvi, D. Muottonnet, Y. L. Guillo // *Electron. Lett.* — 1989. — 25. — P. 718.
2. *Advances in field emission displays phosphors* / P. H. Holloway, T. A. Trottier, B. Abrams, C. Kondoleon, S. L. Jones, J. S. Sebastian, W. J. Thomes, H. Swart // *J. Vac. Sci. Technol.* — 1999. — B 17. — P. 758.
3. *Eu<sup>3+</sup> and Cr<sup>3+</sup> doping for red cathodoluminescence in  $ZnGa_2O_4$*  / P. D. Rack, J. J. Peterson, M. D. Potter, W. Park // *J. Mater. Res.* — 2001. 16. — P. 1429.
4. *Cathodoluminescent characteristics of Sm-doped  $ZnAl_2O_4$  nanostructured powders* / E. Martinez-Sanchez, M. Garcia-Hipolito, J. Guzman, F. Ramos-Brito, J. Santiyo-Salazar, R. Martinez-Martinez, O. Alvarez-Fregoso, M. I. Ramos-Cortes, J. J. Mendez-Delgado, C. Falcony // *Phys. Status Solidi a*, 2005. — 202. — P. 102.
5. *Matsui H., Xu C. N., Tateyama H. Stress-stimulated luminescence from  $ZnAl_2O_4:Mn$*  // *Appl. Phys. Lett.* — 2001. — 78. — P. 1068.
6. *Lou Z., Hao J. Cathodoluminescent characteristics of green-emitting  $ZnAl_2O_4:Mn$  thin-film phosphors* // *Appl. Phys.* 2005. — A 80. — P. 151.
7. *Reaction Sintering of  $ZnO-Al_2O_3$*  / W. S. Hong, L. C. De Jonghe, X. Yang, M. N. Rahaman // *J. Am. Ceram. Soc.* — 1995. — 78. — P. 3217.
8. *Preparation and properties of zinc oxide nanoparticles coated with zinc aluminate* / F. L. Yuan, P. Hu, C. L. Yin, S. L. Huang, J. L. Li // *J. Mater. Chem.* — 2003. — 13. — P. 634.
9. *Zawadzki M., Wrzyszczyk J. Hydrothermal synthesis of nanoporous zinc aluminate with high surface area* // *Mater. Res. Bull.* — 2000. — 35. — P. 109.
10. *Single-Source Sol-Gel Synthesis of nanocrystalline  $ZnAl_2O_4$ : Structural and Optical Properties* / S. Mathur, M. Veith, M. Haas, H. Shen, N. Leckerf, V. Huch, S. Hufner, R. Haberkorn, H. P. Beck, M. Jilavi // *J. Am. Ceram. Soc.* — 2001. — 84. — P. 1921.
11. *Preparation and optical properties of nanocrystalline and nanoporous Tb doped alumina and zinc aluminate* / M. Zawadzki, J. Wrzyszczyk, W. Streck, D. Hreniak // *J. Alloys Compounds.* — 2001. — 323/324. — P. 279.
12. *Characterization of  $ZnAl_2O_4$ : Tb luminescent films deposited by ultrasonic spray pyrolysis technique* / M. Garcia-Hipolito, A. Corona-Ocampo, O. Alvarez-Fregoso, E. Martinez, J. Guzman-Mendoza, C. Falcony // *Phys. Status Solidi.* — 2004. — a 201. — P. 72.
13. *Lou Z., Hao J. Characterization of  $ZnAl_2O_4$ : Tb luminescent films deposited by ultrasonic spray pyrolysis technique* // *Thin Solid Films.* — 2004. — 450. — P. 334.
14. *Synthesis and photoluminescence characteristics of Dy<sup>3+</sup>-doped  $ZnAl_2O_4$  nanocrystals via a combustion process* /

- S. F. Wang, F. Gu, M. K. Lu, X. F. Cheng, W. G. Zou, G. J. Zhou, S. M. Wang, Y. Y. Zhou // *J. Alloys Compounds*. — 2005. — 394. — P. 255.
15. *Bagraev N. T., Romanov N. T.* Magnetism of III–V crystals doped with rare-earth elements // *Semiconductors*. — 2005. — 39. — P. 1131.
16. *Conduction* mechanism of highly conductive and transparent zinc oxide thin films prepared by magnetron sputtering / T. Minami, T. Sato, K. Ohashi, T. Tomofuji, S. Takata // *J. Cryst. Growth*. — 1992. — 117. — P. 370.
17. *Dexpert-Ghys J., Mauricot R., Faucher M. D.* Spectroscopy of  $\text{Eu}^{3+}$  ions in monazite type lanthanide orthophosphates  $\text{LnPO}_4$ , Ln = La or Eu // *J. Luminescence*. — 1996. — 69. — P. 203.

UDC 621.315.592

E. RUSU, V. URSAKI, G. NOVITSCHI, A. BURLACU, P. PETRENKO, L. KULIUK

#### LUMINESCENCE OF $\text{ZnGa}_2\text{O}_4$ AND $\text{ZnAl}_2\text{O}_4$ SPINELS DOPED WITH $\text{Eu}^{3+}$ AND $\text{Tb}^{3+}$ IONS

Spinel type mono-phase the  $\text{ZnGa}_2\text{O}_4$  and  $\text{ZnAl}_2\text{O}_4$  compounds doped with  $\text{Eu}^{3+}$  and  $\text{Tb}^{3+}$  ions were obtained using two methods: solid phase reactions and deposition from chemical solutions. The luminescent analysis of the materials shows that the rare earth ions are localised in the defect sites (regions) at the crystallite (grain) boundaries. The emission spectra of the samples with europium are characterized by an intense emission in red region due to the  ${}^3\text{D}_0 \rightarrow {}^7\text{F}_{1,2}$  transitions of  $\text{Eu}^{3+}$  ions, whereas in the case of terbium the highest intensity corresponds to the green emission due to the  ${}^3\text{D}_4 \rightarrow {}^7\text{F}_5$  transitions of  $\text{Tb}^{3+}$  ions. The intensities of the intra-shell emission of the  $\text{Eu}^{3+}$  and  $\text{Tb}^{3+}$  ions in comparison with luminescence intensity of the chromium impurity traces (residual small amount of the  $\text{Cr}^{3+}$  ions) show that the materials doped with transition metals are more promising for development of phosphors based on oxide spinels than the materials doped with rare-earth elements.

УДК 621.315.592

Е. Русу, В. Урсаки, Ж. Новитши, А. Бурлаку, П. Петренко, Л. Кулюк

#### ЛЮМИНЕСЦЕНЦИЯ ШПИНЕЛЕЙ $\text{ZnGa}_2\text{O}_4$ AND $\text{ZnAl}_2\text{O}_4$ ЛЕГИРОВАННЫХ ИОНАМИ $\text{Eu}^{3+}$ И $\text{Tb}^{3+}$

Методом твердофазных реакций и осаждением из химических растворов изготовлены порошки однофазных соединений со структурой шпинели легированные ионами  $\text{Eu}^{3+}$  и  $\text{Tb}^{3+}$ . На основе люминесцентного анализа материалов сделан вывод о преобладающем внедрении ионов редкоземельных элементов в дефектные области, образованные на границах кристаллических зерен. Спектры люминесценции образцов с примесью европия характеризуются наибольшей интенсивностью в красной области за счет переходов  ${}^3\text{D}_0 \rightarrow {}^7\text{F}_{1,2}$  ионов  $\text{Eu}^{3+}$ , тогда как в случае примеси тербия наибольшая интенсивность соответствует зеленому свечению, за счет переходов  ${}^3\text{D}_4 \rightarrow {}^7\text{F}_5$  ионов  $\text{Tb}^{3+}$ . Результаты анализа интенсивности внутрицентральной люминесценции ионов  $\text{Eu}^{3+}$  и  $\text{Tb}^{3+}$  в сравнении с интенсивностью люминесценции, вызванной остаточной примесью хрома (ионов  $\text{Cr}^{3+}$ ), свидетельствует о том, что большую перспективность для разработки люминофоров на основе оксидных шпинелей имеют материалы, легированные переходными металлами, по сравнению с редкоземельными элементами.

УДК 621.315.592

Е. Русу, В. Урсаки, Ж. Новитши, А. Бурлаку, П. Петренко, Л. Кулюк

#### ЛЮМИНЕСЦЕНЦИЯ ШПИНЕЛЕЙ $\text{ZnGa}_2\text{O}_4$ I $\text{ZnAl}_2\text{O}_4$ , ЛЕГОВАНІХ ІОНАМИ $\text{Eu}^{3+}$ I $\text{Tb}^{3+}$

Методом твердофазних реакцій і осаджуванням хімічних розчинів виготовлені порошки однофазних сполучень  $\text{ZnGa}_2\text{O}_4$  and  $\text{ZnAl}_2\text{O}_4$  з структурою шпінелі, легованих іонами  $\text{Eu}^{3+}$  и  $\text{Tb}^{3+}$ . На основі люмінесцентного аналізу матеріалів зроблено висновок про переважне впровадження іонів рідкоземельних елементів в дефектні області, створені на кордонах кристалічних зерен. Спектри люмінесценції зразків з домішками европія відзначаються найбільшою інтенсивністю у червоній області за рахунок переходів  ${}^3\text{D}_4 \rightarrow {}^7\text{F}_5$  іонів  $\text{Tb}^{3+}$ . Висновки аналізу інтенсивності внутріцентральної люмінесценції іонів  $\text{Eu}^{3+}$  і  $\text{Tb}^{3+}$  у порівнянні з інтенсивністю люмінесценції, викликаний остаточними домішками хрому (іонів  $\text{Cr}^{3+}$ ), свідчать про те, що велику перспективність для розробки люмінофорів на основі оксидних шпінелей мають матеріали, леговані перехідними матеріалами, по зрівнянню з рідкоземельними елементами.

V. A. SMYNTYNA, O. A. KULINICH, M. A. GLAUBERMAN, G. G. CHEMERESYUK, I. R. YATSUNSKIY

Training, Scientific-Investigation and Production Center at Mechnikov Odessa National University (4 Marshala Govorova str., Odessa 65063, Ukraine, e-mail: eltech@elaninet.com)

## THE STRUCTURE INVESTIGATION OF NEAR-SURFACE LAYERS IN SILICON – DIOXIDE SILICON SYSTEMS

The near-surface silicon layers in silicon – dioxide silicon systems with used modern method of research are investigated. It is shown that these layers have compound structure and their parameters depend on oxidation and initial silicon parameters.

### 1. INTRODUCTION

Investigations of  $\text{SiO}_2$  – Si structures is still give a great consideration due to principal position of this structure in micro and nanoelectronics. The technological importance of  $\text{SiO}_2$  – Si systems stems from their ubiquitous presence in Metal-Oxide-Semiconductor (MOS) structures. In consideration of the fact that major processes in  $\text{SiO}_2$  – Si electronics happens in near-surface layers of silicon it is necessary to investigate surface morphology of these layers. As shown in modern researches there is transition layer under the oxide which different from the monocrystalline silicon in structure and composition [1]. But it still not fixed this structure and the depth of these layers. And it still not detects the relation between difference of these layers and other parameters such as oxidation process and characteristics of initial silicon.

The aim of this work is the definition of silicon near-surface structural composition in  $\text{SiO}_2$  – Si and the determination parameters of these layers on oxidation and initial silicon parameters.

### 2. EXPERIMENTAL DETAILS

Investigation of silicon surface after removal of dioxide was carried out by scanning electronic microscopy (electronic scanning microscope “Cam-Scan” with “Link-860” X-Ray microanalyser, used ZAF program for calculation), by optical methods (metallographic microscope MMR-2R), by Auger spectrometer LAS-3000 (beam diameter – 5 micron), by X-ray technique on DRON-2 with silicon grating monochromator (voltage = 16kV, intensity of a current = 2mA). Silicon wafers with different dioxide thickness (range 0.1–1.5 micron) grown in dry oxygen environment on 1100°C temperature were researched (oxygen consumption was about 10 liter in minute).

The  $\text{SiO}_2$  was etched off in hydrofluoric acid followed by washing in deionized water. To detect structural defects, the silicon surface layer-by-layer etching away with selective Sekko (for surface 100) and Sirtl (for 111) etchants with preliminary treatment in Karo intermixture and peroxide-ammonia solution was led [3].

### 3. RESULTS AND DISCUSSION

Fig. 1 shows the typical picture of a silicon surface, received after 5 minutes oxide (the thickness of ox-

ide was 1 micron) etching in selective Sirtl etchant. It's well visible, that typical etch pits dislocation and stacking faults are absent. Presence on a silicon surface such pits is connected with etching oxide which appears at the accelerated thermodiffusion it along structural defects of silicon. Attempts to receive the image of surface Si with the help of the electron microscope “Cam - Scan” turned out unsuccessful. The irradiated silicon surface was strongly charged by an electron beam and there was no opportunity to receive an electron image of the surface. These two facts have enabled to conclude, that the surface of silicon under oxide had strongly disordered structure close to finely polycrystalline or even amorphous. If to consider, that mechanical pressure decrease deep into silicon under the law  $1/r$ , it is possible to conclude, that more disordered layer adjoins directly to the silicon dioxide. Thickness of these layers are proportional to thickness grown up oxides, that it is possible to explain increase mechanical pressure on border of section at increase in thickness of oxides.

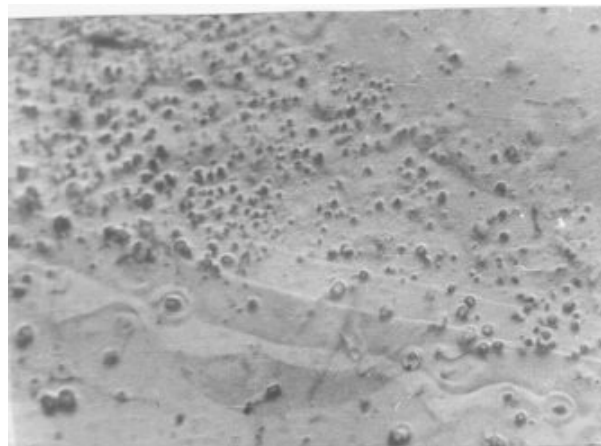


Fig. 1. Optical image of silicon surface (microscope MMR-2P)

At the further etching of a silicon surface (till 3 minutes) were revealed dislocation network (a dislocation density make up to  $10^{10} \text{ m}^{-2}$ ), which have included 60° and partial dislocations and were decorated oxygen (fig. 2). The appeared typical structural defects testify to occurrence of normal crystal structure Si. After 5 minutes etching separate dislocations and glide lines appeared instead of dislocation networks (fig. 3).

In confirmations such complex structure of silicon near-surface region X-ray diffraction method was

made. X-ray diffraction method has shown that near-surface layers of silicon consist of some one which has different structure. Rocking curves presented on Figs. 4a, 4b. The slope of a curve change is explained to presence of the second reflective layer. By means of Gaussian function approximation was determined the maximum and the half-width of “little” curve that could calculate other parameters of silicon. The shift of maximum and the curve broadening comparative the ideal standard specimen are determined of some physical causes such as the macrostress and the microstress. Macrostress are counterbalanced in volume of all samples and cause the diffraction maximum shift and for this one we have such expression as [3]:

$$\frac{\Delta d}{d} = \frac{\beta}{4tg\theta}, \quad (1)$$

where  $\Delta d/d$  – the relative deformation of lattice constant,  $\beta$  – the half-width of the curve,  $\theta$  – the angle of reflection.

Microstresses are caused by polycrystalline structure and they can be associated with dislocations. And for this stress we have such expression as

$$D = \frac{\lambda}{\beta \cos\theta}, \quad (2)$$

where  $\lambda$  – the wavelength, we calculated  $D$  – the crystallite size.

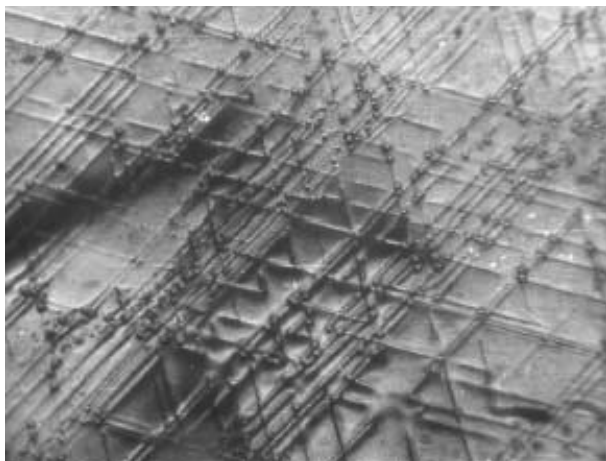


Fig. 2 The electronic image of dislocation networks (1x2300)



Fig. 3 The electronic image of separate dislocations

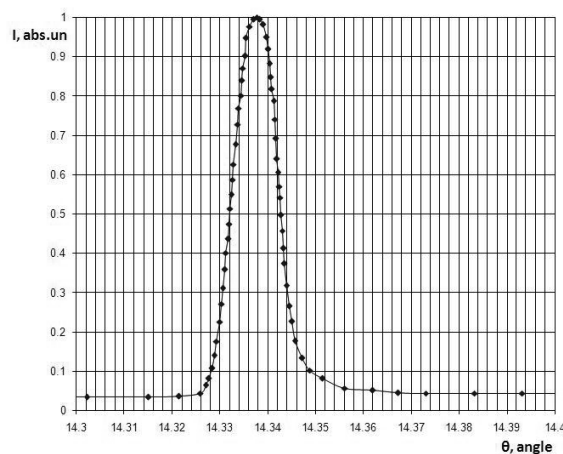


Fig.4 a. The rocking curve (oxide thickness 0.15 micron)

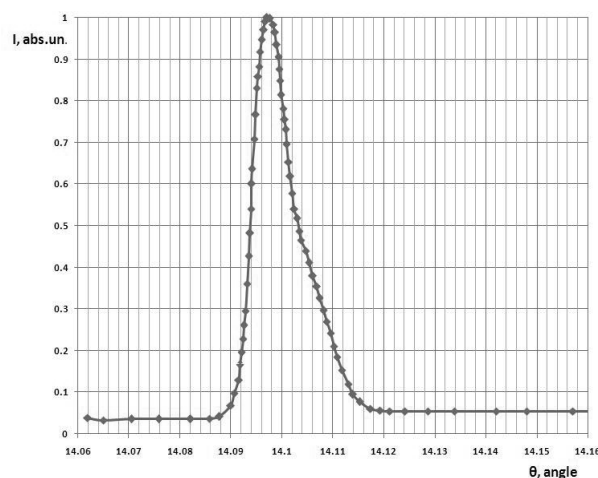


Fig.4 b. The rocking curve (oxide thickness 1.5 micron)

Generally the width of lines depends also on clearly geometrical factors of conditions of shooting, from divergence of a bunch, incomplete splitting of a doublet.

Thus, on broadening of spectral line it is possible to define structural features of a studied crystal. The made calculation of parameters for second curves (Fig. 3 b) has shown the following:

Table 1

	$\Delta a$ (the change of lattice constant) [Å]	$\sigma$ (the stress) [dyne/cm <sup>2</sup> ]	D (the crystalline size) [micron]
The main maximum	0,013	2,2 109	0,87
The “little” maximum	0,019	3 109	0,61

Thereby if we know the curve broadening of 2 orders of reflection for the same reflection plane we can make qualitative evaluation and determine what parameters influence on the curve broadening. Using the following expression

$$\frac{\cos\theta_1}{\cos\theta_2} < \frac{\beta_2}{\beta_1} < \frac{tg\theta_2}{tg\theta_1}, \quad (3)$$

where  $\theta$  – angle of reflection,  $\beta$  – half-width of the rocking curve. We obtained  $1 < 1.11 < 3.35$  Therefore

the layer structure dispersion has the main influence on curve broadening and the near-surface layer of silicon has complex structure and consists of at least two layers, layers differing by thickness and the crystalline sizes.

#### 4. CONCLUSIONS

Thus, proceeding from the received experimental data, it is possible to draw following conclusions:

1. As have shown researches, the near-surface area of silicon in structures silicon - dioxide silicon consists of disordered area adjoining to the silicone dioxide, having complex structure, and the areas containing dislocation networks.

2. The given structure is formed to those residual pressures, caused by the sum of contributions of the interface stresses, and stresses caused by oxygen which diffused deep into silicon in the line of structural defects.

3. More stressed area of silicon adjoins to the interface and leads to dispersivity of this structure. The crystalline sizes increase in process of removal from the interface and pass in not stressed monocrystalline silicon.

4. The depth and block parameters of the given structure depend on dioxide thickness grown up, from quality of initial monocrystalline silicon, from conditions of oxidation.

#### References

1. Красников Г. И., Зайцев Н. А. Система кремний – диоксид кремния в СБИС. М.: Техносфера. — 2003. — 384 с.
2. Рейви К. Дефекты и примеси в полупроводниковом кремнии. — М.: Мир. — 2000. — 471 с.
3. Панов Т. В., Блинов В. И. Определение напряжений в монокристаллах. — Омск, Методическое пособие Омского у-та. — 2004. — 20 с.

UDC 537. 311.33:622.382.33

V. A. Smyntyna, O. A. Kulinich, M. A. Glauberman, G. G. Chemeresyuk, I. R. Yatsunskiy

#### THE STRUCTURE INVESTIGATION OF NEAR-SURFACE LAYERS IN SILICON – DIOXIDE SILICON SYSTEMS

The near-surface silicon layers in silicon – dioxide silicon systems with used modern method of research are investigated. It is shown that these layers have compound structure and their parameters depend on oxidation and initial silicon parameters.

УДК 537. 311.33:622.382.33

В. А. Смынтына, О. А. Кулинич, М. А. Глауберман, Г. Г. Чемересюк, И. Р. Яцунский

#### ИССЛЕДОВАНИЕ СТРУКТУРЫ ПРИПОВЕРХНОСТНЫХ СЛОЕВ КРЕМНИЯ В СИСТЕМАХ КРЕМНИЙ – ДИОКСИД КРЕМНИЯ

В данной работе на основе проведенных с помощью современных методов исследования показана сложная структура приповерхностных слоев кремния в системах кремний – диоксид кремния. Выявлены зависимости параметров этих слоев от условия окислирования и характеристик первоначального кремния.

УДК 537.311.33:622.382.33

В. А. Смынтина, О. А. Кулініч, М. А. Глауберман, Г. Г. Чемересюк, І. Р. Яцунський.

#### ДОСЛІДЖЕННЯ СТРУКТУРИ ПРИПОВЕРХНЕВИХ ШАРІВ КРЕМНІЮ В СИСТЕМАХ КРЕМНІЙ – ДІОКСИД КРЕМНІЮ

В роботі на основі проведених за допомогою сучасних методів досліджень приповерхневих шарів кремнію в системах кремній – діоксид кремнію показано їх складна структура. Показано залежність розмірів цих шарів від параметрів окислення та характеристик кремнію.

## ON THE CHARGE STATE OF RAPID AND SLOW RECOMBINATION CENTERS IN SEMICONDUCTORS

In this work the change of lux-ampere characteristic type from the linear to the super-linear one, being not described in the framework of Rose-Bube model, was registered and explained as the good criterion of the sensitization achieved without the carriers life-time evaluation which could be attributed to developed Rose-Bube-Serdyuk model included the equation of electro-neutrality. Various ratio of S- and R-recombination centers were chosen to be substituted into the equations system and it was shown that the minimal error function corresponding to physically true solution could be achieved by the proper choice of experimental parameters.

Double-level model, proposed by A. Rose and R. Bube [1, 2] explains qualitatively semiconductor photosensitivity enhancement phenomenon at the presence of slow recombination centers. But, as this model is only half-phenomenological one, the following should be attributed to the shortcomings of the model mentioned above:

1. **Coordination influence.** In accordance with Buger-Lambert law, the intensity of the light penetrating into crystal decreases with depth exponentially. The phenomena, mentioned in Section 5 of the present paper, should become apparent in the volume of the crystal when the number of photons absorbed in the chosen layer, becomes equal to and even lower than the number of recombination centers in the same layer. The influence of this factor is diminished during longitudinal conductivity registration but could be determinative in case of transversal contacts placement.

2. **Relaxation phenomena.** The hole, dislodged from the center of the second class (rapid recombination center-RRC) as the result of infra-red (IR) photon absorption, could not be captured immediately by RRC. Besides, there is the possibility of repetitive returns of photo-excited hole to the starting center. All these could initiate the quenching process. The relaxation could be stimulated as well by the migration processes, presented in Section 4.

3. **Concentration dependence.** We have not mentioned yet during the discussion of photo-sensitivity problem about the relationship between the concentrations of centers of 1<sup>st</sup> and 2<sup>nd</sup> types. It is evident that the model should not work while the concentration of the recombination centers of each type will be infinitesimally low. But, even if the concentrations are comparable, the situation will be quite different depending on its absolute value in comparison to the number of absorbed photons. As to the concentration of the local centers, it could be different as well in various parts of the crystal, as it is mentioned in Section 4.

4. **Migration correction.** The recombination centers change their charge state during capture and release of free charge carriers. As the measurement is carried on at the presence of electric field, this field should influence the processes of charge exchange. The recombination centers migrate slowly but steadily. This effect was studied experimentally in [3]. The

relationship between each type of centers is different for each region of the crystal, especially for near-anode and near-cathode ones.

5. **Lux-ampere characteristic.** The intensities of both light fluxes –intrinsically absorbable and IR ones, are not discussed in A. Rose approach at all [1]. The paradox appears when one considers the case when one of the sources is turned off but the model still works. The peculiarities of lux-ampere characteristics are not mentioned despite their possible non-linearity.

6. **Charge carriers balance.** The balance between charge carriers (electrons and holes) and recombination centers of both types is not considered at all. But, all the particles, as well as the centers, are charged while the centers could even change their charge. That's why it is necessary to take into account all the participants of sensitization process. Otherwise, the crystal's electric neutrality may be violated. But, the latest is impossible due to the claim of the fundamental law of electric charge conservation in closed systems.

Certain interest could be attributed as well to the studies in charge state of recombination centers. Rose-Bube model [1, 2] of photo-current IR quenching is being based on the assumption, that two types of recombination centers (RC) presence in the crystal under consideration (RRC and SRC). The most probable realization of RRC is the external doping atom (e.g. Cu in Cd sublattice of CdS crystal) [4]. This dopant, as well as of any other type, could penetrate the crystal in a neutral state only. If it is the hole-capturing center, it should have two charge states – neutral and positively charged ones after the hole capture. After the hole capture, the cross-section value of the center becomes equal to  $10^{-16} \text{ cm}^2$  [1, 2] as compared to  $10^{-15} \text{ cm}^2$  [4]. Such cross-section values are typical for capture processes with the participation of neutral trapping centers.

But, the cross-section value for electron trapping is much smaller –  $10^{-21} \text{ cm}^2$  [1, 2] should be considered as the regular one for the repulsive center. Thus, at the moment of electron capture, the center is charged negatively. In such a case, it is an acceptor type center. It has expelled the hole and become charged negatively. It is the attractive center for holes and should have

the corresponding cross-section value  $\sim 10^{-12} \text{ cm}^2$  [5], which was not registered in experiment.

Thus, one meets the contradiction between the arguments on the charge state of RR centers whether it is a change from neutral to positive state or from neutral to negatively charged state, and this couldn't be met simultaneously.

It is necessary to assume that such a charge states are changing in the presence of the additional intermediate states. The simple scheme realized when the neutral acceptor releases the hole with consequent electron capture, requires that the hole should be captured on doubly negatively charged center at the final stage that was not registered as well.

As to SR centers, it should be mentioned that the experimental data on their charge state are absent in the literature sources up to now. That's why it is almost impossible to make any rational assumption based on the simple analysis of cross-sections for electrons and holes capturing events. It is the equality of cross-sections values, proposed in Rose-Bube model [1, 2], that make the centers under investigation to be effective channels of recombination.

But, in this case, if the centers were neutral at the first stage of the recombination process, then they become positively charged after the finish of the process. And, almost with equal probability, they acquire the excess negative charge after the electron capture on SR centers.

The sequence of carriers captures is not discussed at all in Rose-Bube model [1, 2]. The scenario of these processes is not discussed in literature as well. From the peculiarities of RR centers field drift in the known polarity of applied bias, the assumption of their positive charge was proposed in [3]. The author has studied the sample properties as well as their change under the long-term electric field application. The local probe characteristics of sensitization were studied afterwards [4]. It was shown that the most effective IR quenching of photo-current was registered in the near-cathode zone.

It should be noted that the electronic traps' properties are attributed commonly to RR centers [4]. In this case, the recombination centers could be either neutral or negatively charged. So, it is quite obvious that the question of the recombination centers charge state remained open and requires further resolution.

## MODEL AND DISCUSSION

We have made an attempt to correct some of the contradictions mentioned above in the Rose-Bube model [1, 2].

The interaction of the charge carriers with the local recombination centers in the framework of double-level photo-current quenching model by Rose-Bube is described by the equations:

$$S_{n_1} \nu p_1 n = S_{p_1} \nu n_1 p \quad (1)$$

$$S_{n_2} \nu p_2 n = S_{p_2} \nu n_2 p \quad (2)$$

$$n = f \tau_n = \frac{f}{S_{n_1} \nu p_1 + S_{n_2} \nu p_2}, \quad (3)$$

where  $S_{ij}$  – corresponding cross-sections for electrons and holes capture on the centers of *R*- and *S*-type,  $p$  and  $n$  – free charge carriers concentrations,  $p_1, p_2, n_1, n_2$  – concentrations of electrons and holes captured, on the recombination centers of 1<sup>st</sup> and 2<sup>nd</sup> types (RRC and SRC) correspondingly,  $f$  – photo-excitation intensity,  $\tau_n$  – life-time of intrinsic charge carriers.

The first two equations show the capture rates equality for holes and electrons on SR and RR centers, the third is the condition of the charge non-accumulation.

It is assumed that, hereby, that the specimen resistance is high enough and that the photo-excitation intensity is high enough too.

Under these conditions, the values of concentrations included into equations system (1)-(3), correspond to the non-equilibrium carriers and that the life-time of equilibrium carriers obeys the equation (3).

The number of variables in the system (1)-(3) could be minimized, taking into account that at high intensity of excitation, the number of free charge carriers in volume unit (concentration) becomes comparable and even higher than the recombination centers' concentration. No trap remains inactive in such a case.

As the recombination centers could be occupied, according to their nature, either by electron or by hole, the following equations are effective:

$$n_1 = N_1 - p_1 \quad (4)$$

$$n_2 = N_2 - p_2 \quad (5)$$

where  $N_1$  and  $N_2$  – total concentrations of SR and RR centers, correspondingly.

With the purpose of the (1)–(5) system solution, the system should be equipped with the condition of electro-neutrality. This makes the Rose-Bube model to be transferred into Rose-Bube-Serdyuk model. The form of this condition depends on the possible charge states for all types of recombination centers.

Only four experimentally different cases are possible:

If R-centers are charged positively, the electro-neutrality equation could be presented as follows:

$$n = p + p_1 + p_2 \quad (6a)$$

for positively charged S-centers or

$$n + n_1 = p + p_2 \quad (7)$$

for negatively charged ones.

Taking into account (4), equation (7) could be rewritten as follows:

$$n = p + p_1 + p_2 - N_1 \quad (6b).$$

If R-centers are charged negatively, the corresponding electro-neutrality conditions could be presented as follows:

$$n + n_2 = p + p_1 \quad (8)$$

for positively charged S-centers and

$$n + n_2 + n_1 = p \quad (9)$$

for negatively charged S-centers.

With the account of (5), the expression (8) could be transferred to the following form:

$$n = p + p_1 + p_2 - N_2 \quad (6c)$$

And, using (5) along with (6), equation (9) could be rewritten as:

$$n = p + p_1 + p_2 - N_1 - N_2 \quad (6d).$$

With the scope to simplify the proposed approach as a whole, the possible variants of electro-neutrality conditions are presented in the Table 1.

Table 1

Local levels	R-centers		
	Charge	+	-
S-centers	+	$n = p + p_1 + p_2$ (6a)	$n = p + p_1 + p_2 - N_2$ (8) → (6c)
	-	$n = p + p_1 + p_2 - N_1$ (7) → (6b)	$n = p + p_1 + p_2 - N_1 - N_2$ (9) → (6d)

Without the detailization of the processes occurring, we have resolved four equations-containing system (6a)–(6d) added with (1–3) and (4–5). The unknown values are denoted by  $n_1$ ,  $n_2$ ,  $p_1$ , and  $p_2$ .

It is well known that the system of algebraic equations, containing four equations for four unknown values, has unique solution only. It was stated, also, that for negatively charged R-centers, the system under investigation has no positive solutions for both types of centers charge (6c)–(6d) and electro-neutrality conditions.

For example, the negatively charged recombination centers of 2<sup>nd</sup> type and positively charged centers of the 1<sup>st</sup> type in conditions of:

$$f = 10^{15} \text{ cm}^{-3} \text{ c}^{-1}; N_1^+ = N_2^- = 10^{15} \text{ cm}^{-3}$$

the system (1)–(3) and (6d) has the unique solution:

$$n = 1,005 \cdot 10^{15} \text{ cm}^{-3}; p = 4,988 \cdot 10^7 \text{ cm}^{-3}; \\ p_1 = -4,963 \cdot 10^7 \text{ cm}^{-3}; p_2 = -4,987 \cdot 10^{12} \text{ cm}^{-3}$$

and the error function F (see later, please) was about  $7.7 \times 10^{-6}$ .

This means that, in the framework of the Rose-Bube model, S-centers couldn't be charged negatively. This result correlates well with the value of hole capture cross-section. But, the question how the electron cross-section for these centers is being formed, remains to be open.

In the case of positively charged R-centers and S-centers, the system of equations, after transformation, obtains the following form:

$$n \cdot p_1 = p (N_1 - p_1) \quad (10)$$

$$n \cdot p_2 = A \cdot p (N_2 - p_2) \quad (11)$$

$$B = A n \cdot p_1 + n \cdot p_2 \quad (12)$$

$$n = p + p_1 + p_2, \quad (13)$$

where  $A = S_{p_2}/S_{n_2} = 10^5$ ;  $B = f/(v S_{n_2})$ .

In all cases, the value of carrier velocity was taken equal to  $10^7$  cm/s. Values  $N_1$ ,  $N_2$  and  $f$  could be considered as parameters for the system (10)–(13). Each of these numbers could take the value in the wide range  $10^{12} - 10^{18}$ .

Thus, following paper [1], we have used such a tactics: concentration of S-centers was fixed at the level of  $10^{15} \text{ cm}^{-3}$  and the value of  $N_2$  was changed in the

range of  $10^{14} - 10^{16} \text{ cm}^{-3}$ . The system of equations was solved some times for different levels of excitation intensity  $f = 10^{14}$ ,  $10^{15}$  and  $10^{18} \text{ cm}^{-3} \text{ s}^{-1}$  (these values were chosen as being lower, equal and much higher than R-centers concentration).

Certain asymmetry of the chosen  $f$  values as compared to  $N_1$  could be explained as being due to the fact that the system (1)–(3) is written for high excitation level. It could be obtained from (12) that:

$$p_2 = B/n - A \cdot p_1 \quad (14)$$

and, from (10) – equivalently:

$$p = (n \cdot p_1)/(N_1 - p_1) \quad (15).$$

After dividing (10) by (11), one could obtain:

$$p_1/p_2 = (N_1 - p_1)/[A(N_2 - p_2)] \quad (16)$$

and

$$p_2 = (AN_2 p_1)/[N_1 + p_1(A - 1)] \quad (17).$$

Common solution of (14) and (17) gives:

$$p_1^2 A(A-1) + p_1[A(N_2 + N_1) - (B/n)(A-1)] - (BN_1)/n = 0$$

The corresponding solution of this quadratic equation has the form:

$$p_1 = \frac{-D + [D^2 + 4A(A-1)(B/n)N_1]^{1/2}}{2A(A-1)}, \quad (18)$$

where  $D = [A(N_2 + N_1) - (B/n)(A-1)]$

The sign “-“ before the root in (18) is neglected because it leads to  $p_1 < 0$  which is non-physical. The equations (14)–(15)–(18), after substitution into (13), give the equation with only one unknown value:

$$n = (n p_1)/(N_1 - p_1) - p_1(A-1) + B/n, \quad (19)$$

where  $p_1$  is not presented at all in full accordance with (18).

It is evident that the obtained expressions are too complex for analysis.

As, after  $p_1(n)$  substitution, the structure of expression (19) has the form of:

$$f_1(n + 1/n) = f_2(n + 1/n)^{1/2}$$

It could be stated that one should meet, at least, the equation of the 4<sup>th</sup> exponent order on the unknown  $n$ . The complications arisen from algebraic way of the system solution were, at us, the cause of non-performance of such an analysis before. We have rejected the algebraic approach to the system (10)–(13) solution and propose, instead, the following artificial approach.

The value  $n$  is chosen arbitrarily. Using equation (18), the  $p_1$  value is determined. Then, one, knowing  $p_1$  and  $n_1$  and using (14)–(15), determines  $p_2$  and  $p$ . Afterwards, all four numbers are substituted into starting system of equations and the error function is determined (see (10)–(13)):

$$F = \frac{p(N_1 - p_1)}{n \cdot p_1} + \frac{A \cdot p(N_2 - p_2)}{n \cdot p_2} + \frac{An \cdot p_1 + n \cdot p_2}{B} + \frac{p + p_1 + p_2}{n} - 4. \quad (20)$$

We propose, then to minimize the error function through changing  $n$  value. The number 4 is included into equation (20) for the case of precise solution when  $F = 0$ .

The peculiarity of function (20) lies in that not the traditional differences between left and right parts of the equation are used but the result of their dividing is proposed to use. This detail was used because there are the multiplications of concentrations that are included into first three equations of the system (10)–(13).

In such a case, the difference between left and right parts of the equation (13) will be much less (up to 15 orders of magnitude) as compared to other inputs into error functions, being at the edge of computer zero.

It is interesting, also, to mention that this equation contains the details concerning the charge state of the local centers. Besides, using the proposed approach doesn't require to search the error function sign in each equation. The attractive feature of the proposed approach lies in the possibility of simultaneous determination for all unknown parameter values.

According to the methodology of [1], we have studied the level of photo-sensitization, using the changes of the intrinsic charge carriers life-time, which was determined using both center types hole filling numbers:

$$\tau_n = \frac{1}{Sn_1 p_1 v + Sn_2 p_2 v}. \quad (21)$$

The results of the calculations are presented in Fig.1. It is seen that, if the centers of both types are charged positively, the sensitization process starts at R-centers, which are presented in concentration by two orders lower than that of S-centers. Independently on photo-excitation level, the carriers' life-time value increases by two orders of magnitude when R-centers concentration increases by two orders as compared to the concentration of S-centers. Dotted line in Fig. 1 shows the S-centers concentration value.

As we do obtain, as a result of the discussed problem solution, S-centers concentration  $N_1$  as well as the holes captured at R-centers one  $-p_1$ , one could determine the part of the centers captured positive charge.

Depending on the photo-excitation conditions  $f$  and center concentration  $N_2$ , the ratio  $p_1/N_1$  was in the range of 1–3%.

It should be noted that such S-centers, according to Fig. 1, could provide  $\tau_n$  increase by some orders only. We could consider the sensitization of such a type to be a weak one and the non-effective channel of photo-sensitivity enhancement. Nevertheless, it exists and is in grade to add certain corrections into the processes under investigation.

It is been exposed most distinctively at the lower edge of the parameters determination, e.g. at the lower levels of photo-excitation and low concentration of recombination centers of 2<sup>nd</sup> type, when Rose-Bube mechanism of photo-sensitization is not switched on yet.

For the situation, when positively charged R-centers are combined with negatively charged S-centers, the equations system in accordance with (1)–(3)–(6d) obtains the form:

$$n \cdot p_1 = p (N_1 - p_1) \quad (22)$$

$$n \cdot p_2 = A \cdot p (N_2 - p_2) \quad (23)$$

$$B = A n p_1 + n p_2 \quad (24)$$

$$n = p + p_1 + p_2 - N_1. \quad (25)$$

This system differs from the system (10)–(13) formally by the last term of the fourth equation only. But, the result of the (22)–(25) system solution is totally different.

We would like to mention the additional complication caused by the fact that the system solution in the range  $N_2 \sim N_1$  becomes the stochastic one because the concentration change at the second point after comma stimulates the carriers life-time change up to two orders of magnitude (see Fig. 2). It has to be taken into consideration, during the calculation step value's choice for the 2<sup>nd</sup> type centers concentration.

We have used the same methodology as the described earlier one. The results are presented in Fig. 2. As it was established experimentally, in a sufficiently reliable manner, that the intrinsic charge carriers life-time is changed by 4–5 orders of magnitude in sensitized CdS [1–4]. From the comparison of Fig. 1 and Fig. 2 data, it follows that such a change could occur only when the centers of the 1<sup>st</sup> type are charged negatively and the non-equilibrium electrons are being captured by neutral centers.

The electro-neutrality equation has the form of (6b). We would like to mention the detail, which was not described in [1]. The significant sensitization should be awaited for comparatively low photo-excitation level. When this level is increased, as seen in Fig. 2, the upper part of the plot at  $N_2 \gg N_1$  is displaced to the bottom part of the plot while the lower part of the same plot at  $N_2 \ll N_1$  moved in the opposite direction. As the result, the difference step of carriers life-time value after sensitization becomes lower by the orders of magnitude. Thus, the effect of sensitization diminishes.

This fact gives the proper explanation of the results obtained, if one takes into account that at high photo-excitation level, the carrier concentration is also high. The introduction of the sensitization dopant couldn't change it significantly.

It was cleared as well, that the equation system (1)–(3) added with one of the electro-neutrality conditions (see Table 1), is especially sensitive to the value of the last terms in equations (6a)–(6d). The limiting value, when the system has parameters with physically meaningful values, is about  $10^{15} \text{ cm}^{-3}$ .

This may be the value of  $N_1$  concentration in equation (6c) or  $N_2$  one in (6b) equation, or their sum ( $N_1 + N_2$ ) in expression work (6d) (see, please, Table 1).

It should be noted that exactly this value was used in A. Rose pioneer work [1] without any comments. As the sensitization was described at the semi-phenomenological level and the condition of electro-neutrality was not used at all, the numbers, introduced previously, were fetishized a little bit.

As a result of the discussion, proposed above, one could realize the specific significance of S- and R-centers' concentration value.

In the range of the photo-excitation levels, used in our experiments, and at the recombination centers concentration being lower than  $10^{15} \text{ cm}^{-3}$ , the photo-sensibilization doesn't occur at all. When this level is achieved, (see, Table, please), the sensibilization becomes real but remains still insignificant (Fig.1), while the number of centers able to participate doesn't determine the rate of the process.

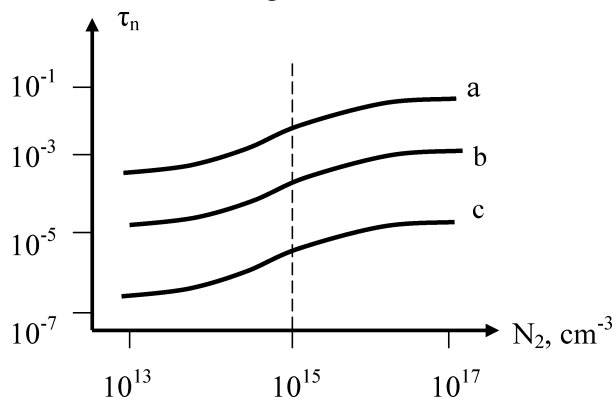


Fig. 1. The change of electrons life-timed under increase of R-centers concentration for the excitation levels: a —  $10^{14}$ , b —  $10^{15}$ , c —  $10^{17} \text{ cm}^{-3} \cdot \text{c}^{-1}$

Under the concentrations exceeding the threshold value of  $10^{15} \text{ cm}^{-3}$ , the equations system solution finds itself in the negative region, having no physical sense (see the 2<sup>nd</sup> row of the Table).

But, at the narrow range of these concentrations, the avalanche type increase of carrier life-time value is possible (Fig. 2). This effect is possible for positively charged R-centers and negatively charged S-centers (see the 1<sup>st</sup> row of the Table).

The results obtained eliminate the contradictions existing between the statements proposed by Rose-Bube model [1, 3, 4]. The properties of S-centers are such that they, being in neutral state, are able to trap both electron and hole with almost equal capture cross-section  $\sim 10^{-15} \text{ cm}^2$ . As the result, there are both positively and negatively charged centers of the 1<sup>st</sup> type. The presence of the last ones was detected experimentally and reported in [3]. But, as the semiconductor material under consideration is of n-type, simple overwhelming of the electron density provides the greater number of their captures and the sensitization occurs mainly in scenario of Fig. 2 as reported in [1].

The view of Fig. 1 and 2 as well as their comparison allow to predict the lux-ampere characteristic type for both channels of sensitization. For fixed values of centers concentrations  $N_1$  and  $N_2$ , in the case, when the positively charged S-centers are engaged (Fig.1), the photo-excitation intensity increase causes almost the same life-time value decrease. This fact should assist to form the lux-ampere characteristic of the linear type. Analogously, for negatively charged S-centers (Fig.2), after the sensitization, (to the right from punctured line), the carriers' life-time decreases with the increase of the photo-excitation level.

Besides, the multiplication of these values  $n = \bar{f} \tau_n$  remains almost the same as to the order of value. One could expect that the lux-ampere characteristic to be quite linear what was registered in our experiments [6].

At the lower part of the plot, presented in Fig. 2, in the region where  $N_2 \ll N_1$  and the sensitization has

not occurred, the carriers' life-time increases with the increase of the photo-excitation intensity. It should cause the super-linearity of LAC. The change in this characteristic could serve as the additional justification of the negatively charged S-centers domination over positively charged ones in the crystal under investigation.

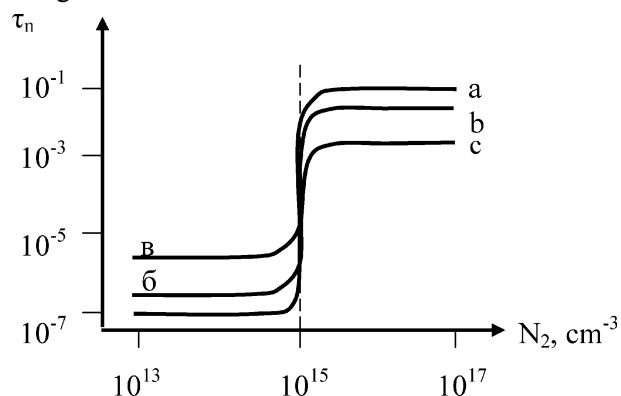


Fig. 2. The change of electrons life-timed under increase of R-centers concentration for the excitation levels: but then calculation is performed for the negatively charged centers of the first class

It is quite difficult to observe experimentally the change of the LAC, predicted above, as a function of R-centers concentration because the structurally identical but differently doped specimens are needed or the dopant should be added to same crystal as the alternative. Both ways are equally non-real from the experimental point of view.

The first approach is forbidden by the existence of statistical errors in crystal parameter values for the specimens taken even from the same technological group.

The second approach is also non-reliable because the initial dopant distribution is changed significantly during the additional dopant introduction to say nothing of the additional S-centers forming substances. The crystal becomes quite non-adequate as to its starting state.

But, one could behave otherwise in such a situation. If the intensity of the IR excitation is such that number of the incident photons is comparable and even lower than the R-centers concentration, such an excitation becomes the modulating one. Quanta of IR irradiation, being absorbed at the centers of slow recombination, resists to the process of holes' capture at these centers. As a result, the effective concentration of R-centers, being engaged in the sensitization process, becomes lower. The part of such centers for the same crystal becomes as lower as the IR irradiation intensity acting on the crystal enhances.

The family of the lux-ampere characteristics obtained in CdS crystal with IR-quenching effect being irradiated with the intrinsic light ( $\lambda = 520 \text{ nm}$ ) is shown in Fig.3. The intensity of IR light was taken to be the parameter.

As the influence of the excited R-centers [2] could be superimposed over the sensitization processes, we have used the multiplicative wavelength spectrum starting from 900 up to 1400 nm. The exciting short-wave irradiation was the monochromatic one.

As it is seen from Fig. 3, IR irradiation diminishes the photo-current absolute value, which could be considered as the IR-quenching process, but increas-

es the degree of plot non-linearity. With the scope of curves comparability convenience, the two limiting cases are presented at the smaller part included into Fig.3, while the curve *a* corresponds to IR irradiation off (curve 1, Fig. 3) and curve *b* – to the highest level of IR irradiation (curve 3, Fig. 3).

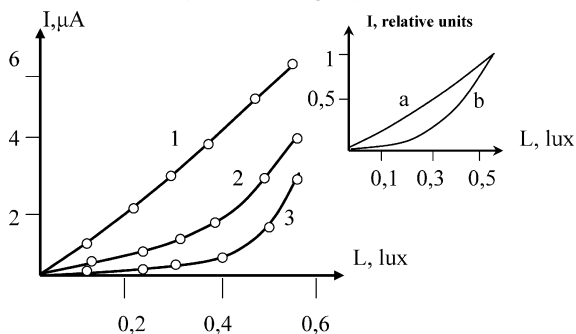


Fig. 3. The photo-current changes in conditions of combined excitation at IR irradiation: 1 – 0; 2 –  $3,0 \cdot 10^{-3}$ ; 3 –  $1,4 \cdot 10^{-2}$  lux

## CONCLUSIONS

1. We have registered and explained the change of lux-ampere characteristic type from the linear to the super-linear one, which was not described in the framework of Rose-Bube model [1], as the good criterion of the sensitization achieved without the carriers

UDC 621.315.592

### ON CHARGE STATE OF RAPID AND SLOW RECOMBINATION CENTERS IN SEMICONDUCTORS

E. V. Britavsky, Y. M. Karakis, M. I. Kutalova, G. G. Chemeresyuk

In this work the change of lux-ampere characteristic type from the linear to the super-linear one, being not described in the framework of Rose-Bube model, was registered and explained as the good criterion of the sensitization achieved without the carriers life-time evaluation which could be attributed to developed Rose-Bube-Serdyuk model included the equation of electro-neutrality. Various ratio of S- and R-recombination centers were chosen to be substituted into the equations system and it was shown that the minimal error function corresponding to physically true solution could be achieved by the proper choice of experimental parameters.

УДК 621.315.592

### О ЗАРЯДОВОМ СОСТОЯНИИ ЦЕНТРОВ БЫСТРОЙ И МЕДЛЕННОЙ РЕКОМБИНАЦИИ

Е. В. Бритавский, Ю. Н. Каракис, М. И. Куталова, Г. Г. Чемересюк

В настоящей работе изменение вида люкс-амперной от линейного до суперлинейного, который не описывался в рамках модели Роуза-Бьюба, было зафиксировано и объяснено как хороший критерий достигнуть очувствления без проведения расчетов времени жизни носителей, что имеет место в расширенной модели Роуза-Бьюба-Сердюка, содержащей уравнение электронейтральности. Различные соотношения S- и R- центров рекомбинации были выбраны для подстановки в систему уравнений, и видно, что функция минимальной погрешности, соответствующая физически правильному решению, может быть достигнута при соответствующем выборе параметров эксперимента.

УДК 621.315.592

Е. В. Бритавський, Ю. Н. Каракіс, М. І. Куталова, Г. Г. Чемересюк

### ПРО ЗАРЯДОВИЙ СТАН ЦЕНТРІВ ШВИДКОЇ ТА ПОВІЛЬНОЇ РЕКОМБІНАЦІЇ.

В роботі зміна характеру люкс-амперної характеристики від лінійного до суперлінійного, який не роз'яснювався в межах моделі Роуза-Бьюба, була зафіксована і пояснена як якісний критерій підвищення чутливості без проведення розрахунків часу існування носіїв, що має місце у розгорненій моделі Роуза-Бьюба-Сердюка, рівняння электронейтральності. Різні співвідношення S- і R- центрів рекомбінації були обрані для підстановки в систему рівнянь, і зрозуміло, що функція мінімальної помилки, яка відповідає вірному рішенню, може бути досягнута при відповідному виборі параметрів дослід.

life-time evaluation which could be attributed to developed Rose-Bube-Serdyuk model, which includes the equation of electro-neutrality [5].

2. The mathematically consistent solution of the equations system added with the electro-neutrality condition was proposed and discussed as the basis of Rose-Bube-Serdyuk model [5].

3. Various ratio of S- and R-recombination centers were chosen to be substituted into the equations system and it was shown that the minimal error function corresponding to physically true solution could be achieved by the proper choice of experimental parameters.

## Literature

1. *Rose A.* Basics of Photo-Conductivity Theory. — Moscow, MIR Publishers. — 1966. — 192 p.
2. *Bube R.* Photo-Conductivity of Solids. Moscow, Foreign Literature Publishers. — 1962. — 558 p.
3. *Victor P. A.* Some Peculiarities of Non-Homogeneous CdS Monocrystals Photo-Conductivity. Ph. D. Thesis Dissertation. — Odesa, 1980. — 58 p.
4. *Lashkarev V. E., Lyubchenko A. V., Sheinkman M. K.* Non-Equilibrium Processes in Photo-Conductors (*in Russian*). Kyiv, Naukova Dumka Publishers. — 1981. — 264 p.
5. *Serdyuk V. V., Chemeresyuk G. G., Terek M.* Photo-Electric Processes in Semiconductors. Kyiv, Naukova Dumka Publishers. — 1982. — 151 p.
6. *Novikova M. A., Karakis Yu. M., Kutalova M. I.* Particularities of Current Transfer in Crystals with Two Types of Recombination Centers. Photoelectronics. — 2005, N 14. — P. 58–61.

## INFLUENCE OF ELECTRIC FIELD ON PHOTOLUMINESCENCE OF POROUS SILICON

Relation between porous silicon photoluminescence and thermoelectric properties was established. The influence of the electrical field on the photoluminescence intensity of porous silicon layers and spectra were studied. The photoluminescence spectra analysis shows the presence of the mechanisms set of charge recombination in porous silicon. The model of light emission from porous silicon is proposed.

### INTRODUCTION

The discovery of the visual light radiation from porous silicon (PS) made by L. Canham in 1990 has stimulated the intensive studies of silicon nano-dimensional structures with the scope of possible fabrication of light emitting optoelectronic devices on their basis. Although most of scientists consider that radiative recombination of charge carriers occurs in silicon nano-crystallites which electronic spectrum is modified by quantum-dimensional effect, there are different views about peculiarities of the recombination mechanism [1, 2]. The possibility of direct recombination of electrons and holes both in volume and at surface states of nanostructure, as well as the radiative annihilation of excitons were discussed. Moreover, the main contribution to the luminescence of PS is assumed to be connected with the processes of optical excitation and relaxation in the molecular cover of nano-crystallites [2]. Investigation of photoluminescence (PL) spectra can provide information about electronic structure, mechanisms of light absorption and charge carrier recombination and contributes to the better understanding of PL nature.

### MATERIALS AND METHODS

For investigation of light emitting properties of PS we used samples with different thickness of porous layers (5–20  $\mu\text{m}$ ) and different degree of porosity (20–70%) which had been obtained on silicon substrates of both *n*- and *p*- types of conductivity. The formation of PS layers was performed by standard technique of electrochemical anodization in the galvanostatic regime. The photoluminescence was excited by pulse nitrogen laser LGI-21 with a radiation wavelength of  $\lambda=337$  nm and a pulse duration of 8 ns. Light radiation of PS was recorded through optical filter JS-17 that cuts off the plasma emission with the help of MDR-12 and photomultiplier FEP-77. Measurements of PL spectra were carried out both in vacuum and on air, however the substantial difference between these spectra was not observed.

### RESULTS AND DISCUSSION

The PL spectra possess the bands with the shape being approximately of Gauss-type and width of about

200 nm and maximum in the 620–730 nm range. The radiation intensity, as well as the maximum position, varies from sample to sample depending of the technological conditions of PS fabrication and environmental details. Analysis of PL spectra has demonstrated the superposition of two bands with maxima in the energy range of 1.94–2.0 eV and 1.65–1.75 eV. Such a character of the PL spectra could be explained not only by quantum-dimensional effects in the system of nano-crystallites, but also by the influence of localized surface states in the forbidden gap of PS.

The studies of PL spectra of PS samples subject to polarization by voltage in the range of (1–12 V) at the temperature of liquid nitrogen ( $T = 77$  K) have shown the shift of radiation band maximum location to the short wavelength range (Fig. 1), with the PL band being narrowed in the longer-wavelength spectral range at the expense of the intensity increase.

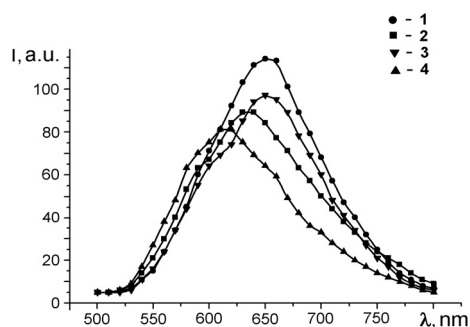


Fig. 1. PL spectra of PS/p-Si (1, 2) and PS/n-Si (3, 4) structures in the case of excitation by nitrogen laser: initial samples (1, 3), after polarization at nitrogen temperatures— (2, 4)

The correlation between the intensity of longer-wavelength region of PL spectra and the thermo-electret properties of porous silicon has been observed [3, 4]. Decrease of the built-in spatial charge via short-circuit contact at PS surface with silicon substrate gives rise to decrease of the intensity of longer-wavelength region of PL spectrum and to the shift of the maximum location towards the larger energies (Fig. 2).

In the case of PL spectra measurement, after prolonged (5 days) exposure in the short-circuit regime, the registered radiation intensity was lower, as well as the further shorter-wavelength shift of the PL band

maximum by  $\Delta\lambda = 20$  nm as related to the initial position of spectral maximum was observed.

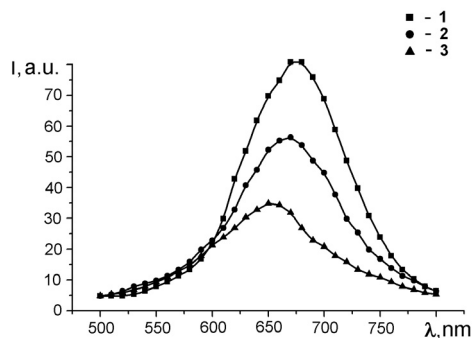


Fig. 2. PL spectra of PS / n-Si structures: initial sample- (1), after compensation for built-in charge at PS surface by means of short-circuit for 1 hour - (2), 5 days - (3)

The shift of PL spectral maximum for PS layers one could logically relate to the action of the near-surface electric field. For this hypothesis check-up, the investigation of PL spectra in the case of application of both forward and reverse biases has been carried out. The change of light emitting spectrum of PS/p-Si structure possessing minimum built-in charge under the influence of external potential is shown at Fig.3.

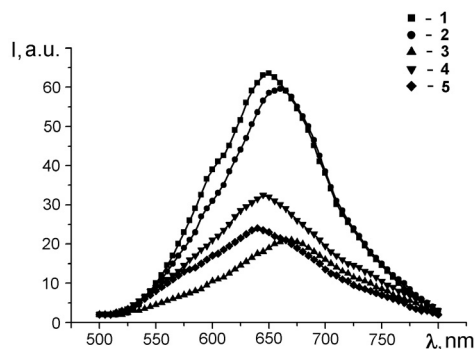


Fig. 3. PL spectra of PS/p-Si structure under the influence of external potential: 1 – initial sample; 2 – reverse bias 20 V (current through the structure  $I = 8$  mA); 3 – reverse bias 40 V ( $I = 26$  mA); 4 – forward bias 30 V ( $I = 12$  mA); 5 – forward bias 30 V ( $I = 4,5$  mA) after total quenching of PL

In the case of positive potential application (reverse bias), PL intensity decreases, and the band maximum shifts towards the long wavelength spectral range by  $\Delta\lambda = 10 \div 15$  nm (curves 2 and 3). The increase of the voltage, gives rise to enhancement of the current through the structure and substantial quenching of the PL. In the case of changing the applied voltage polarity (to forward bias), the shift of the PL maximum into the short wavelength range by  $\Delta\lambda = 5 \div 10$  nm relatively to the PL maximum of initial sample (curves 4 and 5) has been observed. Increase of the voltage difference up to 50 V causes the sharp increase of the current through the structure from 29 mA in the initial time moment to 75 mA after several seconds and, finally, results in total quenching of PL. However, the degradation of PL was reversible. PL emission of the PS layers renews to some extent after cessation of sample's polarization. After repeated polarization, the smaller currents

through the structure and somewhat lower intensity of PL were observed.

## MODEL

The presented experimental results could be explained within the framework of the following model. According to the commonly accepted concept, the main absorption of light takes place in the volume of silicon nano-structures which compose the PS layer. A part of conduction band electrons recombines radiatively with holes, localized at nano-crystallite surface, giving rise to formation of radiation band with maximum in the 1.9÷2.0 eV energy range. The radiative recombination of the other part of electrons occurs via the localized states connected with a number of causes, in particular, with the presence of oxygen and hydrogen bonds at the PS surface. Such a type of recombination is responsible for the longer wavelength component of the PL spectrum (with maximum at 1.65÷1.75 eV). The presence of localized states with an activation energy of 0.2÷0.4 eV in the forbidden gap of PS has been registered by independent investigations of thermo-stimulated depolarization [3] and thermo-stimulated conductivity [5] of PS layers.

It should be mentioned that, along with the radiative recombination, the electrons of the conduction band could recombine non-radiatively at broken bonds of silicon or could be captured by deeper traps. The latter explains the observed quantum yield of photoluminescence of up to 10%.

Under the action of electric field, a bend in the energy bands of porous silicon takes place, what, in turn, changes the filling level of localized levels in the near-surface layer. In the case of positive potential at PS, the population of the levels increases, and, as a consequence, the contribution of longer wavelength component of PL increases. When band bending in the near-surface layer causes an exhaustion of the localized states (negative potential at PS), the concentration of emitting centers, capable to take part in the luminescence, could be substantially reduced. Integral intensity of the longer wavelength component decreases and the spectral maximum of radiation is being shifted to the range of larger energies. The observed increase of the PL intensity of PS could be caused both by the passage of electric current and by transformation of emission centers in the channels of non-radiative recombination under the action of large values of electric field strength in nano-dimensional silicon structures.

## CONCLUSIONS

1. The non-elementary nature of PL spectra maxima of PS layers and the large width of their bands indicates not only the diversity of nano-crystallite sizes, but also the manifestation of several mechanisms of recombination. In the PL spectra experimentally obtained, there is a contribution of both the recombination conduction band electrons of silicon nano-crystallites and the radiative transitions via the localized states in the forbidden gap.

2. The electric field could change the population of the localized states; therefore the concentration of such centers, capable to take part in the luminescence, could change substantially.

3. With the electric field effect factor assumption, one could correlate the observed influence of electric field on the intensity and spectral position of the PL band maximum of PS layers.

#### References

1. *Electronic* states and luminescence in porous silicon quantum dots: The role of oxygen / M. V. Wolkin, J. Jorne, P. M. Fauchet, G. Allan, C. Delerue // *Phys. Rev. Lett.*, **82(1)**. — 1999. — P. 197–200.

2. *Bisi O., Ossicini S., Pavesi L.* Porous silicon: a quantum sponge structure for silicon based optoelectronics // *Surface Science Reports*, **38**. — 2000. P. 1–126.
3. *Monastyrskii L. S., Lesiv T. I., Olenych I. B.* Composition and properties of thin solid films on porous silicon surface // *Thin Solid Films*, **343-344**. 1999. — P. 335–337.
4. *Peculiarities* of lovtage-current characteristics of oxidated porous silicon / M. S. Ablova, M. V. Zamoryanskaya, V. I. Sokolov, R. I. Khasanov // *Pis'ma v Zh. Tekhn. Fiziki*, **29(11)**. — 2003. — P. 41–44.
5. *Transport* properties of thermally oxidated porous silicon / L. V. Grigor'ev, I. M. Grigor'ev, M. V. Zamoryanskaya, V. I. Sokolov, L. M. Sorokin // *Pis'ma v Zh. Tekhn. Fiziki*, **32(17)**. — 2006. — P. 33–41.

UDC 621.378.35

I. B. Olenych, L. S. Monastyrskii

#### INFLUENCE OF ELECTRIC FIELD ON PHOTOLUMINESCENCE OF POROUS SILICON

The relation between porous silicon photoluminescence and thermoelectric properties was established. The influence of the electrical field on the photoluminescence intensity and spectra of the porous silicon layers was studied. The photoluminescence spectra analysis shows the presence of charge recombination mechanisms set in porous silicon. The model of porous silicon light emission was proposed.

УДК 621.378.35

І. Б. Оленич, Л. С. Монастирський

#### ВПЛИВ ЕЛЕКТРИЧНОГО ПОЛЯ НА ФОТОЛЮМІНЕСЦЕНЦІЮ ПОРУВАТОГО КРЕМНІЮ

Виявлений зв'язок між спектрами фотолюмінесценції поруватого кремнію і його термоелектретними властивостями. Досліджено вплив електричного поля на інтенсивність і спектральне положення максимуму смуги фотолюмінесценції шарів поруватого кремнію. Аналіз спектрів світловипромінювання вказував на прояв декількох механізмів рекомбінації носіїв заряду в поруватому шарі. Створена модель світловипромінювання поруватого кремнію, яка підтверджується результатами експериментальних досліджень.

УДК 621.378.35

И. Б. Оленич, Л. С. Монастырский

#### ВЛИЯНИЕ ЭЛЕКТРИЧЕСКОГО ПОЛЯ НА ФОТОЛЮМИНЕСЦЕНЦИЮ ПОРИСТОГО КРЕМНИЯ

Обнаружена связь между спектрами фотолюминесценции пористого кремния и его термоэлектретными свойствами. Исследовано влияние электрического поля на интенсивность и спектральное положение максимума полосы фотолюминесценции пористых слоев. Анализ спектров светоизлучения указал на проявление нескольких механизмов рекомбинации носителей заряда в пористом кремнии. Предложена модель светоизлучения пористого кремния, которая подтверждается результатами экспериментальных исследований.

A. V. LOBODA

Odessa National Polytechnical University

## QUANTUM THEORY OF COLLISIONS OF THE ULTRACOLD ATOMS WITH NANOSTRUCTURES

It is developed a generalized energy approach, based on the operator perturbation theory formalism, to collision of ultracold atoms with nanostructures (nanospheres). The preliminary numerical results for atom of He and firstly atom of Li are presented for different potentials of the “atom-sphere” interaction.

One of the great topics of intense current interest (c.f. [1–4]) is a problem of the interaction of cold atoms with each other and with surfaces, walls, nanostructures. Modern technological advances have made it possible to fulfill experiments with atoms at temperatures in the nanokelvin range [1]. At such low temperatures the quantum effects play an important role. Ultracold atoms approaching a flat surface are generally lost through inelastic reactions or adsorption if they come to within a few atomic units of the surface. At low enough energy they can be spared this fate through classically forbidden (quantum) reflection in the distant tail of the potential [2]. If the surface is curved, e.g. spherical, the scattering cross section is sensitive to both modulus and phase of the partial wave S-matrix, and the radius of the sphere can be tuned to probe different regions of the atom-surface potential. In recent paper [2] a scattering of ultracold atoms by absorbing surfaces is studied. Loss of flux through inelastic reactions and adsorption can be described in an unambiguous and model-independent way by incoming boundary conditions in the semi-classical region near the surface. The near-threshold behavior of the scattering amplitude is defined by a few parameters of the potential tail beyond the semi-classical region. Investigation of quantum reflection and scattering by flat and spherical surfaces shows [1–3] that the curvature of the surface strongly influences the range to which the scattering amplitudes are sensitive in the atom-surface interaction. It is worth to underline that now the corresponding estimates and full calculation of the “atom-nanostructure” scattering cross-sections are quite seldom. It is obvious that this topic will be very actual in the nearest decade. The comprehensive solving cited problem requires a development and using the corresponding quantum approaches.

In our opinion, the correct approach to solution of the atom-nanostructures interaction problems must be based on the consistent quantum-mechanical theory of the complicated atom-nanostructure system. One of the effective approaches to the problem has been proposed in ref. [4]. It is based on the operator perturbation theory [5–10] and energy approach to QED theory [11–15]. Let us at once note that a quality of the modelling “atom-nanostructure” potential may have a decisive importance. The variation of parameters of the cited potential within the reasonable limits may lead to the significant quantitative chang-

ing the scattering cross-sections. In our approach the atomic system and nanostructure have been considered on the equal foot as two parts of the complicated system interacting one with another through the model potential. The inner-atomic dynamics has been treated due to Dirac equation with the model potential. The solution of the total electron-nuclear system quantum-mechanical equation is based on the formally exact perturbation theory with the zeroth order Hamiltonian  $H$  of the total system being determined by its energy spectrum and the set of the eigen functions without specifying analytic form of zero order potential [4, 5, 8]. The subsequent corrections of the perturbation theory can be expressed in terms of the matrix elements of total Hamiltonian, calculated between the zeroth order state functions. The approach treats the widely known distorted waves approximation as the zeroth order approximation in the formally exact quantum-mechanical perturbation theory allowing for successive refinement of calculations [5–8]. Here we will use a generalized energy approach to collision of ultracold atoms with nanostructures (nanospheres). The preliminary numerical results for atom of He and firstly atom of Li are presented for different potentials of the “atom-sphere” interaction.

The formulae of the “atom-nanosphere” scattering cross section can be obtained on the basis of the energy approach [5–10]. This approach allows to use the well developed stationary-state methods to the collisional problem with variable number of particles. In such approximation the calculation of the scattering cross-section is reduced to the solution of the ordinary differential equation system, which includes a relativistic quantum-mechanical equations for atomic systems, equations for all matrix elements of perturbation theory. The non-stationary feature of our problem manifests itself in the way of the normalization of the atomic system initial state function. The correct procedure was developed earlier and is in the following. In zeroth order of perturbation theory it is used the hamiltonian generating the same energy spectrum as the potential  $V(R)$  but possessing only stationary states. Further note that contrary to the case of the stationary states we use the alternative principle of quantization of the quasi-stationary states [5,8]. It can be realized by the following procedure: (i) let the trial atomic system state energy to be  $E$  and preset the function norm by the condition  $F(T=0) = 1$ , (ii)

Let's integrate the Dirac equations system (1) under this conditions up to asymptotically large  $T$  with the simultaneous evaluation of [6, 7]:

$$X(E) = \lim_{T \rightarrow \infty} T^{2|x|} \left( (E + 2M\tilde{\alpha}^2 - V)G^2 + (E - V)F^2 \right) \quad (1)$$

This value defines the norm of the state function of the asymptotically free motion [8]. (iii) the value  $X$  must be minimized as a function of state energy  $E$ . In the lowest perturbation theory approximation, one could carry out calculating the differential cross-section as follows:

$$d\sigma(\varepsilon, E)/d\varepsilon = \pi(M_{\varepsilon S, I, F, \varepsilon S'})^2 (dP_F/dE_F), \quad (2)$$

where  $P$  and  $E$  are the momentum and energy of the atomic system final state; matrix element  $M$  is calculated on the scattering state functions and contains the "atom-nanosphere" potential. As it is indicated above, a choice of adequate atom-sphere potential may have the decisive role. For small atom-nanoobject distances  $r$ , a few atomic units or so, the interaction between an atom and a flat surface depends on details of the structure of both atom and surface and is quite complicated. When ultracold atoms enter this "close" region, excitation modes of atom or surface are easily excited, the atom loses energy and is trapped, adsorbed by the surface ("sticking"). Beyond this close region, the atom-surface interaction is well described by a van der Waals potential  $-C_3/r^3$ . At very large distances, retardation effects become important and an atom in its ground state or in a metastable excited state feels a potential  $-C_4/r^4$ [2]. The coefficients  $C_3, C_4$  depends on the properties of both atom and surface. As the simplest non-flat surface, we consider an atomic scattering by a sphere. Beyond the close region of complicated and consuming atom-surface interactions, the interaction of an atom with a spherical surface is well described by a local potential which depends on the radius  $R$  of the sphere and the distances of the atoms from the surface. For very large  $R$ , and  $r$  small compared to  $R$  but still beyond the close region, the potential behaves as in the case of a flat surface. When  $r$  is large compared to  $R$ , the potential behaves as a nonretarded van der Waals potential  $C_6/r^6$  for small distances  $r$  (still larger than  $R$ ) and as a highly retarded potential,  $-C_7/r^7$ , for large  $r$ . In our opinion, the most adequate function is as follows (c.f. [2] and refs there):

$$V(r) = -C_6/r^6 f(r/L')$$

$$L' = C_7/C_6 \quad (3)$$

where  $f(x)$  is again a shape function (3) describing the transition from the non-retarded to the highly retarded regime, and  $L$  is a length scale for the transition zone. A potential which satisfies all boundary conditions is, e.g. [2]:

$$V_{sph}(r) = -[r^3 f(r/L)/C_3 + r^6 f(r/L')/C_6]^{-1}. \quad (4)$$

For a conducting sphere with radius  $R$ , the coefficients  $C_6, C_7$  are related to the corresponding coefficients  $C_3, C_4$  of the flat-surface case by

$$C_6 = 12R^3 C_3, C_7 = (46/3)R^3 C_4, L' = (23/18)L.$$

The scattering of atoms from a sphere is usually described [1] by the radial Schrödinger equation with the effective potential

$$V_{eff}(t) = V_{sph}(r) + h^2 l(l+1)/2Mt^2, \quad t = r + R > R,$$

for a given angular momentum quantum number  $l$ . As in the flat-surface case, the singular attractive potential tail (beyond the close region) allows the absorption of atoms near the surface to be described unambiguously via incoming boundary conditions. For  $l = 0$ , the radial Schrödinger equation is identical to the equation for normal motion in the flat-surface case, and scattering is essentially quantum reflection by the non-classical region of the attractive potential tail [2]. In our method the Schrödinger equation is replaced by the relativistic Dirac equation, which is solved numerically by the Runge-Cutt method.

We have carried out the numerical calculation of differential cross-section of the scattering for atom of He ( $2^3S$ ) and firstly atom of Li ( $3^2S$ ) by adsorbing nano-sphere of radius 200 a.u. for wave numbers  $k$  up to  $5/\mu\text{m}$ . This corresponds to temperatures up to  $1 \mu\text{K}$  (10nK to 500nK for He and 10nK to 300nK Li). The corresponding results for different potentials of the "atom-sphere" interaction are presented in table 1 (in particular, there are considered the potentials as follows: non-retarded van der Waals potential  $-C_6/r^6$ ; highly retarded case  $-C_7/r^7$ ; realistic potential (2)).

Table 1

**The differential cross-section  $d\sigma/d\Omega$  ( $10^4 \text{ nm}^2$ ;  $\theta = \pi/2$ ) of the scattering for atom of He ( $2^3S$ ), Li ( $3^2S$ ) by adsorbing sphere of radius 200 a.u. for wave numbers  $k$  up to  $5/\mu\text{m}$  (potential A – nonretarded van der Waals potential  $-C_6/r^6$ ; potential B- highly retarded case  $-C_7/r^7$ ; potential C – realistic potential (3))**

He ( $2^3S$ ), radius 200a.u.					Li ( $3^2S$ ), radius 200a.u.
$k$ , in $1/\mu\text{m}$	Poten- tial A [2]	Poten- tial B [2]	Poten- tial C [2]	Poten- tial C, present paper	Poten- tial C, present paper
0.5	0.280	0.39	0.278	0.283	0.309
1.0	0.275	0.38	0.273	0.278	0.300
1.5	0.270	0.37	0.268	0.273	0.292
2.0	0.265	0.36	0.263	0.268	0.284
2.5	0.260	0.35	0.256	0.263	0.278
3.0	0.255	0.34	0.253	0.258	0.272
3.5	0.250	0.33	0.248	0.253	0.266
4.0	0.245	0.32	0.243	0.248	0.260
4.5	0.240	0.31	0.238	0.244	0.255
5.0	0.235	0.30	0.233	0.239	0.250

As one could wait for (especially on the basis of analysis of the data for He from ref.[2] and present paper), the scattering cross section is sensitive to different forms of the atom-surface potential, and the non-retarded van der Waals regime becomes increasingly important for smaller radii. Regarding Li let us note that probably any data regarding Li are absent in the current literature. At last, one can see that for helium and lithium the results for  $d\sigma/d\Omega$  obtained with potential C are much closer to the van der Waals case than to the retarded case. Note that this in contrast to a case of sodium, for example.

## Reference

1. Henkel C., Schmiedmayer J., Westbrook C. (Eds.), Special Issue — Atom chips: manipulating atoms and molecules with microfabricated structures // *Europ. Phys. J. D.* — 2005. — Vol. 35, N 1.
2. Arnecke F., Friedrich H., Madrofinero A. Quantum effects in collisions of ultracold atoms with walls and nanostructures // *Journ. Phys. CS.* — 2007. — Vol. 88. — P. 012041-1–012041-6.
3. Friedberg R., Hartmann S. R., Manassah J. T. Frequency shifts in emission and absorption by resonant systems of two-level atoms // *Phys. Rep.* 2003. — Vol. 37. — P. 101–179.
4. Glushkov A. V., Loboda A. V. New consistent quantum approach to collisions of ultracold atoms with nanostructures // *Proc. 8<sup>th</sup> European workshop on Quantum systems in Physics and Chemistry.* — Spetses (Greece). — 2003. — P. 71.
5. Glushkov A. V., Ivanov L. N. DC strong-field Stark effect: consistent quantum-mechanical approach // *J. Phys. B: At. Mol. Opt. Phys.* — 1993. — Vol. 26. — P. L379–L388.
6. Resonance states of compound super-heavy nucleus and EPPP in heavy nucleus collisions / A. V. Glushkov, V. D. Rusov, S. V. Ambrosov, A. V. Loboda // In: *New projects and new lines of research in nuclear physics.* Eds. G. Fazio, F. Hanappe, Singapore: World Scientific. — 2003. — P. 126–182.
7. Glushkov A. V., Malinovskaya S. V. Co-operative laser nuclear processes: border lines effects // In: *New projects and new lines of research in nuclear physics.* Eds. G. Fazio and F. Hanappe, Singapore: World Scientific. — 2003. — P. 242–270.
8. DC Strong Field Stark Effect for Non-hydrogenic Atoms: Consistent Quantum Mechanical Approach / A. V. Glushkov, S. V. Ambrosov, A. V. Ignatenko, D. A. Korchevsky // *Int. Journ. Quant. Chem.* — 2004. — Vol. 99, N 5. — P. 933–939.
9. Consistent quantum theory of the recoil induced excitation and ionization in atoms during capture of neutron / A. V. Glushkov, S. V. Malinovskaya, E. P. Gurnitskaya, O. Yu. Khetsetius, Yu. V. Dubrovskaya // *J. Phys. CS.* — 2006. — Vol. 35. — P. 425–430.
10. Glushkov A.V., Energy Approach to Resonance states of compound super-heavy nucleus and EPPP in heavy nucleus collisions // *Low Energy Antiproton Physics (AIP Serie).* — 2005. — Vol. 796. — P. 206–210.
11. Glushkov A. V., Ivanov L. N. Radiation decay of atomic states: atomic residue polarization and gauge noninvariant contributions // *Phys. Lett. A.* — 1992. — Vol. 170. — P. 33–36.
12. Cooperative Laser-Electron-Nuclear Processes: QED Calculation of Electron Satellites Spectra for Multi-Charged Ion in Laser Field / A. V. Glushkov, S. V. Malinovskaya, Yu. G. Chernyakova, A. A. Svinarenko // *Int. Journ. Quant. Chem.* — 2004. — Vol. 99, N 5. — P. 889–893.
13. Consistent quantum approach to new laser-electron-nuclear effects in diatomic molecules / A. V. Glushkov, S. V. Malinovskaya, A. V. Loboda, I. M. Shpinareva, G. P. Prepelitsa // *J. Phys. CS.* — 2006. — Vol. 35. — P. 420–424.
14. Diagnostics of the collisionally pumped plasma and search of the optimal plasma parameters of x-ray lasing: Calculation of electron-collision strengths and rate coefficients for Ne-like plasma / A. V. Glushkov, S. V. Malinovskaya, A. V. Loboda, I. M. Shpinareva, E. P. Gurnitskaya, D. A. Korchevsky // *J. Phys. CS.* — 2005. — Vol. 11. — P. 188–198.
15. Consistent QED approach to calculation of electron-collision excitation cross-sections and strengths: Ne-like ions / A. V. Glushkov, S. V. Ambrosov, A. V. Loboda, E. P. Gurnitskaya, G. P. Prepelitsa // *Int. Journ. Quant. Chem.* — 2005. — Vol. 104, N 4. — P. 562–569.

UDC 539.184;539.192

A. V. Loboda

## QUANTUM THEORY OF COLLISIONS OF THE ULTRACOLD ATOMS WITH NANOSTRUCTURES

It is developed a generalized energy approach, based on the operator perturbation theory formalism to collision of ultracold atoms with nanostructures (nanospheres). The preliminary numerical results for atom of He and firstly atom of Li are presented for different potentials of the “atom-sphere” interaction.

УДК 539.184;539.192

А. В. Лобода

## КВАНТОВАЯ ТЕОРИЯ СТОЛКНОВЕНИЙ ХОЛОДНЫХ АТОМОВ С НАНООБЪЕКТАМИ

Развит обобщенный энергетический подход, базирующийся на операторной теории возмущений, в задаче столкновений ультрахолодных атомов с нано-структурами (нано-сферами). Численные результаты представлены для атомов гелия и лития для различных типов потенциала взаимодействия «атом-сфера».

УДК 539.184; 539.192

А. В. Лобода

## КВАНТОВА ТЕОРИЯ ЗІТКНЕНЬ ХОЛОДНИХ АТОМІВ З НАНООБ'ЄКТАМИ

Розвинутий узагальнений енергетичний підхід, який базується на операторній теорії збурень, в задачі зіткнень ультрахолодних атомів з нано-структурами (нано-сферами). Чисельні результати наведені для атомів гелія та літія для різних типів потенціала взаємодії «атом-сфера».

## OPTICAL-FIBRE RAMAN AMPLIFIERS WITH 6.3–12.2 THz WORKING BAND

On the basis of the proposed spectroscopic model of the amplification spectrum analysis under Raman scattering (RS), the design scheme of the RS amplifiers' with the range of 6.3–12.2 THz with the multi-waves pumping is proposed. The oscillator functions of the line form allow to obtain the simple scheme of the RS amplification in optical fibers dependence on the wavelength which is extremely useful during evaluation of the amplification band, of laser threshold in stimulated RS, noise parameters and of the amplification process. The concept of the actual band with the use of oscillator functions of the line form is useful also during the design and development of the RS amplifiers with several pumping wavelengths. With the scope of the amplification band broadening to the L-band, the proposed model was used for analysis of fiber RS amplifier with combined source of pumping containing some wavelengths and allow to obtain wider band ~100 nm (12.2 THz) with small amplification non-regularity not more than 0.5 dB. Proposed spectroscopic model could be used as well in the analysis of complex spectra of spontaneous RS in fibers with other doping materials.

## INTRODUCTION

Fiber Raman scattering (RS) amplifiers (FRSA) are used now in almost all new long fiber-optical system of information transfer [1]. But, despite the simplicity of FRSA construction, it is necessary to consider during the design process, a lot of factors [2], namely the presence of the power exchange as between pumping as well as between signals, pumping decay or saturation, double Raleigh scattering (multi-path interference), spontaneous radiation amplification, etc.[3]. That's why the precise choice of the wavelength and of the power level for each pumping diode is necessary for the provision of the wide-band amplification with small non-regularity.

Direct determination of FRSA with the multi-wave pumping profile from the connected waves' equations should be considered as the extremely complex way. The attempts were realized with the use of the digital optimization methods and burning model [4], monolayer neuron nets with direct bonds [5] and analogous methods [6]. But, these methods, as a rule, give the practically non-realistic power distributions for pumping sources as the result of the error in connected equations coefficients determination which include the FRSA amplification coefficient and effective fiber cross-section for each wavelength. The problem is solved through creation of the most precise model of RS amplification. The optical fiber RS amplification coefficient was theoretically analyzed for one wavelength only in the paper [7].

## MODEL AND DISCUSSION

We propose the spectroscopic model of RS amplification based on the oscillator theory which is used for FRSA modeling. The actual band model is used for the analysis of experimental FRSA configurations with the working frequencies from 6.3 to 12.2 THz and small amplification non-regularity. Such

model allows also to perform the quantitative analysis of pumping power which provides the laser threshold and to evaluate the effective FRSA noise coefficient.

Different forms of the system of connected equations [2-10] are used for RS amplification with some pumping wavelengths modeling. The equations system, considering the fiber's losses  $\alpha(v, T)$  and back Raleigh scattering  $\gamma_b(v)$ , is written down in the form of generalized equation [6], for great number of the channels with optical band  $\Delta v$ , which travels in right direction before pumping (with index "+") and in reverse direction (indexed as "-"):

$$\begin{aligned} \pm \frac{dP_i^\pm}{dz} = & -\alpha(v_i, T)P_i^\pm + \gamma_b(v_i)P_i^\mp + \\ & + P_i^\pm \sum_j^{v_j > v_i} \frac{g_R(v_j, v_i)}{A_{eff}(v_j, v_i)} (P_j^+ + P_j^-) \Delta v + \\ & + 2 \sum_j^{v_j > v_i} (P_j^+ + P_j^-) h v_i \Delta v \frac{g_R(v_j, v_i)}{A_{eff}(v_j, v_i)} \cdot [n_B(v_j - v_i) + 1] - \\ & - P_i^\pm \sum_j^{v_j < v_i} \frac{V_j v_i}{V_i v_j} \frac{g_R(v_i, v_j)}{A_{eff}(v_i, v_j)} (P_j^+ + P_j^-) \Delta v + \\ & + 2 \sum_j^{v_j < v_i} (P_j^+ + P_j^-) h v_i \Delta v \frac{v_i V_j}{v_j V_i} \frac{g_R(v_i, v_j)}{A_{eff}(v_i, v_j)} \cdot n_B(v_i - v_j), \quad (1) \end{aligned}$$

where index  $i$  corresponds to  $i$ -th wavelength with the frequency  $v_i$ , while  $V_i, P_i$  – are the group velocity and optical powers, correspondingly.  $A_{eff}(v)$  – the effective fiber cross-section, and  $g(v_i, v_j)$  – RS amplification coefficient on the signal frequency ( $v_j$ ) with pumping frequency ( $v_i$ ),  $n_B(v) = [\exp(hv/kT) - 1]^{-1}$  – Bose-Einstein phonons' distribution factor, where  $h$  – Planck constant,  $k$  – Boltzmann constant,  $T$  – temperature. The component of (1), containing the multiplier  $(n + 1)$  corresponds to Stokes component of the amplified spontaneous radiation (ASR) and the component with the multiplier with  $n$  describes the anti-Stokes ASR generation.

In general, the RS amplification coefficient on Stokes frequency  $\omega_s = \omega_p - \omega_v$  could be written in the form [7]:

$$g_R = -\frac{3\omega_s}{\varepsilon_0 c^2 n_p n_s} \frac{\text{Im}[\chi_{iii}^{(3)} + \chi_{iii}^{(3)*}]}{2A_{\text{eff}}}. \quad (2)$$

Semi-classic RS theory establishes the connection between the differential polarization  $\partial\alpha_{ij}/\partial q_n$  and the non-linear permeability  $\chi^{(3)}$  [7]:

$$\chi_{ijkl}^{(3)} = \frac{N}{12m\varepsilon_0 V} \frac{1}{\omega_v^2 - \omega^2 + 2i\omega\Gamma} \cdot \sum_n \frac{\partial\alpha_{ij}}{\partial q_n} \left( \frac{\partial\alpha_{kl}}{\partial q_n} \right)^*. \quad (3)$$

where  $\omega_v$  – intrinsic frequency of phonon oscillation,  $\omega$  – phonon frequency,  $\Gamma$  – phonon decay constant,  $q_k$  – normal coordinate, which describes the local move,  $m$  – mass connected with the oscillation,  $N$  – number of oscillators in the interaction volume  $V$ ,  $\varepsilon_0$  – dielectric constant.

Thus, the RS amplification coefficient's frequency dependence  $g(\omega)$  is described, mainly, by the imaginary part of the non-linear permeability  $\chi^{(3)}$  in the form of the resonant denominator which originates from phonon harmonic oscillator.

Taking into account the equations (2) and (3), one could write down the frequency dependence  $S(\nu)$  for the FRSA in the form:

$$S(\nu) = -\text{Im} \left[ \frac{1}{\nu_0^2 - \nu^2 + i\nu\gamma} \right] = \frac{\nu\gamma}{(\nu_0^2 - \nu^2)^2 + \nu^2\gamma^2}, \quad (4)$$

where  $\nu$  – the wave numbers ( $\nu_0 = \omega_v/2\pi c$ ,  $\nu = \omega/2\pi c$  and  $\gamma = \Gamma/\pi c$ ), while  $\gamma$  approximately equals to the value of FWHM for  $S(\nu)$ . We use the normalized function  $S_R(\nu) = \gamma \nu_0 S(\nu)$ , while  $S_R(\nu_0) = 1$ .

The result of the RS Stokes line's approximation was obtained for 20 molecular % of  $\text{Ge}_2\text{O}$  using the line form function  $S_R(\nu)$  is presented at Fig.1 (dotted line at Fig.1). The Fig.1 demonstrates the best fitting the experimental data [11] by the model curve, which is achieved at the resonant phonon frequency ( $\nu_0$ ) and phonon decay constant ( $\gamma$ ) in the function  $S_R(\nu)$  of phonon harmonic oscillator which equal to  $435 \text{ cm}^{-1}$  and  $130 \text{ cm}^{-1}$ , correspondingly.

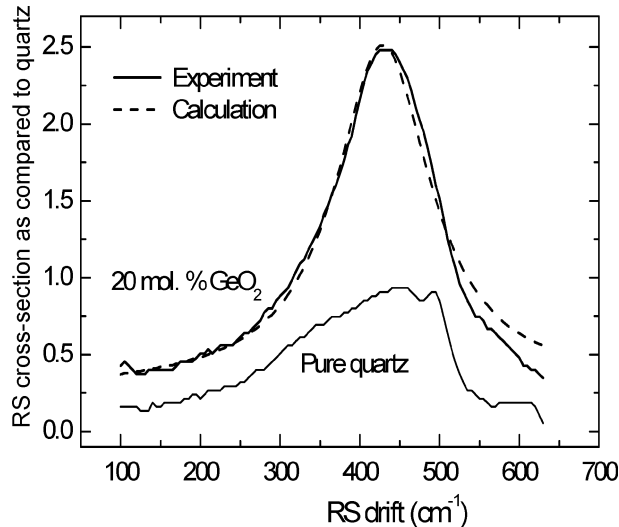


Fig. 1. RS Stokes line approximation (full line) for 20 molecular %  $\text{Ge}_2\text{O}$  with line-form function  $S_R(\nu)$  (dotted line).

We have evaluated the approximation precision using the averaged quadratic dispersion  $\sigma^2 = [S_R(\nu) - S_{\text{exp}}(\nu)]^2 / S_{\text{exp}}^2(\nu_0)$  of the oscillator function of the line form function  $S_R(\nu)$  from the experimental line. In the wave numbers range from  $100 \text{ cm}^{-1}$  to  $600 \text{ cm}^{-1}$ , the dispersion has the value of  $\sigma^2 < 1\%$ , and its average value was equal to  $\sigma^2 = 0.2\%$ .

Besides, good correspondence between the modeling results and the experimental data is supported by the difference of the integral intensities of both amplification profiles which doesn't exceed 0.8% for the amplification band under investigation. We have used these results for the RS amplification processes modeling.

The results of ARS spectra evaluation (full line) are presented at Fig. 2 for the case of published data for RS amplifier which covers both two C + L telecommunication windows.

The experimental data for the effective noise coefficients taken from the paper [12], are presented by dotted lines at Fig. 2. Six pumping wavelengths were used in the experiment: 1428, 1445, 1466, 1480, 1494 and 1508 nm, and the pumping powers were correspondingly: 338, 215, 83, 30, 19 and 39 mW.

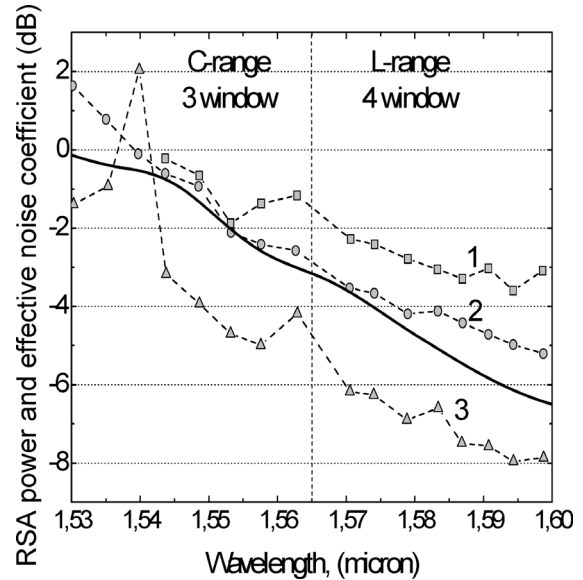


Fig. 2. Calculated ARS spectrum (full line) and measured values of the FRSA noise coefficient for C + L range with pumping on six wavelengths for line lengths: 1 – 60 km; 2 – 100 km; 3 – 140 km (experimental data taken from [11])

The preliminaries of the modeling were [13, 14] as follows. Under the constant value of the signal amplification coefficient, the ASR spectral density at the FRSA output has to repeat the form of the RS amplification at the input. It was the RS amplification coefficient distribution that creates the frequency dependence of the noise coefficient over the FRSA band. As, according to the experimental conditions of the paper [12], the amplification non-regularity was supported at the minimal level, the spectral form of the noise coefficient was proportional to the signal distribution at the FRSA output.

As it could be seen from Fig. 2, we have the correspondence between the ARS spectrum and experimental data of noise coefficient measurements. Really, the ARS distribution curves' inclination over C+L-bands is about  $\sim 7 \text{ dB}$ . The same values (about

7 dB) are registered for the noise coefficient's distribution for all fiber longitudes: 60 km, 100 km and 140 km under investigation, as it is seen from Fig. 2.

The spectroscopic model allows to evaluate directly the FRSA with several pumping sources amplification band in a simple enough way. With the use of the proposed model, it is possible to obtain the FRSA band without the equations' system solution and, even more, to present the results in the graphic way.

The proposed model was used for the test analysis of the industrial sample of FRSA with four pumping wavelength (1426, 1436, 1456 and 1466 nm) from laser diodes (LD), with maximal power of 300 mW.

The calculated FRSA band for this sample with the width at the level 1 dB was about 50 nm (6.3 THz) in the range of 1520–1570 nm, while the amplification non-regularity was in the range 0.5 dB in the working band 1528–1562 nm.

The calculation results, based on the proposed model, are in full correspondence to the digital data, presented by the amplifier's producer.

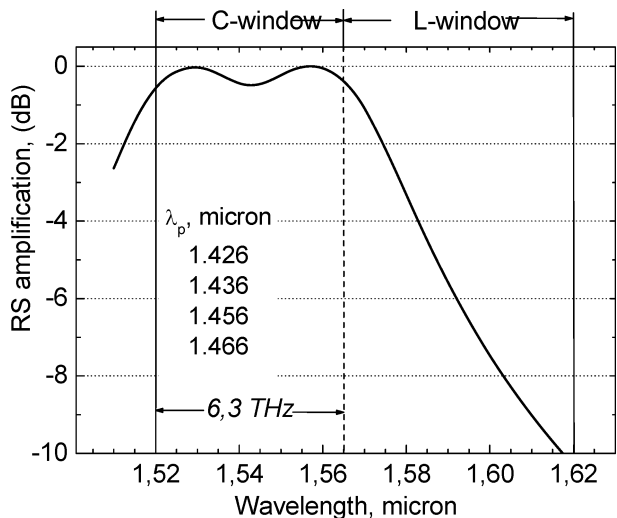


Fig. 3. FRSA band with 4-LD pumping designed within the model of actual band. In L-band amplification decay is more than 10 dB

As it is seen from Fig. 3, this 4- $\lambda$  amplifier has the amplification coefficient decay more than 10dB over L-band, which couldn't be extinguished through the pumping power's change and, that's why, it couldn't be used in the long-wave telecommunication window.

But, as it is known from the practical experience, only about 10% of the maximal power is used for the FRSA with some pumping sources amplification coefficient's equalization. Thus, we proposed to use the part of the non-used power from the long-wave pumping laser diodes, for the generation of additional pumping sources.

The modelling performed, shows that the FRSA amplification band could be widened by L-window with the use only two additional pumping sources with the wavelengths of 1486 nm and 1510 nm.

The six sources scheme of FRSA pumping which widens the amplification band over the L-range, is presented at Fig. 4. It contains 4 pumping LD ( $\lambda_p = 1426, 1436, 1456$  and  $1466$  nm) as well as two additional resonators in RS fiber (with the wavelengths 1486 and 1510 nm), which widens the amplification

band from C-range to C+L-range and guarantees the needed minimum of the amplification non-regularity. The parameters of additional pumping sources, used in the modeling FRSA amplification band, could be optimized in the interactive regime.

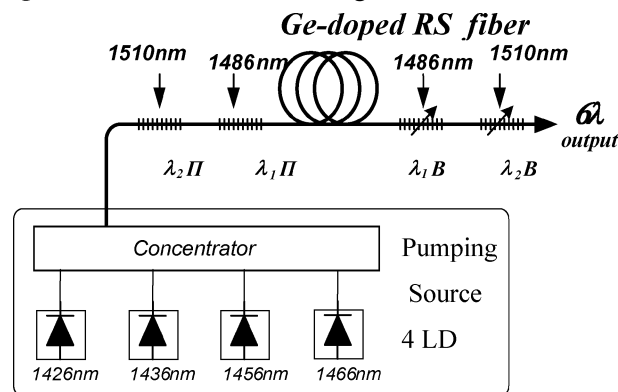


Fig. 4. Scheme of six-wavelengths pumping source for FRSA with widened amplification band in L-range

Evaluation of the wavelengths of the RS lasers needed for the FRSA additional pumping could be considered as the calculation of the fiber Bragg gratings geometrical parameters of the laser resonator presented at Fig. 4.

The results of FRSA design with the amplification band of about 100 nm (12.2 THz) and the amplification non-regularity not more than 0.5 dB are presented at Fig. 5. The amplification non-regularity is minimized through the choice of the pumping power for each source if the effective (acting) power for each channel are in the following relationship — 0.8 : 1.0 : 0.75 : 0.7 : 1.1 : 1.5.

The model of actual band allows not only to make the optimal calculation of the FRSA amplification band with the random sources number as well as to evaluate the threshold power for RS laser pumping, as used in the proposed pumping source [2]. The threshold generation power is reached when the input power guarantees the amplification level for the spontaneous Stokes radiation overwhelms the fiber losses  $\alpha_s$ .

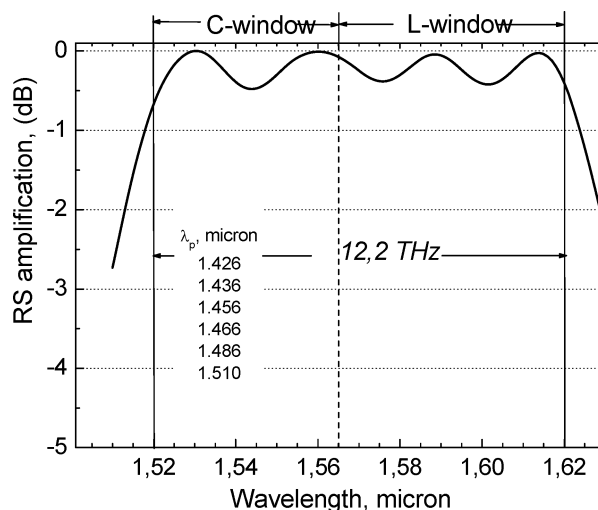


Fig. 5. The FRSA with wide amplification band ~100 nm (12.2 THz) and small non-regularity < 0.5 dB modeling result

The model of actual band allows not only to make the optimal calculation of the FRSA amplification band with the random sources number as well as to

evaluate the threshold power for RS laser pumping, as used in the proposed pumping source [2]. The threshold generation power is reached when the input power guarantees the amplification level for the spontaneous Stokes radiation overwhelms the fiber losses  $\alpha_s$ .

As the proposed spectroscopic model allows to determine the real view of  $g(\omega)$  function for given optical fiber type and, thus, one could calculate the threshold pumping power [14]  $P_p^{thr}(\omega) = \alpha_s A_{eff} / g_r(\omega)$ , what guarantees the RS laser generation at practically random wavelength in the frames of Stokes shift stimulated by pumping in a given optical fiber.

The quantitative data for each of the LD pumping, which guarantee the existence of RS laser generation at both additional wavelengths in the extended pumping source with the use of the resonators on fiber diffraction gratings are presented in Table 1. The calculation results support the hypothesis on the possibility of two-waves RS laser with the resonators based on the fiber Bragg gratings effective pumping from each existing diodes producing maximal output power of 300 mW.

Table 1  
Threshold pumping powers at  $\lambda_p$  for RS laser generation at  $\lambda_l$

Pumping wavelength $\lambda_p$ , mkm	Threshold powers in mW for RS laser at $\lambda_l$	
	1.486 mkm	1.510 mkm
1.426	42.6	9.7
1.436	69.6	20.3
1.456	144.0	62.7
1.466	190.9	93.9

## CONCLUSIONS

On the basis of the discussion of the proposed spectroscopic model one could state the following:

1. We have proposed the scheme of fiber-optical Raman scattering amplifiers with the working frequencies band of 6.3–12.2 THz, which use the multi-wavelengths pumping.

2. The concept of the actual band allows to obtain the simple description of the frequency profile of Raman scattering amplification in optical fibers and is useful during evaluation of the amplification band, laser threshold of stimulated Raman scattering, noise parameters and the amplification process in Raman amplifiers.

3. The proposed model is applied to the analysis of fiber Raman scattering amplifier with combined pumping source what allows to obtain the range width ~100 nm and small amplification non-regularity not more 0.5 dB.

4. The presented approach simplifies significantly the FRSA with multi-wave pumping design process and makes it quite clear.

## Literature

1. *Islam M. N.* Raman Amplifiers for Telecommunications // IEEE Journal of Selected Topics in Quantum Electronics, 8 (3). — 2002. — P. 548–559.
2. *Korotkov P. A., Felinskyi G. S.* Fiber RS permanent action lasers (in Ukrainian) // Ukrainian Physical Journal. Reviews, 3(2), 2006. — P. 126–150.
3. *Pump interactions in 100 nm bandwidth Raman amplifier / H. Kidorf, K. Rottwitt, M. Nissov, M. Ma, E. Rabarijaona // IEEE Photonics Technology Letters, 11(5), 1999. — P. 530–532.*
4. *Automatic Design Scheme for Optical-Fiber Raman Amplifiers Backward-Pumped With Multiple Laser Diode Pumps / M. Yan, J. Chen, W. Jiang, J. Li, J. Chen, X. Li // IEEE Photonics Technology Letters, 13(9), 2001. — P. 948–950.*
5. *A New Optimal Algorithm for Multipump Sources of Distributed Fiber Raman Amplifier / P. Xiao, J. Zeng, Q. Huang, J. Liu // IEEE Photonics Technology Letters, 15(2), 2003. — P. 206–208.*
6. *Mandelbaum I., Bolshtyansky M.* Raman Amplifier Model in Single-Model Optical Fiber // IEEE Photonics Technology Letters, 15(12), 2003. — P. 1704–1706.
7. *Scaling of the Raman Gain Coefficient: Applications to Germanosilicate Fibers / K. Rottwitt, J. Bromage, A. J. Stentz, L. Leng, M. E. Lines, H. Smith // Journal of Lightwave Technology, 21(7), 2003. — P. 1652–1662.*
8. *Dakss M. L., Melman P.* Amplified Spontaneous Raman Scattering and Gain in Fiber Raman Amplifiers // Journal of Lightwave Technology, LT-3(4), 1985. — P. 806–813.
9. *Agrawal G. P.* Nonlinear Fiber Optics. Second ed., San Diego, CA: Academic, 1995.
10. *Loudon R.* The Quantum Theory of Light. Second ed., Clarendon Press, Oxford. — 1983.
11. *Davey S. T., Williams D. L., Ainslie B. J.* Optical gain spectrum of GeO<sub>2</sub>-SiO<sub>2</sub> Raman fiber amplifiers // IEE Proceedings, 136(6), 1989. — P. 301–306.
12. *Six-wavelength Raman fibre laser for C- and L-band Raman amplification and dynamic gain flattening / M. D. Mermelstein, C. Horn, S. Radic, C. Headley // Electronics Letters, 38(13), 2002. — P. 636–638.*
13. *Felinskyi G. S., Korotkov P. A.* Actual band model for design of optical fiber Raman amplifier with multiwave pumping // Proceedings SPIE/Ukraine, 6(1-6), 2006. — P. 409–417.
14. *Felinskyi G. S., Korotkov P. A.* Simulation of multiwave pumped fiber Raman amplifiers // Semiconductor Physics Quantum Electronics and Optoelectronics, 9(3), 2006. — P. 83–93.

UDC 532

G. S. Felinskyi, P. A. Korotkov

## OPTICAL-FIBRE RAMAN AMPLIFIERS WITH 6.3–12.2 THz WORKING BAND

Based on the proposed spectroscopic model for the Raman gain spectrum analysis the simulation procedure of optical fiber Raman amplifiers with a working frequency band from 6.3 to 12.2 Terahertz, which operate in accordance with multi wave pumping scheme is submitted in the present work. The oscillator line-form functions allow us to receive the simple description of the Raman amplification dependence as function of wavelength in optical fibers and they are rather useful for estimation of the amplification bandwidth, the laser threshold at stimulated Raman scattering, noise parameters, and the gain process in Raman amplifiers. The concept of an actual band using the oscillator line-form functions is also useful for development of Raman amplifiers with multiple wavelengths pumping. With the purpose to expand of the amplification bandwidth on a whole L-band the offered model is applied to the analysis of fiber Raman amplifier with the combined pumping source, which contained the several wavelengths and it allows to receive the wide band ~100 nm (12.2 THz) with small gain ripple less than 0.5 dB. The suggested spectroscopic model can be further generalized for application to the analysis of complex spontaneous Raman spectra in fibers with other doping materials.

УДК 532

Г. С. Фелінський, П. А. Коротков

### **ВОЛОКОННО-ОПТИЧНІ ВКР ПІДСИЛЮВАЧІ З ПОЛОСОЮ РОБОЧИХ ЧАСТОТ 6,3–12,2 ТЕРАГЕРЦ**

В даній роботі на основі запропонованої спектроскопічної моделі аналізу спектра підсилення при комбінаційному розсіянні (КР) запропоновано методику розрахунку волоконно-оптичних КР підсилювачів з половою робочих частот 6,3–12,2 терагерц, працюючих за схемою з багато хвильовою накачкою. Осциляторні функції форми лінії дозволяють одержати простий опис залежності КР підсилення у оптичних волокнах від довжини хвилі і вони являються корисними при оцінці полоси підсилення лазерного порогу при вимушеному КР (ВКР), шумових параметрів та процесу підсилення в КР підсилювачах. Концепція актуальної полоси при використанні осциляторних функцій форми лінії корисна також при розробці КР підсилювачів з накачкою на декількох довжинах хвиль. З метою розширення полоси підсилення на L – половою запропонована модель використана для аналізу волоконного КР підсилювача з комбінованим джерелом накачки, який містить декілька довжин хвиль, що дозволяє одержувати широку половою - 100 нм (12,2 ТГц), з малою нерівномірністю підсилення не більше 0,5 дБ. Запропоновану спектроскопічну модель можна розповсюдити на аналіз складних спектрів спонтанного КР у волокнах з іншими легуючими речовинами.

УДК 532

Г. С. Фелинский, П. А. Коротков

### **ВОЛОКОННО-ОПТИЧЕСКИЕ ВКР УСИЛИТЕЛИ С ПОЛОСОЙ РАБОЧИХ ЧАСТОТ 6,3–12,2 ТЕРАГЕРЦ**

В настоящей работе на основе предложенной спектроскопической модели анализа спектра усиления при комбинационном рассеянии (КР) представлена методика расчета волоконно-оптических КР усилителей с полосой рабочих частот 6,3–12,2 терагерц, работающих по схеме с много волновой накачкой. Осциляторные функции формы линии позволяют получить простое описание зависимости КР усиления в оптических волокнах от длины волны и они являются весьма полезными при оценке полосы усиления, лазерного порога при вынужденном КР (ВКР), шумовых параметров и процесса усиления в КР усилителях. Концепция актуальной полосы при использовании осциляторных функций формы линии полезна также при разработке КР усилителей с накачкой на нескольких длинах волн. С целью расширения полосы усиления на L-полосу предлагаемая модель применена к анализу волоконного КР усилителя с комбинированным источником накачки, содержащем несколько длин волн, что позволяет получить широкую полосу ~100 нм (12,2 ТГц) с малой неравномерностью усиления, не более 0,5 дБ. Предлагаемую спектроскопическую модель можно распространить на анализ сложных спектров спонтанного КР в волокнах с другими легирующими материалами.

## PREPARATION AND OPTICAL PROPERTIES OF ZnSe:Co FILMS

ZnSe:Co films were obtained by vacuum deposition. Optical density spectra in the region of 4–0.38 eV are investigated. It is established, that in ZnSe:Co films, as compared to ZnSe films, the absorption edge is displaced to the lower energy region. The analogy of ZnSe:Co films and crystals optical absorption spectra is established. The investigated lines of ZnSe:Co films absorption are caused by electronic optical transitions from Co<sup>2+</sup> ion basic condition level <sup>4</sup>A<sub>2</sub>(F) on the excited states <sup>4</sup>T<sub>1</sub>(P), <sup>4</sup>T<sub>1</sub>(F) and <sup>4</sup>T<sub>2</sub>(F) levels splitted with spin-orbit interaction.

### 1. INTRODUCTION

ZnSe is the perspective material for fabrication of injection electroluminescent structures and lasers which emit in blue spectral region. The possibility of this material use for creation of emission structures in the infra-red (IR) spectral region is shown last years. Doping of ZnSe with transition elements (Fe, Ni, Co, Cr) is carried out for this purpose. We suggest also a method of Co diffusion doping of ZnSe single crystals and their optical properties are investigated [1,2].

However, for fabrication of IR-region emitting structures, the film structures are most appropriate. The purpose of this study is to develop the technology of ZnSe:Co films preparation and to investigate their optical properties.

### 2. EXPERIMENTAL

ZnSe:Co films were obtained by vacuum deposition on quartz substrates. Crushed ZnSe:Co crystals with known cobalt concentration were used as a source. Technology of ZnSe:Co crystals preparation is described in [1]. The source temperature was no less than 1600°C during evaporation. At lower temperatures there was no evaporation of Co atoms and the undoped ZnSe films was obtained. The films thickness was in the range 5–10 μm. Obtained films had a dark grey color.

With the purpose of Co impurity activation and structure crystallization, obtained films were annealed in He and Ar atmosphere. Use of inert atmosphere hindered the films sublimation. The optimum annealing temperature was 650°C and duration of 5 hours was chosen. The lower annealing temperature hasn't led to impurity activation and film structure crystallization. Intensive films sublimation at higher temperatures was registered. After annealing the ZnSe:Co films became dark-brown. Such color was caused by the initial ZnSe:Co crystals. Estimation of the highest cobalt concentration was determined by comparison of optical absorption spectra with present data [1]. The highest concentration of cobalt in the obtained films is estimated as 10<sup>18</sup> cm<sup>-3</sup>.

For comparison, the undoped ZnSe films were obtained by similar method. As a source the undoped ZnSe crystals were used in this case.

The spectra of optical density were measured by the SF-46 diffraction spectrophotometer working within the range 4.1–1.0 eV, and MDR-6 monochromator with diffraction grating of 600 and 325 grooves/mm. The first of devices was used to analyze absorption spectra within energy range 1.2–0.6 eV (middle-1 IR-region), and the second – in an interval 0.6–0.4 eV (middle-2 IR-region). As the recorder of light intensity in middle IR-region PbS photoresistor was used working in the mode of alternating current recording. The optical density spectra were measured at 77 and 293 K.

The obtained results of ZnSe:Co films optical density measurements were compared to the results obtained for the ZnSe:Co crystals, which were used as a source for films deposition.

### 3. DISCUSSION

#### *Optical-density spectra of ZnSe:Co films*

The optical density spectra of ZnSe:Co and ZnSe films in the absorption edge region are investigated. The absorption spectra of undoped ZnSe films are characterized by absorption edge on 2.66 eV at T=300 K. Doping with cobalt results in the shift of absorption edge to the lower energy region. This shift is enlarged by cobalt concentration increase. A similar shift is observed in the ZnSe:Co crystals. The reason of absorption edge displacement in the lower energy region most, probably caused, by formation of Zn<sub>1-x</sub>Co<sub>x</sub>Se solid solution.

It is established that at temperature decrease to 77 K the absorption edge of the investigated films is displaced to the larger energies region by 0.11 eV. The magnitude of this shift corresponds to a temperature-induced variation of the ZnSe band gap.

In the near-IR spectrum of the ZnSe:Co films the broad absorption band at 1.65 eV appears (Fig. 1, curve 1). After annealing in He and Ar atmosphere the sharp series of optical absorption lines at 1.64, 1.71 and 1.78 eV (Fig. 1, curve 2) appear. A similar lines were observed before in ZnSe:Co crystals (Fig. 1, curve 3). They are caused by electrons transitions from <sup>4</sup>A<sub>2</sub>(F) basic state to splitted levels of <sup>4</sup>T<sub>1</sub>(P) excited state of Co<sup>2+</sup> ion. Appearance of absorption lines series after annealing could be explained by cobalt

diffusion in zinc sublattice that is confirmed by color films change.

In middle-IR region the characteristic absorption in two ranges was observed. In higher energy region ZnSe:Co films spectra were characterized by two relatively broad lines at 0.83 and 0.76 eV (Fig. 1, curve 1). The position of these absorption lines did not change with film temperature. After annealing in He and Ar atmosphere these lines as absorption lines in near-IR region become sharper (Fig. 1, curve 2). Similar absorption lines were observed in ZnSe:Co crystals (Fig. 1, curve 3). In accordance with [3], the absorp-

tion line at 0.76eV corresponds to intracenter transition from the basic state  $^4A_2(F)$  to the excited  $^4T_1(F)$  state splitted by spin-orbital interaction. The presence of line at 0.83eV is caused by splitting of excited state level due to spin-orbital interaction.

In the lower energy range of middle-IR region in the optical absorption spectra of ZnSe:Co films, like the absorption spectra of ZnSe:Co crystals there is the resonance absorption line at 0.43eV (Fig. 1). In accordance with [3], this line is caused by the transitions  $^4A_2(F) \rightarrow ^4T_2(F)$  between basic  $^4A_2(F)$  and the nearest excited state  $^4T_1(F)$ .

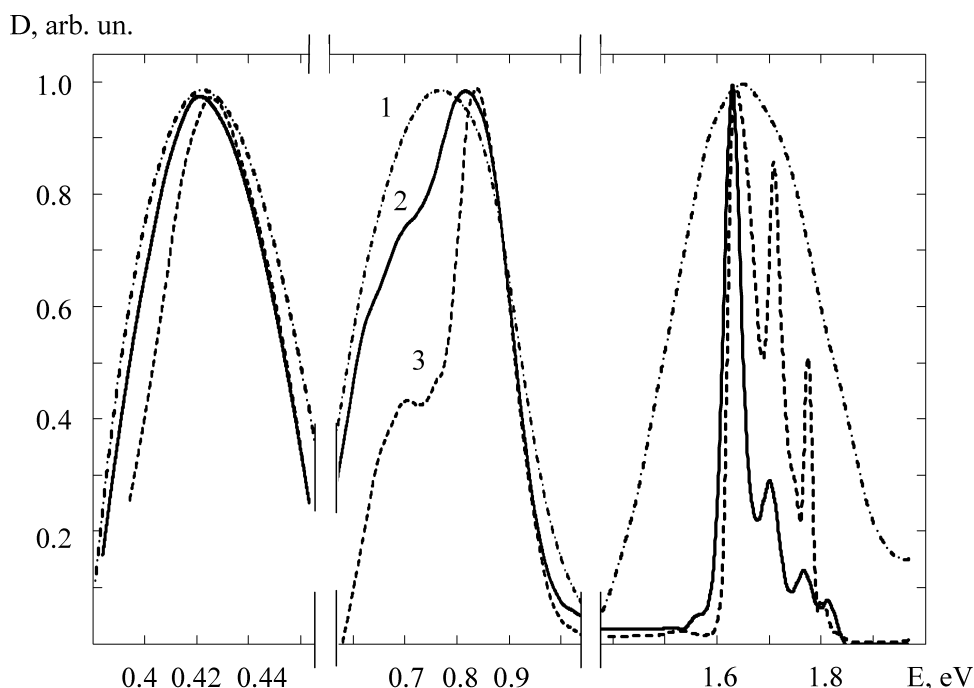


Fig. 1. Absorption spectra of ZnSe:Co films (1), (2) and crystals (3).  $T=77K$ . (Explanation in the text)

It should be noted that in undoped ZnSe films neither before nor after annealing in He and Ar atmosphere the analogous features of the absorption spectra in IR-region was not observed.

#### 4. CONCLUSION

The studies carried out allow us to conclude the following:

1. The method of ZnSe:Co films preparation has been developed. The highest cobalt concentration in the obtained films is estimated as  $10^{18} \text{cm}^{-3}$ .

2. It is established that films annealing in He and Ar atmosphere results in the arrangement of films crystalline structure and effective embuiding of cobalt atoms in to zinc sublattice.

3. It is shown that observed ZnSe:Co films absorption lines are caused by electrons optical transitions

from  $\text{Co}^{2+}$  ion basic state  $^4A_2(F)$  level to the excited states  $^4T_1(P)$ ,  $^4T_1(F)$  and  $^4T_2(F)$  levels splitted by spin-orbital interaction.

4. The present work showed indicate the absence substantial distinctions in the optical absorption spectra of films and crystals ZnSe:Co, what allows to use these films for IR spectral region structures creation.

#### References

1. *Получение и оптические свойства монокристаллов ZnSe, легированных кобальтом* / Ю. Ф. Ваксман, В. В. Павлов, Ю. А. Ницук, Ю. Н. Пуртов, А. С. Насибов, П. В. Шапкин // *Физ. и техн. полупроводников*, 40(7), 2006. — С. 815–818.
2. *Оптические свойства кристаллов ZnSe, легированных переходными элементами* / Ю. Ф. Ваксман, В. В. Павлов, Ю. А. Ницук, Ю. Н. Пуртов // *Вісник Одеського нац. ун-ту*, 11(7), 2006. — С. 47–53.
3. *Radlinski A. P.* On the properties of cobalt impurities in Zinc Selenide crystals (II) // *Phys. Stat. Sol. (b)*, 86, 1978. — P. 41–46.

UDC 546.49

Yu. F. VAKSMAN, Yu. A. NITSUK, Yu. N. PURTOV, A. S. NASIBOV, P. V. SHAPKIN

#### **OBTAINING AND OPTICAL PROPERTIES OF ZnSe:Co FILMS**

ZnSe:Co films were obtained by vacuum deposition. An optical density spectra in the region of 4-0.38eV are investigated. It is established, that in ZnSe:Co films, as compared to ZnSe films, the absorption edge is displaced in lower energy region. Analogy of ZnSe:Co films and crystals optical absorption spectra is established. The investigated lines of ZnSe:Co films absorption are caused by electrons optical transitions from  $Co^{2+}$  ion basic condition level  ${}^4A_2(F)$  on the excited states  ${}^4T_1(P)$ ,  ${}^4T_1(F)$  and  ${}^4T_2(F)$  levels split with spin-orbit interaction.

УДК 546.49

Ю. Ф. Ваксман, Ю. А. Ницук, Ю. Н. Пуртов, А. С. Насибов, П. В. Шапкин

#### **ПОЛУЧЕНИЕ И ОПТИЧЕСКИЕ СВОЙСТВА ПЛЕНОК ZnSe:Co**

Пленки ZnSe:Co были получены путем термического напыления в вакууме. Исследованы спектры оптической плотности в области 4-0.38эВ. Установлено, что в пленках ZnSe:Co, по сравнению с пленками ZnSe, край поглощения смещается в низкоэнергетическую область. Установлена аналогия спектров оптического поглощения пленок и кристаллов ZnSe:Co. Исследуемые линии поглощения в пленках ZnSe:Co объясняются оптическими переходами электронов с уровня основного состояния  ${}^4A_2(F)$  иона  $Co^{2+}$  на расщепленные спин-орбитальным взаимодействием уровни возбужденных состояний  ${}^4T_1(P)$ ,  ${}^4T_1(F)$  и  ${}^4T_2(F)$ .

УДК 546.49

Ю. Ф. Ваксман, Ю. А. Ніцук, Ю. М. Пуртов, О. С. Насібов, П. В. Шапкін

#### **ОТРИМАННЯ І ОПТИЧНІ ВЛАСТИВОСТІ ПЛІВОК ZnSe:Co**

Плівки ZnSe:Co були отримані шляхом термічного напилення в вакуумі. Досліджені спектри оптичної густини в області 4-0.38eV. Встановлено, що в плівках ZnSe:Co, в порівнянні з плівками ZnSe, край поглинання зміщується в низкоенергетичну область. Встановлена аналогія спектрів оптичного поглинання плівок і кристалів ZnSe:Co. Досліджені лінії поглинання плівок ZnSe:Co пояснюються оптичними переходами електронів з рівня основного стану  ${}^4A_2(F)$  іона  $Co^{2+}$  на розщеплені спин-орбітальною взаємодією рівні збуджених станів  ${}^4T_1(P)$ ,  ${}^4T_1(F)$  і  ${}^4T_2(F)$ .

S. V. AMBROSOV<sup>2</sup>, O. Yu. KHETSELIUS<sup>1</sup>, A. V. IGNATENKO<sup>2</sup>

<sup>1</sup> I. I. Mechnikov Odesa National University, Odessa, Ukraine

<sup>2</sup> Odesa State Ecological University, Odessa, Ukraine

## WANNIER-MOTT EXCITONS AND H, RB ATOMS IN A DC ELECTRIC FIELD: STARK EFFECT

A numerical calculation of the DC Stark effect for H, Rb atoms and Wannier-Mott exciton in an external uniform DC electric field is carried out within the operator Glushkov-Ivanov perturbation theory method

### INTRODUCTION

Observation of the Stark effect in a constant (DC) electric field near threshold in hydrogen and alkali atoms led to the discovery of resonances extending into the ionization continuum by Glab et al and Freeman et al (c.f. [1–5]). Calculation of the atomic characteristics in a strong electric DC field remains very important problem of modern atomic physics and physics of semiconductors too [6–30]. It is well known [28] that the availability of excitons in semiconductors resulted experimentally in the special form of the main absorption band edge and appearance of discrete levels structure (f.e. hydrogen-like spectrum in  $\text{Cu}_2\text{O}$ ). Beginning from known papers of Gross-Zaharchenya, Thomas and Hopfield et al (c.f. [28–30]), a calculation procedure of the Stark effect for exciton spectrum attracts a deep interest permanently. As it is well known [11], external electric field shifts and broadens the bound state atomic levels. The standard quantum-mechanical approach mutually relates complex eigen-energies (EE)  $E = E_r + 0,5iG$  and complex eigen-functions (EF) to the resonances' shape. The calculation difficulties in the standard quantum mechanical approach are well known [3]. In refs. [10–13] a principally new consistent uniform quantum — mechanical approach to the non-stationary state problems solution had been developed including the Stark effect and also the scattering problems. The essence of the method is the inclusion of the well known method of “distorted waves approximation” in the frame of the formally exact PT [11]. The zeroth order Hamiltonian  $H_0$  of this PT possesses only stationary bound and scattering states. In order to overcome the formal difficulties, the zeroth order Hamiltonian was defined using the set of the orthogonal EF and EE without specifying the explicit form of the corresponding zeroth order potential. This method is called the operator PT (OPT) approach: Glushkov-Ivanov OPT [10–12]. It is very important to note that the hamiltonian  $H_0$  is defined so that it coincides with the general Hamiltonian  $H$  at  $\varepsilon \Rightarrow 0$ . ( $\varepsilon$  is the electric field strength). Let us note that perturbation in OPT does not coincide with the electric field potential though they disappear simultaneously. An influence of the corresponding electric potential model function choice on the values of the Stark resonances energies and bandwidths does not significantly change the final results for the resonances shifts and widths [11, 12]. All said above regards the

Wannier-Mott exciton characteristics in semiconductors as well. In ref. [13–17] the OPT approach have been used for solution of the isotopes separation problem and an account of the non-hydrogenic effects was done as well as the improvement of the convergence procedure. In ref. [18–24] the OPT approach have been successfully used for studying new laser-electron nuclear spectral effects in thermalized plasma (speech is about new cooperative laser-electron- nuclear processes), new laser-electron-nuclear effects in atoms, ions and diatomic molecules. There is very effective application of the OPT approach in conjunction with S-matrix Gell-Mann and low formalism to studying the resonance states of compound super-heavy nucleus and electron-positron pair production in heavy nucleus and ions collisions and under availability of the external superintense electromagnetic field, when the EPPP channel is opened [22–24].

In this paper we have used the OPT method [11, 12] for studying and exact calculation of the DC Stark effect for hydrogen, rubidium atoms and Wannier-Mott exciton in an external uniform DC electric field (excitons in the  $\text{Cu}_2\text{O}$  semiconductor, yellow series).

### GLUSHKOV-IVANOV OPERATOR PERTURBATION THEORY APPROACH

As usually, the Schrödinger equation for the electronic eigen-function taking into account the uniform DC electric field and the field of the nucleus (Coulomb units are used: a unit is  $\hbar^2 / Ze^2 m$  and a unit of  $mZ^2 e^4 / \hbar^2$  for energy) looks like:

$$[-(1 - N/Z)/r + \varepsilon z - 0,5\Delta - E]\psi = 0 \quad (1)$$

where  $E$  is the electronic energy,  $Z$  — charge of nucleus,  $N$  — the number of electrons in atomic core. Our approach allow to use more adequate forms for the core potential (c.f. [25–27]) for multielectron atoms. The detailed theory of the Stark effect for multielectron systems is given in ref. [3, 14]. After separation of variables, equation (1) in parabolic co-ordinates could be transformed to the system of two equations for the functions  $f$  and  $g$ :

$$f'' + \frac{|m|+1}{t} f + [0,5E + (\beta_1 - N/Z) / t - 0,25 \varepsilon(t) t] f = 0 \quad (2)$$

$$\text{Im}E = G/2 = \pi \langle \Psi_{Eb} | H | \Psi_{Es} \rangle^2 \quad (7)$$

$$g'' + \frac{|m|+1}{t} g' + [0,5E + \beta_2/t + 0,25 \varepsilon(t) t] g = 0 \quad (3)$$

coupled through the constraint on the separation constants:  $\beta_1 + \beta_2 = 1$ .

For the uniform electric field  $\varepsilon(t) = \varepsilon$ . In ref. [11], the uniform electric field  $\varepsilon$  in (3) and (4) was substituted by model function  $\varepsilon(t)$  with parameter  $\tau$  ( $\tau = 1.5 t_2$ ). Here we use similar function, which satisfies to necessary asymptotic conditions (c.f. [11, 12]):

$$\varepsilon(t) = \frac{1}{t} \varepsilon \left[ (t - \tau) \frac{\tau^2}{\tau^2 + t^2} + \tau \right]. \quad (4)$$

Potential energy in equation (4) has the barrier. Two turning points for the classical motion along the  $\eta$  axis,  $t_1$  and  $t_2$ , at a given energy  $E$  are the solutions of the quadratic equation ( $\beta = \beta_1, E = E_0$ ). It should be mentioned that the final results do not depend on the parameter  $\tau$ . It is necessary to know two zeroth order EF of  $H_0$ : bound state function  $\Psi_{Eb}(\varepsilon, \nu, \varphi)$  and scattering state function  $\Psi_{Es}(\varepsilon, \eta, \varphi)$  with the same EE in order to calculate the width  $G$  of the concrete quasi-stationary state in the lowest PT order. Firstly, one would have to define the EE of the expected bound state. It is the well known problem of states quantification in the case of the penetrable barrier. We solve the (2, 3) system here with the total Hamiltonian  $H$  using the conditions [11]:

$$\begin{aligned} f(t) &\rightarrow 0 \text{ at } t \rightarrow \infty \\ \partial x(\beta, E) / \partial E &= 0 \end{aligned} \quad (5)$$

with

$$x(\beta, E) = \lim_{t \rightarrow \infty} [g^2(t) + \{g'(t)/k\}^2] t^{|m|+1}.$$

These two conditions quantify the bounding energy  $E$ , with separation constant  $\beta_1$ . The further procedure for this two-dimensional eigenvalue problem results in solving of the system of the ordinary differential equations(2, 3) with probe pairs of  $E, \beta_1$ . The bound state EE, eigenvalue  $\beta_1$  and EF for the zero order Hamiltonian  $H_0$  coincide with those for the total Hamiltonian  $H$  at  $\varepsilon \Rightarrow 0$ , where all the states can be classified due to quantum numbers:  $n, n_1, l, m$  (principal, parabolic, azimuthal) that are connected with  $E, \beta_1, m$  by the well known expressions. We preserve the  $n, n_1, m$  states-classification in the  $\varepsilon \neq 0$  case. The scattering states' functions must be orthogonal to the above defined bound state functions and to each other. According to the OPT ideology [11, 12], the following form of  $g_{Es}$  is possible:

$$g_{Es}(t) = g_1(t) - z_2' g_2(t) \quad (6)$$

with  $f_{Es}$ , and  $g_1(t)$  satisfying the differential equations (2) and (3). The function  $g_2(t)$  satisfies the non-homogeneous differential equation, which differs from (3) only by the right hand term, disappearing at  $t \Rightarrow \infty$ . The coefficient  $z_2'$  ensures the orthogonality condition and is defined as [11]:

$$z_2' = \frac{\{ \int d\zeta d\eta (\zeta + \eta) f_{Eb}^2(\zeta) g_{Eb}(\eta) g_1(\eta) \}}{\{ \int d\zeta d\eta (\zeta + \eta) f_{Eb}^2(\zeta) g_{Eb}(\eta) g_2(\eta) \}}$$

The imaginary part of state energy in the lowest PT order is [11]:

with the general Hamiltonian  $H$  (G- resonance width). The state functions  $\Psi_{Eb}$  and  $\Psi_{Es}$  are assumed to be normalized to unity and by the  $\delta(k - k')$ -condition, accordingly. Note then that the whole calculation procedure at known resonance energy  $E$  and separation parameter  $\beta$  has been reduced to the solution of one system of the ordinary differential equations. For its solution we use our numeral atomic code ("Superatom" package [3, 10–16, 24–27]).

## STARK RESONANCES ENERGIES AND WIDTHS CALCULATION RESULTS FOR ATOMS

The calculation results for Stark resonances energies and bandwidths for some states of H atom are presented in Table 1. For comparison we have indicated the data, obtained within another approach — complex eigen-values and numerical calculation (c.f. [1, 3, 11]). In fig.1 we present the dependence of critical field strength upon the effective quantum number for  $n^*$  for atoms of  $Na, Rb$ : dots — experiment; solid line 1 — theoretical estimate on the basis of classic treatment; solid line 2 — calculation within naive hydrogen-like approximation; dashed line — our calculation. One can see that the experimental results significantly differ from theoretical estimates in classical treatment and naive hydrogen-like approximation (solid lines 1, 2), in particular the difference is about 15–20% and strongly overcomes the experiment error. Our calculation results are in a good agreement with experiment.

Table 1  
The energies  $E_r$  (at. units) and widths  $G$  (at. units) of Stark resonances of the hydrogen atom in a DC electric field with strength:  $\varepsilon = 6,5 \text{ kV/cm}$ .

(n n <sub>1</sub> n <sub>2</sub> m)	$E_r$ , Ref. [5]	$G$ , Ref. [5]	$E_r$ , Present paper	$G$ , Present paper
24,23,0,0	0,1192	0,2752	0,1194	0,2754
25,23,1,0	0,2748	1,0868	0,2749	1,0871
25,23,0,1	0,8298	0,7484	0,8301	0,7487
25,24,0,0	1,4329	0,4175	1,4331	0,4177

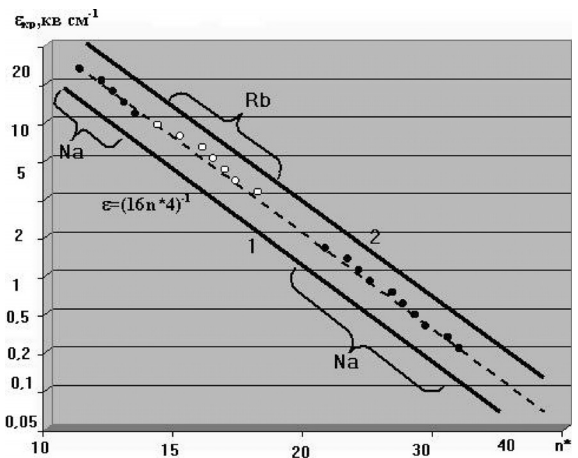


Fig. 1. Dependence of critical field strength upon the effective quantum number for  $n^*$  for atoms of  $Na, Rb$ : dots — experiment; solid line 1 — theoretical estimate on the basis of classic treatment; solid line 2 — calculation within naive hydrogen-like approximation; dashed line — our calculation

## WANNIER-MOTT EXCITONS IN A DC ELECTRIC FIELD

The analogous method can be formulated for description of the Stark effect in the Wannier-Mott exciton in semiconductors (CdS, Cu2O). The Schrodinger equation for the Wannier-Mott exciton has a standard form:

$$[-\hbar^2\nabla_e^2/2m_e^* - \hbar^2\nabla_h^2/2m_h^* - e^2/\epsilon r_{eh} - eEr_e - eEr_h]\Psi = E\Psi. \quad (8)$$

Here all notations are standard. A vector potential is as follows:  $A(r)=1/2 [Hr]$ . Under transition to system of exciton masses centre by means of introducing the relative coordinates:  $r = r_e - r_h$

$$\rho = (m_e^*r_e + m_h^*r_h)/(m_e^* + m_h^*),$$

one could rewrite (9) as:

$$[-\hbar^2\nabla^2/2\mu - e^2/\epsilon r - \hbar/2 \cdot (1/m_h^* - 1/m_e^*)K \cdot p - eEr]F = [E - \hbar^2K^2/8\mu]F. \quad (9)$$

This equation then could be solved by the method, described above. Preliminary estimates show that this approach, in a case of electric DC field, gives the results for Stark states in a reasonable agreement with known results of Thomas and Hopfield (TH) [28–30]. According to our advanced calculation, the Stark shift for the n=2 state of excitons in the Cu<sub>2</sub>O semiconductor (yellow series) at the electric field strength 600 V/cm results in  $-3,1 \cdot 10^{-4}$  eV. This value agrees well with experimental data of Gross et al. [28]. Ionization of the exciton in an electric DC field occurs if a change of potential on a small enough distance (the orbits diameter) is comparable with a bonding energy of particle on this orbit. According to data of Gross et al., the corresponding electric field is  $\sim 9 \cdot 10^3$  V/cm. Our calculation agrees with this value.

**Acknowledgements.** Authors would like to thank Prof. A. Glushkov for task proposal and useful critical comments.

### References

1. *Matter in super-intense laser fields.* Eds. / D. Batani, C. J. Joachain. — AIP Serie. — 2006.
2. *Superintense Laser Atoms Physics.* Eds. / C. A. Ullrich, S. Erhard, E. K. Gross. — N-Y: Kluwer, 2005.
3. *Glushkov A. V.* Atom in electromagnetic field. — Kiev: KNT, 2005. — 400 p.
4. *Lisitsa V. S.* New in Stark and Zeemane effects for Hydrogen Atom // *Usp. Fiz. Nauk.* — 1987. — Vol. 153, N 3. — P. 379–422.
5. *Harmin D. A.* Theory of the Non hydrogenic Stark Effect // *Phys. Rev. Lett.* — 1982. — Vol. 49, N 2. — P. 128–131.
6. *Mercouris T., Nikolaidis C. A.* Solution of the many-electron many-photon problem for strong fields: Application to Li<sup>+</sup> in one and two-colour laser fields // *Phys. Rev. A.* — 2003. — Vol. 67. — P. 063403-1-063403-12.
7. *Krajewska K., Kaminski J. Z., Potvliege R. M.* Stabilization of Resonance States in Crossed Magnetic and Laser Fields in a Parabolic Quantum Well // *Laser Physics.* — 2005. — Vol. 15, N 2. — P. 238–244.
8. *Benvenuto F., Casati G., Shepelyansky D. L.* Rydberg Stabilization of atoms in strong fields: “magic” mountain in chaotic sea // *Z. Phys. B.* — 1994. — Vol. 94. — P. 481–486.
9. *Dando P. A., Monteiro T. S.* Atoms in Static Fields: Chaos or Diffraction // *Photonic, Electronic, Atomic Collisions.* — Singapore: World Sci. Pub. — 1997. — P. 621–630.

10. *Glushkov A. V.* Negative Ions of inert Gases // *JETP Lett.* — 1992. — Vol. 55, N 2. — P. 97–100.
11. *Glushkov A. V., Ivanov L. N.* DC Strong-Field Stark-Effect: Consistent Quantum-mechanical Approach // *J. Phys. B: At. Mol. Opt. Phys.* — 1993. — Vol. 26, N 16. — P. L379–L386.
12. *Glushkov A. V., Ivanov L. N.* DC Strong-Field Stark-Effect: new consistent quantum-mechanical approach // Preprint N 92-1-AS.- Institute for Spectroscopy of RAN. — Moscow, 1992. — 13 p.
13. *Glushkov A. V., Ivanov L. N.* QED theory of shift and deformation of the radiation atomic lines in a laser field // Proc. 3<sup>rd</sup> Symposium on Atomic Spectroscopy. — Chernogolovka (Russia). — 1992. — P. 113–125.
14. *DC Strong Field Stark Effect for Non-hydrogenic Atoms: Consistent Quantum Mechanical Approach / A. V. Glushkov, S. V. Ambrosov, A. V. Ignatenko, D. A. Korchevsky // Int. Journ. Quant. Chem.* — 2004. — Vol. 99, N 5. — P. 936–949.
15. *Glushkov A. V., Ambrosov S. V.* et al, Resonances in Quantum Systems in strong external fields: Consistent Quantum Approach // *Journal of Technical Physics.* — 1997. — Vol. 38, N 2. — P. 215–218.
16. *Glushkov A. V., Dan'kov S. V., Prepelitsa G. P.* et al, QED Theory of nonlinear Interaction of the complex atomic systems with laser field. Multiphoton Resonances // *J. Techn. Phys.* — 1997. — Vol. 38, N 2. — P. 219–224.
17. *Glushkov A. V., Ambrosov S. V., Ignatenko A. V.* Non-hydrogenic Atoms and Wannier-Mott Excitons in a DC Electric Field: Photoionization, Stark Effect, Resonances in Ionization Continuum and Stochasticity // *Photoelectronics.* — 2001. — Vol. 10. — P. 103–106.
18. *Cooperative Laser-Electron-Nuclear Processes: QED Calculation of Electron Satellites Spectra for Multi-Charged Ion in Laser Field / A. V. Glushkov, S. V. Malinovskaya, Yu. G. Chernyakova, A. A. Svinarenko // Int. Journ. Quant. Chem.* — 2004. — Vol. 99, N 5. — P. 889–894.
19. *QED calculation of the superheavy elements ions: energy levels, radiative corrections and hyperfine structure for different nuclear models / A. V. Glushkov, S. V. Ambrosov, A. V. Loboda, A. V. Svinarenko, Yu. G. Chernyakova, O. Yu. Khetselius // Nucl. Phys. A.* — 2004. — Vol. 734. — P. e21–24.
20. *Manifestation of the new laser-electron nuclear spectral effects in thermalized plasma: QED theory of cooperative laser-electron-nuclear processes / A. V. Glushkov, S. V. Malinovskaya, G. P. Prepelitsa, V. M. Ignatenko // J. Phys. CS.* — 2005. — Vol. 178. — P. 199–206.
21. *Consistent quantum approach to new laser-electron-nuclear effects in diatomic molecules / A. V. Glushkov, S. V. Malinovskaya, A. V. Loboda, G. P. Prepelitsa // J. Phys. CS.* — 2006. — Vol. 35. — P. 420–424.
22. *Glushkov A. V.* Energy Approach to Resonance states of compound super-heavy nucleus and EPPP in heavy nucleus collisions // *Low Energy Antiproton Phys., AIP Serie.* — 2005. — Vol. 796. — P. 206–210.
23. *Resonance states of compound super-heavy nucleus and EPPP in heavy nucleus collisions / A. V. Glushkov, V. D. Rusov, S. V. Ambrosov, A. V. Loboda // New Projects and New Lines of research in Nuclear physics. Eds. Fazio G., Hanappe F. — Singapore: World Sci., 2003. — P. 142–154.*
24. *Ivanov L. N., Ivanova E. P., Knight L.* Energy Approach to consistent QED theory for calculation of electron-collision strengths // *Phys. Rev. A.* — 1993. — Vol. 48, N 6. — P. 4365-74.
25. *Glushkov A. V., Ivanov L. N.* Radiation Decay of Atomic States: atomic residue and gauge non-invariant contributions // *Phys. Lett. A.* — 1992. — Vol. 170(1). — P. 33–38.
26. *High order corrections in the Relativistic Perturbation Theory with the model Zeroth Approximation, Mg-like and Ne-like ions / E. P. Ivanova, L. N. Ivanov, A. V. Glushkov, A. E. Kramida // Phys. Scripta* — 1985. — Vol. 32, N 4. — P. 512–524.
27. *Glushkov A. V., Ivanova E. P.* Theoretical Study of Multi-charged Ions Spectra of Ne- and F- isoelectronic sequences // *J. Quant. Spectr. Rad. Transfer.* — 1986. — Vol. 36, N 2. — P. 127–145.
28. *Electron-Hole Drops in Semiconductors.* Eds. / K. D. Jeffriss, L. V. Keldysh. — Moscow, 1988.
29. *Agranovich V. M., Ginzburg V. L.* Crystals Optics with Account of Space dispersion and Theory of Exciton. — Moscow, 1979.
30. *Dynamical Effects in Multicomponent Gas of Quasiparticles / M. C. Brodin, I. V. Blonsky, B. M. Nitsovich, B. B. Nitsovich. — K.: Nauk. Dumka, 1990. — 176 p.*

UDC 539.184

S. V. Ambrosov, O. Yu. Khetselius, A. V. Ignatenko

**WANNIER-MOTT EXCITON AND H, Rb ATOM IN A DC ELECTRIC FIELD: PHOTOIONIZATION, STARK EFFECT**

A numerical calculation of the DC Stark effect for H, Rb atoms and Wannier-Mott exciton in an external uniform DC electric field is carried out within the operator Glushkov-Ivanov perturbation theory method.

УДК 539.184

С. В. Амбросов, О. Ю. Хецелиус, Г. В. Игнатенко

**ЭКСИТОН ВАНЬЕ-МОТТА І АТОМИ Н, Rb У ПОСТІЙНОМУ ЕЛЕКТРИЧНОМУ ПОЛІ: ШТАРК ЕФЕКТ**

На підставі методу операторної теорії збурень Глушкова-Іванова виконано розрахунок Штарк-ефекту для атомів **H, Rb** та екситонів Ван'є-Мотта (напівпровідник  $Cu_2O$ ) у однорідному електричному полі.

УДК 539.184

С. В. Амбросов, О. Ю. Хецелиус, А. В. Игнатенко

**ЭКСИТОН ВАНЬЕ-МОТТА И АТОМЫ Н, Rb В ПОСТОЯННОМ ЭЛЕКТРИЧЕСКОМ ПОЛЕ: ШТАРК ЭФФЕКТ**

На основе метода операторной теории возмущений Глушкова-Иванова выполнен расчет Штарк-эффекта для атомов **H, Rb** и экситона Ванье-Мотта (полупроводник  $Cu_2O$ ) в однородном электрическом поле.

## PHOTODETECTOR ON THE BASE OF UNI-JUNCTION TRANSISTOR AND PHOTO-DIODE

Uni-junction transistor, often named two-base diode consists of the semiconductor plate with two Ohmic contacts and  $p$ - $n$ -junction. Charge carriers, injected from the emitter change the resistance between the base contacts that causes the change of the current  $J_{B_1B_2}$ , namely the output current. Input (the circuit  $p$ - $n$ -emitter – the base  $B_1$ ) volt-ampere characteristics of uni-junction pertains to the  $S$ -type [1]. Such transistor is the simplest element playing the role of the base for construction of the generator of the relaxation oscillations. The scheme of this generator contains the minimal number of the elements, and thus, is simple and stable in operation.

The converters of the different physical values (light, temperature, pressures, etc.) with the frequency output on the base of the uni-junction transistor are broadly used in the technique [2]. The generators on the base of the uni-junction phototransistor (UPhT) are used as the sensor-photo-detectors with the frequency output. The linear dependence of the frequency on the intensity of the light flow and the sensitivity to the weak light signals are the actual problem in this case.

The characteristics of the combined photo-detector on the base of the UPhT with the photo-diode in the input circuit, offered in [3], with the scope of the photosensitivity enhancement and the achievements of the characteristics of the frequency-light's intensity are discussed in this work. Schematic design of the cubic structure photo-detector is presented on Fig. 1.

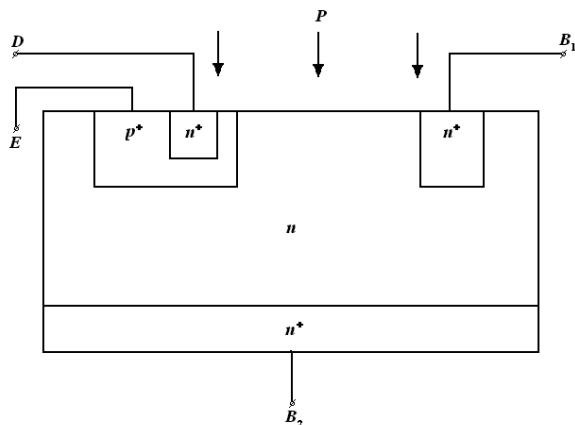


Fig. 1. Scheme of UPhT construction

The semiconductor crystal of the  $n$ -type conductivity contains two Ohmic base contacts of the  $n^+$ -type conductivity (contacts  $B_1$  and  $B_2$ ), as well as injection emitter  $p$ - $n$ -junction  $E$  (the region of the  $p^+$ -type) with the electric connectors. Unlike the known design the addition  $n^+$ -region  $D$  is created in the  $p^+$ -region.

The work of the UPhT in the scheme of the relaxation generator of the vibration is possible to illustrate as follows (Fig. 2).

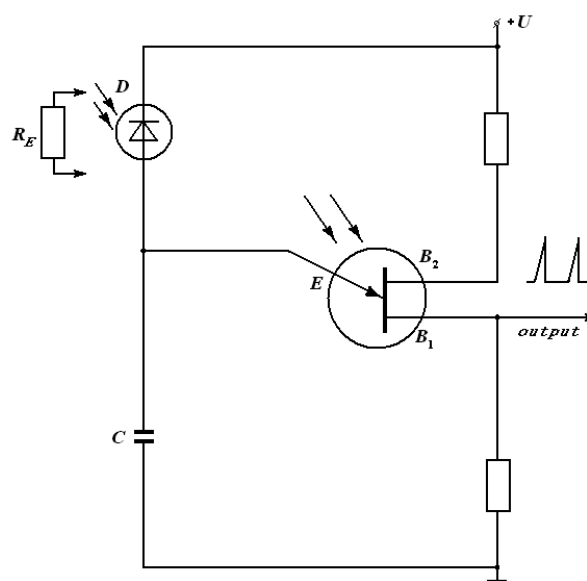


Fig. 2. Generator of the relaxation oscillations

The capacitor  $C$  in usual scheme of the relaxation generator in the circuit of the emitter's network is charged through resistance  $R_E$ . The frequency of the vibrations is defined as

$$f = \left[ R_E C \ln \frac{U - U_0}{U - U_t(P)} \right]^{-1}, \quad (1)$$

where  $U_C$ ,  $U_0$  – voltage of the connection of the emitter and the remaining voltage on it in the switching on condition,  $U$  – voltage of the power supply.

The capacitor  $C$  is charged when the power source is switched on. The injection through  $p$ - $n$ -junction increases in avalanche way, when the capacitor  $C$  is charge to turn-on voltage  $V_r$ . The discharge of the capacitor  $C$  happens after this, through the circuit  $E$ - $B_1$ . The structure is switched on after the discharge on the capacitor and the current in the input circuit decreases, the process of the changing of the capacitor begins once again and again. As the values  $U_0$  and  $U_t$  are stable as to the changes of the temperature, therefore period and frequency of the oscillations of the relaxation generator are enough stable. At the il-

illumination of a part of the semiconductor crystal between the emitter E and the base B1 causes the voltage of the switching on  $U_t$  to be the primary parameter, which depends on the intensity of the light flow  $P$ . The voltage of switching  $U_t = I_{B1B2} \cdot r_{B1}$ , where  $r_{B1}$  – is the resistance of the input element of the UPhT's base,  $I_{B1B2}$  – the current of the base. The resistance  $r_{B1}$  is decreased as the photo-resistor is illuminated what leads to the decrease of the voltage  $U_t(P)$ . As follows from (1), the frequency of the oscillations  $f$ , starting from voltage  $U_0(P)$ , increases nonlinearly with the growth of the light flow.

In present work, we propose to use the generator of the relaxation oscillations voltage drop instead of resistor  $R_E$ , the bias of the  $p^+ - n^+$ -diode (the circuit  $E - D$ , Fig. 1), where a saturation current generator is placed in the circuit of the emitter power supply. The current practically does not depend on the voltage. In this case the current during charge of the capacitor  $C$  is constant and the voltage drop on it increases linearly in time. The equation (1) is, thus, simplified considerably:

$$f = \frac{I_s}{C(U_t - U_0)} \approx \frac{I_s}{C \cdot U_t}, \quad (2)$$

since usually  $U_t \gg U_0$ . Here  $I_s$  – the reverse-bias current (the saturation current) of the  $p^+ - n^+$ -junction.

At illumination switched on, at one hand, as it is shown above, the voltage of the switching on  $U_t(P)$  is decreased. At the other hand, the reverse-bias current grows with the value of the photocurrent  $I_{ph}$  at illumination of the  $p^+ - n^+$ -junction. Accordingly, the frequency of the output signal oscillations under illumination

$$f = \frac{I_s + I_{ph}}{C U_{CPh}}. \quad (3)$$

As it is well known, the photocurrent of the photo-diode is described by linear dependence on the intensity of the light flow  $P$ .

We should note, also, one particularity of the combined photo-detector. The  $n - p^+ - n^+$ -structure in input circuit ( $B_2 - E - D$  electrodes, Fig. 1) acts as bipolar transistor, current of the collector which under illumination is equal to  $I_s + I_{ph}$ . This current is multiplied by the value of the amplifier's coefficient  $\beta = 1/(1 - \alpha)$ , where  $\alpha$  is the coefficient of the current's transfer of the transistor in scheme with the general base [1]. Thereby, under  $I_{ph} \gg I_s$  the frequency of the relaxation generator at the illumination of the combined photo-detector equals to

$$f_{ph} = \frac{\beta I_{ph}}{C U_{ph}}. \quad (4)$$

The relative change of the generator's frequency at illumination is  $I_{ph}\beta/I_s$  times greater, than in usual UPhT (with resistor  $R_E$  in emitter circuit). Taking into account that the coefficient of the transfer  $\alpha$  weakly depends on the illumination intensity, it is possible to consider that the frequency of the generator based on the oscillations photo-detector changes linearly with the intensity value of the light flow.

The combined photo-detector on the base of silicon crystal of the cubic form with size  $200 \times 200 \times 200 \mu\text{m}$  was studied experimentally (Fig. 1). The sizes of contacts were as follows:  $B_1 - 100 \times 40 \mu\text{m}$ ,  $B_2 - 200 \times 200 \mu\text{m}$ , emitter  $E$  ( $p^+$ -type) –  $100 \times 40 \mu\text{m}$ , the additional  $n^+$ -region ( $D$ ) –  $50 \times 20 \mu\text{m}$ . The illumination of the samples was provided with the infrared light-emitting diode AL119B ( $\lambda = 0.93 \dots 0.96 \mu\text{m}$ ). Power of the radiation of the light-emitting diode at the current value of 300 mA was not less than 40 mW. The practically linear graph of the dependence of the emitter's voltage switching on  $U_t(P)$  on the light flow intensity  $P$  is presented at Fig. 3.

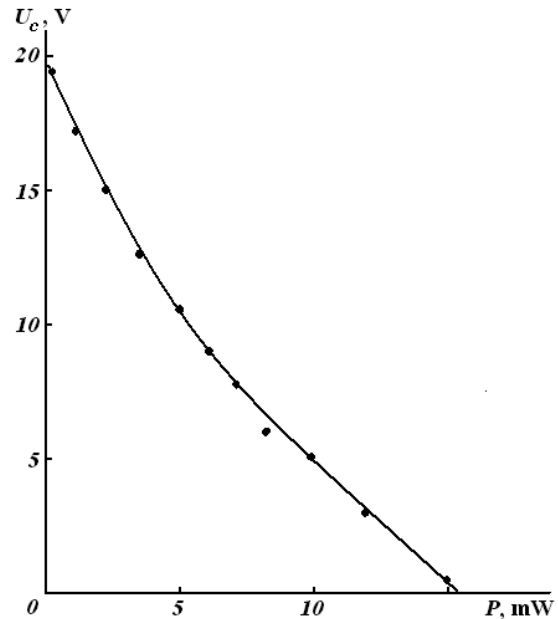


Fig. 3. Dependence of the emitter's turn-up voltage on the intensity of light

The dependence of the relaxation generator frequency  $f$  on the illumination intensity is presented at Fig. 4. The curve 1 was measured for the case, when the electrode  $D$  is switched off and the resistance  $R_E$  is switched on in the circuit of the emitter's power supply, i.e. for the simplest scheme of the UPhT's relaxation generator. The sensitivity of the frequency  $K = \Delta f / \Delta P \approx 0.5 \text{ kHz/mW}$ . The dependence  $f=f(P)$  for the combine photo-detector is presented by curve 2, Fig. 4.

It could be seen that this dependence is practically linear and the sensitivity on frequency is much higher ( $K \approx 7 \text{ kHz/mW}$ ).

It should be noted that the presence of additional bipolar photo-transistor in scheme of the combined photo-detector does not define significant increase of the photo-signal since for bipolar structure specified in this case and the coefficient of the current transfer  $\alpha$  is not large due to small value of the injection's coefficient. However, even though  $\alpha \approx 0.5$ , the amplifier's coefficient  $\beta \approx 2$ . The respective contribution to the increase of the photosensitivity of this structure could be achieved as the result of additional structural element inclusion.

Thus, we have shown the possibility to raise the linearity of the output signal and enlarge the sensitivity of the sensor on the base of uni-junction photo-

transistor through introduction of the additional  $n^+$ -region into  $p^+$ -emitter of the photo-transistor.

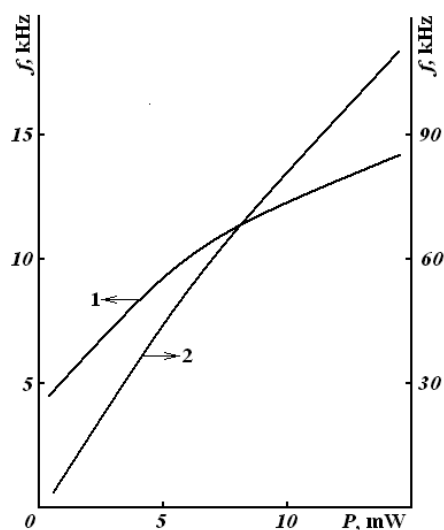


Fig. 4. Dependence of the frequency on the intensity of light 1 — regular UPhT, 2 — combined photo-detector

#### References

1. *Vikulin I. M., Stafeev V. I.* Physics of Semiconductor Devices // Moscow: Radio and Communication, 1999. — 345 p.
2. *Babichev G. G., Gavrylyuk G. P.* et al. Converter of Pressure with Frequency Output on the Base of Uni-junction Tensotransistors // Technology and Design in Electronic Devices. — 2004. — N 3. — P. 48–51.
3. Пат. 20016 У Україна, Н01L 31/10. Одноперехідний фототранзистор / І. М. Вікулін, Ш. Д. Курмашев, С. Н. Никифоров, М. І. Панфілов. — Опубл. 15.01.2007 р.

UDC 621.382

I. M. Vikulin, Sh. D. Kurmashev, S. N. Nikiforov, M. I. Panfilov

#### PHOTODETECTOR ON THE BASE OF UNI-JUNCTION TRANSISTOR AND PHOTO-DIODE

The generators on the base of the uni-junction photo-transistor (UPhT) are used as the sensor-photo-detectors with the frequency output. The semiconductor crystal of the n-type conductivity contains two Ohmic base contacts of the  $n^+$ -type conductivity as well as the injection emitter in a form of  $p-n$ -junction (the region of the  $p^+$ -type) with the electric contacts. The possibility to raise the linearity of the output signal and enlarge the sensitivity of the sensor on the base of UPhT was proposed through introduction of additional  $n^+$ -region into  $p^+$ -emitter.

УДК 621. 382

И. М. Викулин, Ш. Д. Курмашев, С. Н. Никифоров, М. И. Панфилов

#### ФОТОПРИЕМНИК НА ОСНОВЕ ОДНОПЕРЕХОДНОГО ТРАНЗИСТОРА И ФОТОДИОДА

Генераторы на основе однопереходных фототранзисторов (ОФТ) используются в качестве сенсоров-фотоприемников с частотным выходом. Полупроводниковый кристалл  $n$ -типа проводимости содержит два омических базовых контакта  $n^+$ -типа проводимости, а также инжектирующий эмиттерный  $p-n$ -переход (область  $p^+$ -типа) с электрическими выводами. Показана возможность повысить линейность выходного сигнала и увеличить чувствительность датчика на основе однопереходного фототранзистора введением дополнительной  $n^+$ -области в  $p^+$ -эмиттер.

УДК 621. 382

І. М. Вікулін, Ш. Д. Курмашев, С. Н. Никифоров, М. І. Панфілов

#### ФОТОПРИЙМАЧ НА БАЗІ ОДНОПЕРЕХІДНОГО ТРАНЗИСТОРА ТА ФОТОДІОДА

Генератори на базі одноперехідних фототранзисторів (ОФТ) використовуються в якості сенсорів-фотоприймачів з частотним вихідом. Напівпровідниковий кристалл  $n$ -типу провідності містить два омичних базових контакти  $n^+$ -типу провідності, а також інжектуєчий емітерний  $p-n$ -перехід (область  $p^+$ -типу) з електричними выводами. Показана можливість підвищення лінійності вихідного сигналу та зростання чутливості датчика на базі ОФТ шляхом введення додаткової  $n^+$ -області в  $p^+$ -емітер.

A. V. GLUSHKOV<sup>2</sup>, Ya. I. LEPIKH<sup>1</sup>, A. P. FEDCHUK<sup>1</sup>, O. Yu. KHETSELIUS<sup>1</sup>

<sup>1</sup>I. I. Mechnikov Odessa National University

<sup>2</sup>Odessa State Environmental University

## ELECTRODYNAMICAL AND QUANTUM - CHEMICAL MODELLING THE ELECTROCHEMICAL AND CATALYTIC PROCESSES ON METALS AND SEMICONDUCTORS: LANTHANIDE PEROVSKITES

The quantum mechanical and electrodynamical approaches are used in problem of the catalytic activity definition for metals, binary metallic alloys and semiconductor materials. There are found the quantitative link between the electron structure parameters of indicated materials and their catalytic activity on example of a simple model reactions of the following type:  $H = H^+ + e$  and  $O_2^- = O_2 + e^-$ . It has been carried the qualitative estimate of catalytic properties for lanthanides perovskites.

### INTRODUCTION

A new approach in electron theory of catalysis, based on the electrodynamical and quantum mechanical models, is being applied to study of catalytic processes on metallic and semiconductor compounds. We studied only those of the electronic structure parameters of these materials which define directly their catalytic activity in simple model reactions of the following type:  $H = H^+ + e$  and  $O_2^- = O_2 + e^-$ . It has been found that the link between the Fermi level position dependence upon the metal alloys components concentration and their catalytic activity is quite tight. A study of catalytic activity for metals, metallic alloys and semiconductors is of a great importance for different practical applications, for example, during the elaboration of electrochemical solid-state energy sources, planning the efficacy of semiconductor sensors, etc. (c.f. [1–12] and ref. there). It is known [8–9] that the components concentration's change in metallic alloys could result in corresponding variation of catalytic activity as well as of electrochemical properties. The attempts of comprehensive quantitative description of the metal-like systems (metallic alloys, heavily doped semiconductors) electronic structure including the description of processes on electrodes' surfaces of the electrochemical solid-state energy sources have been undertaken in a number of papers (c.f. [1–12]), in particular, within conceptual models which use the density functional formalism [2, 3]. In these models a description in the framework of electron density functional on the metals surface is produced. As a result, these models are not enough sensitive to energy value and states density on the Fermi surface. Naturally, there is a great number of papers (c.f. [1–3]), where the catalysis and hemisorption problems are considered within *ab initio* quantum chemistry methods. These calculations give very useful information about processes considered, however, some quite important moments of the physical and chemical nature of these processes often remain up to known degree veiled. As alternative, the effective model approaches have been developed on the basis of the electrodynamical and quantum-chemical modeling, in particular, this approach could be represented by well known model of Lidorenko and others (c.f. [3–12]). In cited refer-

ences, different versions of indicated models and different catalytic materials are considered. In this paper we consider a problem of catalytic activity definition for binary metallic alloys and heavily doped semiconductor materials. We try to find a quantitative link between the electron structure parameters of indicated materials and their catalytic activity on example of a simple model reactions of the following type:  $H = H^+ + e$  (A) and  $O_2^- = O_2 + e^-$  (B). It should be noted that the level (A) often plays the role of limiting factor in the hydration reactions. In paper it has been carried the qualitative estimate of catalytic properties for lanthanides perovskites too. In last years a great interest attracts studying the perovskites which represent the subgroup of oxides of the transition metals [11]. It has been shown that the rare-earth oxides of cobalt RCoO<sub>3</sub> (R-rare-earth -element) can catalise the reaction in the gas phase. This is related to different exchanged perovskites of the following type:  $(La_{1-x}Pb_x)MnO_3$  and  $(Pr_{1-x}Pb_x)MnO_3$ . The perspective application for cited compounds is the photoelectrolysis of water with the aim of obtaining oxygen and hydrogen. As anodes of photoelectrolytic cells such compounds as SrTiO<sub>3</sub>, BaTiO<sub>3</sub> and others can be used. The biggest efficiency coefficient (10%) has been obtained in the cell with SrTiO<sub>3</sub> of n-type under radiating by light with the photon energy which is less the forbidden zone width. In order to understand the catalytic properties of the cited compounds it is necessary to know electron characteristics of materials and mechanisms of the adsorption and charge transfer processes. As the first step a qualitative estimate of catalytic properties of the cited substances is very much desirable.

### SCOPE OF THE PAPER AND MODEL USED

The electron structure of metallic system in the used approximation could be approximated by a set of isotropic s-d bands [4, 5]. The static dielectric permeability is represented as follows:

$$\varepsilon = 1 + \varepsilon_{ss} + \varepsilon_{dd} + \varepsilon_{sd} + \varepsilon_{ds}, \quad (1)$$

where  $\varepsilon$  (*ij*) describes the contribution into  $\varepsilon$  due to the i-j transitions. In approximation of free electrons the expression for  $\varepsilon_{ss}$  looks as:

$$\varepsilon_{ss} = 2\pi v_s(E_F) k^{-2} \left\{ 1 + \left[ 4(k_F^s)^2 - k^2 \right] \ln \left| (2k_F^s + k) / 2k_F^s - k \right| / 4k_F^s k \right\} \quad (2)$$

where  $k=q a_B$ ;  $q$  – wave number;  $a_B$  – Bohr radius;  $q_F = (3\pi^2 z_i / \Omega)^{1/3}$ ;  $z_i$  – the electrons number in the “i” band;  $v_i(E_F) = N_i(E_F) a_B^3 e^e$ ,  $N_i(E_F)$  – the state density on the Fermi surface in the “i”.

The corresponding expression for  $\varepsilon_{dd}$  is:

$$\varepsilon_{dd} = 2\pi v_d(E_F) k^{-2} |M_{dd}|^2 \left\{ 1 + \left[ 4(k_F^d)^2 - k^2 \right] \ln \left| (2k_F^d + k) / 2k_F^d - k \right| / 4k_F^d k \right\} \quad (3)$$

Here the matrix element  $M_{dd}$  is defined by the superposition of the wave functions for d electrons. The contribution  $\varepsilon(ds)$  is important only for systems containing the non-oxidable precious metals. This contribution is defined as follows:

$$\varepsilon_{ds} = \left[ 2m_s k_d e^2 f_c / \pi \pi^2 k^2 \right] \left\{ 1 + \left[ 4(k_d)^2 - k^2 \right] \ln \left| (2k_d + k) / 2k_d - k \right| / 4k_d k \right\} \quad (4)$$

where  $m_s$  is the effective mass of electron in the conductivity band;  $k_d, f_c$  – numeral parameters [3]. Usually the contribution  $\varepsilon_{ds}$  in (1) for transition metals is about several percents. The effective potential, which imitates an effect of metallic potential field on the inculcated hydrogen atom (for process  $H = H^+ + e$ ) is defined as follows:

$$\Phi(r) = -\frac{2e^2}{\pi r} \int_0^\infty \frac{\sin kr}{k \varepsilon(k)} dk. \quad (5)$$

It is supposed that the problem considered has the spherical symmetry and the crystal potential is fully screened by the conductivity electrons. Substitution of (1) to (5) leads to the following expression:

$$\Phi(r) = -e^2 a/r \exp[-\alpha R] \cos[\alpha R], \quad (6)$$

where

$$\alpha = \left[ \pi^{-1} 12 (k_F^s)^2 \right]^{-1/4} \left\{ v_s(E_F) + (k_F^d / k_F^s) v_d(E_F) + f_c (k_F^d / k_F^s) v_s(E_F) \right\}^{1/4},$$

$$R = 2q_F^s r, \quad a = (k_F^s)^{-1}.$$

The numerical solution of the Schrodinger equation [13] for H atom in a field  $\Phi(r)$  gives the corresponding spectrum of states, which could be continual or discrete depending on the parameter  $\zeta^{-1} = \alpha/a$ . The spectrum is continual, if  $\zeta < \zeta_0 = 0,362$  (c.f. [4] & refs. their) and the corresponding material is a catalyst for the H ionization reaction); if  $\zeta > \zeta_0$ , the spectrum is discrete (metal does not demonstrate catalytic activity for cited reaction). In the binary metallic alloy the Fermi level position  $E_F$  as well as the corresponding state density  $v(E_F)$ , accompanied with electronic structure parameters  $\alpha$  and  $a$  are changing

under change of the admixture concentration  $c$ . It is possible to use the Thomas-Fermi approach As an approximation [14]. We suppose that the admixture's atoms volume has the spherical form. The radius  $R_c$  is connected with concentration by the formula:

$$(qR_c)^{-3} = (qr_s)^{-3}c,$$

where  $r_s$  – the electron gas characteristic parameter. For screened potential  $V(r)$  near the admixture (if  $|\Delta E_F^- - V| < E_F$ ), the corresponding Poisson equation looks as:

$$\Delta V(r) = q^2 \{V(r) - \Delta E_F\} \quad (7)$$

Elementary solution of equation (7) with the boundary conditions:

$$(dV/dr)_{R_c} = 0, \quad V(R_c) = 0, \quad V \rightarrow -Z_v e/r, \quad r \rightarrow 0,$$

where ( $Z_v$  – difference of the components valences) is defined as:

$$V(r, R_c) - \Delta E_F = [-Z_v e/r] \{qR_c \text{ch}[q(R_c - r)]\} / [qR_c \text{ch}(qR_c) + sh(qR_c)] \quad (8)$$

Second boundary condition provides the expression for Fermi level shift in dependence upon the concentration  $c$ :

$$\Delta E_F = Z_v e^2 q / [qR_c \text{ch}(qR_c) + sh(qR_c)] \quad (9)$$

One could see, that for the binary alloy, the value  $v(E_F)$  is substituted by the value  $v(E_F) = v(E_F) + \Delta v(E_F)$ . The parameters, which define the catalytic activity for metallic compounds, are directly dependent upon the components concentration. Let us now establish a link between the electron structure parameters and catalytic activity for the oxygen electrorestoring reaction. We solve again the Schrodinger equation for system: oxygen molecule –electron on the potential field. If negative  $O_2$  ion (experimental value of electron bound energy to oxygen molecule 0,44 eV), has the bound state for given values of (6, 9), then the material under examination is a good catalyst for indicated reaction. Potential  $\Phi$  could be written with an account of the two-center ( $r_a, r_b$ ) approximation as follows:

$$\Phi(r) = -e^2 a/2ra \exp[-\alpha Ra] \cos[\alpha Ra] - e^2 a/2rb \exp[-\alpha Rb] \cos[\alpha Rb]. \quad (10)$$

The solution of Schrodinger equation for oxygen in potential field  $\Phi$  is a well known two-centers problem of quantum mechanics. It is naturally solved in the elliptic coordinates:  $\mu = (r_a + r_b) / R_{ab}$ ,  $\eta = (r_a - r_b) / R_{ab}$ . The variables' separation in the Schrodinger equation and transition to three 1-D differential equations are possible using the approximation:  $1/2 R_{ab}(\mu + \eta) \approx 1/2 R_{ab}\mu$ . Then potential (10) has the form:

$$\Phi(\mu, \eta) = -2\mu a \exp[-\alpha q F^3 R_{ab}\mu] \cos[\alpha q F^3 R_{ab}\mu] / [R_{ab}(\mu^2 - \eta^2)] = g(\mu) / (\mu^2 - \eta^2).$$

The master differential equations system has the following form:

$$\{d/d\mu (\mu^2 - 1) d/d\mu - [\lambda_{ml} + m^2 / (\mu^2 - 1) +$$

$$+ \mu^2 c^2 + R_{ab} g(\mu)/2 \} T_{nlm} = 0 \quad (11)$$

$$\{d/d\eta (-\eta^2 + 1)d/d\eta + [\lambda_{ml} + \eta^2 c^2 m^2 (1 - \eta^2)]\} S_{lm} = 0,$$

$$\{d^2/d\varphi^2 + m^2\} \Sigma_m = 0.$$

Wave function can be represented as follows:

$$\Psi_{nlm} = T_{nlm}(\mu) S_{lm}(\eta) \Sigma_m(\varphi).$$

One- electron energy  $E = -2c^2/Rab^2$  is dependent upon the main quantum number and also the symmetry of quantum numbers  $l, m$ ;  $\lambda_{ml}$  is a coupling constant. Usual molecular orbitals (MO) correspond to the orbitals-solutions (MOS) of (11) as follows:

$$(MO) - (MOS) = 1\sigma_g - 1s\sigma; 1\sigma_u - 2p\sigma; 2\sigma_g - 2s\sigma; \\ 2\sigma_u - 3p\sigma; 3\sigma_g - 3d\sigma; 1\pi_u - 2p\pi; 1\pi_g - 3d\pi; 3\sigma_u - 4p\sigma.$$

The ground configuration of the oxygen molecule:  $1\sigma_g^2 1\sigma_u^2 2\sigma_g^2 2\sigma_u^2 3\sigma_g^2 1\pi_u^4 1\pi_g^2$ . Our task is to calculate the bond energy  $E(1\pi_g)$ . A standard approach to numerical solution is based on the Numerov method and matrix technique with using the Newton-Rafson scheme (c.f. [15-17]). A new, more effective method of the eigen-values definition and functions problem solution, which is based on the operator perturbation theory and Runge-Kutta integration procedure, was proposed in ref. [13, 12, 15-18].

## MODEL TO CATALYTIC ACTIVITY OF SEMICONDUCTORS

Now, let us formulate a new effective approach to description of catalytic processes on semiconductors and determine connection between the semiconductors electron structure parameters and their catalytic activity in the relation to simple model reaction of the  $H = H^+ + e$  type. Above proposed model is transformed through the following way. In order to describe the electronic structure of semiconductor let us use the known Resta model in the Thomas-Fermi theory for semiconductors (c.f. [14]). We consider the model semiconductor as the electron gas with non-perturbed density  $n_0$ . The corresponding Poisson equation is as follows:

$$V(r) = q \{V(r) - A\},$$

where  $q = 4k_f/\pi a_B$  and  $A$  is a constant. Let us suppose that there is the finite screening radius  $R$  near the probing charge  $Z_e$  and  $n(R) = n_0$ . Then a constant  $A$  is equal  $V(R)$ . Beyond the radius  $R$  the point charge  $Z_e$  potential is equal to:  $V(R) = -Ze^2/[\varepsilon(0)r], r > R$ , where  $\varepsilon(0)$  is a static dielectric permeability. Independent solutions for the Poisson equation have the following form:  $Ze^2 \exp[qr]/r$ . So, the general expression for potential energy is:

$$V(r) = -Ze^2/r \{C_1 \exp(qr) + \\ + C_2 \exp(qr)\} + A, r < R. \quad (12)$$

Taking into account the continuity condition, boundary condition ( $V(r) \rightarrow 0, r \rightarrow 0$ ) and formula  $A = V(R)$ , the expression for  $V$  (12) looks as follows:

$$V(r) = -\{Ze^2/r\} \{sh[q(R-r)]/sh[qR] -$$

$$- Ze/\varepsilon(0)R, r < R. \quad (13)$$

The continuity condition for electric field under  $r = R$  allows to define a link between the screening parameter and  $\varepsilon(0)$  as:  $\varepsilon(0) = sh[qR]/qR$ . If  $\varepsilon(0) > 1$ ,  $R$  is equal to finite value comparable with distance to the nearest atoms for example, for Si, Ge semiconductors  $R = 4,4$  a.u.). The Schrödinger equation with potential (12) allows to define the corresponding energy spectrum in dependence upon the parameters  $\varepsilon(0), k_f$  and then a link between the semiconductors electron structure parameters and their catalytic activity likely above described one.

## QUALITATIVE ESTIMATE FOR CATALYTIC ACTIVITY OF THE ABO3 COMPOUNDS

We are interested by a search of the most optimal and active catalyzers of the model reactions  $H = H^+ + e$  and  $O_2^- = O_2 + e^-$  among the compounds ABO3 (B=Fe, Ni, Co; A=La, Ce, Tb, Dy). We have applied our scheme of the electrodynamic modeling for the case of the model reaction  $O_2 + e^- = O_2^-$ . Calculation is resulted in solution of the Schrödinger equation (the Kohn-Sham equations system) for system: oxygen molecule – electron in the potential field of a material. If for the corresponding parameter  $\xi$  the negative ion has the bound state then the material is the catalyzer of reaction. And if the bond energy is more them the catalytic properties will be manifested in the more degree. We present the corresponding bond energies for different compounds in table 1.

Table 1

Bond energies for system $O_2 + e^-$			
Compound	Bond energy, eV	Compound	Bond energy, eV
LaFeO3	1,76	TbFeO3	1,82
LaCoO3	1,75	TbCoO3	1,81
LaNiO3	1,73	TbNiO3	1,78
CeFeO3	1,67	DyFeO3	1,64
CeCoO3	1,67	DyCoO3	1,63
CeNiO3	1,65	DyNiO3	1,61

As the estimate shows, the most active catalyzers among considered materials are the compounds as follows: LaFeO3, LnCoO3, TbFeO3, TbCoO3. It is of a great interest that this is in a full correspondence with preliminary experimental studies [10,11]. It is obvious that the further studying of the electrocatalytic properties of the cited compounds requires the detailed calculation of the electron structure parameters, ab initio quantum modelling catalytic reactions, which possibly run with forming the corresponding adsorption complexes etc.

## CONCLUSIONS

We present here the quantum mechanical and electrodynamic approaches in problem of the catalytic activity definition for metals, metallic and semiconductor materials. On its basis it has been carried the qualitative estimate of catalytic properties for lanthanides perovskites. The proposed approach could

be modified for the semiconductor surface catalytic reactions product and charge exchange processes evaluation and, in such a way, could be used for the semiconductor sensors efficacy prediction for the given reaction type. We believe that approach proposed can be improved on the way of account for the whole number of additional factors (the electrolyte influence, surface effects, electrode potential, the electrolyte type, the electron concentration in the layer and many other [8–12]).

#### References

1. *Glushkov A. V.* Electron theory of Catalysis on Metallic Alloys: Electrodynamical model // *Electrochemistry*. — 1991. — Vol. 27, N 1. — P. 131–133.
2. *Glushkov A. V.* Electron theory of Catalysis on Metals: Quantum Chemical model // *Electrochemistry*. — 1993. — Vol. 29, N 3. — P. 369–376.
3. *Bound States in Catalysis: New electro-dynamical & quantum chemical models in electron theory of catalysis / A. V. Glushkov, V. D. Parkhomenko, P. N. Teybulev, M. V. Belous, A. K. Katashinsky // Uzhgorod Univ. Sci. Herald. Series. Physics*. — 2000. — Vol. 8, N 2. — P. 361–365.
4. *Quantum Chemical Modeling of Catalytic properties of Lanthanide Perovskites / A. V. Glushkov, V. D. Parkhomenko, P. N. Teybulev, M. V. Belous, A. K. Katashinsky // Proc. European Science Foundation REHE School and Workshop on “Spin-Orbit Coupling in Chemical Reactions”, Torun (Poland), 1998. — P. 12.*
5. *Glushkov A. V., Fedchuk A. P., Khetselius O. Yu.* Heavy Elements, Relativistic SOC Effects in Catalysis Processes // *Proc. European Science Foundation REHE School and Workshop on “Spin-Orbit Coupling in Chemical Reactions”, (Poland), 1998. — P. 11.*
6. *Glushkov A. V.* A new approach in Electron theory of Catalysis: Electrodynamical and Quantum Chemical models. Catalysis modeling in Plasma Chemical Reactors // *Proc. 220<sup>th</sup> National Meeting of American Chemical Society: Catalysis and Plasma Technologies, Washington, 2000. — P. 221–224.*
7. *Glushkov A. V.* New Approach in Electron Theory of Catalysis: Electrodynamical and Quantum Mechanical Models for binary metallic alloys // *Proc. 12<sup>th</sup> International Congress on Catalysis, Granada (Spain), 2000. — P. Th31.*
8. *Glushkov A. V.* New Quantum Mechanical and Electro-dynamical Models of the Catalytic Processes on Metallic Systems and Semiconductors // *Proc. 5<sup>th</sup> European Workshop “Quantum Systems in Chemistry and Physics”, Uppsala (Sweden), 2000. — P. 131.*
9. *Vol'kenstein F. F.* Electron Processes on surface of semiconductors under chemisorbtion, Moscow: Nauka, 1991. — 580 p.
10. *Waite R. E., Bockris J., Conway B. E.* Modern Aspects of Electrochemistry, N-Y: Plenum Press, 1993. — Vol. 21.
11. *Austin S.* Material Solid State Batteries, Singapore: World. Sci., 1996. — 370 p.
12. *DC Strong Field Stark Effect for Non-hydrogenic Atoms: Consistent Quantum Mechanical Approach / A. V. Glushkov, S. V. Ambroso, A. V. Ignatenko, D. A. Korchevsky // Int. Journ. Quant. Chem.* — 2004. — Vol. 99, N 5. — P. 936–939.
13. *Glushkov A. V., Ivanov L. N.* DC Strong-Field Stark-Effect: consistent quantum-mechanical approach // *J. Phys. B: At. Mol. Opt. Phys.* — 1993. — Vol. 26, N 16. — P. L379–389.
14. *Lundqvist S., March N.* Theory of Inhomogeneous Electron Gas, N-Y.: Plenum Press, 1993. — 480 p.
15. *Glushkov A. V.* New method for calculation of ionization potentials for molecules by Green's functions method // *Journ. Phys. Chem.* — 1992. — Vol. 66, N 4. — P. 589–596.
16. *Glushkov A. V.* Calculation of molecular constants of diatomic molecules in quasiparticle approximation of density functional // *J. Phys. Chem.* — 1989. — Vol. 63, N 11. — P. 3072–3074.
17. *Glushkov A. V.* Account of 2p-2h correlations in the equations of motion method for complex molecules // *J. Phys. Chem.* — 1990. — Vol. 64, N 11. — P. 3100–3103.
18. *Electrodynamical and quantum — chemical modelling the electrochemical and catalytic processes on metals and semiconductors / A. V. Glushkov, Ya. I. Lepikh, A. P. Fedchuk, O. Yu. Khetselius // Ukr. Phys. Journ.* — 2008, in print.

UDC 541.27:541.128

A. V. Glushkov, Ya. I. Lepikh, A. P. Fedchuk,  
O. Yu. Khetselius

#### ELECTRODYNAMICAL AND QUANTUM - CHEMICAL MODELLING THE ELECTROCHEMICAL AND CATALYTIC PROCESSES ON METALS AND SEMICONDUCTORS: LANTHANIDE PEROVSKITES

The quantum mechanical and electro-dynamical approaches are used in problem of the catalytic activity definition for metals, binary metallic alloys and semiconductor materials. There are found the quantitative link between the electron structure parameters of indicated materials and their catalytic activity on example of a simple model reactions of the following type:  $H = H^+ + e$  and  $O_2^- = O_2 + e^-$ . It has been carried the qualitative estimate of catalytic properties for lanthanides perovskites.

УДК 541.27:541.128

О. В. Глушков, Я. И. Лепих, О. П. Федчук,  
О. Ю. Хецеліус

#### ЕЛЕКТРОДИНАМІЧНЕ ТА КВАНТОВОХІМІЧНЕ МОДЕЛЮВАННЯ ЕЛЕКТРОХІМІЧНИХ ТА КАТАЛІТИЧНИХ ПРОЦЕСІВ НА МЕТАЛАХ ТА НАПІВПРОВІДНИКАХ: ПЕРОВСКІТИ ЛАНТАНІДІВ

Викладено новий квантово- механічний й електродинамічний підхід до визначення каталітичної активності напівпровідникових та бінарних металічних матеріалів. Виявлено кількісну кореляцію параметрів електронної структури шуканих матеріалів і їх каталітичною активністю у відношенні до модельних реакцій типу:  $H = H^+ + e$ ,  $O_2^- = O_2 + e^-$ . Виконано якісну оцінку каталітичних властивостей перовскитів лантанідів.

УДК 541.27:541.128

А. В. Глушков, Я. И. Лепих, А. П. Федчук,  
О. Ю. Хецелиус

**ЭЛЕКТРОДИНАМИЧЕСКОЕ И КВАНТОВОХИМИЧЕСКОЕ МОДЕЛИРОВАНИЕ ЭЛЕКТРОХИМИЧЕСКИХ И КАТАЛИТИЧЕСКИХ ПРОЦЕССОВ НА МЕТАЛЛАХ И ПОЛУПРОВОДНИКАХ: ПЕРОВСКИТЫ ЛАНТАНИДОВ**

Изложен квантово - механический и электродинамический подход к определению каталитической активности полупроводниковых и металлических материалов. Выявлена количественная корреляция параметров электронной структуры изоляционных материалов и их каталитической активности по отношению к модельным реакциям вида:  $H = H^+ + e$ ,  $O_2^- = O_2 + e^-$ . Выполнена качественная оценка каталитических свойств перовскитов лантанидов.

## SILICON SURFACE WITH CLUSTERS

The (111) surfaces of the tetrahedral semiconductors C, Si, and Ge are found to undergo a remarkable variety of surface reconstruction's. A possible common denominator its the apparent occurrence of a  $2 \times 1$  reconstruction on all three surfaces. This holds presumably also for the (111) surface of a-Sn though no experimental data are available for this zero-gap semiconductor. The  $2 \times 1$  reconstruction occurs upon cleavage at low temperatures in Si and Ge, but is only metastable, it transforms irreversibly into the stable  $7 \times 7$  or  $c(2 \times 8)$  structure upon annealing at 500–700 and 380 K, respectively. On diamond the  $2 \times 1$  structure appears upon annealing at  $\sim 1200$  K and is probably the thermodynamically stable surface phase.

The atomic and electronic structures of the (111)  $2 \times 1$  surfaces, especially in the case of silicon, have been extensively studied by a variety of experimental methods: low-energy electron diffraction (LEED), medium-energy ion scattering using the effects of channeling and blocking, scanning tunneling microscopy (STM), angle-resolved photoemission spectroscopy (ARPES), inverse photoemission, surface-induced core-level shift measurements, electron-energy loss spectroscopy (EELS), and optical studies. They are accompanied by powerful total energy calculations to optimize the atomic geometries.

Although the (111) surfaces of covalent semiconductors, particularly of silicon, are the most studied objects in surface physics, questions regarding their structural and electronic properties persist. Whereas the  $2 \times 1$  reconstruction type is given by static LEED measurements the actual surface topology can be extracted only indirectly, from experiment if an appropriate model for the bonding topology and the displacements of surface atoms is available.

The some STM pictures appear to include new structural elements as cluster. Magic numbers (extreme) for these properties are observed which presumably reflect differences in cluster structures of the silicon surface (see fig. 1) [1]. Fig 2 represents STM images acquired from the same region of the cluster deposited Si(111)  $7 \times 7$  surface [2].

The aim of the present paper is the theoretical study of the atomic geometry of a silicon surface for the two fundamental reconstruction models due to formation of the polyhedral and fractal clusters by means of self-consistent total energy minimization procedure [3].

Small Si clusters have usually been produced by pulsed-laser-evaporation methods [4, 5]. Since discovery of visible light emission from por-Si, great deals of efforts have been devoted to investigate the optical properties of Si nanostructures. However, little is known about the electronic states associated with impurity atoms doped into nanostructures, although they are very interesting from the viewpoints of fundamental physics and future applications. Therefore the optical properties of semiconductor nanostructures have been the subject of intense investigations.

Besides the quantum confinement of electrons and holes leads to linear and nonlinear optical properties much different from those of bulk crystals [6, 7].

The study of the structure and properties of semiconductor clusters, particularly silicon clusters, has been an extremely active area of current research [8–11]. Vapour-phase clusters of silicon have been prepared and analyzed for trends in relative abundance and chemical reactivity for  $3 < n < 60$ , where  $n$  is amount of the atoms at the cluster.

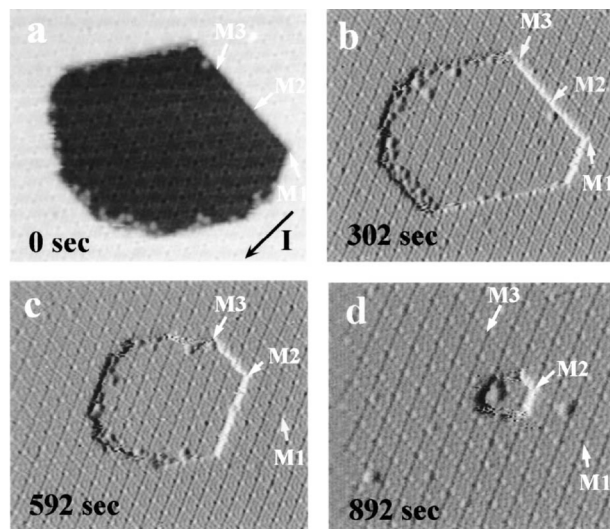


Fig. 1. “Magic” clusters (are designated by the M-letter) and Si craters. STM-samples (different exposition) have the size  $350 \text{ \AA} - 300 \text{ \AA}$  (a) – (c) and  $300 \text{ \AA} - 270 \text{ \AA}$  (d) [1]

Here we show how these magic numbers can be understood based on structures predicted by a quantum-mechanical calculations molecular dynamic classical force field developed by us to fit the equations of state of bulk phases and energies and average co-ordination numbers of small clusters of Si. First-principles quantum-mechanical calculations [3, 8] have successfully predicted the structures and properties of  $\text{Si}_n^+$  clusters for  $n < 10$ .

Prof. J. R. Chelikowsky shows that covalent-metallic phase transitions are the key to the functional form used to construct the force field [12]. The primary reason for the stability of the theory, as compared to the kaleidoscopic variations in analytic detail and parametric values which have characterised almost all other work is that their treatment of bond-bending forces is physically consistent. The former provides the rapid angular variation needed describe the “phase

transition” between metallic ( $\theta = 60^\circ$ ) and covalent ( $\theta = 110^\circ$ ) bonding of silicon clusters.

We calculate the electronic structure of Si-spherical-like clusters using the PDFT model [3, 8]. The interaction parameters are limited to first-nearest neighbors and the usual  $d^{-2}$  Harrison law can be used to calculate their variation with interatomic distance  $d$ . Due to the new boundary conditions the structure is no more in equilibrium and we have thus relaxed the atomic positions using a Stillinger-Weber modified potential. Illustration of transition from polyhedral cluster structure to spheroids and fractal structures shows in the fig 3.

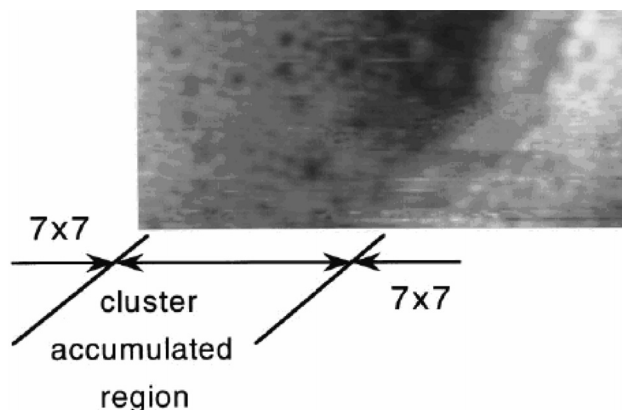


Fig. 2. STM images acquired from the same region of the cluster deposited Si(111) 7x7 surface. The image represents an empty state image with bias of 1,5 V [2]

First, was shown that smaller bond-angle distribution for all clusters in the range  $5 \leq n \leq 20$ . While previous potentials based on  $\cos\theta$  were always designed to favor tetrahedral angles  $\theta_n$ , there is no such bias in our functions. Instead that the smaller bond angles are all concentrating near  $\theta = \pi/3$  (close packing) or near  $\theta_i$  (tetrahedral packing). This is what one would have expected from a bond-bending energy dependent on  $\cos3\theta$ , but the virtual absence of bond angles near  $\theta = \pi/2$  reflects, in addition, certain geometrical constraints, which one might not have anticipated. These packing constraints in effect amplify the significance of the covalent-metallic distinction. For  $n > 10$ , the cluster geometries turn out to be very different from what one might have expected, based on the bulk phase diagram. At  $n = 13$  the structure is that of an atom-centred icosahedron.

The icosahedral-pentagonal growth sequence is well known for two-body central forces appropriate to inert gases, and indeed magic numbers  $n = 13, 19, 23, 25 \dots 55$  etc have been observed for Xe and other inert gas clusters [ref in 12].

Our calculations show that back-bonding forces in small clusters can cause a remarkable reappearance of these simple geometrical structures [3, 7, 8]. The models also shows for a wide range of parameters that at  $n = 11, 12, 16, 17, 18$  the cluster donor belong to the pentagonal growth sequence but may instead have layered character similar to that of one of the  $n = 10$  isomers, which has a 3-3-3-1 trigonal prismatic structure.

Thus our and others authors results indicate that in the range  $n = 10 \div 20$  the polyhedral  $\text{Si}_n$  cluster structures oscillate between metallic pentagonal growth

structures and covalent molecular structures. In effect, in this range  $\text{Si}_n$  clusters are vicinal to a covalent-metallic “phase transition”. This appears to be a case of “like prefers like,” which often occurs in covalent network structures. This preference originates from the persistence of the covalent energy gap, accompanied by phase-matched occupied valence orbital, from the rings of  $\text{Si}_n$  ( $n$  is a number of atoms in cluster) into interlocking rings including matrix surrounding segments.

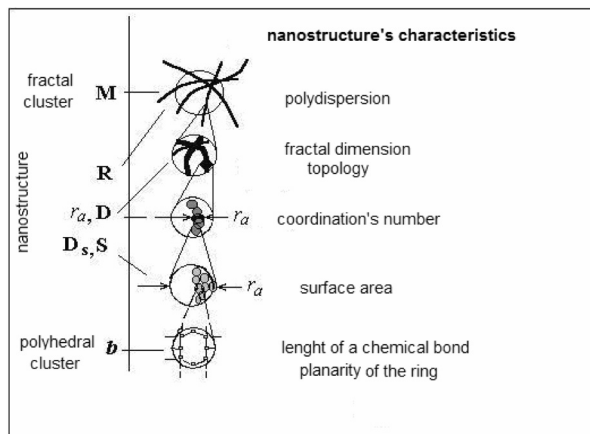


Fig. 3. The scheme of formation of nanostructure on the silicon surface (see results of experiments [1, 2]). Designations of characteristics:  $M$  is a molecular weight of a fractal,  $R$  is a fractal's geometrical size,  $D$  is a fractal dimension,  $r_a$  is radius of a nanostructure,  $D_s$  is degree of a roughness of nanostructure,  $b$  is length of a chemical bond

Our model also yields relative cluster energies and it predicts that  $n = 13$  will be especially stable. However, careful studies of the effect of ionising laser energy and intensity on beam distributions have revealed many effects (including cluster fragmentation, which is likely to be especially strong for “metallic” clusters), which preclude inference of relative cluster energies from beam distribution intensities in cases where the ionisation energies (here known to be  $\geq 7\text{eV}$ ) are large.

In the paper of [13], prof. Kamenutsu Y. with co-workers, report the luminescence properties of a polyhedral  $\text{Si}_8$  cluster, octasilacubane. The study of optical properties of a cubic  $\text{Si}_8$  cluster becomes important for the understanding of the nature of the geometry and chemical bonding of small Si clusters on the silicon surface and the stability of magic-number  $\text{Si}_4$  and  $\text{Si}_{10}$  clusters [7, 8]. Broad PL with a peak of 1.7 eV was observed only at low temperatures. The PL intensity and PL lifetime decrease with increasing temperature above 40 K. The PL process is controlled by non radioactive recombination processes. The slow-decay and temperature-sensitive PL is attributed to “forbidden” radioactive recombination. The optical properties of the cubic  $\text{Si}_8$  cluster are quite different from those of chain and ladder  $\text{Si}_8$  clusters. This is because the orbital hybridisation and bonding in the cubic cluster are different from those in the other  $\text{Si}_8$  clusters.

We would like to stress, that a whole new class of materials called clathrates can be generated by altering the bond angles from their ideal tetrahedral value in the diamond structure [14]. The clathrates form local minima of the total energy and some of them are only slightly less stable than the diamond phase. The

silicon-clathrate compounds are not attacked even by strong acids except for HF. Importantly, the band gaps of these structures are substantially larger than that of Si in the diamond structure and well into the visible region. It is worth noting that the high pressure phases of bulk Si such as  $\beta$ -Sn, on the other hand, are metallic with no gap. The clathrate structures are relatively open, allowing for endohedral impurity atoms. The experimental synthesis of clathrates involves two steps. The first step involves reacting of Si powder or pieces of Si wafer with alkali metal (A) at 580°C for few hours inside an airtight stainless steel bomb sealed in a quartz tube under vacuum of 10–3 Torr. This reaction yields alkali metal silicide A Si, together with excess alkali metal. In the second step, the A Si/A mixture is heated under a dynamic vacuum for about 30 hours at temperatures 300–450°C, to form Si clathrate phase. The results of our study of structural and vibration properties of Si clathrates using a PDFT method will present in the next paper.

In conclusion, we have shown that our previously published PDFT methods [8] gives an excellent fit to the properties of state of two cluster phases. It also predicts very surprising pentagonal growth structures for clusters in the range  $n = 10 \div 25$ . These structures partially explain magic numbers observed experimentally [1, 2]. We believe that these successes demonstrate that we have constructed the satisfactory model of the silicon surface with silicon clusters.

Cluster approach allows formulating in a new fashion material sciences concept, it is essential to expand its possibilities for the decision of modern problems of nanoelectronics.

We would like to express our deep thanks to Prof. Dr. M. Drozdov for the helpful comments of the calculation results. We wish to thanks to Prof. Dr. M. O. Watanabe from Joint Research Center for Atom Technology, 1-1-4 Higashi, Tsukuba, Japan for experimental images of a silicon cluster surface.

UDC 530.145+678.9

V. V. Kovalchuk, O. V. Osipenko

#### SILICON SURFACE WITH CLUSTERS

The experimental data about silicon surface with clusters was discussed. The theoretical study of the atomic geometry of a silicon surface for the two fundamental reconstruction models due to formation of the polyhedral and fractal clusters by means of self-consistent total energy minimization procedure are given.

УДК 530.145+678.9

В. В. Ковальчук, О. В. Осипенко

#### ПОВЕРХНОСТЬ КРЕМНИЯ С КЛАСТЕРАМИ

Обсуждены экспериментальные данные о поверхности кремния с кластерами. С применением процедуры минимизации полной энергии, представлены теоретические результаты об атомной геометрии поверхности кремния для двух фундаментальных моделей ее реконструкции благодаря формированию полиэдров и фракталов.

#### References

1. Ho M. S., Hwang I. S., Tsong T. T. Direct Observation of Electromigration of Si Magic Clusters on Si(111) Surfaces // Phys. Rev. Lett. — Vol. 84, N 25. — 2000. — P. 5792–5795.
2. Watanabe M. O., Miyazaki T., Kanayama T. Deposition of Hydrogenated Si Clusters on Si(111) - (7 x 7) Surfaces // Phys. Rev. Lett. — 1998. — Vol. 81, N 24. — P. 5362–5365.
3. Kovalchuk V. V. Cluster modification semiconductor's heterostructures. — Kiev: Hi-Tech Press, 2007. — 309 p.
4. Jarrold M. F. Nanosurface chemistry on size-selected silicon clusters // Science. — 1991. — Vol. 252. — P. 1085–1092.
5. Bloomfield L. A., Freeman R. R., Brown W. L. Photofragmentation of Mass-resolved  $\text{Si}_{2-12}^+$  clusters // Phys. Rev. Lett. — 1985. — Vol. 54, N 20. — P. 2246–2249.
6. The effect of size distributions of Si nanoclusters on photoluminescence from ensembles of Si nanoclusters / X. Chen, J. Zhao, G. Wang, X. Shen // Phys. Lett. A. — 1999. — Vol. 212. — P. 285–289.
7. Quantum Confinement and Optical Properties of Clusters / V. A. Drozdov, V. V. Kovalchuk, L. M. Moiseev, O. V. Osipenko // Photoelectronics, 2007. — N 16. — P. 3–6.
8. Optical spectra of polyhedral clusters: influence of the matrix surroundings / V. V. Kovalchuk, V. A. Drozdov, L. M. Moiseev, V. O. Moiseeva // Photoelectronics. — 2005. — N 14. — P. 12–18.
9. Drozdov V. A., Kovalchuk V. V. Electronic processes in nanostructures with silicon subphase // J. of Phys. Studies. — 2003. — Vol. 4, N 7. — P. 393–401.
10. Delerue C., Allan G., Lannoo M. Optical band gap of Si nanoclusters // J. Lum. — 1999. — Vol. 80. — P. 65–73.
11. Optical gain in silicon nanocrystals / L. Pavesi, L. Dal Negro, C. Mazzoleni, G. Franzo, F. Priolo // Nature. — 2000. — Vol. 408. — P. 440–444.
12. Chelikowsky J. R., Phillips J. C. Chemical Reactivity and Covalent-Metallic Bonding of  $\text{Si}_N^+$  ( $N=11-25$ ) Ousters // Phys. Rev. Lett. — 1989. — Vol. 63, N15. — P. 1653–1655.
13. Kamenutsu Y., Suzuki K., Kondo M. Luminescence properties of a cubic silicon cluster octasilacubane // Phys. Rev. — 1992. — B 51. — P. 10666–10669.
14. Menon M., Richter E., Subbaswamy K. R. Structural and vibration properties of Si clathrates in a generalised tight-binding molecular-dynamics scheme // Phys. Rev. B. — 1997. — Vol. 56, N 19. — P. 12290–12295.

УДК 530.145+678.9

В. В. Ковальчук, О. В. Осипенко

### **ПОВЕРХНЯ КРЕМНІЮ З КЛАСТЕРАМИ**

Обговорені експериментальні дані щодо поверхні кремнію з кластерами. З використанням процедури мінімізації повної енергії, представлені теоретичні результати про атомну геометрію поверхні кремнію для двох фундаментальних моделей її реконструкції завдяки формуванню поліедрів і фракталів.

R. M. BALABAY, D. V. RYABCHIKOV

Krivoy Rog State Pedagogical University, Department of Physics, 54 Prospect Gagarina, Krivoy Rog, 50086, tel: 8-0564-71-57-21, e-mail: oks\_pol@cabletv.dp.ua

**ELECTRONIC STRUCTURE OF THE SURFACE OF THE SINGLE-WALLED CARBON NANOTUBE: *AB INITIO* CALCULATION**

Data on the ground state electronic and atomic structures of the carbon nanotube and its energy were obtained by “dynamical simulated annealing” (the Car-Parrinello method).

**INTRODUCTION**

Carbon nano-tube that decorates nano-size particles of noble metals is became objects of fundamental and applied studies. The operations on their synthesis and the study of their properties are being performed actively in the USA, China, Korea, Japan and others. The association of unique properties of nanostructure substrates and nanosize particles allows effectively using such composite materials in nano-electronics, as effective catalysts, chemical sensors, and adsorbent of hydrogen, as well as electro-catalyst for fuel cells of new generation.

The methods of wet chemistry are used for production of the composite structures more often. However, there are some other ways. The US researchers [1] developed the controlled method of assembly with use of high electric field (ESFDA – electrostatic force directed assembly). It is based on creation of the charge nano-size particles stream, which is being deposited on single-shell (or multi-shell) carbon tubes placed on copper mesh with DC voltage applied. It is possible to monitor and control the density of packed nano-size particles on surface of the carbon nano-tube, and to obtain a condensation of nano-size particles with the needed size. Method also allows the plotting the scheme of metal and semiconductor nano-size particles mixture on the nano-tube.

The studies of the properties of nano-tube walls in nanometer scale are very much difficult due to their sub-molecular diameters and curved surface [2]. Therefore, the study of general nano-tube properties remains perspective due to the possibility of the methods of computer simulation and calculations of first principles (*ab initio*) use [3].

**METHOD OF CALCULATION**

The calculations for carbon nano-tube were performed within the local density approximation according to the density functional formalism. The electron-ion interaction has been modeled by *ab initio* norm-conserving pseudopotentials proposed in [4]. The ground state electronic and atomic structures and its energy were obtained by “dynamical simulated annealing” (Car-Parrinello method – (CP) method) [5].

The CP method is being based on density-functional theory (DFT) and the Born-Oppenheimer (BO)

adiabatic approximation. For conventional DFT electronic structure calculations, the Kohn-Sham (KS) equations [6] were solved self-consistently. In BO approximation, wave function are considered as the functions of ionic positions  $\{\vec{R}_i\}$ :  $\{\psi_i(\vec{r}; \vec{R}_i)\}$ , but in

CP method  $\{\psi_i(\vec{r})\}$  are treated as classical dynamical

variables independent of  $\{\vec{R}_i\}$ . They are postulated to be evolves of Newton’s equations of motion so that “dynamical simulated annealing” can be performed to search a global minimum of the electronic configuration.

The Lagrangian in CP method is introduced as

$$L\{\psi, \dot{\psi}, \vec{R}, \dot{\vec{R}}\} = \mu \sum_i |\dot{\psi}_i(\vec{r})|^2 d\vec{r} + \frac{1}{2} \sum_i M_i \dot{\vec{R}}_i^2 - E[\{\psi_i(\vec{r})\}, \{\vec{R}_i\}] + \sum_{i,j} \varepsilon_{ij} (\int \psi_i^*(\vec{r}) \psi_j(\vec{r}) d\vec{r} - \delta_{ij}) \quad (1)$$

where  $\{\psi_i\}$  are single-electron orbitals, and the electronic density  $\rho(\vec{r})$  is assumed to be given by

$$\rho(\vec{r}) = \sum_i |\psi_i(\vec{r})|^2 \quad (2)$$

The first term of Eq. (1) is a fictitious classical mechanical kinetic energy of  $\{\psi_i\}$ . The second term is an ionic kinetic energy, and  $E$  is the total energy (the sum of the electronic energy and the ion-ion Coulomb interaction energy). Lagrangian multipliers  $\varepsilon_{ij}$  are introduced to satisfy the orthonormality constraints on  $\{\psi_i\}$ . The detail of the electronic energy is described in many papers [for example, 7]. From Eq. (2), equations of motion for  $\psi_i$  and  $\vec{R}_i$  are derived as

$$\mu \psi_i(\vec{r}) = -\frac{\delta E}{\delta \psi_i^*(\vec{r})} + \sum_j \varepsilon_{ij} \psi_j(\vec{r}) \quad (3)$$

$$M_i \ddot{\vec{R}}_i = -\nabla_i E \quad (4)$$

If an electronic structure reaches to the state, in which no force acts on  $\psi_i$ , that is, the left-hand side of Eq. (3) is equal to zero, the equation is identical with the KS equation and  $\psi_i$  becomes the eigen-state of the KS equation. To attain this, the kinetic energy of  $\{\psi_i\}$  is being gradually reduced until  $\{\psi_i\}$  are frozen. This procedure is called “dynamical simulated annealing.” If one also relaxes the ions with Eq. (4), the minimi-

zation with respect to electronic and ionic configurations could be performed simultaneously.

It is also possible to evolve  $\{R_i\}$  and  $\{\psi_j\}$  without reducing the kinetic energy. If  $\{\psi_j\}$  are kept close to eigen-states during the time evolution, ionic trajectories generated by Eq. (4) are physically meaningful. When the CP method is applied to study the dynamic evolution of a system consisting of ions and electrons, it is called “*ab initio* molecular dynamics”.

## RESULTS AND DISCUSSION

The superlattice geometry was chosen for our calculations. The atomic basis of the primitive tetragonal unit cell of the superlattice consisted of 12 carbon atoms. Their location simulated the infinite single-wall nanotube with diameter: 0.4 nm and with chirality: (3,0). The parameters of the unit cell has said meaning in X- and Y- directions and simulated insulation of a nano-tube, but in Z- direction we assume the of a nano-tube (A=9.15516 Å; B=9.15516 Å; C=2.8 Å). The equilibrium characteristics of the atoms complexes were calculated at a plane wave cutoff energy of 1.5 Ry at the center of Brillion zone, using 900 iterations in author’s original software program code.

Inspection of the of valence electron density distributions maps allowed to define the principal properties of the electronic structure of the nano-tube. So, the density forms along the across atom some kind of a zigzag (Fig. 1 a).

The remaining portion of a cylindrical surface of the nano-tube is formed having smaller density and could be characterized as more homogeneous (Fig 1 b, Fig 1 c).

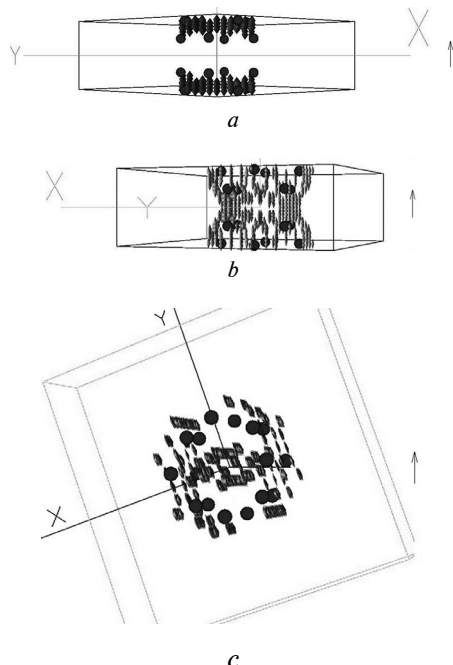


Fig. 1. Space distribution of the valence electron density for carbon nano-tube atomic complexes (a — for density from 0.9 to 1.0 (part of the maximum value), b — for density from 0.6 to 0.7, c — for density from 0.6 to 0.7 (transversal view of nano-tube))

At the same time, the insignificant part of valence electron density is located on internal areas of the nano-tube (Fig. 2).

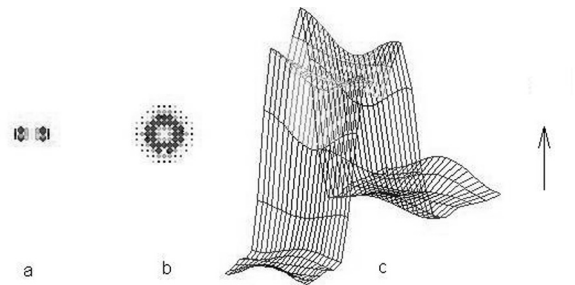


Fig. 2. Distribution map of electronic density of valence electron in the (110) plane (a), in the (100) plane (b), in the plane (110) — the space projection (c)

Electronic distribution for infinite nano-tube is possible to draw in the flanks form, which are drawn with hoops and walls are constructed from soft material. Obtained picture of electron density distribution explains the super flexibility of the nano-tube.

For the isolated fragment of nano-tube with the open edge presence of  $\pi$  — bounds is observed in electronic distribution, which are oriented perpendicularly to cylindrical surface of the nano-tube (Fig. 3).

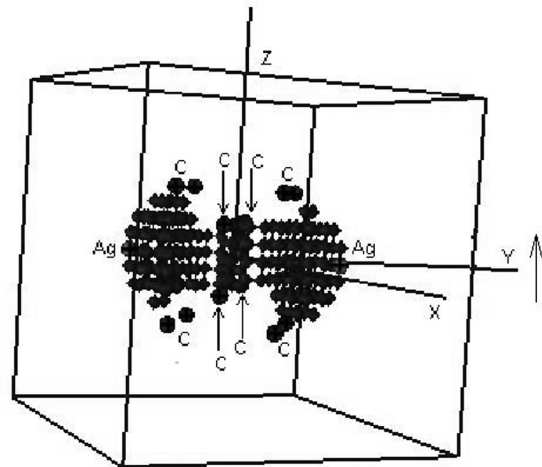


Fig. 3. Space distribution of the valence electron density for isolated fragments of carbon nano-tube atomic complexes for density from 0.9 to 1.0 (part of the maximum value)

In the presence of silver atoms on the surface of nano-tube the significant reorganization of electronic charge is observed, with silver atoms located in the center of hexagonal ring in the middle of tube (Fig. 4).

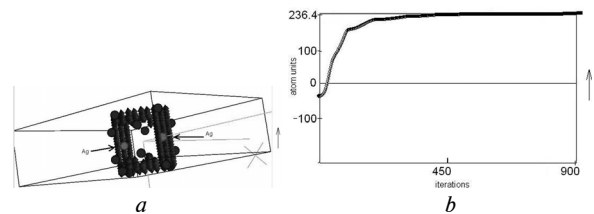


Fig. 4. Space distribution of the valence electron density for carbon nano-tube atomic complexes with silver in centre of hexagonal ring for density from 0.9 to 1.0 (part of the maximum value) (a), (b) — its total energy on the unit cell

When silver atoms reside in positions of cross zig-zag of atomic nano-tube, the electronic charge is not changed so significantly (Fig. 5).

## CONCLUSION

Comparing energies for each atom configuration (Fig. 4, Fig. 5, Fig. 6) and their electronic distributions, it is possible to draw the conclusion, that the positions of silver atoms location in the middle of hexagonal ring, in crossed zigzag and in the corner of zigzag are almost energetically equal.

### References

1. *Chen I., Ganhua Lu.* Controlled decoration of carbon nanotubes with nanoparticles // *Nanotechnology* 17, 2006. — P. 2891-2894.
2. *Kröger H., Reinke P.* Gold cluster formation on a fullerene surface // *The Journal of Chemical Physics* 123, 2005. — 11470b.
3. *Макаренко И. В., Тутков А. М. и др.* Структурные свойства монослойной графитовой пленки на поверхности (111) иридия // *ФТТ* 49(2), 2007. — С. 357–363.
4. *Hartwigsen C., Goedecker S., Hutter J.* Relativistic separable dual-space Gaussian pseudopotentials from H to Rn // *Physical Review B* 58(7), 1998. — P. 3641–3662.
5. *Car R., Parrinello M.* Unified Approach for molecular Dynamics and Density-Functional Theory // *Physical Review Letters* 55(22), 1985. — P. 2471–2474.
6. *Kohn W., Sham L. J.* Self – consistent equations including exchange and correlation effects // *Phys. Rev. A* 140(4), 1965. — P. 1133–1137.
7. *Sham L. J., Kohn W.* One-particle an inhomogeneous interacting electron gas // *Phys. Rev.* 145 (2), 1966. — P. 561–567.
8. *Marx D., Hutter J.* *Ab initio* molecular dynamics: Theory and implementation. In *Modern Methods and Algorithms of Quantum Chemistry*, Eds. Jgrotendorst, John von Neumann Institute for Computing, Julich, NIC Series 1, 2000. — P. 301–449.

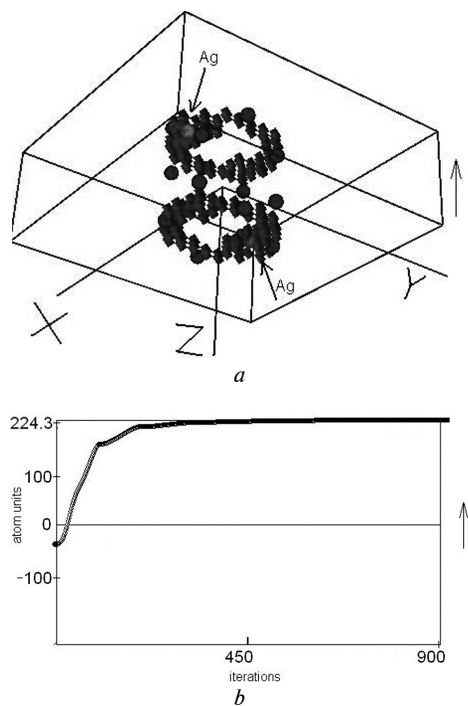


Fig. 5. Space distribution of the valence electron density for carbon nano-tube atomic complexes with silver cross zigzag for density from 0.9 to 1.0 (part of the maximum value) (a), (b) – its total energy on the unit cell.

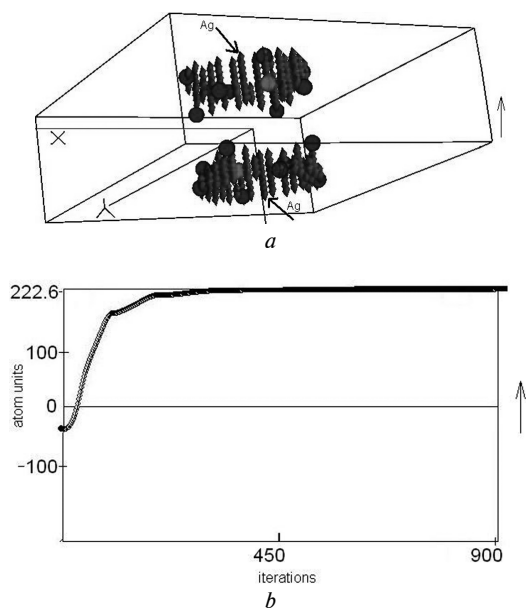


Fig. 6. Space distribution of the valence electron density for carbon nano-tube atomic complexes with silver in corner of zigzag for density from 0.9 to 1.0 (part of the maximum value) (a), (b) – its total energy on the unit cell

UDC 539.216

R. M. Balabay, D. V. Ryabchikov

### ELECTRONIC STRUCTURE OF THE SURFACE OF THE SINGLE-WALLED CARBON NANOTUBE: AB INITIO CALCULATION

Data on the ground state electronic and atomic structures of the carbon nanotube and its energy were obtained by “dynamical simulated annealing” (the Car-Parrinello method).

УДК 539.216

Р. М. Балабай, Д. В. Рябчиков

**ЭЛЕКТРОННАЯ СТРУКТУРА ПОВЕРХНОСТИ ОДНО-СТЕНКОВОЙ УГЛЕРОДНОЙ НАНОТРУБКИ: РАСЧЕТЫ ИЗ ПЕРВЫХ ПРИНЦИПОВ**

На основе «динамического модельного отжига» (метод Кар-Парринелло) получены данные по электронной и атомной структурам основного состояния углеродной нанотрубки и ее энергия.

УДК 539.216

Р. М. Балабай, Д. В. Рябчиков

**ЕЛЕКТРОННА СТРУКТУРА ПОВЕРХНІ ОДНО-СТІНКОВОЇ ВУГЛЕЦЕВОЇ НАНОТРУБКИ: РОЗРАХУНКИ ІЗ ПЕРШИХ ПРИНЦИПІВ**

На підставі «динамічного модельного відпалу» (метод Кар-Паррінелло) отримані дані з електронної та атомної структур основного стану вуглецевої нанотрубки та її енергія.

T. N. SHCHUROVA<sup>1</sup>, N. D. SAVCHENKO<sup>1</sup>, A. B. KONDRAT<sup>2</sup>, K. O. POPOVYCH<sup>2</sup>, V. M. RUBISH<sup>3</sup>, G. LEISING<sup>4</sup>

<sup>1</sup> Department of Electronic Systems, Faculty of Engineering, Uzhgorod National University, 13 Kapitulna St., 88000 Uzhgorod, Ukraine, tel. +380 3122 30656, e-mail: root@tv.uzhgorod.ua

<sup>2</sup> Department of Solid State Electronics, Faculty of Physics, Uzhgorod National University, 54 Voloshyn St., 88000 Uzhgorod, Ukraine, tel. +380 3122 32318, e-mail: akondrat@univ.uzhgorod.ua

<sup>3</sup> Uzhgorod Scientific-Technological Center of the Institute for Information Recording, NASU, 4 Zamkovi Skhody Str., Uzhgorod 88000, Ukraine, tel. +380 3122 37397, e-mail: vrubish@ustc.org.ua

<sup>4</sup> Institute for Solid State Physics, Technical University Graz, 16 Petersgasse, 8010 Graz, Austria, e-mail: gleising@issp.tugraz.at

## SIMULATION OF THE SURFACE BENDING OF ENERGY BAND FOR BINARY CHALCOGENIDE SEMICONDUCTORS

We have calculated the surface bending of energy bands for binary ZnS(Se), GeS(Se)<sub>2</sub>, As<sub>2</sub>S(Se)<sub>3</sub>, Sb<sub>2</sub>S(Se)<sub>3</sub> alloys. The calculations were based on the methods of linear combination of atomic orbitals and pseudopotential developed in the works by W. A. Harrison. We have constructed the energy band diagrams and analyzed dependences of the surface bending of energy bands on the ionicity and band gap width. The experimental spectral dependences of photoemission quantum yield, photoconduction and absorption coefficient near the fundamental absorption edge for As<sub>2</sub>S<sub>3</sub> and Sb<sub>2</sub>S<sub>3</sub> are presented.

### 1. INTRODUCTION

Chalcogenide semiconductors find novel applications as sensor materials for opto-, micro- and nano-electronics due to their special optical, mechanical and electrical properties. The prediction of bulk and surface properties of sensor material is one of the top problems in the development of solid-state sensors. Earlier we have performed calculations of the main bulk parameters of energy bands for ZnS, GeS(Se)<sub>2</sub>, As<sub>2</sub>S(Se)<sub>3</sub>, Sb<sub>2</sub>S<sub>3</sub> binary chalcogenide semiconductors within different approximations [1–5]. In this work the problem search for the materials with specified properties is considered in terms of relationships between electronic structure and properties accounting modern achievements in this area. To do this we have calculated bulk and surface electronic structure for including possibility of formation of fast surface states and surface bending of energy bands in view of surface reconstruction.

### 2. COMPUTATIONAL PROCEDURE

Calculations were performed on binary ZnS(Se), GeS(Se)<sub>2</sub>, As<sub>2</sub>S(Se)<sub>3</sub>, Sb<sub>2</sub>S(Se)<sub>3</sub> alloys. The calculations were based on the methods of linear combination of atomic orbitals and pseudopotential [6]. The energy values have been determined in the  $\Gamma$ -point - the centre of the Brillouin zone. In construction of the energy band diagrams we have used the atomic terms within Hartree-Fock approximation ( $\varepsilon_s$ ,  $\varepsilon_p$ ,  $\varepsilon_h$ ,  $V_1$ ) [7] and intratomic Coulomb repulsion energies ( $U$ ) [8]. The difference between crystalline and non-crystalline states has been taken into account by the variation of interatomic distance between anion and cation atoms.

We have calculated the main energy contributions to the energy band formation, i.e. covalent bond energy over  $p$ -,  $s$ - and hybrid states ( $V_2^p$ ,  $V_2^s$ , and  $V_2^{ph}$ ), energy of polar bonds ( $V_3^p$ ,  $V_3^s$ , and  $V_3^{ph}$ ), metallic bond energy calculated in terms of bonding ( $V_1^\sigma$ ) and antibonding ( $V_1^{\sigma^*}$ ) orbitals with account of polar bond ( $V_1^{\sigma} = [(1-\alpha_p)V_{1+} + (1+\alpha_p)V_{1-}]/2$ ,  $V_1^{\sigma^*} = [(1+\alpha_p)V_{1-}$

$+ (1-\alpha_p)V_{1+}]/2$ ,  $\alpha_p = V_3^{ph}/(V_2^2 + V_3^2)^{1/2}$ ). Then, for different materials we have been computed the valence-band maximum ( $E_v$ ) accounting for spin-orbital splitting ( $\Delta E_{s-o}$ ) [9] following Eq. (1, 3, 5), the conduction-band minimum ( $E_c$ ) from Eq. (2, 4, 6), and the band gap. Fermi level ( $E_F$ ) was determined with account of position of the levels formed by homopolar bonds, non-bonding and hybrid orbitals according the procedure described in Ref. [5]. The general formulae for different compounds ( $X = S, Se$ ) are listed below, for ZnX (Eq. 1, 2), GeX<sub>2</sub> (Eq. 3, 4), and As(Sb)<sub>2</sub>X<sub>3</sub> (Eq. 5, 6), respectively.

$$E_v = \frac{\varepsilon_p^{Zn} + \varepsilon_p^X}{2} + \sqrt{(V_2^p)^2 + (V_3^p)^2} + \Delta E_{s-o} - V_1^\sigma + \frac{U}{2}, \quad (1)$$

$$E_c = \frac{\varepsilon_s^{Zn} + \varepsilon_s^X}{2} - \sqrt{(V_2^s)^2 + (V_3^s)^2} + V_1^{\sigma^*} + \frac{U}{2}, \quad (2)$$

$$E_v = \varepsilon_h^{Ge} + \sqrt{(V_2^{ph})^2 + (V_3^{ph})^2} + \Delta E_{s-o} - V_1^\sigma + \frac{U}{2}, \quad (3)$$

$$E_c = \varepsilon_h^{Ge} - \sqrt{(V_2^{ph})^2 + (V_3^{ph})^2} + V_1^{\sigma^*} + \frac{U}{2}, \quad (4)$$

$$E_v = \frac{\varepsilon_p^{As} + \varepsilon_p^X}{2} + \sqrt{(V_2^p)^2 + (V_3^p)^2} + \Delta E_{s-o} - V_1^\sigma + \frac{U}{2}, \quad (5)$$

$$E_c = \frac{\varepsilon_p^{As} + \varepsilon_p^X}{2} - \sqrt{(V_2^p)^2 + (V_3^p)^2} + V_1^{\sigma^*} + \frac{U}{2}. \quad (6)$$

### 3. RESULTS AND DISCUSSION

Fig. 1 shows the procedure of the construction of the energy band diagram beginning from the atomic terms, and the peculiarities of the energy band formation for chalcogenides under investigation. We see, that the energy band for ZnS is formed by Zn 4*p*, Zn 4*s*, S 3*p* and S 3*s* atomic terms (a), for GeS<sub>2</sub> by atomic terms Ge4*p*, Ge4*s*, Ge *sp*<sup>3</sup> and S 3*p* (b); for As<sub>2</sub>S<sub>3</sub> by atomic terms As 4*p* and S 3*p* (c), and for Sb<sub>2</sub>S<sub>3</sub> by atomic terms Sb 5*p* and S 3*p* (d).

The sequence of the energy band formation is shown in details in Fig. 1 (d), where 1 - Sb 5*p* and

S 3*p* atomic terms; 2 - average energy; 3 - the splitting into bonding ( $\sigma$ ) and antibonding ( $\sigma^*$ ) states; 4 - account of the spin-orbital splitting ( $\Delta E_{s-o}$ ); 5 - account of the metallicity energy over bonding ( $V_1\sigma$ ) and antibonding ( $V_1\sigma^*$ ) states; 6 - account of the intratomic Coulomb repulsion ( $U/2$ ). The calculated energy values are given in electron-volts. Experimental data for the photoemission threshold and optical band gap are given in parentheses.

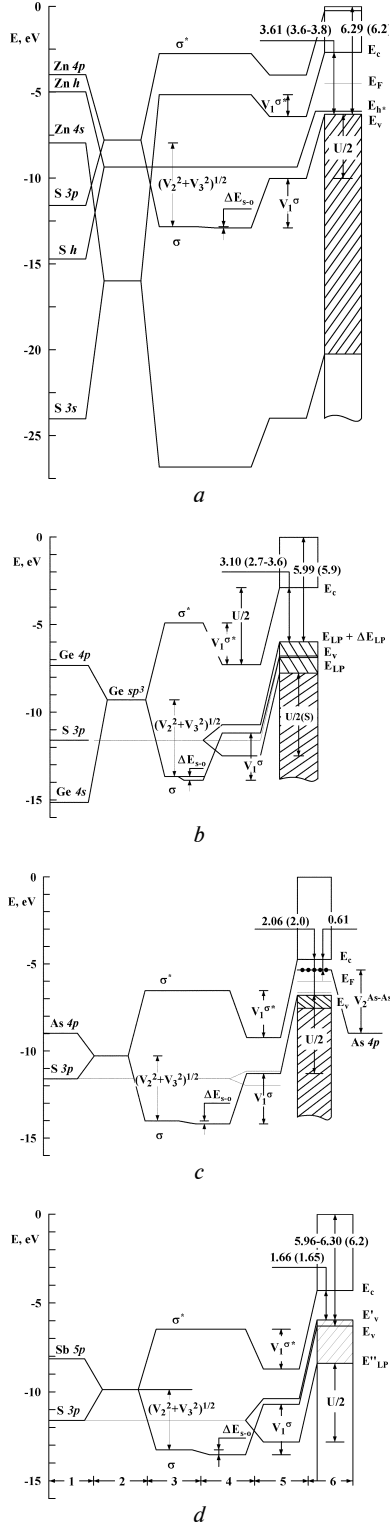


Fig. 1. Formation of the energy bands from the atomic terms for ZnS (a), GeS<sub>2</sub> (b), As<sub>2</sub>S<sub>3</sub> (c) and Sb<sub>2</sub>S<sub>3</sub> (d). The energy values are given in electron-volts. Experimental data for the photoemission threshold and optical band gap are given in parentheses

The surface bending of energy bands ( $\Delta\phi$ ) for all compounds were calculated as

$$\Delta\phi = E_s - E_F, \quad (7)$$

where  $E_s$  is the energy of the surface states before reconstruction. We took that the  $E_s$  levels are shifted towards the Fermi level under the reconstruction. In the calculations we have kept in mind that ZnX and GeX<sub>2</sub> compounds are tetrahedral, when As(Sb)<sub>2</sub>X<sub>3</sub> are trigonal ones. For tetrahedral structure  $E_s$  is determined by the hybrid states of the bonds directed inside, and thus can be found for ZnX and GeX<sub>2</sub> compounds as

$$E_s = \frac{\varepsilon_h^{Zn} + \varepsilon_h^X}{2} + \frac{U}{2}, \quad (8)$$

$$E_s = \varepsilon_h^{Ge} + \frac{U}{2}. \quad (9)$$

For As(Sb)<sub>2</sub>X<sub>3</sub> compounds the energy of the surface states before reconstruction is determined by the surface states of lone pair *p*-electrons of S(Se) atoms.

$$E_s = \varepsilon_{3p}^X + \frac{U}{2}. \quad (10)$$

The calculated values for ZnS(Se), GeS(Se)<sub>2</sub>, As<sub>2</sub>S(Se)<sub>3</sub> and Sb<sub>2</sub>S(Se)<sub>3</sub> compounds are listed in the Table 1.

Figure 2 *a* shows the correlation between surface bending of the energy band and polarity. We see that surface bending increases with polarity. Surface bending of the energy band versus band gap is given in Figure 2, *b* for sulphides (crosses) and selenides (solid circles) of zinc, germanium, arsenic and antimony.

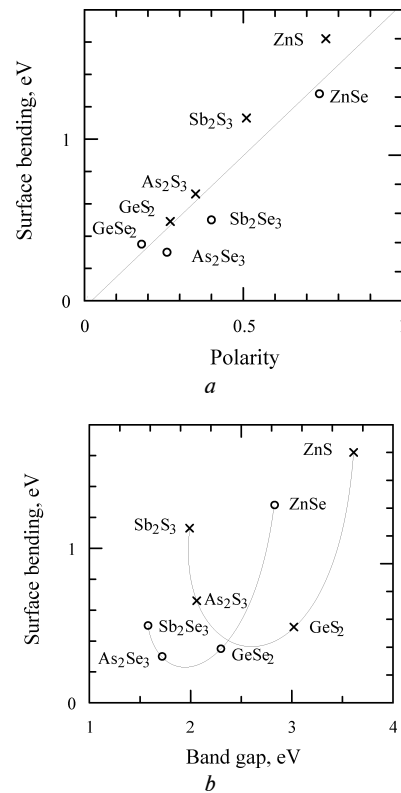


Fig. 2. Surface bending of the energy band versus polarity (a) and band gap (b) for sulphides (crosses) and selenides (solid circles) of zinc, germanium, arsenic and antimony. Line in (a) is a linear fit for all compounds. Lines in (b) are given as guides to the eye

The  $p$ -bond polarity ( $\alpha_p$ ), Coulomb intratomic repulsion energy ( $U/2$ ), the valence-band maximum ( $E_v$ ), the conduction-band minimum ( $E_c$ ), the Fermi level ( $E_F$ ), energy of the surface states before reconstruction ( $E_s$ ), the surface bending of energy band ( $\Delta\phi$ )

Compound	$\alpha_p$	$U/2$ , eV	$-E_v$ , eV	$-E_c$ , eV	$-E_F$ , eV	$-E_s$ , eV	$-\Delta\phi$ , eV
ZnS	0.76	3.74	6.29	2.68	4.49	4.05	1.62
ZnSe	0.74	4.23	5.26	2.43	3.85	3.10	1.28
GeS <sub>2</sub>	0.27*	4.40	5.91	2.89	4.40	4.89	0.49
GeSe <sub>2</sub>	0.18*	4.27	5.82	3.52	4.67	5.02	0.35
As <sub>2</sub> S <sub>3</sub>	0.35	4.49	6.80	4.74	6.01	5.80	0.66
As <sub>2</sub> Se <sub>3</sub>	0.26	4.38	5.71	3.99	4.85	5.45	0.30
Sb <sub>2</sub> S <sub>3</sub>	0.51	4.31	6.17	4.53	5.33	5.56	1.13
Sb <sub>2</sub> Se <sub>3</sub>	0.40	3.73	6.33	4.75	5.55	5.68	0.50

\*) The value was determined from the hybrid states

These results can be used for the procedure of material selection in the design and development of solid-state sensor for different applications.

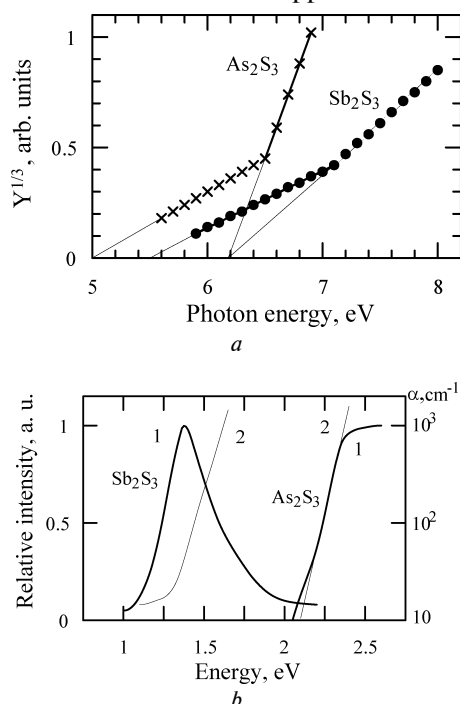


Fig. 3. Photoemission quantum yield versus photon energy (a); photoconduction spectrum (curve 1) and fundamental absorption edge (curve 2) (b) for  $As_2S_3$  and  $Sb_2S_3$  glasses

An example of the applicability of the developed approach for simulation of the surface bending of the energy band for binary chalcogenides is seen in Figure 3, where the experimental results of photoemission and photoconduction studies are presented. Fig. 3 a shows spectral dependences of photoemission quantum yield. Fig. 3 b gives absorption coefficient near the fundamental absorption edge (curve 1) and photoconduction (curve 2) for  $Sb_2S_3$  and  $As_2S_3$  glasses. The absorption edge and photoconduction for  $As_2S_3$  glasses is taken from reference [10], the data for  $Sb_2S_3$  glasses — from Ref. [2]. Extrapolation of the steep parts of  $Y^{1/3} \div E$  dependencies to zero value (Fig. 3, a) give equal energy values of 6.2 eV for both compounds. Extrapolation of the flat parts of these dependencies to zero value give the energy values for  $As_2S_3$  and  $Sb_2S_3$  glasses of 5.0 eV and 5.5 eV, respectively. The calculated values for these parameters have

been found to be 6.30 eV and 5.96 eV, respectively [3]. From Fig. 3, a and b we see that for  $Sb_2S_3$  above the valence band formed by LP states there are electronic states extending into the band gap and giving rise to the tail in photoemission and weak absorption tail. They could be attributed to the surface effects. Their existence results in the photoconduction in this spectral range (Fig. 3 (b) curve 1). The results shown in Fig. 3 (a) and (b) confirm the agreement in calculated and experimental surface bending of the energy bands in  $As_2S_3$  and  $Sb_2S_3$  glasses.

## CONCLUSIONS

The procedure of the simulation of the surface bending of the energy bands based on the combination of tight-binding and pseudopotential picture proposed by W.A.Harrison has been developed and tested for ZnS(Se), GeS(Se)<sub>2</sub>, As<sub>2</sub>S(Se)<sub>3</sub>, Sb<sub>2</sub>S(Se)<sub>3</sub> binary chalcogenide alloys. Good quantitative agreement between calculated and experimental values has been found. The results are applicable to the prediction of material properties for the development of nanoelectronic sensors.

## References

1. Bands splitting in heterojunctions chalcogenide film — crystalline semiconductor / N. D. Savchenko, A. B. Kondrat, T. N. Shchurova, N. I. Dovgoshey // Proc. Ukr. Vac. Soc., eds. V. G. Cherepin, V. M. Shulayev. — Mater. 8<sup>th</sup> Int. Symp. "Thin Films in Electronics". — Kharkiv. — 1997. — P. 262–265.
2. Spectral distribution of photoemission quantum efficiency for  $(As_2Se_3)_{1-x}Ge_x$  glasses / T. Shchurova, N. Savchenko, A. Spesivkykh, N. Baran // Jap. J. Appl. Phys. — 2000. — Vol. 39, Suppl. 39-1. — P. 334–335.
3. Electric and optical properties of  $Sb_xS_{1-x}$  alloys / T. Shchurova, N. Savchenko, V. M. Rubish, V. V. Rubish, A. Spesivkykh, I. Opachko // Journal of Optoelectronics and Advanced Materials. — 2005. — Vol. 7, N 2. — P. 2021–2027.
4. Auger analysis and simulation of electronic states for  $Ge_{33}As_{12}Se_{55}$  - p-Si heterojunction / T. N. Shchurova, N. D. Savchenko, A. B. Kondrat, I. I. Opachko // Surface and Interface Analysis. — 2006. — Vol. 38. — P. 448–451. — DOI: 10.1002/sia2297.
5. Simulation of the electronic states in the band gap for ZnS: Cu, Cl crystalline phosphors / N. D. Savchenko, T. N. Shchurova, K. O. Popovych, I. D. Rubish, G. Leising // Semiconductor Physics, Quantum Electronics & Optoelectronics. — 2004. — Vol. 7, N 2. — P. 133–137.
6. Harrison W. A. Elementary Electronic Structure / New Jersey, London, Singapore, Shanghai, Hong Kong, Taipei, Chennai: World Scientific Publishing Co., 2004. — 838 p.

7. *Mann J. B.* Atomic Structure Calculations, 1: Hartree-Fock Energy Results for Elements from Hydrogen to Lawrencium / Springfield: Clearinghouse, 1967. — 22151.
8. *Harrison W. A.* Total energies in tight-binding theory // *Phys. Rev. B.* — 1981. — Vol. 23. — P. 5230-5241.
9. *Chadi D. J.* Spin-orbit splitting in crystalline and compositionally disordered semiconductors // *Phys. Rev. B.* — 1977. — Vol. 16. — P. 790–796.
10. *Tanaka Ke.* Charge defect exists? // *Journal of Optoelectronics and Advanced Materials.* — 2001. — Vol. 3, N 2. — P. 189–198.
11. *Preparation, structure and photoelectric properties for the glasses of Sb-S family* Shtez P. P., D. I. Bletskan, I. D. Turianitsa, M. P. Bodnar, V. M. Rubish // *Proc. Acad. Sci. USSR. Inorgan / Materials* -t 1989. — Vol. 25, N 6. — P. 939–937.

UDC: 71.23.

T. N. Shchurova, N. D. Savchenko, A. B. Kondrat,  
K. O. Popovych, V. M. Rubish, G. Leising

#### SIMULATION OF THE SURFACE BENDING OF ENERGY BAND FOR BINARY CHALCOGENIDE SEMICONDUCTORS

We have calculated the surface bending of energy bands for binary ZnS(Se), GeS(Se)<sub>2</sub>, As<sub>2</sub>S(Se)<sub>3</sub>, Sb<sub>2</sub>S(Se)<sub>3</sub> alloys. The calculations were based on the methods of linear combination of atomic orbitals and pseudopotential developed in the works by W.A.Harrison. We have constructed the energy band diagrams and analyzed dependences of the surface bending of energy bands on the ionicity and band gap width. The experimental spectral dependences of photoemission quantum yield, photoconduction and absorption coefficient near the fundamental absorption edge for As<sub>2</sub>S<sub>3</sub> and Sb<sub>2</sub>S<sub>3</sub> are presented.

УДК: 71.23.

М. Д. Савченко, О.Б. Кондрат, Т. М. Щурова, К. О. Попович, В. М. Рубіш, Г. Лайзинг

#### МОДЕЛЮВАННЯ ПОВЕРХНЕВОГО ВИГИНУ ЕНЕРГЕТИЧНОЇ ЗОНИ БІНАРНИХ ХАЛЬКОГЕНІДНИХ НАПІВ-ПРОВІДНИКІВ

Теоретично розраховано поверхневий вигин зон у бінарних сполуках ZnS(Se), GeS(Se)<sub>2</sub>, As<sub>2</sub>S(Se)<sub>3</sub> та Sb<sub>2</sub>S(Se)<sub>3</sub>. Використано метод, який поєднує методи лінійної комбінації атомних орбіталей та псевдопотенціалу, розроблений в роботах У. Харрісона. Побудовані енергетичні діаграми заборонених зон досліджуваних матеріалів та аналізується залежність поверхневого вигину зон від ступеня іонності та ширини забороненої зони. Наводяться експериментальні спектральні залежності квантового виходу фотоелектронів, фотопровідності та коефіцієнта поглинання в області краю фундаментального поглинання для стекел As<sub>2</sub>S<sub>3</sub> та Sb<sub>2</sub>S<sub>3</sub>.

УДК: 71.23.

Т. Н. Щурова, Н. Д. Савченко, А. Б. Кондрат,  
К. О. Попович, В. М. Рубиш, Г. Лайзинг

#### Моделирование поверхностного изгиба энергетической зоны бинарных халькогенидных полупроводников

Теоретически рассчитан поверхностный изгиб зон в бинарных соединениях ZnS(Se), GeS(Se)<sub>2</sub>, As<sub>2</sub>S(Se)<sub>3</sub>, Sb<sub>2</sub>S(Se)<sub>3</sub>. Использован метод, основанный на методах линейной комбинации атомных орбиталей и псевдопотенциала, развитый в работах У. Харрисона. Построены энергетические диаграммы запрещенных зон указанных материалов и анализируется зависимость поверхностного изгиба зон от степени ионности и ширины запрещенной зоны. Приводятся экспериментальные спектральные зависимости квантового выхода фотоэлектронов, фотопроводимости и коэффициента поглощения в области края фундаментального поглощения для стекел As<sub>2</sub>S<sub>3</sub> и Sb<sub>2</sub>S<sub>3</sub>.

A. F. BUTENKO, S. N. FEDOSOV, A. E. SERGEEVA

Department of Physics and Material Science, Odesa National Academy of Food Technologies, ul. Kanatnaya, 112, 65039, Odesa, Ukraine, tel. +38 048 712-41-80, e-mail: fedosov@optima.com.ua

## COMPONENTS OF DEPOLARIZATION CURRENTS IN POLYVINYLIDENE FLUORIDE CAUSED BY RELAXATION OF HOMO- AND HETEROCHARGE

A procedure has been developed for homocharge and heterocharge components separation of the total thermally stimulated depolarization current in corona polarized PVDF films. The relaxation behavior of both components has been analyzed and such important parameters of the relaxation processes, as activation energies, characteristic frequencies and time constants have been evaluated by processing TSD current curves, measured using four modifications of the TSD method and supplemented with measurements of isothermal currents and of the electret potential.

### 1. INTRODUCTION

Polyvinylidene fluoride (PVDF) and its co-polymers have received considerable attention during the last years because of their high piezo- and pyroelectric activities which origin is not understood fully [1–8]. Their specific properties are being attributed usually to the high level of the residual polarization [4–7], although some researchers believe that the injected charge can also play an important role [8].

Despite the fact that PVDF is often considered as a ferroelectric polymer [5], and some of its electrical properties could be explained in terms of the conventional theory of polar dielectrics and electrets. The phenomenological Gross-Swann-Gubkin model of electrets [9] assumes the availability of two kinds of charges in polar dielectrics, namely the homocharge  $\sigma(t)$  which sign coincides with the polarity of electrodes during polarization and the heterocharge  $P(t)$  (internal polarization) arising from micro- and macrodisplacement of intrinsic charges in the dielectric under action of the electric field. In the case of PVDF one could assume that the heterocharge represents the dipole polarization, while the homocharge is formed by charges trapped at or near the surface [10].

Stability of the electret state in a polar dielectric depends on the interaction and the resulting mutual relaxation of the homocharge and the heterocharge. Since the heterocharge (polarization) is usually of the primary importance for PVDF, the role of the homocharge was not given enough consideration so far, although the stabilizing effect of the space charge on the residual polarization has been already discussed [10,11].

Thermally stimulated depolarization (TSD) is a commonly method used commonly for relaxation processes identification in charged polymer electrets [12–16]. However, it is very difficult to separate the influence of the homocharge and the heterocharge on the TSD currents, especially if the corresponding peaks are superimposed in a wide range of temperatures.

In the present work, we illustrate how to extract depolarization currents caused by relaxation of the homocharge and the heterocharge from the total TSD current by solving the inverse problem and revealing

the relaxation behavior of both components from the TSD current measured experimentally. Moreover, it is shown that application of different TSD modes supplemented with the isothermal depolarization currents makes it possible to evaluate important parameters of the relaxation processes, such as activation energies, characteristic frequencies and time constants.

### 2. EXPERIMENTAL PROCEDURE

The study was performed on uniaxially stretched 25  $\mu\text{m}$  thick PVDF films supplied by Plastpolymer (Russia) and composed of  $\beta$ -form crystallites and amorphous phase in nearly equal volume fractions. Metal electrode of 0.1  $\mu\text{m}$  thickness was deposited on one surface of each sample by thermal evaporation of Al. The other side of the sample was subjected to a negative corona discharge initiated by a pointed tungsten electrode with the automatically controlled potential, while the metallized rear sample surface was grounded. The vibrating control grid between the sample surface and the corona electrode was kept at a constant potential of 3 kV. All samples were charged at room temperature under a constant charging current density [17–18] of 90  $\mu\text{A}/\text{m}^2$  for 30 min and then short-circuited and conditioned at room temperature for 24 hours (except those prepared for measuring of the electret potential kinetics).

Four versions (modes) of depolarization were applied to study relaxation processes, namely thermally stimulated (T) and isothermal (I) depolarization of short-circuited (S) and open-circuited (O) samples. The modes were thus referred as TS, TO, IS and IO modes with the first letter indicating the temperature regime (thermally stimulated or isothermal) and the second one indicating the electric state (short-circuited or open-circuited). Additional experiments have been also performed on the thermally stimulated kinetics of the electret potential (TP) after 24 hours of conditioning in the open circuit configuration. Teflon film of 10  $\mu\text{m}$  thickness was used as a dielectric gap in TO and IO modes. All thermally stimulated experiments were performed under a constant heating rate of 3 K/min. In isothermal experiments, temperature was maintained constant after the desired value was

achieved by fast heating. The electret potential in the TP mode was measured by the Kelvin method and recorded continuously.

### 3. RESULTS AND DISCUSSION

The following main features of experimental curves are seen in Fig. 1 and Fig. 2

- The depolarization current in the TS mode shows a broad “non-classical” peak with a maximum around 65°C;

- The inversion of the TSD current is observed in the TO mode, while the direction of the current coincides with that in the TS mode during the initial stage of the heating;

- The electret potential in the TP mode has a maximum at 40°C.

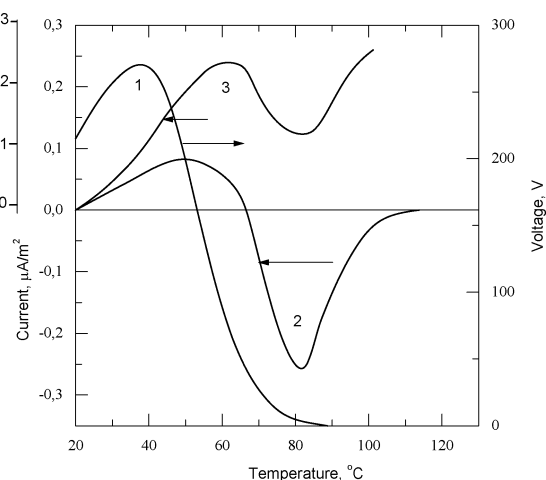


Fig. 1. Thermally stimulated currents in the TS mode (1) and the TO mode (2) and the electret potential in the TP mode (3)

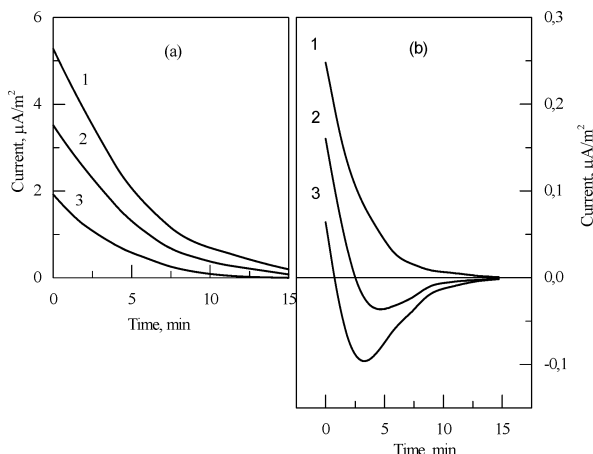


Fig. 2. Isothermal transient currents at different temperatures in IS mode (a) and IO mode (b); 1 – 45°C, 2 – 55°C, 3 – 70°C

- The current slowly decreases with time in the IS mode at all temperatures, while the isothermal current changes its direction in the IO mode at elevated temperatures.

The above mentioned features could be explained in the framework of a model, assuming the existence of the homocharge and the heterocharge in the samples [1, 9], with the former representing the charge trapped at the surface and the latter standing for the polarization formed in the bulk due to the electric

field created by the homocharge. The two types of the charge are obviously interdependent.

At first, we examine charging and relaxation processes qualitatively. It is reasonable to assume that the negatively charged particles (ions and/or electrons), supplied by corona discharge are adsorbed and thermalized on the surface of the sample because of their low (thermal) energy. The redundant charge, localized on the surface or in the near-to-surface layer, forms the homocharge having a certain surface density  $\sigma$  and producing the uniform field  $E$  in the bulk of the sample. The high electron affinity of the fluorine atoms facilitates the charge trapping and formation of the stable homocharge.

The uniform internal polarization  $P$  (heterocharge) appears mainly due to alignment of  $\text{CH}_2\text{-CF}_2$  dipoles in the field created by the homocharge. This is equivalent to developing the bound surface charge  $P$  having the sign opposite to that of the homocharge  $\sigma$ . Among all polarization processes in PVDF, the alignment of  $\text{CH}_2\text{-CF}_2$  dipoles is the main one, because of their large dipole moment of 2.1 D [1, 2].

If the polarization  $P$  is zero, the field in the bulk of the sample is created by the total surface charge  $\sigma$ . When polarization  $P$  starts to grow, the depolarizing field appears, which is being immediately “neutralized” by a fraction of the surface charge equal to the neutralized (screened) polarization. Thus, the electric field in the bulk is created now not by the total charge  $\sigma$ , but by the difference  $(\sigma - P)$  between the surface charge and the polarization. Hence, one can consider the total surface charge  $\sigma$  as consisting of two parts  $\sigma = \sigma_1 + \sigma_2$ , the first one representing the compensating charge ( $\sigma_1 = P$ ) and the second one  $\sigma_2 = \sigma - P$  creating the electric field in the bulk of the sample.

After short-circuiting of the charged samples (in the TS and the IS modes), the “excessive” charge  $\sigma_2$  disappears. Then the equilibrium between the homocharge and the heterocharge ( $\sigma = \sigma_1 = P$ ), as well as zero internal field ( $E=0$ ) are maintained due to the current flowing through the external circuit, so the measured current corresponds to the relaxation of the heterocharge.

However, if, after the short-circuiting and the  $\sigma = \sigma_1 = P$  equilibrium creation, a non-conductive dielectric gap is introduced between one of the electrodes and the surface of the sample (TO and IO modes), one could observe the relaxation currents of both, the heterocharge and the homocharge flowing in opposite directions. The field in the bulk is not zero any more, so the surface charge (homocharge) is either forced to drift in its own field from one surface of the sample to another one through the whole thickness of the sample (in the absence of the intrinsic conductivity), or it is slowly neutralized by the charge carriers responsible for the intrinsic conductivity. In any case, the relaxation of the heterocharge takes place in non-zero field conditions and is caused by thermal disordering of the aligned dipoles [1, 12].

It will be shown now that the two components of the total depolarization current could be obtained from the experimental  $i(T)$  dependence in the TO mode (Fig. 1, curve 2). It is known [1, 12] that the TSD current  $i(t)$  and the electret potential  $V(t)$  in experiments with a non-conducting spacer or an air gap

introduced between the sample surface and the electrode depend not only on the interrelation between the homocharge and the heterocharge, but also on their time derivatives, so that

$$i(t) = s \left[ \frac{dP(t)}{dt} - \frac{d\sigma(t)}{dt} \right], \quad (1)$$

$$V(t) = \frac{s x_1}{\varepsilon_0 \varepsilon_1} [\sigma(t) - P(t)], \quad (2)$$

$$i(t) = -\frac{\varepsilon_0 \varepsilon_1}{x_1} \frac{dV(t)}{dt}, \quad (3)$$

where  $s = x_0 \varepsilon_1 / (x_1 \varepsilon + x_0 \varepsilon_1)$ ,  $t$  is the time,  $\varepsilon$  and  $x_0$  the dielectric constant and the thickness of the sample,  $\varepsilon_1$  and  $x_1$  the corresponding values of the dielectric gap,  $\varepsilon_0$  is the permittivity of a vacuum.

The conductive component  $i_c(t)$  of the total current could be expressed as

$$i_c(t) = \frac{g}{x_0} V(t) = -\frac{d\sigma(t)}{dt}, \quad (4)$$

where  $g = g_0 \exp(-Q/kT)$  is the specific conductivity,  $k$  – Boltzmann's constant,  $T$  – the temperature,  $Q$  – the activation energy of the intrinsic conductivity,  $g_0$  being the pre-exponential factor. Integrating Eq.(3) and substituting time  $t$  for temperature  $T$  in Eq. (1)–(4) according to  $T = T_0(1 + bt)$ , where  $b$  is the heating rate,  $T_0$  the initial temperature, we obtain expressions for temperature dependences of the homocurrent  $i_1(T)$  and the heterocurrent  $i_2(T)$ , as well as for the voltage across the sample (electret potential)  $V(T)$

$$i_1(T) = \frac{d\sigma}{dt} = -\frac{x_1 g_0}{b T_0 x_0 \varepsilon_0 \varepsilon_1} \exp\left(-\frac{Q}{kT}\right) \int_T^\infty i(T') dT', \quad (5)$$

$$i_2(T) = \frac{dP}{dt} = \frac{i(T)}{s} + \frac{d\sigma}{dt}, \quad (6)$$

$$V(T) = \frac{x_1}{b T_0 \varepsilon_0 \varepsilon_1} \int_T^\infty i(T') dT'. \quad (7)$$

All the values at the right hand side of eq. (5)–(7) are known, or could be found experimentally. Results of the calculations according to the eq. (5)–(7) based on the data of Fig. 1 are shown in Fig. 3. Values of  $Q = 0.76$  eV and the pre-exponential factor  $g_0 = 0.18 \Omega^{-1} \cdot \text{m}^{-1}$  were obtained from the steady-state values of the isothermal charging currents and voltages.

As one could see from Fig. 3, the homocurrent and the heterocurrent form two broad peaks with almost coinciding maxima. The heterocharge decays faster in the low-temperature region, while the homocharge remains relatively stable. This is probably the reason of the initial increase of the thermally stimulated potential (see curve 3 in Fig. 1 and curve 3 in Fig. 3). The current inversion in TO and IO modes is caused by the change of ratio between the homocurrent and the heterocurrent at high temperatures (curves 1 and 2 in Fig. 3).

It is known that the inversion of the TSD current could be caused by the over-polarization, i.e. by ap-

pearing of the additional heterocharge in the field of the homocharge, the voltage in this case should be decreasing [12]. However, this has not been observed experimentally in our case (Fig. 1). From the other side, the initial growth of the electret potential during the heating couldn't be caused by the increase of the surface charge density  $\sigma$ , because the charges in this case should move in the direction opposite to that of the electric field created by the charges, that is not possible. Therefore, the first TSD peak and the corresponding increase of the electret potential (Fig. 1) are caused by the faster decay of the heterocharge (polarization) in comparison with the homocharge. It is possible that not all polarization is being destroyed in PVDF during the first stage of the heating, but only the least stable part.

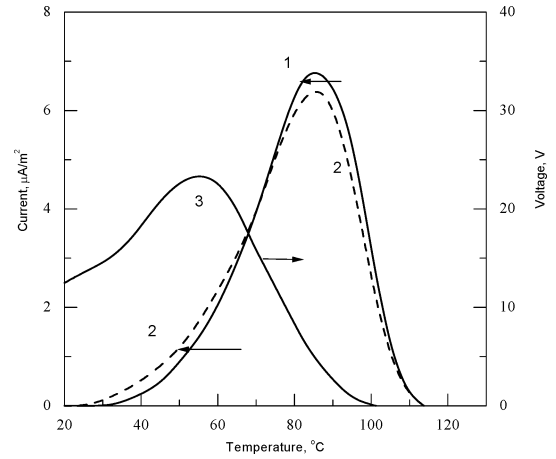


Fig. 3. Temperature dependences of the homocurrent (1), the heterocurrent (2) and the voltage across the sample (3) calculated according to the model proposed

Thus, the heterocharge in PVDF films is not sufficiently stable, therefore its lasting conservation is possible only in presence of the stabilizing field of the homocharge. We believe that many specific properties of PVDF are related to a fortunate combination of the large dipole moment of  $\text{CH}_2\text{-CF}_2$  units (2.1 D) [2], promoting formation of the important heterocharge and the high electron affinity of the fluorine atoms (3.37 eV) promoting creation of the stable homocharge. Although the electret state in PVDF is unstable, the self-balanced mutual relaxation of the homocharge and the heterocharge is delayed due to the stabilizing action of the homocharge.

It is assumed in the theory of electrets [1, 9] that the homocharge and the heterocharge decay exponentially with the temperature dependent time constants. Therefore, the following expressions are valid for IO and IS modes

$$i_1(t) = -\frac{s\sigma_0}{\tau_1} \exp\left(-\frac{t}{\tau_1}\right), \quad (8)$$

$$i_2(t) = -\frac{P_0}{\tau_2} \exp\left(-\frac{t}{\tau_2}\right), \quad (9)$$

$$\tau_1(T) = \frac{\varepsilon_0 \varepsilon}{g_0} \exp\left(\frac{Q}{kT}\right), \quad (10)$$

$$\tau_2(T) = \tau_0 \exp\left(\frac{W}{kT}\right), \quad (11)$$

where  $W$  is the activation energy of the heterocharge relaxation,  $\tau_1$  and  $\tau_2$  the corresponding time constants.

Applying Eq. (8)–(11) to the experimental curve shown in Fig. 2, we calculated the following parameters of the homocharge and heterocharge relaxations: the activation energies ( $Q = 0,76\text{eV}$  and  $W = 0,54\text{eV}$ ), the characteristic frequencies ( $f_2 = 1/\tau_0 = 7,4\text{ MHz}$  and  $f_1 = (g_0/\varepsilon_0\varepsilon) = 1,7\text{ GHz}$ ), the time constants at  $20^\circ\text{C}$  ( $\tau_1 = 31\,000\text{ s}$  and  $\tau_2 = 2\,800\text{ s}$ ). The results indicate that the homocharge is much more stable than the heterocharge.

#### 4. CONCLUSIONS

It is shown how to extract depolarization homocharge and heterocharge currents from experimentally measured TSD current and reveal the relaxation behavior of the both components. The application of different TSD modes supplemented with the isothermal depolarization currents has allowed to find important parameters of the relaxation processes, such as activation energies, characteristic frequencies and time constants.

The uniform field approximation assumed in this paper is justified only in the case of high poarizing fields exceeding  $50\text{--}60\text{ MV/m}$ . At lower fields, one should consider injection of charge carriers in the bulk, resulting in non-uniformity of the field and the polarization in the thickness direction [6,7].

The proposed method allows to analyze the interrelation between the homocharge and the heterocharge not only in PVDF, but also in other dielectrics as well. Introduction of polar groups with simultaneous creation of deep traps for the charge carriers might be a promising procedure for increasing stability of the residual polarization in polar polymer dielectrics. Therefore, if the appropriate conditions exist for creation and trapping of the homocharge, then the high level of the residual polarization could also be ensured for a long period of time.

UDC 537.226:678.01

A. F. Butenko, S. N. Fedosov, A. E. Sergeeva

#### COMPONENTS OF DEPOLARIZATION CURRENTS IN POLYVINYLIDENE FLUORIDE CAUSED BY RELAXATION OF HOMO- AND HETEROCHARGE

A procedure has been developed for separating homocharge and heterocharge components of the total thermally stimulated depolarization current in corona polarized PVDF films. The relaxation behavior of the both components has been analyzed and such important parameters of the relaxation processes, as activation energies, characteristic frequencies and time constants have been obtained by processing TSD current curves measured using four modifications of the TSD method and supplemented with measurements of isothermal currents and the electret potential.

#### References

1. *Sessler G. M.* (ed.) *Electrets*, Laplacian Press, Morgan Hill. — 2000.
2. *Lines M. E., Glass A. M.* *Principles and Applications of Ferroelectrics and Related Materials*, Oxford University Press, Oxford. — 1999.
3. *Gerhard-Mulhaupt R.* A Piezo, Pyro-, and Ferroelectric Polymer and its Poling Behavior // *Ferroelectrics*, 235(1-3), 2000. — P. 385–396.
4. *Fedosov S., von Seggern H.* Piezoelectricity and TSD currents in room temperature poled PVDF // *Inter.Symp. Electrets, ISE-2005*. — P. 145–149.
5. *Furukawa T.* Ferroelectric Properties of VDF Copolymers // *Inter.Symp. Electrets, ISE-2005*. — P. 129–132.
6. *Eberle G., Schmidt H., Eisenmenger W.* Piezoelectric Polymer Electrets // *IEEE Transaction on Dielectric and Electrical Insulation* 12(4), 2005. — P. 624–646.
7. *Eisenmenger W., Schmidt H., Dehlen B.* Piezoelectricity in Polymer Electrets // *Brazilian Journal of Physics* 30(2), 2000. — P. 295–318.
8. *Sessler G. M.* et al. Piezo- and Pyroelectricity in Electrets // *IEEE Trans. El. Insul.* 40(4), 2005. — P. 872–897.
9. Процеси електричної релаксації в легованих плівках полістиролу, електризованих у коронному розряді / Т. А. Ревенюк, С. Н. Федосов, Ж. А. Джакометті, О. Є. Сергеева // *Фізика і хімія твердого тіла* 3(3), 2004. — С. 345–349.
10. *Von Seggern H., Fedosov S. N.* Conductivity-induced Polarization Buildup in Poly(vinylidene fluoride) // *Applied Physics Letters* 81(15), 2002. — P. 2830–2832.
11. *Fedosov S. N., von Seggern H.* Back-switching of ferroelectric polarization in two-component systems // *J. Appl. Phys.* 94(4), 2004. — P. 2173–2180.
12. *Van Turnhout J.* *Thermally Stimulated Discharge of Polymer Electrets*, Elsevier, Amsterdam, 2000.
13. *Eliasson S.* On TSD in PVDF in the Temperature Range // *J. Phys. D: Appl. Phys.* 33(10), 2000. — P. 1965–1972.
14. *Hilczner B., Kulek J.* The effect of dielectric heterogeneity on the pyroelectric response of PVDF // *IEEE Trans. Dielectr. Electr. Insul.* 7(1), 2000. — P. 45–50.
15. *Doughty K., Das Gupta D. K.* On the Origin of Space TSDC Peaks in PVDF // *J. Phys. D: Appl. Phys.* 33(2), 2000. — P. 229–232.
16. *Teyssedre G., Demont L., Lacabanne C.* Analysis of the Experimental Distribution of Relaxation Times Around the Liquid — Glass Transition of PVDF // *J. Appl. Phys.* 85(12), 2002. — P. 9258–9267.
17. *Giacometti J. A., Fedosov S., Costa M. M.* Corona Charging of Polymers: Recent Advances on Constant Current Charging // *Brazilian Journal of Physics.* 30(2), 2000. — P. 269–279.
18. *Corona* poling of a ferroelectric polymer (PVDF) / S. N. Fedosov, A. E. Sergeeva, J. A. Giacometti, P. A. Ribeiro // *Polymers and Liquid Crystals, Proceedings of SPIE*, 4019, 2001. — P. 53–58.

УДК 537.226:678.01

А. Ф. Бутенко, С. Н. Федосов, О. Є. Сергеева

**КОМПОНЕНТИ СТРУМІВ ДЕПОЛЯРИЗАЦІЇ В ПОЛІВІНІЛІДЕНФТОРИДІ, ЯКІ ОБУМОВЛЕНІ РЕЛАКСАЦІЄЮ ГОМО- І ГЕТЕРОЗАРЯДУ**

Розроблений метод розділення складових частин повного струму термостимульованої деполяризації (ТСД), обумовлених релаксацією гомо- та гетерозаряду в короннозаряджених плівках полівиніліденфториду (ПВДФ). Проаналізовано релаксаційну поведінку обох компонент і розраховані такі важливі параметри релаксаційних процесів, як енергії активації, характеристичні частоти і постійні часу шляхом обробки кривих струму деполяризації, виміряного чотирма модифікаціями методу ТСД, доповнених вимірюваннями ізотермічних струмів та електретного потенціалу.

УДК 537.226:678.01

А. Ф. Бутенко, С. Н. Федосов, А. Е. Сергеева

**КОМПОНЕНТЫ ТОКОВ ДЕПОЛЯРИЗАЦИИ В ПОЛИВИНИЛИДЕНФТОРИДЕ, ОБУСЛОВЛЕННЫЕ РЕЛАКСАЦИЕЙ ГОМО- И ГЕТЕРОЗАРЯДА**

Разработан метод разделения составляющих полного тока термостимулированной деполяризации (ТСД), обусловленных релаксацией гомо- и гетерозаряда в короннозаряженных пленках поливинилиденфторида (ПВДФ). Проанализировано релаксационное поведение обеих составляющих и рассчитаны такие важные параметры релаксационных процессов, как энергии активации, характеристические частоты и постоянные времени путем обработки кривых тока деполяризации, измеренного четырьмя модификациями метода ТСД, дополненных измерениями изотермических токов и электретного потенциала.

## EFFECT OF AMMONIA VAPORS ON SURFACE CURRENTS IN INGAN P-N JUNCTIONS

The influence of ammonia vapors in the ambient atmosphere on  $I-V$  characteristics of the forward and reverse currents in InGaN p-n junctions is studied. The characteristics of the additional surface current, due to  $\text{NH}_3$  ions adsorption, are explained by the model taking into account formation of a surface conductive channel in the electric field of these ions. The advantages of InGaN p-n junctions as ammonia vapors sensors are a high sensitivity, low background currents, an extended linear section of the  $I-V$  characteristic.

### 1. INTRODUCTION

Forward and reverse currents in p-n junctions on GaAs [1], GaP [2], Si [3] are sensitive to ammonia vapors at room temperature. This effect can be used for creation of gas sensors, which have crystal structure, selectivity to gas components, and can be manufactured in microelectronic technology. The ammonia sensitivity of the sensors on GaAs and GaP is due to forming of a surface conductive channel in the electric field induced by the ammonia ions adsorbed on the surface of the natural oxide layer [1, 2]. The surface current induced by adsorption of  $\text{NH}_3$  molecules in p-n structures on GaAs linearly depends on the applied voltage (at low biases) and on the ammonia partial pressure (in some range of pressures, depending on device parameters). In Si p-n junctions, the electric field of ammonia ions enhances the surface recombination rate [3].

As observed in [1–4], mechanism of gas sensitivity and parameters of p-n junctions as sensors depend on parameters of the semiconductor and in particular, on band gap and on the surface states density. Wide-band semiconductors have higher maximum sensitivity at forward biases. On the other hand, the chemical stability of the wide-band III–V materials, such as GaN and InGaN, is higher than GaAs, which is very important for sensors of aggressive gases.

The aim of this work is a study of the influence of ammonia vapors on surface currents in InGaN p-n junctions of several band gaps.

### 2. EXPERIMENT

$I-V$  measurements were carried out on InGaN p-n junctions with the structure optimized for LED manufacturing. The band gap of the ternary material in the p-n structures was 2.46 eV (for bluish green LED), 2.64 eV (blue) and 3.1 eV (violet). The effect of saturated ammonia vapors over water solutions of several  $\text{NH}_3$  concentrations was studied on stationary  $I-V$  characteristics, as well as on kinetics of surface current in p-n junctions.

$I-V$  characteristic of the forward current in a typical InGaN p-n structure with  $E_g = 2.64$  eV is presented as curve 1 in Fig. 1. Over the current range between 10 nA and 1 mA the  $I-V$  curve can be described with the expression

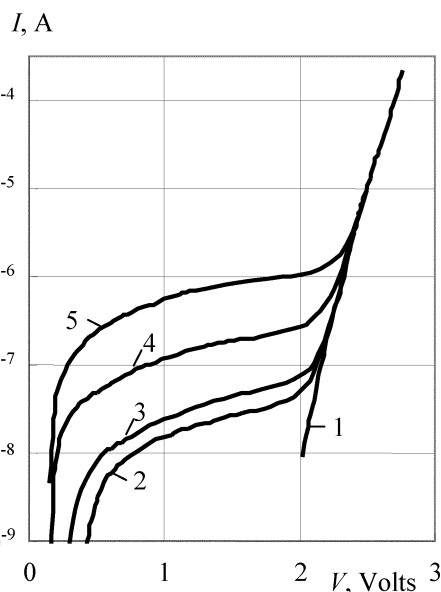


Fig. 1. Forward branches of  $I-V$  characteristics of a p-n structure in air (1) and in  $\text{NH}_3$  at pressures: 2 – 5 Pa; 3 – 50 Pa; 4 – 200 Pa; 5 – 500 Pa

$$I(V) = I_0 \exp(qV/nkT), \quad (1)$$

where  $I_0$  is a constant;  $q$  is the electron charge;  $V$  denotes bias voltage;  $k$  is the Boltzmann constant;  $T$  is temperature;  $n \approx 2$  is the ideality constant. Such  $I-V$  curves are due to recombination on deep levels in the bulk and at the surface [1, 2]. Curves 2 to 5 in Fig. 1 were measured in air at several ammonia vapor partial pressures. It is seen that  $\text{NH}_3$  molecules adsorption drastically enhances forward current of the p-n structure at low biases ( $V < 2$  Volts). The effect increases with the  $\text{NH}_3$  pressure. Curves 2–5 cannot be described by formula (1). The comparison of curves 2–5 with curve 1 shows that the surface current due to  $\text{NH}_3$  molecules adsorption cannot be attributed to surface recombination. Similar results are obtained on InGaN p-n junctions of other band gaps mentioned.

Fig 2 depicts the reverse branches of the  $I-V$  characteristic of the same sample, obtained at diverse ammonia pressures. In air without  $\text{NH}_3$  vapors, reverse current was  $I_r < 1$  nA.

It is evident that ammonia vapors in ambient atmosphere essentially enhance the reverse current in studied structures.  $I-V$  characteristic of the reverse

current due to ammonia molecules adsorption cannot be ascribed to minority carrier generation in p-n junction. Such results are characteristic of all the p-n structures studied.

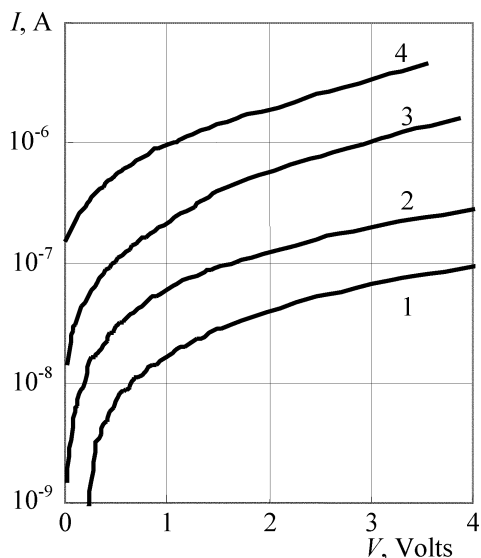


Fig. 2. Reverse branches of I-V characteristics of a p-n structure in NH<sub>3</sub> at pressures: 1 – 5 Pa; 2 – 50 Pa; 3 – 200 Pa; 4 – 500 Pa

Fig. 3 illustrates the dependence of the additional surface forward current, due to NH<sub>3</sub> molecules adsorption, on the bias voltage at several ammonia partial pressures. *I-V* characteristics of the additional current have linear sections at bias voltages up to 1.7 Volts. At higher biases, the forward current non-linearly grows, and then sharply falls down. Such behavior of *I-V* curves is characteristic of the studied p-n junctions and was observed previously on GaAs, AlGaAs, GaP, and Si p-n structures [1–4]. The difference is that, in the case of wide-band semiconductors InGaN, *I-V* curve, measured at high ammonia pressures (see curve 4 in Fig. 3), does not have a non-linear section.

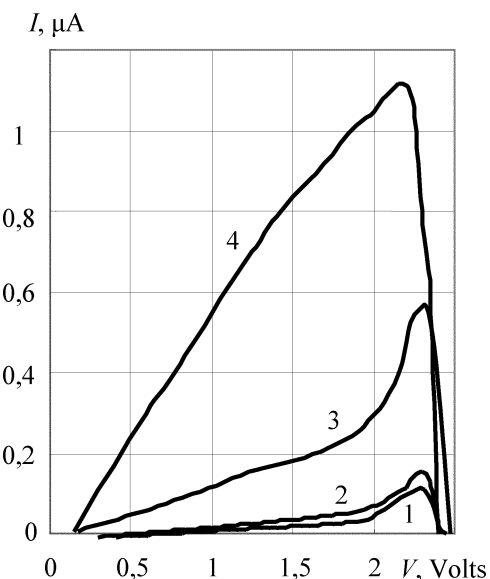


Fig. 3. *I-V* characteristics of the additional forward current in a p-n structure due to ammonia molecules adsorption at NH<sub>3</sub> pressures: 1 – 5 Pa; 2 – 50 Pa; 3 – 200 Pa; 4 – 500 Pa

Fig. 4 represents *I-V* characteristics of the additional reverse current in the p-n junction due to NH<sub>3</sub>

molecules adsorption, measured at several ammonia partial pressures. The characteristics have linear parts at low biases, similar to those of the forward current. A comparison between the corresponding curves in Figs 3 and 4 shows that the reverse current is more sensitive to ammonia vapors contamination in the ambient atmosphere, than the forward current.

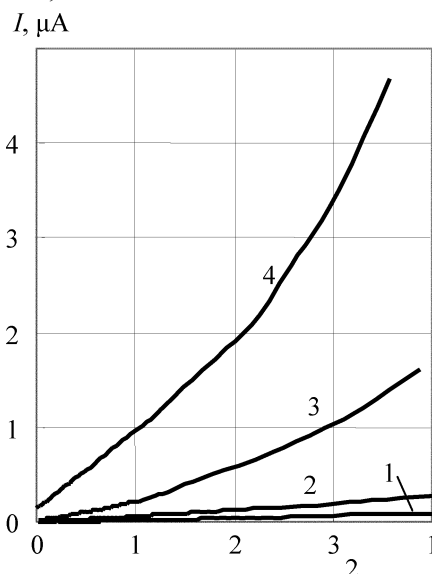


Fig. 4. *I-V* characteristics of the additional reverse current in a p-n structure due to ammonia molecules adsorption at NH<sub>3</sub> pressures: 1 – 5 Pa; 2 – 50 Pa; 3 – 200 Pa; 4 – 500 Pa

### 3. DISCUSSION

The effect of ammonia vapors on the forward and reverse currents in InGaN p-n junctions can be explained using the model, developed in [4]. Fig. 5 depicts the schematic of a p-n structure in NH<sub>3</sub> vapors. The positive ammonia ions are placed on the external surface of the natural oxide layer. The compensating negative charge is formed by (a) electrons captured on surface states; (b) free electrons in the conductive channel, which can be formed in the electric field of ions; (c) electrons located on the acceptors in the surface depletion region. The linear sections of the *I-V* curves in Figs 3 and 4 are the witness of conductive channel forming in p-n junctions, caused by NH<sub>3</sub> ions adsorption. In NH<sub>3</sub> vapors, the charge on surface states is negative, and the conductive channel is formed only in the case of the inequality

$$N_i > N_s, \quad (2)$$

where  $N_i$ ,  $N_s$  is the surface density of adsorbed ions and surface states, respectively. The conductive channel shorts the depletion region and gives rise to the linear additional current.

At high enough forward bias voltages, electrons and holes are injected into the surface conductive channel and recombine at the surface states. Thus, the additional current nonlinearly rises with the bias voltage due to surface recombination enhanced by lateral electric field. It is evident that concentrations of electrons and holes, injected into the surface channel at a fixed temperature exponentially depends on the potential barrier height. Therefore, in p-n structures on semiconductors of wider band gap, the nonlinear

section of  $I-V$  curve of the additional current must begin at higher forward bias voltages.

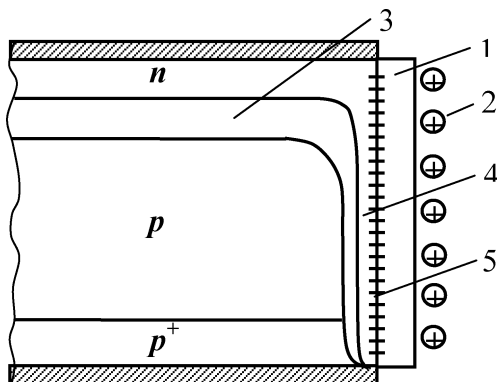


Fig. 5. Schematic of the p-n structure in  $\text{NH}_3$  vapors: 1 – oxide layer; 2 – ions; 3 – depletion layer; 4 – conducting channel; 5 – surface states

Curve 1 in Fig. 6 illustrates the influence of the band gap on the forward bias voltages, corresponding to the beginning of the nonlinear  $I-V$  curve section. The data, obtained on InGaN structures, are completed by an analysis of  $I-V$  curves for p-n junctions in GaAs, AlGaAs, GaP, and Si in our previous works [1–4].

Fig. 6. Influence of the band gap on the forward bias voltages, corresponding to the beginning of the nonlinear  $I-V$  curve section (1) and to maximum  $\text{NH}_3$  sensitivity (2).

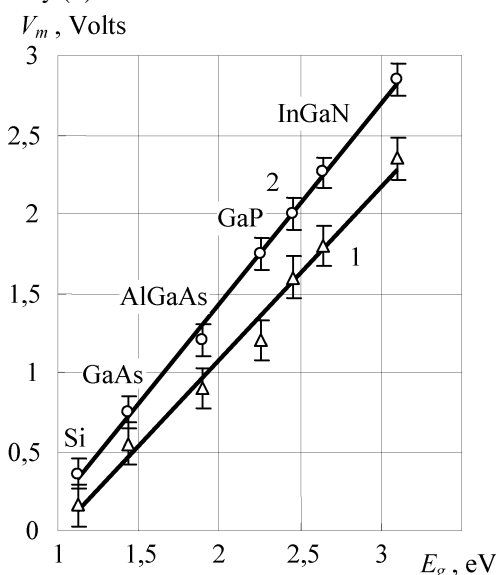


Fig. 6. Influence of the band gap on the forward bias voltages, corresponding to the beginning of the nonlinear  $I-V$  curve section (1) and to maximum  $\text{NH}_3$  sensitivity (2)

UDC 621.315.592

F. O. Ptashchenko

#### EFFECT OF AMMONIA VAPORS ON SURFACE CURRENTS IN INGAN P-N JUNCTIONS

The influence of ammonia vapors in the ambient atmosphere on  $I-V$  characteristics of the forward and reverse currents in InGaN p-n junctions is studied. The characteristics of the additional surface current, due to  $\text{NH}_3$  ions adsorption, are explained by the model taking into account formation of a surface conductive channel in the electric field of these ions. The advantages of InGaN p-n junctions as ammonia vapors sensors are a high sensitivity, low background currents, an extended linear section of the  $I-V$  characteristic.

As seen in Fig. 3, the  $I-V$  characteristics of the additional forward current, caused by ammonia molecules adsorption, have maximum. In our model, the fall down of the additional current at high enough forward bias voltages is explained as a result of destroying the surface channel by the injected electrons and holes. This effect occurs at such biases when the concentration of carriers, injected into the channel, exceeds the electrons concentration, caused by the electric field of adsorbed ions.

Curve 2 in Fig. 6 illustrates the influence of the band gap of p-n junction on the forward bias voltage, corresponding to maximum  $\text{NH}_3$  sensitivity. The data of curve 2 are obtained similarly to those of curve 1.

#### 4. CONCLUSIONS

$I-V$  characteristics of the forward and reverse currents in InGaN p-n junctions are strongly affected by ammonia vapors in the ambient atmosphere. The characteristics of the additional surface current, due to  $\text{NH}_3$  ions adsorption, are explained by the model taking into account formation of a surface conductive channel in the electric field of these ions.

The advantages of the InGaN p-n junctions as ammonia vapors sensors are a high sensitivity, low background currents, an extended linear section of the  $I-V$  characteristic.

#### References

1. Ptashchenko O. O., Artemenko O. S., Ptashchenko F. A. Vliyanie gazovoi sredy na poverhnostnyi tok v p-n geterostrukturakh na osnove GaAs-AlGaAs // Fisika i khimiya tverdogo tela. – 2001. – Vol. 2, N 3. – P. 481–485.
2. Ptashchenko O. O., Artemenko O. S., Dmytruk M. L. et al. Effect of ammonia vapors on the surface morphology and surface current in p-n junctions on GaP. // Photoelectronics. – 2005. – N 14. – P. 97–100.
3. Ptashchenko F. O. Vplyv pariv amiaku na poverkhnevij strum u kremniyevykh p-n perekhodakh // Visnyk ONU, ser. Fizyka. – 2006. – Vol. 11, N 7. – P. 116–119.
4. Ptashchenko A. A., Ptashchenko F. A. P-n perekhody na osnove GaAs i drugih poluprovodnikov  $A^{III}B^V$  kak gazovye sensory // Ninth conference "Gallium arsenide and III-V group related compounds". Abstracts. – Tomsk: Tomskiy gosuniversitet, 2006. – P. 496–499.

УДК 621.315.592

Ф. О. Птащенко

#### **ВПЛИВ ПАРІВ АМІАКУ НА ПОВЕРХНЕВИЙ СТРУМ У P-N ПЕРЕХОДАХ НА ОСНОВІ INGAN**

Досліджено вплив парів аміаку в навколишній атмосфері на вольт-амперні характеристики прямого і зворотного струмів у р-п переходах на основі InGaN. Характеристики додаткового поверхневого струму, обумовленого адсорбцією іонів NH<sub>3</sub>, пояснюються на основі моделі, що враховує утворення поверхневого провідного каналу в електричному полі вказаних іонів. Перевагами р-п переходів на основі InGaN як сенсорів парів аміаку є висока чутливість, низькі фонові струми, витягнута лінійна область вольт-амперної характеристики.

УДК 621.315.592

Ф. А. Птащенко

#### **ВЛИЯНИЕ ПАРОВ АММИАКА НА ПОВЕРХНОСТНЫЙ ТОК В P-N ПЕРЕХОДАХ НА ОСНОВЕ INGAN**

Исследовано влияние паров аммиака в окружающей атмосфере на вольт-амперные характеристики прямого и обратного токов в р-п переходах на основе InGaN. Характеристики дополнительного поверхностного тока, обусловленного адсорбцией ионов NH<sub>3</sub>, объясняются на основе модели, учитывающей формирование поверхностного проводящего канала в электрическом поле указанных ионов. Преимущества р-п переходов на основе InGaN как сенсоров паров аммиака являются высокая чувствительность, низкие фоновые токи, протяженная линейная область вольт-амперной характеристики.

## INVESTIGATIONS OF Si/Si-O<sub>y</sub>-Si<sub>4-y</sub> NANOSYSTEM BY THE COMPUTER SIMULATION METHOD

The atomic system is simulated by the Monte-Carlo method of computer modeling. Analyzing results of computer modeling, we have found out some features of structure of thin oxide of silicon. In particular, the function of radial distribution demonstrates certain disorder in an arrangement of atoms Si and O and the decrease of values of Si-O-Si bond angle near the surface is observed as well as the critical concentration of oxygen, at which silicon cluster is formed, makes 0.9 from a stoichiometric value.

### INTRODUCTION

The systems Si/SiO<sub>2</sub> and Si/Si<sub>3</sub>N<sub>4</sub> are present almost in all devices of modern microelectronics, for example, in the devices on SONOS-structures (Silicon-Oxide-Nitride-Oxide-Silicon). Considering the increase of volumes of information preservation results in diminishing of thicknesses of SONOS-structures layers to the nano-scale range.

The features of technology of such nano-sizing systems preparation, determine the non-stoichiometry of chemical composition and probability Si, O or N precipitates' generation into the of dielectric phases. This leads to the change of conductivity type of the layers. Nowadays, the development of data storage which are based on the conducting nano-clusters (Si, Ge, Si<sub>x</sub>, Ge<sub>y</sub>) in the dielectric layer is carried out [1–3].

The interest is, therefore, supported by the research of atomic structure and chemical composition of interface Si/SiO<sub>2</sub> and Si/Si<sub>3</sub>N<sub>4</sub> with the thicknesses of dielectric layers not more than 10 nm.

### MODEL AND DISCUSSION

By means of computer modeling, we have created the model of system with free surfaces and layers thickness of 16.26 Å. The inter-atomic interaction was described by the three-particle Keating potential [4]. It takes into account not only the pair, but also angular interaction between particles. The repulsive between atoms of oxygen was taken into account with the help of potential Born-Maier-Haggins without the dispersion terms:

$$V_{ij} = \frac{z_i z_j}{R_{ij}} \cdot \left( \frac{r_0}{L} \right) + A_{ij} \exp\left( -\frac{R_{ij}}{\rho} \right),$$

where  $z_i, z_j$  — are the charges of the ions in terms of an elementary charge;  $r_0$  — Bohr radius;  $L$  — a length of a cube edge,  $R_{ij}$  — a distance between cooperating ions;  $r = 0.29$  Å — the constant;  $A_{ij}$  — the energetic repulsive parameter, which depends on the sorts of the interacting ions.

The real multi-atomic system was replaced with the limited cubic cell with introduction of periodic

boundary conditions, which were imposed on the cube face with side 37.94 Å in X and Y directions. The choice of such a size depends, first and foremost, on significant duration of time relaxation of large volume systems, secondly by experimental results, which specify thickness of a transitive layer between and approximately 1 nm.

The prototype system was filled by atoms at the positions approximate to ideal crystal and contained 2352 atoms. The vacuum was simulated on the part of Si and Si-O<sub>y</sub>-Si<sub>4-y</sub> layers Si each by the thickness up to 16.26 Å. In such a way, we have received the model of the continuous interface with free surfaces (Fig. 1).

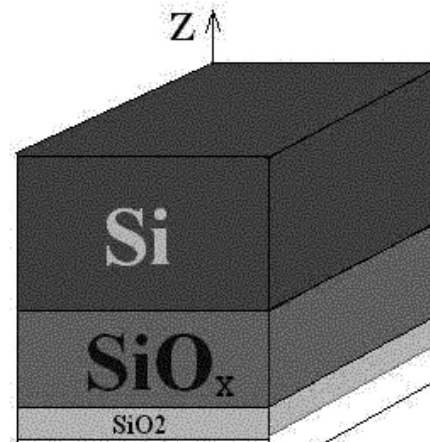


Fig. 1. The schematic image of an experimental cell Si-O<sub>y</sub>-Si<sub>4-y</sub>

The interface Si(100)/Si-O<sub>y</sub>-Si<sub>4-y</sub> ( $1 \leq y \leq 4$ ) was investigated. The equilibrium atomic configuration was determined by dint of application to model a Monte-Carlo procedure at decrease of temperature from 1000K to 300K. 1000 shifts of the atomic system were made in every 50K. At such shifts' range, the amplitude of shifts depended on temperature.

For definition of concentration of oxygen, depending on depth, the formula was used [5]:

$$x(d) = 2 \cdot \left[ 1 - \exp\left( -\frac{d}{d_0} \right) \right],$$

where  $d$  — is a distance from a surface of silicon;  $d_0$  — a characteristic length, which depends on conditions of oxidation.

For the analysis of details of the atomic structure the following structural characteristics were used:

- Radial distribution functions.
- The energy of the atomic system.
- Three-body correlation functions.
- The value of bond-angle distributions.
- The arrangement of atoms in planes (100), (110) and (111).

— The spatial picture of atomic array.  
 — The presence Si precipitate as the fractal clusters.

As a result of computing experiments the following results have received.

The radial distribution function received as a result of modeling of structure is presented at Fig. 2.

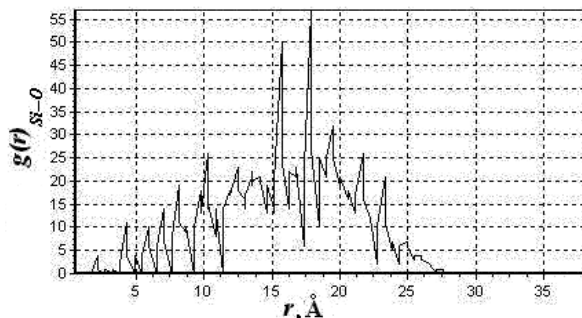


Fig. 2. The radial distribution function  $g(r)_{Si-O}$  in the region of  $Si-O_y-Si_{4-y}$

The coordination number (the first peak) is equal to 4, that is characteristic for volume. For other coordination, the spheres in significant deviations from arrangement are observed. These deviations increase in proportion to the distance from the central atom. Analyzing the radial distribution functions (Fig. 2–3), we have the conclusion, that for thin oxide of silicon, which thickness does not permit to measure up the volume stoichiometric composition and the disorder in an arrangement of atoms Si and O is observed.

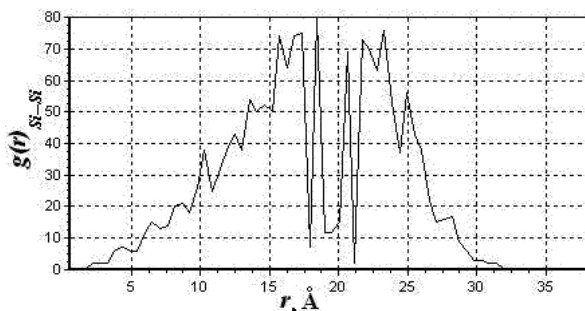


Fig. 3. The radial distribution function  $g(r)_{Si-Si}$  in the region of  $Si-O_y-Si_{4-y}$

The spatial picture demonstrates almost the same (Fig. 4).

On the diagram of the correlation function (Fig. 5) near the surface the appearance of peak is observed. It is caused by the increase of number of  $s$ , which values are less than 120 (the value of a Si-O-Si bond angles taken as in the volume).

On the surface of thin oxide, after relaxation, the reconstruction is observed, which are similar to formation of a super-lattice, but due to the small thickness of oxide, the formation hasn't the clearly defined character (Fig. 5–6).

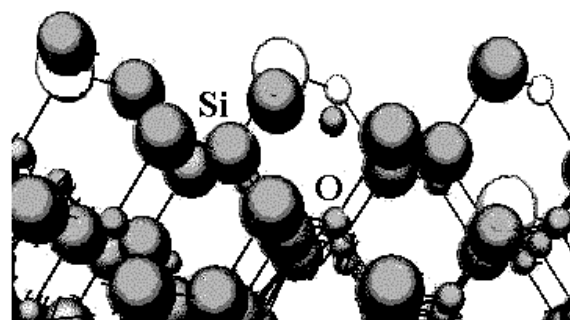


Fig. 4. The fragment of a spatial picture of arrangement of atoms in the model of the system on the part of the surface (unpainted spheres — starting positions of atoms)

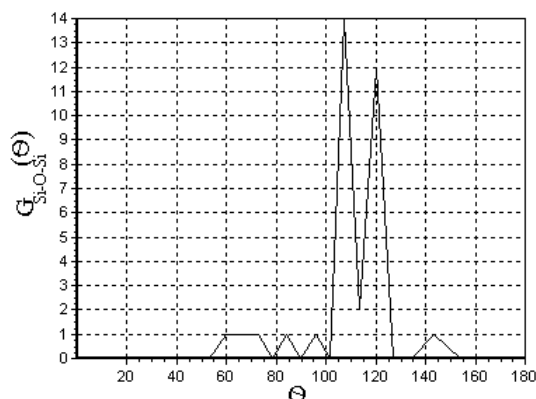


Fig. 5. The three-particle correlation function

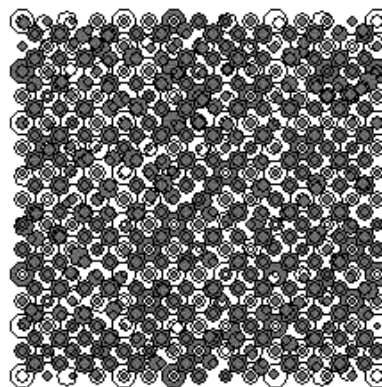


Fig. 6. The arrangement of atoms the surface (100) (painted circles — atoms of silicon unpainted - atoms of oxygen, radius of circles is increased with depth).

The critical concentration of oxygen, at which penetrating structure silicon cluster (Fig. 7) is formed according to our experiment makes 0.9 from a stoichiometric value.

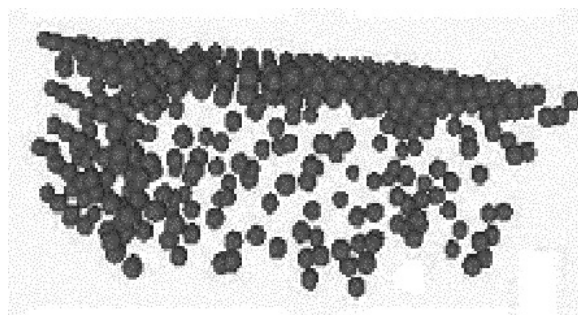


Fig. 7. The fractal cluster of Si atoms in the volume  $Si-O_y-Si_{4-y}$

## CONCLUSIONS

1. Analyzing results of computer modeling, we have found out that some features of structure of thin oxide of silicon, in particular, the function of radial distribution demonstrates the disorder in an arrangement of Si and O atoms

2. Near the surface, the decrease of values of a Si-O-Si bond angle is observed; the critical concentration of oxygen, at which silicon cluster is formed, makes 0.9 from a stoichiometric value.

### References

1. Puglisi R. A., Lombardo S., Ammendola G. et al. Imaging of Si Quantum Dots as Charge Storage Nodes. // *Material Science and Engineering C* – 2003. – Vol. 23. – P. 1047–1051.

2. Trukhin A. N., Jansons J., Fitting H.-J. et al. Cathodoluminescence decay kinetics in  $\text{Ge}^+$ ,  $\text{Si}^+$ ,  $\text{O}^+$  implanted  $\text{SiO}_2$  layers. // *J. Non-Cryst. Solids*. – 2003. – Vol. 331. – P. 91–99.
3. Griusenko V. A., Nasyrov K. A. et al. A new memory element based on silicon nanoclusters in the  $\text{ZrO}_2$  dielectric with high permittivity for Electrically Erasable Read Only Memory. // *Fizika i tehnika poluprovodnikov*. – 2005. – Vol. 39, N 6. – P. 748–753 (in Russian).
4. The structural models of the Si/ $\text{SiO}_2$  interface / I. Ohdomari, H. Akatsu, Yu. Yamarkoshi, K. Kishimoto // *J. Non-Cryst. Solids*. – 1987. – Vol. 89. – P. 239-248.
5. Hübner K. Structure and properties of the microelectronic Si- $\text{SiO}_2$  inter-region. // *Phys. Solid Surfaces, Proc. 3<sup>rd</sup> Symp Surface Phys. Smolenia Castle 3-7 September, Amsterdam*. – 1984. – P. 115-129.

UDC 621.235

R. Balabay, E. Chernonog

## INVESTIGATIONS OF Si/ Si-O<sub>y</sub>-Si<sub>4-y</sub> NANOSYSTEM BY THE COMPUTER SIMULATION METHOD

The atomic system is simulated by the Monte-Carlo method of computer modeling. Analyzing results of computer modeling, we have found out some features of structure of thin oxide of silicon, in particular function of radial distribution demonstrates disorder in an arrangement of atoms Si and O; near the surface the decrease of values of a corner Si-O-Si of connection is observed; the critical concentration of oxygen, at which silicon cluster is formed makes 0.9 from a stoichiometric value.

УДК 621.235

Р. Балабай, О. Черноног

## ДОСЛІДЖЕННЯ НАНОСИСТЕМИ Si-O<sub>y</sub>-Si<sub>4-y</sub> ЗАСОБАМИ КОМП'ЮТЕРНОГО МОДЕЛЮВАННЯ

Методом комп'ютерного моделювання Монте-Карло змодельована атомна система Si-O<sub>y</sub>-Si<sub>4-y</sub>. Аналіз результатів обчислювального експерименту виявив деякі особливості структури тонкого окислу кремнію, зокрема функція радіального розподілу  $g(r)_{\text{Si-O}}$  демонструє порушення порядку в розташуванні атомів Si та O; спостерігається зменшення значення кута Si-O-Si зв'язку поблизу поверхні; гранична концентрація кисню, при якій утворюється кремнієвий кластер, становить 0.9 від стехіометричного значення.

УДК 621.235

Р. Балабай, Е. Черноног

## ИССЛЕДОВАНИЕ НАНОСИСТЕМЫ Si/Si-O<sub>y</sub>-Si<sub>4-y</sub> СРЕДСТВАМИ КОМПЬЮТЕРНОГО МОДЕЛИРОВАНИЯ

Методом компьютерного моделирования Монте-Карло смоделирована атомная система Si-O<sub>y</sub>-Si<sub>4-y</sub>. Анализ результатов вычислительного эксперимента выявил некоторые особенности структуры тонкого оксида кремния, в частности, функция радиального распределения  $g(r)_{\text{Si-O}}$  демонстрирует нарушение порядка в расположении атомов Si и O; наблюдается уменьшение значения угла Si-O-Si связи вблизи поверхности; граничная концентрация кислорода, при которой образуется кремниевый кластер, равняется 0.9 от стехиометрического значения.

## WAVELET AND MULTIFRACTAL ANALYSIS OF NONLINEAR FEATURES IN THE ACOUSTIC DETECTING THE GRANULATED MATERIALS

It is carried out an analysis of nonlinear features in the acoustic detecting and diagnostic of the granulated mediums on the basis of wavelet analysis and multifractal formalism. The fractals dimensions are lying in the interval  $[1,3-2,1]$ .

In last years it is of a great importance the experimental and theoretical studying of the non-linear dynamical systems with aim to discover the fractal features and elements of dynamical chaos (c.f. [1–25]). This is regarding different wave phenomena in the granulated mediums. It is very important to note that these phenomena are characterized by the strong non-linearity (c.f. [1]). The matter is in the fact that non-linearity parameter in the granulated mediums is on three-four orders higher than in homogeneous mediums, i.e. it is worth to say about a giant non-linearity (see below). From the other side it is well known that many physical, chemical and biological systems, including the multi-element semiconductors and gas lasers, different radio-technical devices etc can be considered in the first approximation as a self-adapted complicated systems, coupled by different way. The interesting example – system of two auto-generators (semiconductor) quantum generators, coupled by means optical waveguide, have been in details considered in ref. [5, 6, 23, 24]. It has been studied a regular and chaotic dynamics of the system of the Van-der-Poll auto-generators in different cases. An important feature of these systems is connected with possibility of realizing the stochastic regime of oscillations and manifesting the chaos. The PC wavelet and fractal complex “Geomath” was used. Earlier it was used in solving a whole number of tasks of the modern environmental and atmosphere physics. In particular, speech is about such problems as [14–22]: sensing the nonlinear interaction between global teleconnection patterns, temporal variability of the atmosphere ozone content and prediction of the effect of North-Atlantic oscillation, using non-decimated wavelet decomposition to analyze time variations of North Atlantic Oscillation, eddy kinetic energy, sensing nonlinear interaction between global teleconnection patterns and firstly a prediction of the possible genesis of fractal dimensions in the turbulent pulsations of cosmic plasma – galactic-origin rays – turbulent pulsation in planetary atmosphere system [22]. The fundamental problem here is a determination of the fractal and multi-fractal characteristics for mediums and processes and their numerical estimates. In this paper we carry out an analysis of nonlinear features in the acoustic detecting and diagnostic of the granulated mediums (granite crumb) on the basis of wavelet analysis and multi-fractal formalism and find the corresponding fractals (dimensions) spectrum.

The physical features of propagation of the acoustic oscillations in the granulated mediums significantly differs from propagation in the continuous mediums. The acoustical properties of the corresponding mediums such as mono-crystals and homogeneous liquids are defined by the deformation features on molecular level and the same in the granulated mediums is connected with their structure. The matter is in the fact that mechanical properties of the granulated materials are provided by contacts between granules. In this essence it attracts a great interest studying these materials on the example of separated granule. The important result is that the oscillations of separated granule in an acoustic field are characterized by the slow fluctuations (c.f. [1]). Experimental studying slow fluctuations of the nonlinear oscillations of granules under action of propagating acoustic field has been carried out in ref. [25]. As the granulated medium it was used the granite crumb (size 1–2 cm). The sound emitting is produced by piezoceramic plate and the sound receiving is realized by the accelerometers. The tone frequency is 5,6 kHz. The maximal level of the received signal corresponds to vibrations of the emitted plate with acceleration 0,6 m/cm<sup>2</sup> and the amplitude of vibrations is 5E. These parameters of vibrations the plate correspond to emission level 10 dB. The level of the granule vibrations is less on 10 dB. Non-monotonic dependence of the received response level for separated granule upon the medium loading value is treated usually as a result of percolation realization of links between separated granules. In figure 1 there are presented the experimental dependences of the signal harmonic components upon a time (in hours): 1 – levels of signal on the receivers in a granulated medium, frequency 5,6 kHz; 2 – levels of the second harmonics on the receivers in a granulated medium, frequency 11,2 kHz; 3- levels of the sub harmonics on the receivers in a granulated medium, frequency 2,8 kHz (the detailed data are presented in [1, 25]). It is important to note that there is a sub harmonics component in the spectrum of received signal. In general a character of the signal fluctuations is similar for all components. The signal level on the main frequency 5,6 kHz is randomly changed more on more than 5-6dB. The levels of fluctuations of the harmonics components are very big, i.e. speech is about giant fluctuations of the acoustic signals in the granulated medium. The most intensive are the fluctuations of the sub harmonics components. The detailed analysis

of the obtained experimental data is presented in ref. [1, 25].

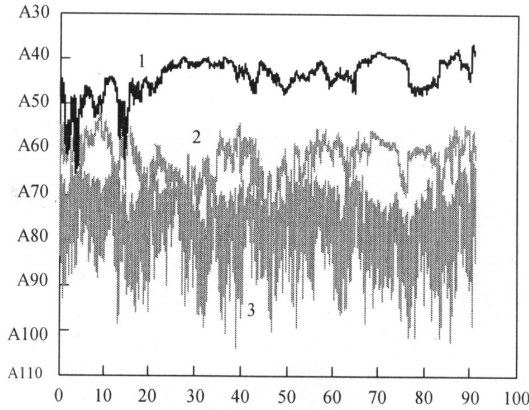


Fig. 1. The experimental dependences of signal harmonic components on a time (hours): 1 – level of signal on the receivers in a granulated medium (RGM), frequency  $w=5.6$  kHz; 2-level of 2<sup>nd</sup> harmonics on RGM, 11.2 kHz; 3-level of sub harmonics on RGM, 2.8 kHz [25]

Further let us analyze a spectrum of fluctuations of the harmonics components of the signal and estimate the fractal properties of the corresponding dependences. The main purpose is estimating of the fractal dimensions too. As the detailed description of the fractal and wavelet methodic (our version) is earlier given (c.f. [11–22]), below, following these refs., we remember the key moments of the used wavelet analysis and multi-fractal formalism.

Here we use non-decimated wavelet transform that has temporal resolution at coarser scales. The dilation and translation of the mother wavelet  $\psi(t)$  generates the wavelet as follows:  $\psi_{j,k}(t) = 2^{j/2}\psi(2^j t - k)$ . For a suitably chosen mother wavelet  $\psi(t)$ , the set  $\{\psi_{j,k}\}_{j,k}$  provides an orthogonal basis, and the function  $f$  which is defined on the whole real line is

$$f(t) = \sum_{k=-\infty}^{\infty} c_{0k} \varphi_{0,k}(t) + \sum_{j=1}^J \sum_{k=-\infty}^{\infty} d_{jk} \psi_{j,k}(t), \quad (1)$$

where the maximum scale  $J$  is determined by the number of data, the coefficients  $c_{0k}$  represent the lowest frequency smooth components, and the coefficients  $d_{jk}$  deliver information about the behaviour of the function  $f$  concentrating on effects of scale around  $2^{-j}$  near time  $k \times 2^{-j}$ . The non-decimated wavelet transform (WT) of data  $(f(t_1), \dots, f(t_n))$  at equally spaced points  $t_i = i/n$  is defined as the set of all decimated WT's formed from the  $n$  possible shifts of the data by amounts  $i/n$ ;  $i = 1-n$ . There are  $2^j$  coefficients on the  $j$ th resolution level, there are  $n$  equally spaced wavelet coefficients in non-decimated WT:

$d_{jk} = n^{-1} \sum_{i=1}^n 2^{j/2} \psi[2^j(i/n - k/n)] y_i$ ,  $k = 0, \dots, n-1$ , on each resolution level  $j$ . Another way of viewing the result of a non-decimated WT is to represent the temporal evolution of the data at a given scale. To obtain the results, smooth signal  $S_0$  and the detail signals  $D_j$  ( $j=1, \dots, J$ ) are

$$S_0(t) = \sum_{k=-\infty}^{\infty} c_{0k} \varphi_{0,k}(t) \text{ and } D_j(t) = \sum_{k=-\infty}^{\infty} d_{jk} \psi_{j,k}(t) \quad (2)$$

The fine scale features are captured mainly by the fine scale detail components  $D_j$  and  $D_{j-1}$ . The coarse

scale components  $S_0$ ,  $D_1$ , and  $D_2$  correspond to lower frequency oscillations of a signal. Using a link of wavelets and fractals, one can calculate the multi-fractal spectrum. A task of its calculation reduces to definition of singular spectrum  $f(\alpha)$  of measure  $\mu$ . It associates Hausdorff dimension and singular indicator  $\alpha$ , that allows calculating a degree of singularity:  $N_\alpha(\varepsilon) = \varepsilon^{-f(\alpha)}$ . The way of estimate of  $f(\alpha)$  is in analysis of changing a dependence of distribution function  $Z(q, a)$  on modules of maxs of splash-transforms under scale changes:

$$Z = \sum_{i=1}^{N(a)} (\omega_i(a))^q, \quad (3)$$

where  $I = 1, \dots, N(a)$ ;  $N(a)$  is a number of localized maximums of transformation  $W_\psi[F](b, a)$  for each scale  $a$ , where function  $x$  is considering; function  $\omega(a)$  can be defined in terms of coefficients of the splash-transformations as:

$$\omega_i(a) = \max_{\substack{(x,a') \in L \\ a' < a}} |W_\psi[F](x, a')|, \quad (4)$$

where  $l_i \in L(a)$ ;  $L(a)$  is a set of such lines, which make coupling the splash-transformation coefficient maximums. To calculate the singularity spectrum, a canonical approach is used:

$$h(a, q) = \frac{1}{Z(a, q)} \frac{\partial Z(a, q)}{\partial q},$$

$$\frac{\partial Z}{\partial q} = \sum_{i=1}^{N(a)} \omega_i(a)^q \ln \omega_i(a), \quad (5)$$

$$D(a, q) = qh(a, q) - \ln Z(a, q).$$

Spectra  $D(q)$  and  $h(q)$  are defined as:

$$D(q) = \lim_{a \rightarrow 0} \frac{D(a, q)}{\ln a}, \quad h(q) = \lim_{a \rightarrow 0} \frac{h(a, q)}{\ln a}. \quad (6)$$

We have applied the wavelet and multifractal formalism to analysis of the nonlinear features in the acoustic detecting and diagnostic of the granulated material on results of the experiment [25]. Finally we found that the corresponding fractals dimensions are lying in the interval  $[1, 3-2, 1]$ .

#### References

1. *Esipov I. B., Rybak S. A., Serebryany A. N.* Nonlinear diagnostics of the earth rocks and ocean // *Physics Uspekhi. UFN.* — 2006. — Vol. 176. — P. 102–108.
2. *Likhtenberg A., Liberman M.* Regular and stochastic dynamics, Mir, Moscow, 1994.
3. *Schertzer D., Lovejoy S.* Fractals: Physical Origin and Properties. Ed. L. Peitronero, Plenum Press, N-Y., 1990. — P. 71–92.
4. *Zaslavsky G. M.* Stochasticity of dynamical systems, Nauka, Moscow, 1998.
5. *Vedenov A. A., Ezhov A. A., Levchenko E. B.* Non-linear systems with memory and functions of neuron ensembles, In: Non-linear waves. Structure and bi-furcations Eds Gaponov-Grekhov A. V., Rabinovich M. I., Nauka, Moscow, 1987. — P. 53–69.
6. *Ezhov A. A., Knizhnikova L. A., Levchenko E. B.* Chaotic oscillations in system of autogenerators // *Izv. Vuzov. Ser. Phys.* — 1001. — Vol. 36. — P. 1167–1169.
7. *Glushkov A. V.* Thomas-Fermi model of multibody oscillator // *Soviet Physics. Izv. Vuzov. Ser. Phys.* — 1992. — Vol. 37. — P. 41–47.

8. *Minabudinova S. A., Yugay K. I.* Dynamical chaos in high-excited states of ungarmonic oscillator in external electric field // *Izv. Vuzov. Ser. Phys.* 43, P. 11-18 91998).
9. *Svinarenko A. A.* Regular and chaotic dynamics of multi-oscillator dynamical systems // *Photoelectronics.* — 2002. — Vol. 11. — P. 81–84.
10. *Stochastic* instability of multioscillator systems in electromagnetic field and chaotic dynamics of diatomic molecules in resonance IR field / A. V. Glushkov, S. V. Ambrosov, V. M. Ignatenko, G. P. Prepelitsa // *Proc. V Int. Conf. on Atomic and Molecular Physics.* — Berlin (Germany). — 2001. — P. A313.
11. *Daubechies I.* Ten Lectures on Wavelets. Philadelphia: SIAM. — 1992. — 360 p.
12. *Wave* propagation and sampling theory / J. Morlet, G. Arens, E. Fourgeau, D. Giard // *Geophysics.* — 1982. — Vol. 47. — P. 203–236.
13. *Nason G., von Sachs R., Kroisand G.* Wavelet processes and adaptive estimation of the evolutionary wavelet spectrum // *J. Royal Stat. Soc.* — 2000. — Vol. B-62. — P. 271–292.
14. *Sensing* the correlation between atmospheric teleconnection patterns and sea ice extent: micros technology “Geomath” / A. V. Glushkov, V. N. Khokhlov, Y. Y. Bunyakova, A. A. Svinarenko, T. V. Solonko // *Sensor Electr. Microsyst. Techn.* — 2006. — N 2. — P. 16–19.
15. *Sensing* the kinetical features of energy exchange in mixture of atmospheric gases under interacting with laser radiation / N. G. Serbov, A. V. Glushkov, Yu. Ya. Bunyakova, G. P. Prepelitsa, A. A. Svinarenko // *Sensor Electr. and Microsyst. Techn.* — 2006. — N 4. — P. 20–22.
16. *Sensing* the nonlinear interaction between global teleconnection patterns: micros technology “Geomath” / A. V. Glushkov, V. N. Khokhlov, Yu. Ya. Bunyakova, G. P. Prepelitsa, A. A. Svinarenko, I. A. Tsenenko // *Sensor Electr. and Microsyst. Techn.* — 2006. — N 1. — P. 64–70.
17. *Temporal* variability of atom-sphere ozone content: Effect of NAO / A. V. Glushkov, V. Khokhlov, G. Prepelitsa, I. Tsenenko // *Optics atm. and ocean.* — 2004. — Vol. 14. — P. 219–223.
18. *Glushkov A. V., Khokhlov V., Tsenenko I.* Atmospheric teleconnection patterns and eddy energy content: wavelet analysis // *Nonlin. Proc. Geophys.* — 2004. — Vol. 11. — P. 285–293.
19. *Glushkov A. V., Loboda N. S., Khokhlov V. N.* Using meteorological data for reconstruction of annual runoff series over an ungauged area: Empirical orthogonal functions approach // *Atmospheric Research (Elseiver).* — 2005. — Vol. 77. — P. 100–113.
20. *Using* non-decimated wavelet decomposition to analyse time variations of North Atlantic Oscillation, eddy kinetic energy / A. V. Glushkov, N. S. Loboda, V. N. Khokhlov, L. Lovett // *Journal of Hydrology (Elseiver).* — 2006. — Vol. 322, N 1–4. — P. 14–24.
21. *Glushkov A. V., Khokhlov V. N., Loboda N. S.* On the nonlinear interaction between global teleconnection patterns // *Quart. J. Royal Meteorol. Soc.* — 2006. — Vol. 132. — P. 447–465.
22. *On possible* genesis of fractal dimensions in the turbulent pulsations of cosmic plasma – galactic cosmic rays – turbulent pulsation in planetary atmosphere system / A. V. Glushkov, V. N. Rusov, V. N. Khokhlov, N. S. Loboda, V. N. Vaschenko, G. P. Prepelitsa // *Advances in Space Res.* — 2008. — Vol. 56. — P. 1313–1320.
23. *Serbov N. G., Svinarenko A. A.* Wavelet and multifractal analysis of oscillations in system of coupled autogenerators in chaotic regime // *Photoelectronics.* — 2006. — N 15. — P. 27–30.
24. *Serbov N. G., Svinarenko A. A.* Wavelet and multifractal analysis of oscillations in a grid of coupled autogenerators // *Photoelectronics.* — 2007. — N 16. — P. 53–56.
25. *Bazhenova E., Willman A., Esipov I. B.* Acoustic diagnostics of the granulated mediums // *Acoust. Journ.* — 2005. — Vol. 51. — P. 46–52.

UDC 539.124:541.47

A. A. Svinarenko

#### WAVELET AND MULTIFRACTAL ANALYSIS OF NONLINEAR FEATURES IN THE ACOUSTIC DETECTING THE GRANULATED MATERIALS

It is carried out an analysis of nonlinear features in the acoustic detecting and diagnostic of the granulated mediums on the basis of wavelet analysis and multifractal formalism. The fractals dimensions are lying in the interval [1,3–2,1].

УДК 539.124:541.47

А. А. Сви́наренко

#### ВЕЙВЛЕТ И МУЛЬТИФРАКТАЛЬНЫЙ АНАЛИЗ НЕЛИНЕЙНЫХ ОСОБЕННОСТЕЙ ПРИ АКУСТИЧЕСКОЙ ДИАГНОСТИКЕ ГРАНУЛИРОВАННЫХ МАТЕРИАЛОВ

Выполнен анализ нелинейных особенностей при акустической диагностике гранулированных сред на основе вейвлет и мультифрактального формализма. Спектр фрактальных размерностей лежит в интервале [1,3–2,1]

УДК 539.124:541.47

А. А. Сви́наренко

#### ВЕЙВЛЕТ І МУЛЬТИФРАКТАЛЬНИЙ АНАЛІЗ НЕЛІНІЙНИХ ОСОБЛИВОСТЕЙ ПРИ АКУСТИЧНІЙ ДІАГНОСТИЦІ ГРАНУЛЬОВАНИХ МАТЕРІАЛІВ

Виконано аналіз нелінійних особливостей при акустичній діагностиці гранульованих середовищ на підставі вейвлет та мультифрактального формализму. Спектр фрактальних розмірностей лежить у інтервалі [1,3–2,1].

A. N. NAZAROV<sup>1</sup>, I. N. OSIYUK<sup>1</sup>, I. P. TYAGULSKYY<sup>1</sup>, V. S. LYSENKO<sup>1</sup>, S. I. TIAGULSKYY<sup>1</sup>, V. N. TORBIN<sup>1</sup>, V. V. OMELCHUK<sup>1</sup>, T. M. NAZAROVA<sup>2</sup>, T. GEBEL<sup>4</sup>, L. REBOHLE<sup>3</sup>, W. SKORUPA<sup>3</sup>

<sup>1</sup>V. E. Lashkarev Institute of Semiconductor Physics NAS Ukraine, 45, prospekt Nauki, 03028 Kiev, Ukraine

<sup>2</sup>National Technical University "KPI", 37, prospekt Peremogy, 03056 Kyiv, Ukraine

<sup>3</sup>Institute of Ion Beam Physics and Materials Research, Forschungszentrum Rossendorf e.V., POB 510119, D-01314, Dresden, Germany

<sup>4</sup>Nanopark GmbH, 45, Bautzner Landstrasse, D-01454 Dresden, Germany

## ELECTROLUMINESCENCE, CHARGE TRAPPING AND DEGRADATION OF THE SILICON DIOXIDE IMPLANTED BY CARBON AND SILICON IONS

In this paper we explore the electroluminescence (EL) properties of thermally grown 350 nm thick SiO<sub>2</sub> layers co-implanted with Si<sup>+</sup> and C<sup>+</sup> ions. The implant fluences were chosen in such a way that peak concentration of excess Si and C of 5010 at.% were achieved. Combined measurements of charge trapping and EL intensity as a function of injected charge and current have been carried out with the aim of clarifying the mechanisms of electroluminescence. EL was demonstrated to have defect-related nature. Cross sections of both electron traps and hole traps were determined. EL quenching at a great levels of injected charge is associated with strong negative charge capture, next positive charge capture leading to electrical breakdown of SiO<sub>2</sub> structures.

### INTRODUCTION

Silicon-based light emission is a promising approach to design and realization of optoelectronic inter- and intra-chip communication in future computer systems. Additionally, there is a great interest in multi-functional micro-systems (e.g. lab-on-chip applications). Since a lot of such micro-systems are based on standard Si-SiO<sub>2</sub> technology, there is also a strong demand for Si-based light emitters, especially to achieve low-cost production processes. One method for the formation of the Si-based light emitting structures is ion beam synthesis. Electroluminescence (EL) from the Ge-rich SiO<sub>2</sub> layers was found to be in the red/infrared and in the blue/violet spectral regions [1]. The Si-rich SiO<sub>2</sub> layer emits red light [2]. Ion-beam implantation, using a few co-implants, is of interest from the two standpoints.

At first, such procedure allows to expend spectral range of light emission. Secondly, co-implantation can create more stable precipitates and/or stable impurity distribution inside the SiO<sub>2</sub>. Using this approach, white photoluminescence and electroluminescence of co-implanted SiO<sub>2</sub> by silicon and carbon ions have been observed respectively in [3] and [4]. However, from our knowledge, the study of electrical characteristics and degradation of electrical and luminescent properties during operation of such light-emitting devices was studied insufficiently. Thus, the present paper addresses the research of electroluminescence, electrical characterization and their degradation in the Si/C co-implanted SiO<sub>2</sub> structures.

### 2. SAMPLES AND EXPERIMENTAL TECHNIQUES

The SiO<sub>2</sub> layers with 350 nm thickness were thermally grown on <100>-oriented, n-type Si-substrates at 1000°C.

Firstly, the oxide films were double-implanted with Si<sup>+</sup> ions at an energy of 90 keV followed by a second Si<sup>+</sup> implantation at 47 keV. Three sets of samples with different implanted doses were prepared. The doses were chosen in such a way, that a broad implant profile with a nearly constant concentration of excess Si about 5%, 7.5% and 10% at a depth of 60–180 nm below the oxide surface was formed.

Fig. 1 shows the implantation profile, calculated with the TRIM code [5]. After such implantations, the devices were annealed at 1100 °C for 30 min in a N<sub>2</sub> ambient. This annealing step was carried out in order to initiate the formation of first Si nano-clusters which have to be acted as seeds for the final clusters. Then, C<sup>+</sup> ions were implanted at energy of 43 keV, followed by a second C<sup>+</sup> implantation at 22 keV. A post-implantation heat treatment at 800°C for 60 min was followed by a final annealing step at 1100°C for 60 min was performed.

The investigation of the EL requires transparent and conductive gate electrodes. On the top of the oxide an indium-tin-oxide (ITO) layer, a special kind of a transparent conductive oxide, was deposited using a sputtering process. The thickness of the layers was 80 nm. The gate electrode was processed using standard lithography. The sizes of the devices were 0.5 mm in diameter in a periodic pattern of 2 mm pitch.

A portion of so fabricated MOS Light Emitting Devices (MOSLEDs) had been subjected to RF plasma treatment (13.56 MHz) in a low pressure, parallel plate (diode type) reactor, with the ITO electrode being exposed to the plasma discharge. The plasma working gas was a mixture of 90% nitrogen and 10% hydrogen. The plasma power density was in range of 0.5–1.5 W cm<sup>-2</sup>. Additional substrate pre-heating from a heat source, independently of the plasma discharge, was used over the temperature range of 100°C to 300°C and elevated temperature was maintained during the plasma treatment. The plasma treatment duration was 15 min. Details of the plasma reactor

and the used processing parameters were published in [6].

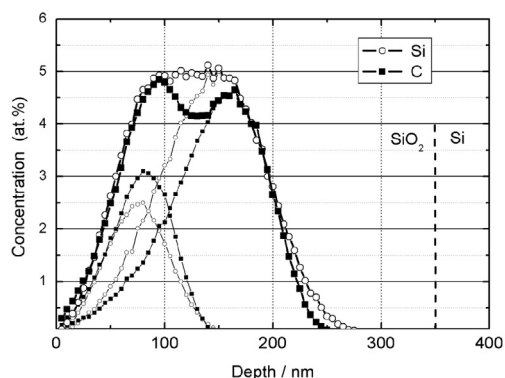


Fig. 1. TRIM-profile of a Si/C co-implanted SiO<sub>2</sub> layer. Two implantations at different energies were carried out for both, Si and C. The small symbols are related to the each single implantation

EL spectra were measured on MOSLEDs with a circular ITO at a constant current supplied by a multi-meter Keithley 2410. The EL signal was recorded at room temperature with a monochromator Jobin Yvon Triax 320 and a photo-sensor module Hamamatsu H7732-10 in the range of wave lengths between 300 and 750 nm. The measurement was performed with electron injection in constant-current mode from ITO electrode into the SiO<sub>2</sub>. The typical current density for EL excitation was  $10^{-3}$  to  $10^{-5}$  A/cm<sup>2</sup>. The charge trapping during EL excitation was studied by the analyse of the applied voltage at constant current injection ( $V_{CC}$ ) from the ITO to the SiO<sub>2</sub>.

### 3 RESULTS AND DISCUSSION

#### 3.1. The distinguishing features of the EL spectra

Fig 2 represents EL spectra for the MOSLEDs, fabricated at different implantation doses. In this experiment the MOSLEDs were operated under electron injection from ITO at a current density  $2.5 \cdot 10^{-3}$  A·cm<sup>-2</sup>.

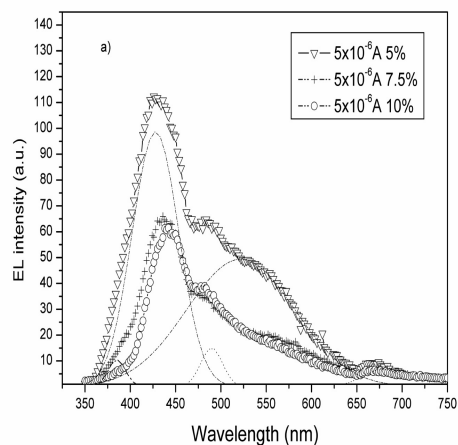


Fig. 2 a

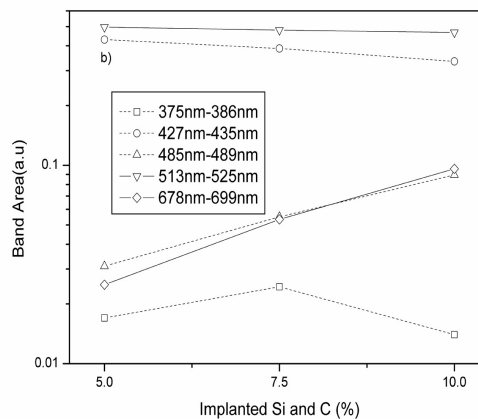


Fig. 2. The EL spectra of the Si and C co-implanted SiO<sub>2</sub> layers as a function of implantation dose. Dashed line presents multi-Gaussian fitting for 5% Si/C implants. (Current of  $5 \cdot 10^{-6}$  A was used for all samples) (a); Variation of the EL intensity sub-peaks (see Fig. 2) as a function of implanted dose (b)

As seen from Fig. 2 a, the EL spectra peaks are relatively broad and consist of several peaks. There is visible correlation between EL spectra and concentration of implants. The multi-Gaussian deconvolution of all spectra could be performed and the set of band positions have been determined. For the lowest concentration (5%) the clear double-peak structure is observed with maxima about at 425÷435 nm and 515÷525 nm.

The latter maximum belongs to relatively broad peak which consists of two sub-peaks on the shoulders. Integral intensity of EL spectra falls down when concentration of implanted Si and C increases, high energy peak decreases too, but relative intensities of broad peaks are nearly constant (Fig. 2 a). Similar characteristics of photoluminescence (PL), showing a decrease of the high energy tail (340÷410 nm) for higher Si/C concentration, have been observed early [4].

Additional measurements were carried out in order to investigate the influence of the injection current density on the shape of the EL spectrum (Fig. 3).

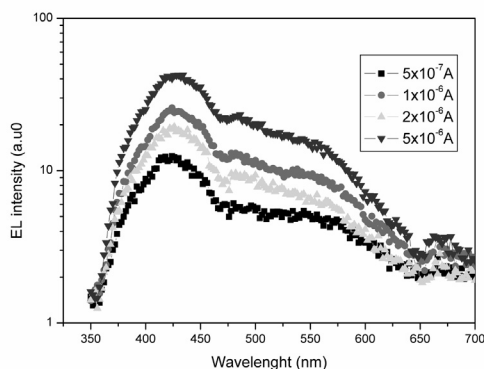


Fig. 3. The EL spectra of Si/C co-implanted MOSLEDs, operated at different currents (dot area: 0.2 mm<sup>2</sup>)

Basically no changes occur in the spectrum with increasing current density and, therefore, also with increasing electric field. This means that the difference in the shape of the spectra for different Si/C concen-

trations is related only to the different microstructure and not to the distribution of hot electrons, but effect of the injected charge on the EL spectra demands further investigation.

Thus, we have analyzed the variation of the EL spectra while multi scanning regime: that is EL spectra have been recorded repetitively one after another (Fig. 4). It should be noted, that about  $3.725 \cdot 10^{18} \text{ e/cm}^2$  are injected during one EL scan. As one could see, high energy band (in interval of 390–400 nm) is suppressed strongly when number of EL scans increased, during which integral EL intensity decreased just linearly (see the insert in Fig. 4).

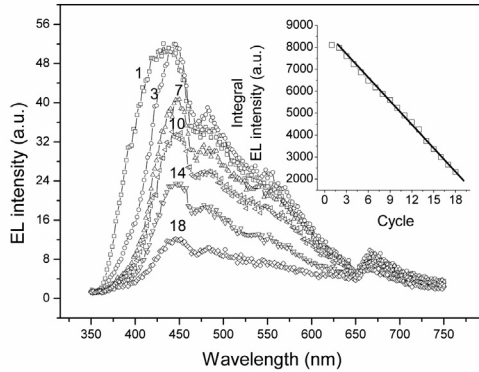


Fig. 4. The EL spectra of the 7.5 % Si/C co-implanted MOSLED, obtained in multi-scanning procedure. Scan numbers are shown near the curve

Insert: variation of integral EL intensity as a function of numbers of scans.

The mechanism of the MOSLED operation is believed to be based upon impact ionization of specific defect-type luminescent centers (LCs) by hot electrons moving in the conduction band of the oxide [1]. It follows that observed line of 520 nm could be attributed to  $E_s$  center [7], the lines of 385 nm and 490 nm are related to the Si-C bonds [8] and the Si/C/O complexes [9], correspondingly, and line of 390–400 nm — to the oxygen deficiency centre ( $\equiv\text{Si-Si}\equiv$ ) [10] or two-fold coordinated silicon ( $=\text{Si}$ ) [11]. Line of 440–450 nm could be described both SiC precipitates [12, 13] and neutral oxygen vacancy [7]. On the low energy shoulder one can see increasing of line 620 nm for the largest current density. This line could be attributed to non-bridging oxygen hole center [14]

As it was considered earlier, in [15–17], the radio-frequency (RF) plasma treatment (PT) of ion-implanted MOS structures may result in a considerable modification of their structural and electrical properties. Especially it is regarded to post implanted defects both in Si and  $\text{SiO}_2$ . Low temperature defect annealing in  $\text{SiO}_2$  under the PT can be explained within the framework of the recombination enhanced defect reactions [18, 19] caused by alternate injection both electrons and holes and there recombination at the defects. Effect of the RF plasma treatments on the EL characteristics is exhibited at the Fig. 5.

It should be noted that the integral EL intensity tends to decrease when the RF plasma power exceeds  $0.7 \text{ W/cm}^2$ , the high energy shoulder is suppressed considerably. Such a manner of the EL spectra varia-

tion at RF plasma treatment is the demonstration that the studied EL is determined by complexes of post implanted defects with inclusion of implanted ions.

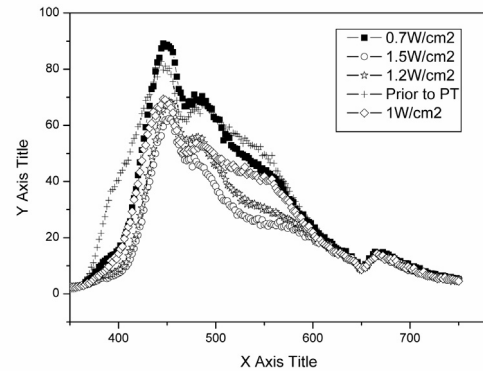


Fig. 5. Influence of plasma treatment on the EL spectra of Si/C co-implanted MOSLED

### 3.2 Current-voltage characteristics of the Si / C co-implanted MOS structures

Current-voltage (I-V) characteristics for the case of electron injection from ITO are represented in Fig. 6.

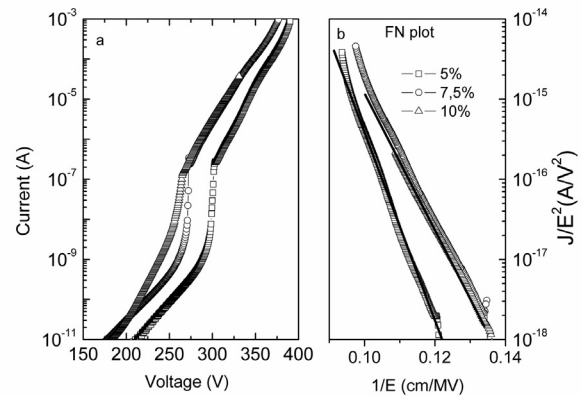


Fig. 6. The current –voltage characteristics of the MOSLEDs (injection from ITO) (a); The same characteristics, converted to the Fowler-Nordheim coordinates (b)

The constant current regime used for the EL excitation corresponds to high-field portions in the I-V characteristics of the MOS structures. As it could be seen, the cut-off injection voltage (manifested as a sharp bend in the I-V curve) shifts to lower value when dose of implantation increases; that is, the EL emission arises at the lower electric field.

Actually, (for the EL processes) section of the I-V curve is linearized well in coordinates  $J/E^2$  vs  $1/E$ , where  $E$  is the electric field in the oxide layer. Therefore, the charge transport in the Si/C implanted  $\text{SiO}_2$  is governed by Fowler-Nordheim tunneling, or tunnel injection of carriers to the conduction band of the oxide through a triangularly shaped barrier. Current density of the F-N tunneling may be expressed, as

$$J_{FN} = \frac{q^2}{8\pi h \varphi_B} E^2 \exp\left(-\frac{8\pi\sqrt{2m^*q}}{3hE} \varphi_B^{3/2}\right), \quad (3.1)$$

where  $\varphi_B$  is the barrier height,  $m^*$  is the effective mass of electron, other quantities are common accepted.

From the slope of linear part  $\ln(J/E^2)-f(1/E)$  dependence, for the Si-SiO<sub>2</sub> structures with 5% of Si/C implants, the barrier height have been obtained as 3.05 eV (in assumption of  $m^* = 0.52m_0$ ). The barrier height falls up to 2.8 eV when the dose of the Si/C implantation increases up to 10% (at the same value of effective mass). It is notice worthy, that the value is significantly lower than the injection barrier of electrons for pure SiO<sub>2</sub> (3.15eV [20]). This phenomenon is the evidence of enhancement of the electron injection into SiO<sub>2</sub> due to the increasing concentration of SiC-related complexes and associated with trap-assisted tunneling mechanisms [21].

### 3.3. EL intensity and charge trapping as a function of injected charge

Changing the voltage ( $V_{cc}$ ), applied to the MOS structure, at constant current regime of high-field electron injection from ITO one could obtain the function of injected charge, depicted by Fig. 7. The decrease of the voltage during the high-field electron injection (up to  $\sim 9 \cdot 10^{14}$  electron/cm<sup>2</sup>), suggests the positive charge trapping in the oxide at the distance more that tunneling length from injecting ITO-SiO<sub>2</sub> interface. Then, the voltage tends to increase steadily, what is indicative for negative charge trapping.

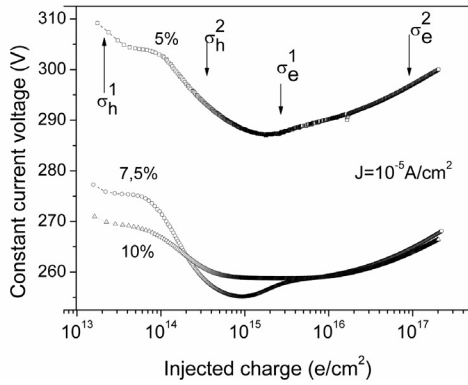


Fig. 7. Constant current voltage ( $V_{cc}$ ), as a function of injected charge

Assuming the first-order trapping kinetics, the trapped charge (both negative and positive one) versus injected charge could be described by following expression [22]

$$Q_t = Q_t^{\max} [1 - \exp(-\sigma_i Q_{inj})], \quad (3.2)$$

where  $Q_t$  is the trapped charge,  $Q_t^{\max}$  is the maximal trapped charge and  $\sigma_i$  is the effective capture cross-section of the trap.

If trapping efficiency ( $P$ ) is presented as the first derivative of injected charge of Eq. (3.2), then one obtains

$$P = \frac{dQ_t}{dQ_{inj}} = \sigma_i Q_t^{\max} \exp(-\sigma_i Q_{inj}) \quad (3.3)$$

From Eq. (3.3), it is easy to see, that for every trap, the plot of  $\ln(P)$  vs.  $Q_{inj}$  will consist of linear part with the slope corresponding to  $\sigma_i$ . The extrapolation to  $Q_{inj}=0$  for such a plot, provides  $\sigma_i Q_t^{\max}$ . Thus, using the

proposed method [23], the number and main trap parameters could be estimated.

Our calculations have demonstrated, that three kind of electron traps with average value of the capture cross-section ( $\sigma_e^1 = 3.6 \times 10^{-16}$  cm<sup>2</sup>,  $\sigma_e^2 = 8 \times 10^{-18}$  cm<sup>2</sup> and  $\sigma_e^3 = 2 \times 10^{-19}$  cm<sup>2</sup>), and the two kinds of hole traps ( $\sigma_h^1 > 1 \times 10^{-14}$  cm<sup>2</sup>,  $\sigma_h^2 = 6.6 \times 10^{-15}$  cm<sup>2</sup>) could be found by proposed method. It should be noted, that hole traps with  $\sigma_h^2 = 6.6 \times 10^{-15}$  cm<sup>2</sup> is typical for Si-SiO<sub>2</sub> structures with excess Si content in SiO<sub>2</sub>, subjected to rapid thermal annealing [24].

In order to study the relationship between the EL intensity and the charge trapping in the dielectric, the results of combined measurements of the EL intensity at 440 nm and  $\Delta V_{cc}$  versus injected charge ( $Q_{inj}$ ) at high constant current levels were studied. The injected charge could be calculated from the measurement time using the expression:

$$Q_{inj} = \int_0^t J(t) dt. \quad (3.4)$$

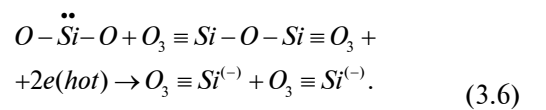
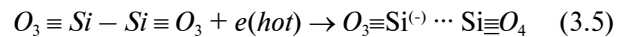
Fig. 8 demonstrates the direct correlation between EL intensity and constant current voltage up to injected charge  $\sim 2 \cdot 10^{18}$  electron/cm<sup>2</sup>, or that the excitation of the EL is governed by impact ionization.

When injected charge reaches  $3 \cdot 10^{19}$  electron/cm<sup>2</sup>, the EL intensity tends to decrease, though the applied voltage increases. The dependence  $V_{cc}$  as the function of  $Q_{inj}$  manifests strong electron capture by traps with cross section estimated above as  $\sigma_e^3 = 2 \times 10^{-19}$  cm<sup>2</sup>. This process is seen clearly on the  $V_{cc} - Q_{inj}$  curve for 7.5% Si/C co-implantation (see Fig. 8).

Fowler-Nordheim tunnelling is offered as the main mechanism of charge transport in the Si/C co-implanted Si-SiO<sub>2</sub> structures in actual for the EL voltage range.

Modification of the EL spectra by plasma treatment testifies that the EL mechanism has its origins in defect-related processes more, than in SiC cluster-related ones.

In paper [25] it was shown, that small capture cross-section values of negative charge, correlated with quenching of some EL lines, are associated with a probability of defect luminescent centers reconstruction during their excitation by electron impact ionization and have to be designated for clarity as a quenching cross-section,  $\sigma_q$ , for given EL line. So, a value of the  $\sigma_e^3 \equiv \sigma_{q, 440nm}$  has to be linked with a probability of reconstruction and/or destroying of the EL center, revealing a light emission at 440 nm, with following electron trapping in the new generated defect. Since, the EL at 440 nm in SiO<sub>2</sub> can be associated with excitation of neutral vacancy ( $O_3 \equiv Si-Si \equiv O_3$ ) or two-fold coordinated silicon ( $=Si$ ) the quenching process can be described the following reactions



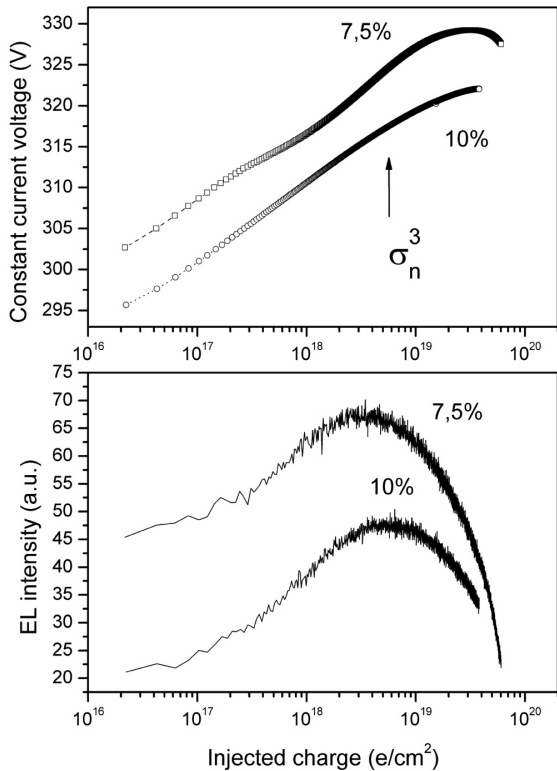


Fig. 8. Constant current voltage ( $V_{cc}$ ), as a function of injected charge (a); the EL intensity ( $\lambda=440$  nm) as a function of injected charge (b). Injection is performed from ITO, current density is  $1 \times 10^{-3}$  A/cm $^2$

The reaction (3.6) assumes a breakup of Si-Si bond by hot electron and relaxation of Si atom on distance more than  $4E$  with bonding of neighbor oxygen atom. Such the four-fold coordinated Si and the silicon dangling bond can represent the electron trap [26].

In case of the reaction (3.6), two-fold coordinated Si interacts with broken Si-O bond in neighbor Si-O-Si fragment that results in formation of two silicon dangling bonds ( $O_3=Si$ ) which could work as the electron traps.

Further electron injection (more than  $3 \times 10^{19}$  e/cm $^2$ ) leads to positive charge generation and drastic EL quenching, resulting to electrical breakdown of the MOSLEDs.

#### 4. CONCLUSIONS

1. Combined studies of the MOSLED's EL intensity and charge trapping vs. time for high field electron injection into the Si/C implanted SiO $_2$  have shown, for the first time, that EL correlates well with charge trapping governed by that three kind of electron traps with average value of the capture cross-section ( $\sigma_e^1 = 3.6 \times 10^{-16}$  cm $^2$ ,  $\sigma_e^2 = 8 \times 10^{-18}$  cm $^2$  and  $\sigma_e^3 = 2 \times 10^{-19}$  cm $^2$ ), and two kind of hole traps ( $\sigma_h^1 > 1 \times 10^{-14}$  cm $^2$ ,  $\sigma_h^2 = 6.6 \times 10^{-15}$  cm $^2$ ).

2. The EL quenching caused by electron impact ionization resulting in reconstruction of defect LC with following electron trap generation. The quench-

ing cross-section for observed process is  $\sigma_{q,440nm} = 2 \times 10^{-19}$  cm $^2$ .

3. Positive charge generation arises at high levels of charge injection leading to electrical breakdown.

#### References

1. Blue photo- and electroluminescence of silicon dioxide layers ion-implanted with group IV elements / L. Rebohle, J. von Borany, H. Fröb, W. Skorupa // Appl. Phys. B, 2000, 70 (1). — P. 1–21.
2. Influence of average size and interface passivation on the spectral emission of Si nano-crystals embedded in SiO $_2$  / B. Garrido, D. Fernandez, M. Lypez, C. Garsha, A. Pérez-Rodríguez, J. R. Morante, C. Bonafos, M. Carrada, A. Claverie // Journ. Appl. Phys. — 2002. — 91 (2). — P. 798–807.
3. Ion beam synthesis of semiconductor nano-particles for Si based optoelectronic devices / O. Gonzalez-Varona, A. Perez-Rodriguez, B. Garrido, C. Bonafos, M. Lopez, J. R. Morante, J. Montserrat, R. Rodriguez // Nucl. Instr. and Meth. Phys. Res. 2000 B161-163. — P. 904–908.
4. Electroluminescence from thin SiO $_2$  layers after Si- and C-coimplantation / T. Gebel, L. Rebohle, J. Sun, W. Skorupa // Physica E.2003. — 16. — P. 366–369.
5. Ziegler J. F. (Ed.) // www.srim.org
6. Nazarov A. N., Lysenko V. S. RF plasma treatment as a method of radiation and thermal hydrogenation of Si microelectronics structures // Mikroelektronika, 1994. — 23 (4). — P. 45–64.
7. Lin G. R., Lin C. J. Improved blue-green electroluminescence of metal-oxide-semiconductor diode fabricated on multi-recipient Si-implanted and annealed SiO $_2$ /Si substrate // J. Appl. Phys. 2004. — 95 (12). — P. 8484–8486.
8. Visible photoluminescence of SiO $_2$  implanted with carbon and silicon / B. Garrido, M. López, S. Ferré, A. Romano-Rodriguez, A. Pérez-Rodriguez, P. Rutewrana, J. R. Morante // Nucl. Instr. and Meth. Phys. Res. — 1996, B120 (1). — P. 101–105.
9. White luminescence from Si $^+$  and C $^+$  ion-implanted SiO $_2$  films / A. Pérez-Rodriguez, O. González-Varona, B. Garrido, P. Pellegrino, J. R. Morante // J. Appl. Phys. — 2003, 94 (1). — P. 254–262.
10. Ultraviolet excitation fine tuning of luminescent bands of oxygen deficient centers in silica / A. Anedda, C. M. Carbonaro, F. Clemente, R. Corpino // J. Appl. Phys. — 2002. — 92 (6). — P. 3034–3038.
11. Skuja L. Optical properties of defects in silica, in Defects in SiO $_2$  and Related Dielectrics: Science and Technology // Ed. by G. Pacchioni, L. Skuja, D. L. Griscom, Kluwer, Dordrecht 2000. — P. 73–116.
12. Synthesis of luminescent particles in SiO $_2$  films by sequential Si and C ion implantation / O. González-Varona, C. Bonafos, M. López, B. Garrido, A. Pérez-Rodriguez, J. R. Morante, J. Montserrat, R. Rodriguez // Microelectronics Reliability 2000. — 40 (4–5). — P. 885–888.
13. Analysis of the white emission from ion beam synthesised layers by in-depth resolved scanning photoluminescence microscopy / O. González-Varona, B. Garrid, A. Pérez-Rodriguez, J. R. Morante, C. Bonafos, M. Carrada, L. F. Sanz, M. A. González, J. Jiménez // Mater. Sci. Eng. 2002. — B91-B92 (1). — P. 51–54.
14. Optical and electron paramagnetic resonance study of light-emitting Si $^+$  ion implanted silicon dioxide layers / M. Ya. Valakh, V. A. Yukhimchuk, V. Ya. Bratus', A. A. Konchits, P. L. F. Hemment, T. Komoda // J. Appl. Phys. — 1999, 85 (1). — P. 168–173.
15. RF plasma annealing of implanted MIS structures / V. S. Lysenko, M. M. Lokshin, A. N. Nazarov, T. E. Rudenko // Phys. Stat. Sol. (a), 1985. — 88 (2). — P. 705–712.
16. Relaxation of amorphous structure of implanted Si under RF plasma treatment: Raman and EPR study / V. V. Artamonov, V. S. Lysenko, A. N. Nazarov, V. V. Strelchuk, M. Ya. Valakh, I. M. Zaritskii // Semicond. Sci. Technol. — 1990, 6 (2). — P. 1–5.
17. Radio frequency plasma annealing of positive charge generated by Fowler-Nordheim electron injection in buried oxides in silicon / A. N. Nazarov, V. I. Kilchitska, I. P. Barchuk, A. S. Tkachenko, A. Ashok // J. Vac. Sci. Technol., 2000, 18 (3). — P. 1254–1261.

18. *Kimmerling L. C.* Recombination enhanced defect reactions // Sol. St. Electron. — 1978, 21 (11–12). — P. 1391–1401.
19. *Ma T. P., Chin M. P.* RF annealing mechanisms in metal-oxide-semiconductor structures—an experimental simulation // J. Appl. Phys. — 1980, 51 (10). — P. 5458–5463.
20. *Weinberg Z. A., Harstein A.* Effect of silicon orientation and hydrogen annealing on tunneling from Si into SiO<sub>2</sub> // J. Appl. Phys. — 1983, 54. — P. 2517–2521.
21. *Houng M. P., Wang Y. H., Chang W. J.* Current transport mechanism in trapped oxides: A generalized trap-assisted tunnelling model // J. Appl. Phys. — 1999, 86 (3). — P. 1488–1491.
22. *Afanas'ev V. V., Adamchuk V. K.* Progress in Surface Science, 47, 301. — 1994.
23. *Ning T. N., Yu H. N.* Optically induced injection of hot electrons into SiO<sub>2</sub> // J. Appl. Phys. — 1974, 45 (12). — P. 5373–5378.
24. *Comparative Study of Charge Trapping in High-Dose Si and Ge-Implanted Al/SiO<sub>2</sub>/Si Structures* / A. N. Nazarov, W. Skorupa, I. N. Osiyuk, I. P. Tyagulskii, V. S. Lysenko, R. A. Yankov, T. Gebel // Journal of the Electrochemical Society. — 2005, 152 (2). — P. F20–F25.
25. *Quenching of electroluminescence and charge trapping in high-efficiency Ge-implanted MOS light-emitting silicon diodes* / A. N. Nazarov, I. N. Osiyuk, J. M. Sun, R. A. Yankov, W. Skorupa, I. P. Tyagulskii, V. S. Lysenko, S. Pruchnal, T. Gebel, L. Rebohle // Appl. Phys. B. — 2007, 87. — P. 129–134.
26. *Nicklaw C. J.* Multi-level modeling of total ionizing dose in a-SiO<sub>2</sub>: First principles to circuits design // Ph. D. Thesis, Vanderbilt University 2003. — P. 163.

UDC 68.35,78.55

A. N. Nazarov, I. N. Osiyuk, I. P. Tyagulskyy, V. S. Lysenko, S. I. Tyagulskiy, V. N. Torbin, V. V. Omelchuk, T. M. Nazarova, T. Gebel, L. Rebohle, W. Skorupa

#### ELECTROLUMINESCENCE, CHARGE TRAPPING AND DEGRADATION OF THE SILICON DIOXIDE IMPLANTED BY CARBON AND SILICON IONS

In this paper we explore the electroluminescence (EL) properties of thermally grown 350 nm thick SiO<sub>2</sub> layers co-implanted with Si<sup>+</sup> and C<sup>+</sup> ions. The implant fluences were chosen in such way that peak concentration of excess Si and C of 5010 at.% were achieved. Combined measurements of charge trapping and EL intensity as a function of injected charge and current have been carried out with the aim of clarifying the mechanisms of electroluminescence. EL was demonstrated to have defect-related nature. Cross sections of both electron traps and hole traps were determined. EL quenching at a great levels of injected charge is associated with strong negative charge capture, next positive charge capture leading to electrical breakdown of SiO<sub>2</sub> structures.

УДК 621.15

А. Н. Назаров, И. Н. Осіюк, І. П. Тягульський, В. С. Лысенко, С. І. Тягульський, В. Н. Торбін, В. В. Омельчук, Т. М. Назарова, Т. Гебел, Л. Реболе, В. Скорупа

#### ЭЛЕКТРОЛЮМИНЕСЦЕНЦИЯ, ЗАХВАТ ЗАРЯДА И ДЕГРАДАЦИЯ ДВУОКИСИ КРЕМНИЯ, ИМПЛАНТИРОВАННОЙ ИОНАМИ УГЛЕРОДА И КРЕМНИЯ

В статье исследованы электролюминесцентные (ЭЛ) свойства слоев SiO<sub>2</sub>, имплантированных ионами Si и C. Слои SiO<sub>2</sub> толщиной 350 нм были получены термическим окислением Si. Потоки ионов были выбраны таким образом, чтобы избыточная концентрация атомов Si и C составляла 5–10 объемных процентов. Комбинированные измерения захвата заряда и ЭЛ, как функции захваченного заряда и плотности тока проводились с целью выяснения природы электролюминесценции. Показано, что электролюминесценция в основном обусловлена дефектами структуры. Были определены сечения захвата ловушек электронного и дырочного типов. Показано, что гашение электролюминесценции при больших уровнях инжектированного заряда связано с сильным захватом отрицательного заряда, причём последующий захват положительного заряда приводит к электрическому пробое SiO<sub>2</sub> структуры.

УДК 621.15

О. М. Назаров, І. М. Осіюк, І. П. Тягульський, В. С. Лисенко, С. І. Тягульський, В. М. Торбін, В. В. Омельчук, Т. М. Назарова, Т. Гебел, Л. Реболе, В. Скорупа

#### ЭЛЕКТРОЛЮМИНЕСЦЕНЦИЯ, ЗАХОПЛЕННЯ ЗАРЯДУ І ДЕГРАДАЦІЯ ДВООКИСУ КРЕМНІЮ, ІМПЛАНТОВАНОЇ ІОНАМИ ВУГЛЕЦЮ ТА КРЕМНІЮ

У роботі досліджені електролюмінесцентні (ЕЛ) властивості шарів SiO<sub>2</sub>, що імплантовані іонами Si та C. Шари SiO<sub>2</sub> товщиною 350 нм були отримані за допомогою термічного окислення Si. Потоки іонів були обрані таким чином, щоб надлишкова концентрація атомів Si та C становила 5–10 об'ємних відсотків. З метою з'ясування природи електролюмінесценції були проведені комбіновані виміри захоплення заряду та ЕЛ, як функції захопленого заряду і густини струму. Показано, що електролюмінесценція переважно обумовлена дефектами структури. Були визначені перетини захоплення пасток електронного й діркового типів. Показано, що гасіння електролюмінесценції при великих рівнях заряду, що інжектується пов'язане з сильним захопленням негативного заряду, до того ж подальше захоплення позитивного заряду приводить до електричного пробую SiO<sub>2</sub> структури.

## CONSISTENT QUANTUM APPROACH TO QUARKONY ENERGY SPECTRUM AND SEMICONDUCTOR SUPERATOM AND IN EXTERNAL ELECTRIC FIELD

The problems of calculation of the bound states energies for semiconductor superatom (spherical nucleus of some semiconductor material that is selectively doped by donors; it is surrounded by the intrinsic matrix from material with low band gap) and heavy quarkony in external strong electric field are considered. Ab initio effective potential approach in combination with the operator perturbation theory method is used in calculation.

In last years studying behaviour of the mesosystems such as superatom and 1D super-lattice attracts, exciton, bi-exciton complexes, elementary atomic systems etc. in external electric and magnetic field attracts a great interest (c.f. [1–5]). Superatom represents the spherical nucleus of some semiconductive material, that is selectively doped by donors and surrounded by the intrinsic matrix of material with low band gap. All these systems can be calculated on the basis of the same unified quantum mechanical method. In this paper we consider the corresponding method (energy approach) in order to carry out the accurate calculations of the energy characteristics for systems above cited. Earlier we have developed the accurate consistent methods for calculation of properties of such systems (c.f. [5, 6]), in particular, relativistic perturbation theory with effective potential of the zeroth order (energy approach), ab initio quasi-particle density functional formalism (Dirac-Kohn-Sham-Ivanov schemes). The main purpose of this work is to make more exact the data regarding the energy characteristics of the quarkony and semiconductor superatom systems. We will use these approaches, namely, ab initio effective potential approach in combination with the operator Glushkov-Ivanov perturbation theory method [7] as basis for formulation of the corresponding theory cited systems in an external strong electric and magnetic field. Let us note that earlier we gave the preliminary estimates for cited characteristics [12].

2. Let us start from considering superatom [3–5]. In the zeroth approximation we use usually the effective ab initio model functional, constructed on the basis of the gauge invariance principle [6]. The zeroth order basis is generated by the solution of the Dirac equation with spherically symmetric potential that includes the potential of ionized donors, the Dirac-Fock-Kohn-Sham functional. The relativistic Dirac equation can be written in the central field in a two-component form as follows (relativistic units are used):

$$\begin{aligned} \frac{\partial F}{\partial r} + (1 + \chi) \frac{F}{r} - (\varepsilon + m - V)G &= 0 \\ \frac{\partial G}{\partial r} + (1 - \chi) \frac{G}{r} + (\varepsilon - m - V)F &= 0. \end{aligned} \quad (1)$$

Here we put the fine structure constant  $\alpha = 1$ . The moment number

$$\chi = \begin{cases} -(1+1), & j > 1 \\ 1, & j < 1 \end{cases},$$

where F and G are the big and small components of the Dirac wave function,  $\varepsilon$  — energy,  $r$  — distance from center of nucleus, other designations are standard. Effective potential  $V(r)$  for super atom is supposed to be by the spherically symmetric and has the following form:

$$V(r) = V_0 \theta(r_0 - r) + V_N(r) + V_H + V_{XC}(r), \quad (2)$$

where  $r_0$  is the nuclear radius,  $V_0$  is the positive overfall of minimums of conductivity zones for nucleus and matrix;  $\theta(x) = 0, x < 0$  and  $= 1$  if  $x > 0$ ;  $V_N$  is a potential of the ionized donors;  $V_H, V_{XC}$  are the Hartree and exchange-correlation potentials. The shape of potential (2) is presented in the fig. 1.

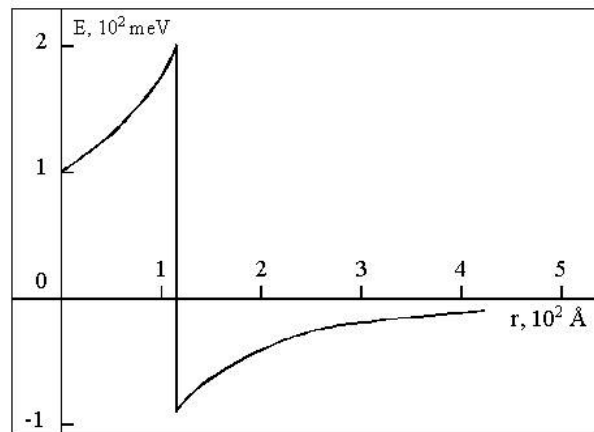


Fig. 1. The shape of potential (2) (see text)

The next step is an account the external electric field potential. As it is well known, external electric field shifts and broadens the bound state atomic levels. The standard quantum-mechanical approach relates complex eigen-energies (EE)  $E = E_r + 0,5iG$  and complex eigen-functions (EF) to the shape resonances [6]. The calculation difficulties in the standard quantum mechanical approach are well known. In Glushkov-

Ivanov paper [6,7] it has been developed a consistent uniform quantum — mechanical approach to the non-stationary state problems solution including the Stark effect and also scattering problems. The essence of the method is the inclusion of the well-known method of “distorted waves approximation” in the frame of the formally exact perturbation theory. In the case of the optimal zeroth order spectrum, the PT smallness parameter is of the order of  $G/E$ , where  $G$  and  $E$  are the field width and bound energy of the state level. It has been shown that  $G/E \leq 1/n$  even in the vicinity of the “new continuum” boundary ( $n$  is the principal quantum number). This method is called as the operator PT (OPT) [6,7]. It is very important to note that the hamiltonian  $H_0$  is defined so that it coincides with the total Hamiltonian  $H$  at  $\varepsilon \Rightarrow 0$  ( $\varepsilon$  is the electric field strength; potential is  $-z\varepsilon$ ).

The Dirac equation for the electron function with taking into account the uniform electric field and the field of the nucleus:

$$[\alpha cp - \beta mc^2 - V(r) + \varepsilon z - E] \psi = 0. \quad (3)$$

Here  $E$  is the electron energy. The key moment of the further considering is to establish coupling between basis of functions of the zeroth approximation (eq. (1)) in the spherical coordinates and corresponding basis in parabolic co-ordinates. According to standard quantum defect theory for multielectron systems with the separated closed shells core and external quasiparticles, relation between quantum defect value  $\mu_r$ , electron energy  $E$  and principal quantum number  $n$  is:  $\mu_r = n - z^*(-2E)^{-1/2}$ . In an electric field all the electron states can be classified due to quantum numbers:  $n, n_1, n_2, m$  (principal, parabolic, azimuthal:  $n = n_1 + n_2 + m + 1$ ). Then the quantum defect in the parabolic co-ordinates  $\delta(n_1, n_2, m)$  is connected with the quantum defect value of the free ( $\varepsilon=0$ ) atomic system by the following relation [7]:

$$\delta(n_1, n_2, m) = (1/n) \sum_{l=m}^{n-1} (2l+1) (C_{J, M-m; lm}^{JM})^2 \mu_l, \quad (4)$$

$$J = (n-1)/2, \quad M = (n_1 - n_2 + m)/2.$$

Naturally, it is possible to use more complicated forms for the ion core potential. Equation 95) gives the receipt of coupling between basis of functions of the zeroth approximation (eq. (1)) in the spherical coordinates and corresponding basis in parabolic co-ordinates.

3. The next key moment is connected with account of the correlation corrections to energy. It can be done by means relativistic density functional formalism and QED perturbation theory (c.f. [6, 8, 12]). This approach allows accounting all correlation corrections of the perturbation theory second order and also a contribution of the high orders diagrams (particle-hole interaction, mass operator iterations etc.). It is very important to note that the nuclear diameter in the superatom is compared with the general size of system and a singularity in the coordinates center is absent in contradistinction of the heavy atom. That is why, the levels with large angular moment become more energetically profitable. In ref. [5, 12, 13] it has been carried out a calculation, which has shown for superatom (nucleus:  $Al_{0,35}Ga_{0,65}As$ ; nuclei charge

$Z=20$ ; nucleus radius: 175A; matrice: GaAs) that the configuration  $1s^2 2p^6 3d^{10} 2f^2$  is corresponding to the ground state of system. The calculation of the superatom system (superatomic nucleus  $Al_{0,35}Ga_{0,65}As$ ; nuclear charge  $Z=20$ ; matrix: GaAs; radius of the nucleus: 125A) was carried out and obtained the corresponding sequence of energy levels  $1s^2 2p^6 3d^{10} 2s^2$ . With other parameters (radius of the nucleus 170A and  $Z=20$ ) the ground state of system is corresponding to another configuration  $1s^2 2p^6 3d^{10} 2f^2$ . The superatomic radius is estimated 351A. It is clear that the properties of the superatom can be changed according to the shape of potential (2). It is obvious that these properties can be essentially changed in a presence of external field. The preliminary estimate shows that the Stark shift for the considered super atom in DC external electric field (strength 0,001 atomic units) is 0,15 meV.

4. For heavy quarkony the corresponding theory has the same form, excepting only the numerical parameters of corresponding effective potential. Earlier in ref. [5] we presented the results of calculating the energy splitting for quarkony with the use of the different forms of potential [9–11]. We have also carried out the energy splitting calculation for quarkony system with the use of the different forms of potential. In the zeroth limit for E(2s)-E(2p) the more exacted value is 830 MeV under  $m(Q)=45$  GeV. If  $r \rightarrow \infty$ , the 2s-2p and 2s-1s splitting results in  $\sim 145$  MeV. Especial interest attracts behavior of the value:

$$|\Psi(0)_{2\sigma}^2| / |\Psi(0)_{1s}^2| = 0,5 - 0,6 \quad (5)$$

under  $m(Q)=45$  GeV (this value is obtained in a case of the use of the potential:  $V(r) \sim 1/r \ln(Ar)$  when  $r \rightarrow 0$  and  $V \sim ar$  when  $r \rightarrow \infty$ ;  $A=0,1$  GeV and  $a=0,2$  GeV). These properties can be essentially changed in a presence of the strong external electric or magnetic field.

5. So, we present here a consistent quantum approach to calculation of the bound states energies for following systems: superatom (spherical nucleus of some semiconductor material that is selectively doped by donors; it is surrounded by the intrinsic matrix from material with low band gap) in weak external electric field and more exacted data for heavy quarkony. As it has been indicated earlier a consideration together such different physical systems as semiconductor superatom and heavy quarkony is connected with a fact that the mathematical structure of the master equations is practically the same, excepting surely the energy parameters of the corresponding effective potentials.

## References

1. Gallium Arsenide and Related Compounds, Eds. F. H. Kuchar and H. Henrich, World Sci., Heidelberg, 2000. — P. 1–85.
2. Heterojunctions and Semiconducting Superlattices, Ed. G. Allan. — Springer-Verlag, Berlin, 1998. — P. 3–135.
3. Andryushin E. A., Bykov A. A. From superlattices to superatoms // Usp. Phys. Nauk, 1988. — 15, P. 724–730.
4. Loboda A. V. Structure of ground state of superatom. Ionized superatom as single electrons counter // Photoelectronics. — 10, 2001. — P. 110–112.
5. Vitavetskaya L. A. Consistent relativistic quantum mechanical calculation of the bound states for semiconductor superatom and quarkony // Photoelectronics. 14, 2005. — P. 48–50.
6. Glushkov A. V. Atom in electromagnetic field. — Kiev: KNT, 2005. — 400 p.

7. *Glushkov A. V., Ivanov L. N. DC Strong-Field Stark-Effect: consistent quantum-mechanical approach // J. Phys. B: At. Mol. Opt. Phys.* 26(16), 1993. — P. 379–386.
8. *DC Strong Field Stark Effect for Non-hydrogenic Atoms: Consistent Quantum Mechanical Approach / A. V. Glushkov, S. V. Ambrosov, A. V. Ignatenko, D. A. Korchevsky // Int. Journ. Quant. Chem.* 99(5), 2004. — P. 933–939.
9. *Calculation of bond energy in negative ions of heavy elements / A. V. Glushkov, L. A. Vitavetskaya, A. V. Malinovsky, Yu. V. Butenko, E. A. Ryazanov // J. Struct. Chem.* — 39(2), 1998. — P. 217–224.
10. *QED calculation of the superheavy elements ions: energy levels, radiative corrections and hfs for different nuclear models / A. V. Glushkov, S. V. Ambrosov, A. V. Loboda, Yu. G. Chernyakova, O. Yu. Khetselius, A. A. Svinarenko // Nucl. Phys. A.* 734, 2004. — P. e21–26.
11. *Resonance states of compound super-heavy nuclei and EPPP in heavy nucleus collisions / A. V. Glushkov, V. D. Rusov, S. V. Ambrosov, A. V. Loboda // In: New projects and new lines of re-search in nuclear physics. Eds. G. Fazio, F. Hanappe. — World Sci. — Singapore, 2003. — P. 126–152.*
12. *Quantum calculation of cooperative muon-nuclear processes: discharge of metastable nuclei during negative muon capture / S. V. Malinovskaya, A. V. Glushkov, Yu. V. Dubrovskaya, L. A. Vitavetskaya // Progress Theor. Phys. and Chem.* 11 (1), 2005. — P. 371–376.
13. *Vitavetskaya L. A. Consistent quantum approach to semiconductor superatom and quarkony in external electromagnetic field // Photoelectronics.* — 2006. — N 16. — P. 35–37.

UDC 538.913.,539.184

O. Yu. Khetselius, E. P. Gurnitskaya, A. V. Loboda,  
L. A. Vitavetskaya

#### **CONSISTENT QUANTUM APPROACH TO QUARKONY ENERGY SPECTRUM AND SEMICONDUCTOR SUPERATOM AND IN EXTERNAL ELECTRIC FIELD**

The problems of calculation of the bound states energies for semiconductor superatom (spherical nucleus of some semiconductor material that is selectively doped by donors; it is surrounded by the intrinsic matrix from material with low band gap) and heavy quarkony in external strong electric field are considered. Ab initio effective potential approach in combination with the operator perturbation theory method is used in calculation..

УДК 538.913.,539.184

О. Ю. Хецелиус, Е. П. Гурницкая, А. В. Лобода,  
Л. А. Витавецкая

#### **ПОСЛЕДОВАТЕЛЬНЫЙ КВАНТОВЫЙ ПОДХОД В ТЕОРИИ КВАРКОНИЯ И ПОЛУПРОВОДНИКОВОГО СУПЕР-АТОМА ВО ВНЕШНЕМ ЭЛЕКТРИЧЕСКОМ ПОЛЕ**

Рассмотрена проблема расчета энергий связанных состояний систем: тяжелого кваркония и полупроводникового суператома (сферическое ядро полупроводникового материала, легированного донорами и окруженного беспримесной матрицей из материала с меньшей шириной запрещенной зоны) во внешнем сильном электрическом поле. Метод ab initio эффективного потенциала в комбинации с операторной теорией возмущений использован для расчетов.

УДК 538.913.,539.184

О. Ю. Хецелиус, О. П. Гурницька, А. В. Лобода,  
Л. А. Вітавецька

#### **ПОСЛІДОВНИЙ КВАНТОВИЙ ПІДХІД У ТЕОРІЇ КВАРКОНІЮ ТА НАПІВПРОВІДНИКОВОГО СУПЕРАТОМУ У ЗОВНІШНЬОМУ ЕЛЕКТРИЧНОМУ ПОЛІ**

Розглянуто проблему розрахунку енергій зв'язаних станів систем: важкого кварконія та суператома (сферичне ядро півпровідникового матеріалу, легірованого донорами та оточеного бездомішковою матрицею з матеріалу з меншею шириною забороненої зони) у зовнішньому сильному електричному полі. Метод ab initio ефективного потенціалу у комбінації з операторною теорією збурень використано для розрахунків.

G. YA. KOLBASOV, I. A. RUSETSKII

Institute of General & Inorganic Chemistry, Ukrainian National Academy of Sciences,  
32/34 Palladin str., 03680 Kiev-142, Ukraine, e-mail: kolbasov@ionc.kiev.ua

## PHOTOSENSITIVITY OF NANOSTRUCTURED GALLIUM ARSENIDE IN CONTACT WITH ELECTROLYTE

It has been shown that the nanostructurization of the gallium arsenide surface with metal and CdS particles affected greatly the photoelectrochemical properties of GaAs. The increase in the quantum yield of photocurrent  $\eta_i$  in the visible region after the nanostructurization of GaAs surface with Pt, CdS and Zn accounted for by an decrease in the rate of surface recombination of holes. In the ultraviolet region the decrease in  $\eta_i$  is attributed to an increase in the contribution of cathodic photocurrent (for a KOH solution, photocathodic reaction is hydrogen evolution and for polysulfide solution - photoreduction of polysulfide ions). For nanostructured GaAs the efficiency of the conversion of solar to electrical energy in polysulfide electrolyte was 23–24%.

The physicochemical properties of semiconducting nanomaterials differ greatly from those of similar materials, which have no pronounced nanostructure or characteristic size. This relates both to the set of their electrophysical, optical and luminescent properties and to the ability to exhibit a high electrocatalytic and photocatalytic activity in many chemical reactions [1–3]. One of the methods for the nanostructurization of the semiconductor surface is deposition of layers of nanosized particles of metals or semiconducting compounds. The properties of the material obtained depend largely both on the physicochemical properties of the deposited particles and on the mode of their interaction with the semiconductor surface, which is determined to a large extent by the method for producing the nanostructured surface.

This paper presents results of studying the photoelectrochemical properties of a GaAs electrode nanostructured with Zn, Pt and CdS particles. A salient feature of this material is a high quantum yield of photoelectrochemical current, which makes it promising for use in electrochemical systems for solar energy conversion.

### EXPERIMENTAL

We performed the nanostructurization of the GaAs surface with metal particles by the electrochemical and photoelectrochemical methods. For instance, to apply Pt nanoparticles to the GaAs surface with electronic conduction type (n-type), we employed the method of cathodic electrodeposition from a solution of chloroplatinic acid under strong semiconductor lighting ( $P=0,4-0,5$  watt/cm<sup>2</sup>) in the fundamental light absorption region [4]. Zn nanoparticles were produced under strong lighting of semiconductor by cathodic electrodeposition at low current densities ( $10 - 20$   $\mu$ A/cm<sup>2</sup>) from an aqueous solution of ZnCl<sub>2</sub>. CdS nanoparticles were deposited on GaAs during the formation of colloidal CdS particles in aqueous solution. To produce CdS nanoparticles, we used solutions containing cadmium citrate (or acetate) and sodium sulfide at a reagent concentration of  $10^{-4} - 10^{-2}$  mol/L; to stabilize the solution, gelatin was used; the dep-

osition temperature was 20–22°C. The GaAs surface was studied by means of a 09–I–OC–10–005 Auger spectrometer and EM–200 electron microscope. The spectral dependences of photocurrent were measured in a quartz cell on a setup, which included an MDR–2 monochromator, and the light source was a DKSSh–500 xenon lamp with stabilized discharge current. The absorption spectra of CdS colloidal solutions were measured with a Specord UV–VIS spectrophotometer. The photoelectrochemical measurements have been made using a PI–50–1 potentiostat. The electrode impedance was measured with a Tesla BM 401 ac bridge. The solar energy conversion efficiency was determined in a polysulfide electrolyte of the composition 2 mol/l Na<sub>2</sub>S + 2 mol/l NaOH + 1 mol/l S + 0.02 mol/l Se, in which GaAs is relatively stable. The electrode potential was measured with respect to a silver–chloride reference electrode.

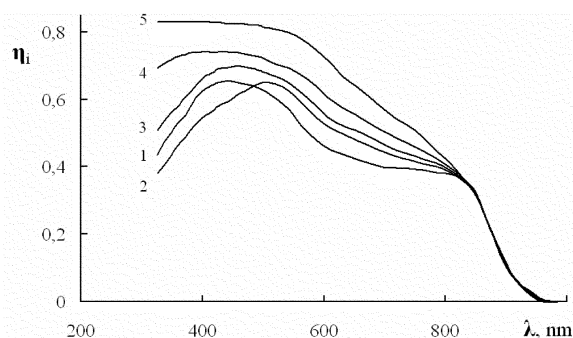


Fig. 1. Spectral dependence of the quantum yield of photoelectrochemical current,  $\eta_i$ , for a GaAs electrode, on whose surface Pt (2), Zn (3) and CdS (4) nanoparticles have been deposited; (1) starting electrode; (5) theoretical plot of  $\eta_i(\lambda)$ . 1 mol/l KOH solution, potential  $E = -0.4$  V (with respect to Ag/AgCl reference electrode)

### RESULTS AND DISCUSSION

Figure 1(a) shows a micrograph of the surface of monocrystalline n-type GaAs modified by Pt nanoparticles. It was found that the diameter of platinum particles ranged between several nanometers and tens of nanometers, most particles having a mean diam-

eter of  $d \sim 10$  nm. The coverage of the surface with Pt nanoparticles was  $\delta = 30 - 70\%$ . The  $d$  values for Zn particles did not exceed 10 nm in the low deposition current range, at high currents, became larger, and threadlike particles appeared. To determine the size of colloidal CdS particles ( $d$ ) in solution, a standard approach was used, which consists in determining the energy gap width of particles,  $E_g$ , from measurements of colloid absorption spectrum and calculation of the  $d$  value using the results of quantum-chemical calculations [1, 2]. It was found that the mean particle diameter ranged between 1.3 and 5.5 nm, depending on the concentration of the starting reagents. The CdS particles deposit on the surface were uniformly as aggregates, whose mean size is larger by several fold than that of CdS particles in colloidal solution.

The nanostructurization of the gallium arsenide surface with metal and CdS particles affected greatly in some cases the photoelectrochemical properties of GaAs. Figure 1 shows the spectral dependence of the quantum yield of photoelectrochemical current,  $\eta_i$ , for GaAs electrode. A decrease in  $\eta_i$  in the short-wavelength region of the spectrum (Fig. 2, curve 1) is characteristic of the starting GaAs electrode, on whose surface there were no nanoparticles [5].

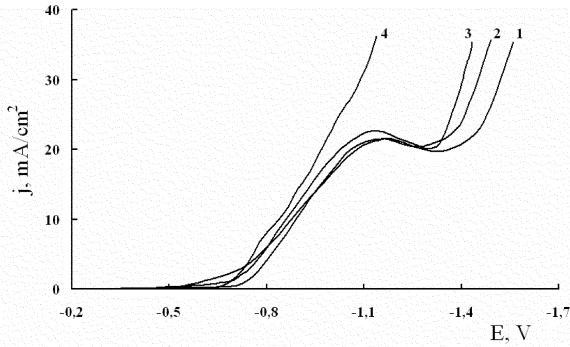


Fig. 2. Current-voltage curves for GaAs electrode, nanostructured with CdS (2), Zn (3) and Pt (4), in 1 mol/l KOH; (1) starting electrode

It was found that nanostructurization of the surface led to an increase in  $\eta_i$  in a wide spectral range. The largest increase in  $\eta_i$  was observed in the case of CdS (Fig. 2, curve 4). After the deposition of Pt nanoparticles, an increase in  $\eta_i$  in the visible region and its decrease in the ultraviolet region were observed (Fig. 2, curve 2).

To analyze the results obtained, use may be made of the theory of photogenerated charge carrier transfer across the semiconductor/electrolyte interface [5] with allowance for the fact that the total photocurrent across the interface consists of minority-carrier current (hole photocurrent  $i_p(\lambda)$ ) for GaAs with n-type conductivity and majority-carrier current (electronic photocurrent  $i_c(\lambda)$ ):

$$i(\lambda) = i_p(\lambda) - i_c(\lambda), \quad (1)$$

where hole photocurrent is given by:

$$i_p = e\Phi \left\{ \frac{1 - e^{-kl} / (1 + KL_p) + \frac{kT}{eF_s L_p} (1 - e^{-kl})}{1 + \frac{kT}{eF_s L_p} + \frac{D_p e^{Y_s}}{L_p (S_p + k_s^a)}} \right\}, \quad (2)$$

and electronic photocurrent by:

$$i_c = \frac{e\Phi K}{K + eF_s / kT} \left[ 1 + \frac{eF_s D_n}{kT(S_n + k_s^c)} \right]^{-1}, \quad (3)$$

Here  $\Phi$  is the light intensity,  $F_s$  is the electric field at the semiconductor surface,  $D_p$  and  $L_p$  are the diffusion coefficient and diffusion length of minority carriers (holes) respectively,  $D_n$  is the diffusion length of electrons,  $l$  is the width of space-charge region (SCR) near the semiconductor surface,  $K$  is the light absorption coefficient, which depends on the optical wavelength  $\lambda$ ,  $Y_s$  is the potential drop in the semiconductor SCR (in  $kT/e$  units),  $k_s^a$  and  $k_s^c$  are the rates of anodic and cathodic reactions respectively,  $S_p$  and  $S_n$  are the rates of surface recombination of holes and electrons. It should be noted that equations (1) and (2) take into account the general case of photoelectrochemical reaction involving charge carriers of permitted semiconductor bands and surface electronic states (SES) with the electron and hole flows on SES's being not equal. The increase in the quantum yield of photocurrent,  $\eta_i$ , in the visible region after the nanostructurization surface with Pt, Zn and CdS (Fig. 2) may be accounted for by an increase in the photocatalytic activity of the nanostructured surface (increase in  $k_s^a$ ) and hence by an increase in anodic photocurrent  $i_p$  (expression (2)).

As was shown in Refs [5], the decrease in the quantum yield of photocurrent,  $\eta_i$ , in the ultraviolet region for GaAs electrode with n-type conductivity is due to the high rate of electron transfer (increase in cathodic photocurrent) into the electrolyte via SES's and to their surface recombination. As follows from expression (3), the  $i_c$  value depends both on the cathodic reaction rate  $k_s^c$  and on the rate of surface recombination of electrons,  $S_n$ , surface electronic states being also involved in the electron transfer across the interface for the case where  $S_p \neq S_n$ . The calculation of the quantum yield of photoelectrochemical current,  $\eta_i$ , was performed by us in a wide spectral range for the following parameters of the semiconductor investigated by us:  $L_p = 1.5 \mu\text{m}$ ,  $D_p = 15 \text{ cm}^2/\text{s}$ ,  $D_n = 35 \text{ cm}^2/\text{s}$ . The  $Y_s$  values were determined using a linear dependence, obtained by us, of the reciprocal square of differential capacity,  $C^{-2}$ , measured at a high frequency ( $f = 30 \text{ kHz}$ ) on electrode potential  $E$  (in this case,  $Y_s = 0$  at the flat-band potential  $E_{fb}$ ). The value of  $l$  was determined on the basis of bulk electron concentration in semiconductor,  $n_0$ :

$$l = \sqrt{\frac{2\varepsilon\varepsilon_0 Y_s kT}{e^2 n_0}}, \quad (4)$$

(for the electrodes under study,  $n_0 = 3 \times 10^{16} \text{ cm}^{-3}$ );  $\varepsilon$  and  $\varepsilon_0$  are the permittivity of semiconductor and free space respectively;  $F_s = (E - E_{fb})/l$ .

Figure 2 (curve 5) shows a theoretical plot of  $\eta_i(\lambda)$  in the anodic potential region  $Y_s = 20$ , when the contribution of cathodic photocurrent  $i_c$  to  $\eta_i$  is small. In this case, the  $\eta_i$  quantity is a weak function of optical wavelength in the short-wavelength region of the spectrum and decreases in its long-wavelength region because of a decrease in light absorption coef-

ficient  $K$ . In this case, a noticeable decrease in  $\eta_i$  in the short-wavelength region of the spectrum due to the contribution of photocathode reaction occurs at  $K \geq 5 \times 10^4 \text{ cm}^{-1}$  and  $F_s \leq 1.2 \times 10^4 \text{ V/cm}$  and on condition that  $(S_n + k_s^e) > eF_s D_n / kT$  [5], as was found experimentally for starting GaAs electrode (Fig. 2, curve 1). Analysis of experimental data using expression (3) shows that after modifying the GaAs surface by Pt, an additional increase in cathodic reaction rate (for a KOH solution, cathodic reaction is hydrogen evolution and for polysulfide solution photoreduction of polysulfide ions). The experimental data presented in Fig. 3 speak in favor of this fact. The voltammetric curve for the starting GaAs electrode exhibited at potentials of  $E = -0.8$  to  $-1.3 \text{ V}$  in a NaOH solution limiting oxygen reduction current (Fig. 2, curve 1) (which decreased as a rule after blowing through the solution with purified Ar) and hydrogen evolution current at  $E < -1.3 \text{ V}$ .

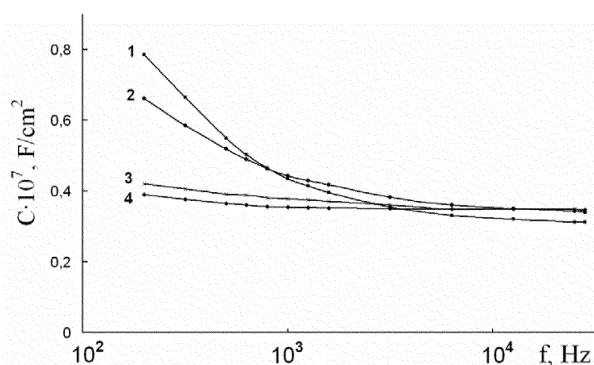


Fig. 3 Frequency dependence of differential capacity  $C$  of GaAs electrode nanostructured with Zn (2), Pt (3) and CdS (4); (1) starting electrode. Solution: 2 mol/l  $\text{Na}_2\text{S}$  + 2 mol/l NaOH + 1 mol/l S.  $E = -0.4 \text{ V}$

After the deposition of Pt nanoparticles, the hydrogen evolution overpotential decreased substantially (Fig. 3, curve 4), which was caused by an increase in the catalytic activity of the nanostructured Pt surface. The CdS nanoparticles deposited on the GaAs surface had a lower electrocatalytic activity in the hydrogen evolution reaction as against platinum (Fig. 3, curves 2); at the same time, the electrocatalytic activity of Zn nanoparticles was somewhat higher than that of CdS nanoparticles (Fig. 3, curve 3). Therefore, the effect of CdS nanoparticles on the trend of the plot of  $\eta_i(\lambda)$  mainly reduces to an increase in the photocatalytic activity of the surface and a possible decrease in the surface recombination rate of electrons,  $S_n$ , as a result of which the total photocurrent in the short-wavelength region of the spectrum also increased (Fig. 1, curves 4). At the same time, Zn nanoparticles, as Pt nanoparticles, led to a greater increase in cathodic photocurrent and caused a stronger spectral dependence  $\eta_i(\lambda)$  in the ultraviolet region (Fig. 1, curve 2, 3). A decrease in surface recombination rate after the nanostructurization of GaAs electrode is also indicated by a decrease in the frequency dependence of differential capacity  $C$ , measured according to a parallel equivalent circuit (Fig. 4). From capacity measurements, one can determine the concentration of surface electronic states (SES),  $N_s$ , on GaAs after its modification by Pt nanoparticles. The  $N_s$  quantity was defined as follows:

$$N_s = \frac{kT\Delta C}{e^2\theta(1-\theta)}, \quad (5)$$

where  $\theta$  is the electron population of SES's ( $\theta = 0.5$  when SES's are not involved in the electrochemical reaction),  $\Delta C = C_l - C_{SCR}$  is the difference between low-frequency capacitance (the calculations were made for  $f = 200 \text{ Hz}$  (Fig. 2)) and SCR capacitance, determined at  $f = 30 \text{ kHz}$ . It was found that the electronic state concentration determined in this way was lowest after the deposition of CdS and Pt nanoparticles on the GaAs surface and was  $N_s = (0.3 - 0.5) \times 10^{10} \text{ cm}^{-2}$ , whereas the SES concentration on starting samples was higher by an order of magnitude. This effect of nanoparticles on recombination processes may be accounted for by the fact that they deposit mainly on active centers on the surface, which are formed by surface defects of different types or surface oxides, and are charge carrier recombination or trapping centers; they neutralize the action of these centers by reducing their concentration and changing their energetics and electron and hole trapping coefficients. We found that after the nanostructurization of the GaAs electrode surface, the efficiency of the conversion of solar to electrical energy in polysulfide solution reached 23–24% when  $\text{Cu}_2\text{S}$  was used as counter electrode. In this case, the short-circuit current was 25–28  $\text{mA/cm}^2$  at a solar illumination power of 100  $\text{mW/cm}^2$ , the open-circuit voltage was 1.15–1.20 V, the fill factor of current-voltage curve varied between 0.53 and 0.76.

#### CONCLUSIONS

The nanostructurization of the GaAs electrode surface with Zn and CdS particles leads to an increase in the quantum yield of photoelectrochemical current in a wide spectral range, which is attributed to an increase in the photocatalytic activity of the surface and to decrease in the rate of surface recombination of electrons. For Pt nanoparticles, an increase in electrode photosensitivity in the visible region and its decrease in the ultraviolet region, which is associated with the influence of cathodic photocurrent, were observed. The nanostructured GaAs electrodes were characterized by high efficiency of conversion of solar energy to electrical.

#### References

1. *Khairutdinov R. F.* Chemistry of semiconductor nanoparticles // Russian Chemical Reviews. — 1998. — Vol. 67, N 2. — P. 109–122.
2. *Quantum size effects in photonics semiconductor nanoparticles* / A. L. Stroyuk, A. I. Kryukov, S. Ya. Kuchmy, V. D. Pokhodenko // Teoreticheskaya i Experimental'naya Khimiya. — 2005. — Vol. 41, N 2. — P. 67–87.
3. *Gaya U. I., Abdullah A. H.* Heterogeneous photocatalytic degradation of organic contaminants over titanium dioxide: A review of fundamentals, progress and problems // J. Photochem. Photobiology C: Photochemistry Reviews. — 2008. — Vol. 9, N 1. — P. 1–12.
4. *Kolbasov G. Ya., Krasnov Yu. S., Volkov S. V.* Cathodic modification of amorphous  $\text{WO}_3$  films with nanosized Pt and Pd particles // 55th ISE Annual Meeting, 19–24 September 2004, Thessaloniki, Greece. Book of Abstracts I. — P. 541.
5. Surface effect of gallium arsenide on its photosensitivity in contact with electrolyte / N. L. Dmitruk, G. Ya. Kolbasov, N. I. Taranenko, I. I. Karpov // Poverchnost. Fizika, Khimiya, Mekhanika. — 1985. — N 11. — P. 34–38.

UDC 544.52:541.138:621.352

G. Ya. Kolbasov, I. A. Rusetskii

#### **PHOTOSENSITIVITY OF NANOSTRUCTURED GALLIUM ARSENIDE IN CONTACT WITH ELECTROLYTE**

It has been shown that the nanostructuring of the gallium arsenide surface with metal and CdS particles affected greatly the photoelectrochemical properties of GaAs. The increase in the quantum yield of photocurrent  $\eta_i$  in the visible region after the nanostructuring of GaAs surface with Pt, CdS and Zn accounted for by an decrease in the rate of surface recombination of holes. In the ultraviolet region the decrease in  $\eta_i$  is attributed to an increase in the contribution of cathodic photocurrent (for a KOH solution, photocathodic reaction is hydrogen evolution and for polysulfide solution - photoreduction of polysulfide ions). For nanostructured GaAs the efficiency of the conversion of solar to electrical energy in polysulfide electrolyte was 23–24%.

УДК 544.52:541.138:621.352

Г. Я. Колбасов, И. А. Русецкий

#### **ФОТОЧУВСТВИТЕЛЬНОСТЬ НАНОСТРУКТУРИРОВАННОГО АРСЕНИДА ГАЛЛИЯ В КОНТАКТЕ С ЭЛЕКТРОЛИТОМ**

Показано, что наноструктурирование поверхности арсенида галлия частицами металлов и CdS существенно влияет на фотоэлектрохимические свойства GaAs. Увеличение квантового выхода фототока  $\eta_i$  в видимой области спектра после наноструктурирования поверхности GaAs Pt, CdS и Zn объясняется уменьшением скорости поверхностной рекомбинации дырок. В ультрафиолетовой области уменьшение  $\eta_i$  вызвано увеличением вклада катодного фототока (для раствора KOH - фотокатодной реакцией выделения водорода и для полисульфидного раствора - фотовосстановлением полисульфид-ионов). Для наноструктурированного GaAs эффективность преобразования солнечной энергии в электрическую в полисульфидном электролите составляла 23–24%.

УДК 544.52:541.138:621.352

Г. Я. Колбасов, И. А. Русецкий

#### **ФОТОЧУТЛИВІСТЬ НАНОСТРУКТУРОВАНОГО АРСЕНІДУ ГАЛІЮ В КОНТАКТІ З ЕЛЕКТРОЛІТОМ**

Показано, що наноструктурування поверхні арсеніду галію частками металів і CdS істотно впливає на фотоелектрохімічні властивості GaAs. Збільшення квантового виходу фотоструму  $\eta_i$  у видимій області спектра після наноструктурування поверхні GaAs Pt, CdS і Zn пояснюється зменшенням швидкості поверхневої рекомбінації дірок. В ультрафіолетовій області зменшення  $\eta_i$  викликано збільшенням внеску катодного фотоструму (для розчину KOH - фотокатодною реакцією виділення водню й для полісульфідного розчину - фотовідновленням полісульфід-іонів). Для наноструктурованого GaAs ефективність перетворення сонячної енергії в електричну у полісульфідному електроліті становила 23–24%.

A. G. BALOGH<sup>1</sup>, S. M. DUVANOV<sup>2</sup>, D. I. KURBATOV<sup>3</sup>, A. S. OPANASYUK<sup>3</sup>

<sup>1</sup>Institute of Material Science, Darmstadt University for Technology, Germany

<sup>2</sup>Applied Physics Institute, NAS of Ukraine, Petropavlovskaya str.58, Sumy, Ukraine, E-mail: smduvanov@ukr.net

<sup>3</sup>Sumy State University, Rimsky-Korsakov str. 2, Sumy, Ukraine, E-mail: kurd@ukr.net

## RUTHERFORD BACKSCATTERING AND X-RAY DIFFRACTION ANALYSIS OF Ag/ZnS/glass MULTILAYER SYSTEM

Experimental results on the study of the element depth profiles, structural and roughness properties of Ag/ZnS/glass multilayer system are reported. The ZnS films in this system were obtained by close-spaced vacuum sublimation method (CSVs) under different substrate temperature. Examination of layers morphology and structure was performed by optical microscopy with laser interferometry phase shifting and X-ray diffraction method respectively. Element depth profiles and film thickness were studied using energy dispersive X-ray analysis (EDAX), such non-destructive accurate qualitative absolute techniques as Rutherford backscattering spectrometry (RBS) and elastic Backscattering Spectroscopy (BS) of <sup>4</sup>He<sup>+</sup> and <sup>1</sup>H<sup>+</sup> ions, respectively. Two temperature ranges where the film growth is going under different mechanism were determined. It was established that ZnS films deposited at 373 < T<sub>s</sub> < 573 K have ZB structure. At T<sub>s</sub> > 573 K the traces of WZ phase are appearing in ZnS films, their amount somewhat increases under increasing the T<sub>s</sub>. RBS and BS techniques allow to determine atomic concentration of compound elements and atomic concentration of the element depth distributions. It was shown that thickness averaged stoichiometry of ZnS films were determined by deposition regimes.

### 1. INTRODUCTION

The maximum efficiency of the best thin film solar cells (SC) based on heterojunctions n-CdS/p-CdTe is 16.5%, but the rate of its increasing became considerably slower [1]. The most effective back-contact solar cells have close-spaced chemical deposited semiconductor layers are formed at high temperature (T<sub>n</sub> ~ 873 K). This process needs the use of the special heat-resistant glass substrates. Therefore for industry producing of solar cells base layers common use low-temperature (~773 K) method of gas-transport reactions. It enables to use low-cost soda-lime glass substrates. However the efficiency of these solar cells does not exceed 10%, and a prime price of energy is high enough [2].

It is thought that the increase of the efficiency of SCs with CdTe absorbing layer may be achieved by change of the material of optical window [3–5]. Thin ZnS layers (E<sub>g</sub> = 3.68 eV) can be considered as an alternative to CdS (E<sub>g</sub> = 2.42 eV) films. Zinc sulfide has a sufficiently larger gap than cadmium sulfide, what makes it possible to expand the photosensitivity range and to increase short circuit currents of the corresponding SCs. ZnS has the same type of the crystal lattice as CdTe and both materials form a continuous row of solid solutions. Besides that, ZnS is not a toxic material due to absence of hard metals as compound components and appears as a friendly material for the environment. At the same time, a large lattice mismatch of ZnS and CdTe (~18%) causes a low efficiency of available ZnS/CdTe SCs (~4%) [3]. However, this disadvantage can be compensated by forming transition layers at the interface under the diffusion process as well as by technological way [4].

The efficiency of ZnO/CBD-ZnS/CIGS solar cells increased to 18.6% in recent years [5]. However vacuum condensates of ZnS as wide-gap solar cell windows in this case practically were not used

and their properties are investigated poorly. Optimization of ZnS thin films characteristics is important. Interaction processes also require research between a glass lining and a semi-conductor layer which occur at the moment of halcohenide condensation. It also has caused the work purpose.

### 2. EXPERIMENTAL DETAILS

Zinc sulfide thin films were deposited on soda-lime glass substrates by the close-spaced vacuum sublimation (CSVs) method [6]. The evaporation of two-phased stoichiometric ZnS powder with exceeded content of hexagonal phase (wurtzite) in the charge was carried out. The temperature T<sub>ev</sub> of evaporator was 1273 K. The temperature T<sub>s</sub> of substrate was varied in the range 373 ÷ 973 K.

The thin Ag layer was applied on the ZnS film for support of charge gathering from the film surface during measurements using charge particles. Under such conditions the temperature of the ZnS surface was 573 K.

Surface morphology of the films had been investigated by optical microscopy. The calculation of surface roughness was performed according the standard ISO/R 468 [7], while the average arithmetic deviation R<sub>a</sub> of profile was defined by formula

$$R_a = \frac{1}{n} \sum_{i=1}^n y_i,$$

where y<sub>i</sub> — profile deviation of film surface from the mean line, n — the number of profile peaks.

Structural investigations of the films were performed with X-ray diffractometer DRON 4-07 using Ni-filtered K<sub>α</sub> Cu radiation source and conventional Bragg-Brentano geometry. Continuous mode scanning over the range of diffraction angles 20° ≤ 2θ ≤ 60° (where 2θ is the Bragg angle) was applied to examine the surface of the samples. Obtained diffraction patterns were normalized to the intensity of (111) peak

of the cubic phase. Phase analysis was done by comparison of interplane distances and relative intensities from the investigated samples and references according to Joint Committee on Powder Diffraction Standards (JCPDS) data [8].

Chemical composition and films thickness studied by energy dispersive X-ray analysis (EDAX) and Rutherford back scattering (RBS) method of protons and high energy (2,5 MeV) helium ions [9]. Distribution of concentration in EDAX method was probed in five points on films surfaces.

As the source of charged protons (in RBS method) the electrostatic accelerator on 2 MeV (Institute of nuclear physics, Frankfurt University, Germany) was utilized. As the source of helium ions was used electrostatic accelerator on 2.5 MeV (Scientific institute of nuclear physics, Moscow State University, Russia). The primary beam of protons bombarded the target normally, scattering angle was 170° and 171° respectively. As the detecting system the semiconductor detector of charged particles were used. The energy resolution of this detector was ~15 keV.

SIMNRA and DVBS programs performed the RBS spectra processing. It is considered that oxygen is compulsory part of  $A_2B_6$  compounds. Coming from it chemical composition of ZnS films is certain in supposition, that in a layer except for basic material is contained this impurity and hydrogen, absorbable from substrate.

### 3. RESULTS AND DISCUSSION

Surface morphology and condensate structure studies showed that zinc sulfide films are transparent, polycrystalline and homogeneous in area with a good adhesion to the substrate. Growth of ZnS layers takes place as follows. A fine-grained transition region is forming on the substrate with following overgrowth of crystallites oriented by the (111) plane parallel to the substrate.

The increase of crystallite sizes  $D$  with the increasing film thickness  $l$  as a consequence of a secondary nucleation during their condensation is almost not occurred at  $T_s < 720$  K. As a result, the grains become a form close to a uniaxial one. Increasing the substrate temperature leads to another growth mechanism: a columnar-like mechanism becomes dominant.

The rise of condensation temperature is going with increase in height of layers relief and therefore it's surface roughness. The typical micrographs of condensates surfaces and surface profilograms are presented in fig. 1.

The determination of parameter  $R_a$  shows that under rising in temperature from  $T_s = 423$  K to 863 K the surface roughness is increasing from  $R_a \approx 0.062 \mu\text{m}$  to  $0.147 \mu\text{m}$  at  $L \sim 3 \mu\text{m}$ . The dependence of profile average arithmetic deviation for ZnS films versus  $T_s$  is shown in fig. 2. The sharper arising of average arithmetic deviation  $R_a$  of films surface profile occurs in the range of deposition temperature, where the column mechanism of film growth is realized.

Analysis of XRD patterns demonstrated that ZnS films deposited at  $373 < T_s < 573$  K have ZB structure. Hexagonal phase in the as-grown films is not observed

in X-ray diffractograms of the condensates (fig.3) despite the double-phase composition of the initial charge characterized by dominating WZ amount. As a rule, XRD patterns show reflexes from (111), (311), (222), (331) planes of ZB. The (111) peaks with dominant maximum intensities are presenting in most cases and exhibit the strong texture of the films.

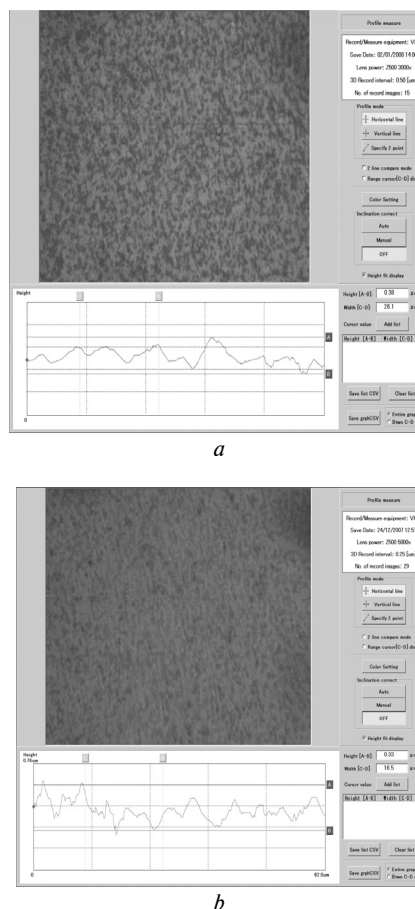


Fig. 1 – The optical morphology with surface profiles of the films grown under different substrate temperatures:  $T_s = 573$  K (a);  $T_s = 863$  K (b)

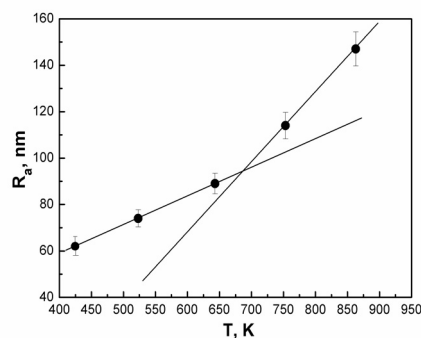
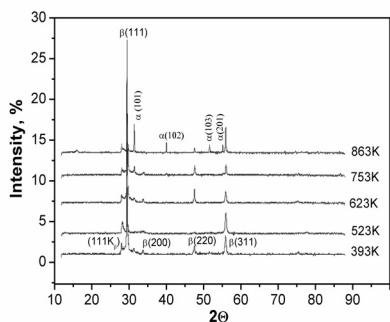


Fig. 2 – Dependencies of arithmetic average to absolute surface deviation  $R_a$  values on the substrate temperatures  $T_s$

At  $T_s > 573$  K the traces of WZ phase are appearing in ZnS films, their amount somewhat increases under increasing the  $T_s$ . It should be noted that in bulk samples the WZ phase is stable at  $T > 1297$  K. XRD patterns mainly demonstrate reflexes only from (101) wurtzite plane and indicate existence of texture in

this phase. In the issue the high-temperature condensates of ZnS are double-phased compounds. X-ray analysis not found out oxides and other extraneous



phases.

Fig. 3 – X-ray patterns of ZnS films obtained under different condensation temperatures  $T_s$

The typical EDAX spectrums from the “ZnS/sodalime glass” films is illustrated in fig. 4. Along with lines from Zn and S on spectrums there are lines from Si, Ca, K, which belong to lining material. It is related to the small thickness of investigational films by comparison to the depth of X-radiation. The lines of Na, which is one of basic constituents of substrate, coincide with lines of other elements and that is why does not appear.

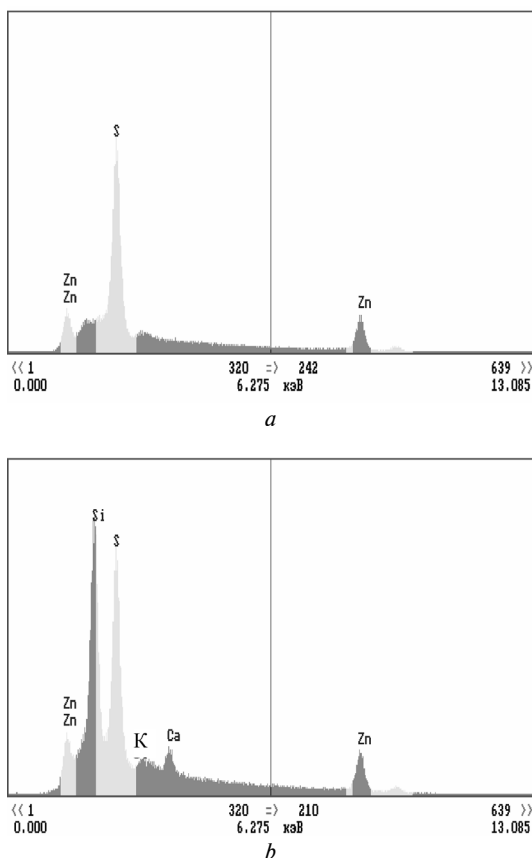


Fig. 4 – Typical EDAX spectrums of the ZnS films on sodalime glass substrates: *a* – depth  $L=3,2 \mu\text{m}$ ; *b* –  $L=1,1 \mu\text{m}$

This is why such techniques as RBS and BS were applied to explore an elemental composition of the multilayer Ag/ZnS/glass system. It is necessary to mention that these techniques were used very seldom to study ZnS films [10–12]. The BS has improved

sensitivity to detect low-Z traces in high-Z matrix and deeper probing. At the same time, the RBS technique has better sensitivity to analyze high-Z elements in low-Z substrates, lower value of profiling depth. From the other side RBS has higher depth resolution and more accurate detection of the absolute trace element concentration [10]. Thus both techniques are complementary each other and give us possibility to obtain more detailed information about the ZnS film depth, thickness averaged stoichiometry of ZnS films and roughness of the Ag-ZnS and ZnS-glass interface layers.

Typical BS and RBS spectra obtained from Ag/ZnS/glass system are shown in Fig. 5,6. As we can see, overlapping of the partial spectra from the matrix and thin layers occurs. Values of thickness were extracted from BS spectra and found out to be  $L=1.1, 1.8$  and  $3.2 \mu\text{m}$ .

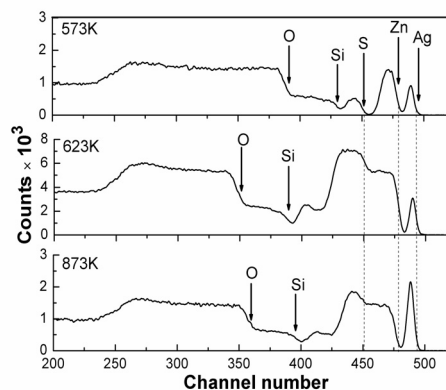


Fig. 5. Elastic proton backscattering spectras from multilayer Ag/ZnS/glass system obtained by different grow conditions. Kinematic edges of the elemental partial spectra are shown by arrows

Fig. 5 shows that the peaks from Zn, S are good separated from each other at 573 K in the case of ZnS thin film ( $L=1.1$  microns), but in the case of more thick layers ( $L=1.8-3.2$  microns) the partial spectra overlap at 623 and 873 K, and it makes data handling more difficult. Using  $^4\text{He}^+$  analysing beam, the spectra overlap even in the case of ZnS thinnest layer (Fig. 6).

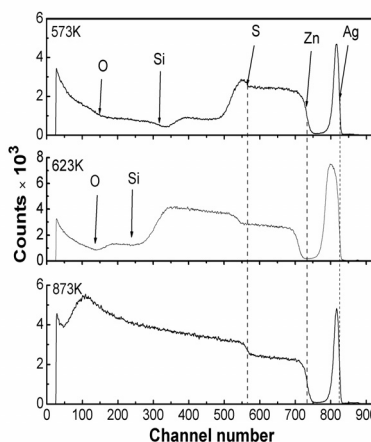


Fig. 6. Energetic  $^4\text{He}^+$  RBS spectra from multilayer Ag/ZnS/glass systems obtained by different grow conditions. Kinematic edges of the elemental partial spectra are shown by arrows

As a result of the simulations using SIMNRA and DVBS codes, depth concentration distribution of the multi-layer system was extracted. Some results of the

data handling for the sample prepared at  $T_s = 873$  K are presented in Table 1.

Table 1

Elemental depth distribution in multilayer Ag/ZnS/glass system

L, nm	C, atomic %									
	Ag	Zn	S	Ca	Si	Al	Mg	Na	O	H
104,7	73,0	24,6	2,4	0	0	0	0	0	0	0
166,5	17,2	32,7	48,9	0	0	0	0	0	0	1,1
219,0	1,2	34,9	51,5	0	0	0	0	0	6,7	5,6
250,4	0	42,1	55,3	0	0	0	0	0	1,7	1,0
399,2	0	43,1	55,8	0	0	0	0	0	0	1,1
763,8	0	43,6	56,1	0	0	0	0	0	0	0,2
1146,9	0	43,8	56,0	0	0	0	0	0	0	0,2
1534,2	0	43,8	56,0	0	0	0	0	0	0	0,2
1836,8	0	43,1	55,1	0	0	0	0	0	0	0,8
1989,6	0	37,4	54,4	0,4	0,1	0	0	0	7,7	0,7
2096,7	0	32,7	49,4	2,5	2,9	0	0	0	9,2	3,3
2350,8	0	25,1	38,6	2,3	12,3	0	0	0	10,9	10,8
2611,1	0	13,5	8,0	2,7	17,4	0	0	0	29,3	29,0
35340,5	0	0	0	3	25	1	1	10	60	0

Traces of Si, Ca, Na diffused from glass substrate to chalcogenide were explored in ZnS film at high temperatures of the layer growth  $T_n$ . Some small concentration of W impurity caused by using of tungsten evaporator for the deposition to obtain ZnS films was detected on the surface of the films. Oxygen was observed only in the near-surface layers of the film where the oxide phase formation is possible, for example, ZnO, and in the film interface layers. It is necessary to mention that oxygen concentration reaches 3–8% in the ZnS films prepared by pyrolysis and chemical solutions methods and such films are rather solid state solution like  $ZnS_xO_{1-x}$  [3]. In the vacuum condensates, typical concentration of oxygen does not exceed 1–2% which has been confirmed experimentally. Carbon impurities were also found out on the surface of ZnS films. As additional studies have shown, these impurities ingress into samples from the residual gas atmosphere of the vacuum scattering chamber of RBS beam lines. For RBS spectra simulation hydrogen concentration is usually used in the sample composition as a model of the film pores, single vacancies etc.

Fig. 7 shows the resulted types of depth distributing of concentrations components (Zn, S) of Ag/ZnS/glass multilayer structure obtained by RBS method. Results of «tailing» size of Zn/S concentration profiles in the transitional layer of Ag-ZnS in number and

high-quality conform to information from measuring of roughness of films surfaces resulted on Fig. 2.

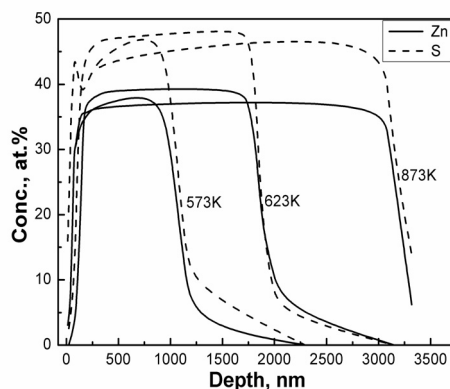


Fig. 7 – Effective elemental depth profiles of Ag/ZnS/glass system obtained by Elastic backscattering spectrometry

Fig. 7 shows that stoichiometry of ZnS films depending on  $T_s$  and layer thickness. For the film deposited at  $T_s = 863$  K, it is observed some increasing in S in the narrow near-surface sublayer.

Table 2 presents the results of average layer ZnS film stoichiometry obtained using RBS and BS techniques.

Table 2

Estimation of the effective stoichiometric composition of ZnS layer

Sample	$T_e$ , K	$T_s$ , K	BS data			RBS data		
			$C_{Zn}$ , at. %	$C_S$ , at. %	$C_{Zn}/C_S$	$C_{Zn}$ , at. %	$C_S$ , at. %	$C_{Zn}/C_S$
ZnS-1	1373	573	49,5	48,9	1,01	39,0	49,0	0,80
ZnS-3	1373	623	43,8	56,1	0,78	39,5	49,0	0,81
ZnS-2	1373	873	42,6	57,2	0,75	38,0	49,0	0,77

A relative error of the effective stoichiometry composition value of ZnS layer extracted from the BS data could be more than 20%, at the same time that derived from the RBS spectra does not exceed 2–4%.

Comparing the results obtained using different techniques, it is clear that those are within the limits of experimental error.

The obtained element concentration ratio  $C_{Zn}/C_S \sim 0.8$  of the compound is found out quite unexpected and require to be elucidated using different analysing techniques. According to RBS results, ZnS films ought to be double phase and sulphur reached. But XRD, optical and SEM data are in contradiction with the RBS findings. The last techniques do not detect the sulphur precipitates.

The other literature works on the using of the RBS technique to study of ZnS films show that ratio of  $C_{Zn}/C_S \sim 0.91$  [11], 1.02 [12] and 1.22 [13] that is to say there are enrichment of Zn-atoms in the condensates. From the other side in the Ref. [15] where explored ZnS films were deposited using photo-chemical deposition method and characterised using SEM/EDAX technique the authors had obtained the results similar to our ones —  $C_{Zn}/C_S \sim 0.71-0.81$ . The paper [16] attracts especial interest where the authors were studied a variation of the stoichiometric composition ZnS films at different substrate temperatures using SEM/EDAX which is quite similar to RBS technique. It was found out that  $C_{Zn}/C_S$  ratio increase from 0.88 up to 1.19 at increasing of  $T_s$  from 473 to 623 K, respectively. The  $C_{Zn}/C_S$  ration is also varied in depth from the value of 0.97 near substrate up to 1.11 near the surface layer, respectively [17].

#### 4. CONCLUSIONS

The structural investigation was spent and non-destructive elemental analysis of multilayer Ag/ZnS/glass structure obtained by CSVS technique under different grow temperatures was carried out. Two temperature ranges where the film growth is going under different mechanism were determined. It was established that ZnS films deposited at  $373 < T_s < 573$  K have ZB structure. At  $T_s > 573$  K the traces of WZ phase are appearing in ZnS films, their amount somewhat increases under increasing the  $T_s$ . By means of RBS and BS methods the chemical composition of condensates was determined and component distribution of compound as function of multilayer system depth was obtained. It was shown that thickness averaged stoichiometry of ZnS films were determined by deposition regimes and were varying in Zn-to-S ratio range  $0.77 \div 0.81$ .

#### 5. ACKNOWLEDGEMENT

The authors would like to thank Prof. V.Kulikauskas (Scientific institute of nuclear physics, Moscow State

University, Russia) and K.Stibing (Institute of nuclear physics, Frankfort University, Germany) for RBS and BS investigations of multilayer system.

#### 6. References

1. Wu X., Keane J. C., Dhare R. G. et al., 16.5%-efficient CdS/CdTe polycrystalline thin-film solar cells // Proc. 17<sup>th</sup> European Photovoltaic Solar Energy Conference, Munich, Germany, 2001. — P. 995–1000.
2. Romeo N., Basio A., Romeo A. et al., High Efficiency CdTe/CdS Thin Film solar Cells by a Process Suitable for Large Scale Production // „PV in Europe from PV Technology to Energy Solutions” Conference and Exhibiton, Rome, Italy, 2002.
3. Contreras-Puente G., Vigill O., Ortega-Lypez M. et al., New window materials used as heterojunction partners on CdTe solar cells // Thin Sol. Film. 361-362, 2000. — P. 378–382.
4. Metal/CdTe/CdS/Cd<sub>1-x</sub>Zn<sub>x</sub>S/TCO/glass: A new CdTe thin film solar cell structure / I. O. Oladeji, L. Chow, C. S. Ferekides, V. Viswanathan, Z. Zhao // Solar Energy Materials. Solar Cells. 61, 2000. — P. 203–211.
5. Hariskos D., Spiering S., Powalla M. Buffer layers in Cu(In,Ga)Se<sub>2</sub> solar cells and modules // Thin Sol. Film. 480-481, 2005. — P. 99–109.
6. Close-Spaced Evaporated ZnSe Films: Preparation and Characterization / Y. P. V. Subbaiah, P. Prathap, M. Devika, K. T. R. Reddy // Physica B 365, 2005. — P. 240.
7. ISO Recommendations on Roughness Measurements. — ISO/R 468, 1878, 1880, TC 57.
8. Umansky J. S., Skakov J. A., Ivanov A. N. et al., Crystallography, radiography and electron microscopy, Metalurgiya publisher, Moscow, 1982. — P. 1–632.
9. Selected powder diffraction data for education straining (Search manual and data cards). Published by the International Centre for diffraction data, USA, 1988. — P. 1–432.
10. Tesma J. R., Nastasi M., Barbow J. C. et al., Handbook of modern ion beam materials analysis. Materials Research Society, Pittsburgh, 1995.
11. Kashani H. Production and evaluation of ZnS thin films by the MOCVD technique as alpha-particle detectors // Thin Sol. Film. 288, 1996. — P. 50–56.
12. Oladeji I. O., Chow L. Synthesis and processing of CdS/ZnS multilayer films for solar cell application // Thin Sol. Film. 474, 2005. — P. 77–83.
13. Yun S. J., Dey S., Nam K. S. Zinc sulfide and terbium doped zinc sulfide films grown by traveling wave reactor atomic layer epitaxy // J. Korean Physical Society 33. — 1998. — P. 454–457.
14. Morosova N. K., Karetnikov I. A., Golub K. V. et al., The action of oxygen on ZnS electronic band structure // Semiconductors 39(5), 2005. — P. 513–520.
15. Photochemical deposition of ZnS thin films from C<sub>4</sub>H<sub>4</sub>KNaO<sub>6</sub>-added solutions / R. Kobayashi, N. Sato, M. Ichimura, E. Arai // J. of Opt. and Adv. Mat. 5 (4), 2003. — P. 893–898.
16. Subbaiah Y. P. V., Prathap P., Ramakrishna K. T. Reddy Structural, electrical and optical properties of ZnS films deposited by close-spaced evaporation // Appl. Surf. Sci. 253, 2006. — P. 2409–2415.

UDC 621.382

A. G. Balogh, S. M. Duvanov, D. I. Kurbatov,  
A. S. Opanasyuk

#### RUTHERFORD BACKSCATTERING AND X-RAY DIFFRACTION ANALYSIS OF Ag/ZnS/glass MULTILAYER SYSTEM

Experimental results on the study of the element depth profiles, structural and roughness properties of Ag/ZnS/glass multilayer system are reported. The ZnS films in this system were obtained by close-spaced vacuum sublimation method (CSVS) under different substrate temperature. Examination of layers morphology and structure was performed by optical microscopy with laser interferometry phase shifting and X-ray diffraction method respectively. Element depth profiles and film thickness were studied using energy dispersive X-ray analysis (EDAX), such non-destructive accurate qualitative absolute techniques as Rutherford backscattering spectrometry (RBS) and elastic Backscattering Spectroscopy (BS) of <sup>4</sup>He<sup>+</sup> and <sup>1</sup>H<sup>+</sup> ions, respectively. Two temperature ranges where the film growth is going under different mechanism were determined. It was established that ZnS films deposited at  $373 < T_s < 573$  K have ZB structure. At  $T_s > 573$

K the traces of WZ phase are appearing in ZnS films, their amount somewhat increases under increasing the  $T_s$ . RBS and BS techniques allow to determine atomic concentration of compound elements and atomic concentration of the element depth distributions. It was shown that thickness averaged stoichiometry of ZnS films were determined by deposition regimes.

УДК 621.382

А. Г. Балог, С. М. Дуванов, Д. І. Курбатов,  
А. С. Опанасюк

#### **ДОСЛІДЖЕННЯ ЕЛЕМЕНТНОГО СКЛАДУ ТА СТРУКТУРИ БАГАТОШАРОВОЇ СИСТЕМИ Ag/ZnS/СКЛО**

В роботі проведено дослідження профілів розподілу елементів за товщиною, структурних властивостей та шорсткості поверхні плівок ZnS в багатошаровій системі Ag/ZnS/скло. Шари сульфідів цинку в системі були отримані методом вакуумної сублімації в замкнутому об'ємі (CSVS) при різних температурах конденсації. Вивчення морфології поверхні проводилось за допомогою лазерної інтерферометрії зі зміщеною фазою. Структурні дослідження проводились з використанням методу рентгенівської дифракції (XRD). Вивчення розподілу елементів за товщиною та товщини плівок ZnS було здійснено за допомогою резерфордівського і пружного зворотного розсіювання протонів та іонів гелію-4 (RBS). Показано, що при  $373 < T_n < 573$  К плівки ZnS мають кубічну структуру, в той час як при вищих температурах підкладки вони стають двофазними. В результаті визначений елементний склад конденсатів, побудований розподіл елементів багатошарової системи та стехіометрія плівок ZnS за товщиною.

УДК621.382

А. Г. Балог, С. М. Дуванов, Д. І. Курбатов, А. С. Опанасюк

#### **ИССЛЕДОВАНИЕ ЭЛЕМЕНТНОГО СОСТАВА И СТРУКТУРЫ МНОГОСЛОЙНОЙ СИСТЕМЫ Ag/ZnS/СТЕКЛО**

В работе проведено изучение профилей распределения элементов по толщине, структурных свойств и шероховатости поверхности для пленок ZnS в многослойной пленочной системе Ag/ZnS/стекло. Пленки сульфида цинка в системе были получены методом вакуумной сублимации в замкнутом объеме (CSVS) при разных температурах конденсации. Изучение морфологии поверхности проводилось с помощью лазерной интерферометрии со смещенной фазой. Структурные исследования проводились с использованием метода рентгеновской дифракции (XRD). Изучение профилей распределения элементов по толщине и толщины пленок ZnS было осуществлено с помощью резерфордского и упругого обратного рассеяния протонов и ионов гелия-4 (RBS). Показано, что при  $373 < T_n < 573$  К пленки ZnS имеют кубическую структуру, а при более высоких температурах подложки они становятся двухфазными. В результате определен элементный состав конденсатов, построено распределение элементов многослойной системы и стехиометрии пленок ZnS по толщине.

## ТРЕБОВАНИЯ К ОФОРМЛЕНИЮ СТАТЕЙ В СБОРНИК «ФОТОЭЛЕКТРОНИКА» ИНФОРМАЦИЯ ДЛЯ АВТОРОВ

В сборнике «Фотоэлектроника» печатаются статьи, содержащие результаты фундаментальных и прикладных исследований, по следующим направлениям:

- физика полупроводников;
- гетеро- и низкоразмерные структуры;
- физика микроэлектронных приборов;
- линейная и нелинейная оптика твердого тела;
- оптоэлектроника и оптоэлектронные приборы;
- квантовая электроника;
- сенсорики.

Материалы, присылаемые в Редакцию, должны быть написаны с максимальной ясностью и четкостью изложения текста на английском и русском языках. В представленной рукописи должна быть обоснована актуальность решаемой задачи, сформулирована цель исследования, содержаться оригинальная часть и выводы, обеспечивающие понимание сути полученных результатов и их новизну.

Редакция журнала просит авторов при направлении статей в печать руководствоваться следующими правилами:

1. Рукописи должны направляться в двух экземплярах на английском и русском языках и сопровождаться файлами текста и рисунков на дискете. Электронная копия может быть представлена электронной почтой.

2. Приемлемые форматы текста: MultiEdit (txt), WordPerfect, MS Word (.rtf).

3. Приемлемые графические форматы для рисунков: .EPS, .TIFF, .BMP, .PCX, .CDR, .WMF, MS Word и MS Graf, JPEG. Рисунки созданные с помощью программного обеспечения для математических и статистических вычислений, должны быть преобразованы к одному из этих форматов и находиться в том месте статьи, где автор на них ссылается.

### ПРАВИЛА ПОДГОТОВКИ РУКОПИСИ:

Рукописи должны быть снабжены:

— Разрешением публикации: в открытой печати (экспертным заключением) — только для авторов из Украины.

Авторское право переходит Издателю.

#### Титульный лист

1. PACS и Универсальный Десятичный Код Классификации (УДК) (для авторов из стран СНГ) — в верхнем левом углу. Допускается несколько отделенных запятой кодов.

2. **Фамилия(и) автора (-ов)** ниже, через один интервал, отдельной строкой (по центру, шрифт 12 pt).

3. **Название учреждения**, полный адрес, телефоны и факсы, e-mail для каждого автора

ниже, через один интервал, отдельной строкой (по центру, шрифт 12 pt).

4. **Название работы** (по центру шрифт 14 pt, жирно).

**Текст** должен быть напечатан через 1,5 интервала на белой бумаге (формата А4) с полями: слева — 3 см, справа — 1,5 см, сверху и снизу — 2,5 см. Шрифт 12 pt. Подзаголовки, если они вводятся, должны быть напечатаны прописными буквами, жирно.

**Уравнения** должны быть введены, используя MS Equation Editor или MathType. Работы с рукописными вставками не принимаются.

**Список литературы** должен быть напечатан через 1,5 интервала, в соответствии со ссылками, пронумерованными в порядке их появления в тексте, **на языке оригинала**. Желательно ссылаться на литературу, изданную в 2000—2008 гг.

#### Примеры оформления литературы:

1. Берестовский В. Б., Лифшиц Е. М., Питаевский Л. П. Квантовая электродинамика. — М.: Наука, 1984. — 430 с.
2. Сергиенко А. М., Чернова Р. И., Сергиенко А. Я. Оптимизация цифровой сети // ФТТ. — 1992. — Т. 7, № 6. — С. 34—38.
3. Gas sensor research / R. Bramley, J. M. Faber, C. N. Nelson et al. // Phys. Rev. — 1978. — N 6. — P. 34—38.
4. Stirling A. N., Watson D. Progress in Low Temperature Physics / Ed. by D. F. Brewer. — North Holland, Amsterdam, 1986. — 248 p.
5. Громов К. Д., Ландсберг М. Э. Оптимальное назначение приоритетов // Тр. междунар. конф. «Локальные вычислительные сети» (ЛОКСЕТЬ 88). — Рига, 1988. — Т. 1. — С. 149—153.
6. Elliot M. P., Rumpf V., Smith A. A. The research of the optical sensors. — N. Y., 1976. — 37 p. — (Reprint./ ТН 4302-CERN).
7. Шалимова А. Н., Крюков А. С. Исследование оптических сенсоров. — К.: 1976. — 37 с. — (Препр./АН Украины. Ин-т кибернетики; 76—76).
8. Васильев Н. В. Оптичні сенсори на  $A_2B_6$ ; Дис... канд. фіз.-мат. наук: 05.05.04 / Ін-т кибернетики. — К., 1993. — 212 с.

**Рисунки** будут сканированы для цифрового воспроизведения. Поэтому принимаются только высококачественные рисунки.

Надписи и символы должны быть напечатаны внутри рисунка. Негативы, слайды, и диапозитивы не принимаются. *Иллюстрации* будут сканироваться цифровым сканером. Принимаются в печать только высококачественные иллюстрации. Подписи и символы должны быть впечатаны. Не принимаются в печать негативы, слайды, транспоранты.

Рисунки должны иметь соответствующий к формату журнала размер не больше 160 × 200. Текст на рисунках должен выполняться шрифтом 12 пунктов. На графиках единицы измерения указываются через запятую (а не в скобках). Если рисунок делится на части (а, б, ...), то соответствующее обозначение приводится под рисунком курсивом.

**Подписи к рисункам** должны быть напечатаны в рукописи под рисунками с двумя пробелами.

К тексту статьи прилагаются Аннотации:

**Аннотация:** до 200 слов на английском, украинском (только для авторов из Украины) и русском языках. Перед текстом аннотации нужно указать на том же языке: УДК, фамилии и инициалы всех авторов, название работы.

**РУКОПИСИ НАПРАВЛЯЮТСЯ ПО АДРЕСУ:**

Куталовой М. И. – отв. секр. сб.» Фото-электроника».

ул. Пастера, 42, Физический фак. ОНУ г. Одесса, 65026

E-mail: wadz@mail.ru, тел. 0482 – 726 6356.

Правила оформления и справки находятся на сайте:<http://photoelectronics.onu.edu.ua>

---

Здано у виробництво 21.02.2008. Підп. до друку 22.07.2008.  
Формат 60×84/8. Папір офсетний. Гарнітура Newton.  
Друк офсетний. Ум. друк. арк. 16,74. Тираж 300 прим. Зам. № 221.

Видавництво і друкарня «Аст р о п р и н т»  
65091, м. Одеса, вул. Разумовська, 21.  
Тел.: 37-07-95, 37-14-25, 33-07-17.

**[www.astroprint.odessa.ua](http://www.astroprint.odessa.ua)**

Свідоцтво суб'єкта видавничої справи ДК № 1373 від 28.05.2003 р.